TEMPERATURE-STABILIZED SILICON RESONATORS FOR FREQUENCY REFERENCES

A DISSERTATION
SUBMITTED TO THE DEPARTMENT OF MECHANICAL ENGINEERING
AND THE COMMITTEE ON GRADUATE STUDIES
OF STANFORD UNIVERSITY
IN PARTIAL FULFILLMENT OF THE REQUIREMENTS
FOR THE DEGREE OF
DOCTOR OF PHILOSOPHY

Matthew A. Hopcroft

September 2007

I certify that I have read this dissertation and that, in my opinion, it is fully adequate in scope and quality as a dissertation for the degree of Doctor of Philosophy.

_____

Prof. Thomas W. Kenny (Principal Advisor)
Department of Mechanical Engineering

I certify that I have read this dissertation and that, in my opinion, it is fully adequate in scope and quality as a dissertation for the degree of Doctor of Philosophy.

_____

Prof. Roger T. Howe
Department of Electrical Engineering

I certify that I have read this dissertation and that, in my opinion, it is fully adequate in scope and quality as a dissertation for the degree of Doctor of Philosophy.

_____

Prof. Kenneth E. Goodson
Department of Mechanical Engineering

Approved for the University Committee on Graduate Studies.

Abstract

Frequency references are the beating heart of all modern electronics. A frequency reference provides the pulse of the computer processor, the radio channel for the mobile phone, and the timekeeping for the GPS navigation unit. However, modern frequency references are made from quartz crystals, not silicon, so they have been unable to benefit from the exponential advances in silicon-based electronic technology of the past three decades. A single quartz part now requires the same area as 1 million silicon transistors! This work describes the design and demonstration of the first stable silicon MEMS resonator suitable for high-precision frequency reference applications, with frequency stability approaching 1 part in 10 million and power consumption of less than 20 mW. At this level of precision the primary obstacle is the temperature sensitivity of the resonator. This performance is achieved with new designs that enable "micro-ovenized" resonators- resonators in a micro-scale insulated enclosure with heating and sensing elements for temperature control. Using wafer-scale silicon encapsulation technology ("epi-seal"), these devices have been fabricated in silicon volumes of less than 0.3 mm^3. The resonator temperature is stabilized with closed-loop control using a novel method of temperature sensing based on the resonator quality factor. The frequency stability performance of these CMOS-compatible silicon MEMS resonators is comparable with commercially available quartz devices, while at the same time they are several orders of magnitude smaller and more power efficient.

Acknowledgements

This thesis represents the summary of a complex project with many facets, and it would not have been possible without important contributions from a number of people; too many to list without forgetting someone, but I'll try:

First, I would like to thank my advisor, Tom Kenny, who has been as good a role model and mentor as anyone could hope for, as well as a fun guy to work with, and that combination is rare. I was fortunate to have been able to do this thesis under his supervision. Moreover, at the end of the day, his suggestions and observations were right 99.9% of the time, and I finally learned to stop betting against him.

Our research program was sustained by a partnership with Bosch RTC Palo Alto. I am thankful to Markus Lutz, Aaron Partridge, and Gary Yama at Bosch for doing the hard work of motivating the project in the early years and learning things the hard way so that they could pass that knowledge on to me.

The members of the Kenny Research Group have been an unending source of inspiration and are a great pleasure to work with. This thesis was performed as part of a large collaborative research effort, and so I had the privilege of working closely with a large team of talented people. Special thanks to Rob Candler, who shared an office corner with me and answered so many questions. Woo-Tae Park was also there at the beginning of the project and helped me understand the way things worked. The individual contributions of the team members are too many to list, but Bongsang Kim, Manu Agarwal, Renata Melamud, Saurabh Chandorkar, Chandra Mohan Jha, Suhrid Bhat, Kwan Kyu Park, Jeff Li, Hyungkyu Lee, and Jim Salvia were all invaluable team members. If I was going to do it all over again, I would ask for the same group. Klint Rose and Roger Flynn, while not Kenny Group members, get an honorary mention in this category.

My gratitude to the staff members at the Stanford Nanofabrication Facility (SNF), who work hard to keep the equipment working for students to abuse. Mahnaz Mansourpour, Nancy Latta, Uli Thumser, Maurice Stevens, and Caesar Baxter were especially helpful. And of course, nobody leaves SNF without owing a big debt of

gratitude to Eric P. Pauline Prather's amazing wirebonder skills made many of these results possible.

My thesis reading committee, Prof. Roger Howe, Prof. Ken Goodson, Prof. Bill Nix, and Dr. Kurt Petersen, were an excellent resource, and the results presented here benefited greatly from their input.

Of course, my family and friends who encouraged me, or simply tolerated my unpredictable schedule, made this work possible, and you should take your share of credit for this work. And of course Beth, who puts up with all of this for some reason, and I am eternally grateful that she does.

Table of Contents

Appendices

List of Tables

Appendices

List of Illustrations

[it is desired to have] a Watch to keep Time exactly: But, by reason of the Motion of a Ship, the Variation of Heat and Cold, Wet and Dry, and the difference of Gravity in different Latitudes, such a Watch hath not yet been made.

-Sir Isaac Newton, report to the House of Commons, 1714 [1]

Chapter 1 Introduction

It must have been quite early in the history of civilization that man felt the need to measure time. The requirements for time measurement likely began with the need to measure time scales of months for planting crops, and soon progressed to measuring hours for meetings, prayers, mealtimes, etc. With the advent of regular global travel in the 1600's, navigation became the driving force for improved timekeeping [2]. Modern timekeeping requirements are numerous and growing, from recording hours worked by laborers to synchronizing international flights and calculating interest rates. A timekeeping device has two components: a frequency reference, which indicates the passage of a time interval, and a counter, which records the number of intervals. For most of history, these two components have been inseparable, but with the advent of the radio and digital technologies in the 20th century, the frequency reference has evolved independently and become an essential part of modern life. All digital devices require a frequency reference in order to regulate their operation, and all radio devices require a frequency reference to determine the period of their radio signals. Some 10 billion frequency reference devices are manufactured every year [3], as each mobile phone, camcorder, television, personal computer, etc., requires at least one, and often as many as five or six (one for

each subsystem). The design and manufacture of frequency references is therefore a subject of active research and development, and this thesis presents the results of an investigation into the engineering of a new type of advanced frequency reference which has the potential to meet the requirements of the future.

1.1 Frequency References

An electronic frequency reference is a device that generates an oscillatory output signal (usually a voltage waveform) with a fixed period. A frequency reference is based on an oscillator, which is composed of a resonant tank element and the sustaining circuit which drives the resonant element (Figure 1.1). The resonant tank may be any kind of system that exhibits resonant behavior: pendulum, resistor-inductor-capacitor (RLC) circuit, guitar string, tuning fork, etc., while the oscillator sustaining circuit and any additional signal conditioning circuitry are usually electronic circuits. The characteristics of the resonant element, including resonant frequency, quality factor, temperature sensitivity, etc., largely determine the characteristics of the oscillator output. The design of a frequency reference, therefore, begins with the choice of the resonant tank element, or resonator, and the essential difference between frequency reference technologies is the resonator.

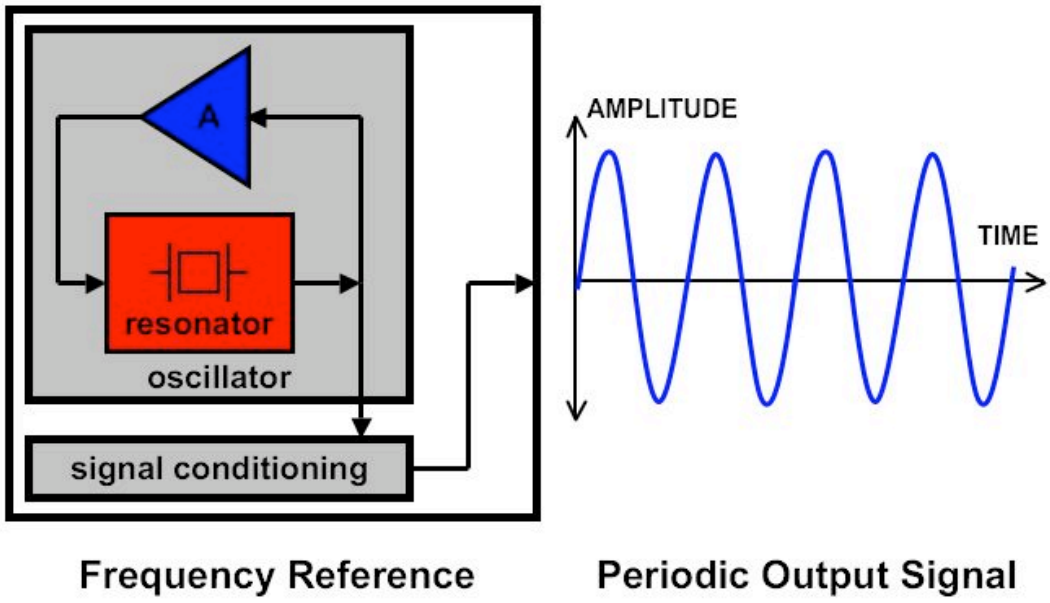

Figure 1.1: Frequency reference schematic
The oscillator consists of a resonator and feedback amplifier. The output of the oscillator may be modified (buffered, multiplied, filtered, etc) to produce a useful frequency reference signal. The final output signal is [ideally] a sine wave with high spectral purity and stability. Another common output format is the pulse-per-second (pps), which is a low duty-cycle 1 Hz pulse used for digital timing applications.

The most popular technology for manufacturing modern frequency references is based on quartz crystals. Quartz is a piezoelectric material, so an electric voltage can be used to induce a vibration in a properly designed piece of quartz. This vibration produces a corresponding output voltage which is the basis for the resonator frequency output. This means that quartz can be easily used with electronic technology, unlike, say, a swinging pendulum or a metal spring. Quartz technology has been the focus of intense research and development since the first quartz crystal was demonstrated in 1922 [4] (see [5] for a history of quartz crystal development), and quartz-based devices have achieved very high levels of performance. A detailed discussion of the uses and requirements of modern frequency references is given in [6]. The essential feature of frequency reference performance is that the frequency of the output signal should be constant over time; it should have good *stability*. Quartz crystal frequency reference products are sold in a dizzying array of sizes, shapes, and acronyms, but they

can be classified into four broad categories based on the method of achieving stability [7]:

1) The basic Crystal Oscillator (XO). These are the cheapest and most common frequency references, with the lowest levels of performance. Often they are sold simply as a packaged quartz piece without any oscillator circuitry. The customer must supply a circuit to complete the system.

2) Temperature-Compensated Crystal Oscillator (TCXO). These are sold as a single component which includes the oscillator circuitry required to generate the frequency output. This circuitry is temperature-compensated using circuit components with opposing temperature coefficients chosen so that the stability of the output frequency over temperature changes is increased.

3) Microprocessor-Controlled Crystal Oscillator (MCXO). These are oscillators whose output frequency is modified by a dedicated microprocessor, typically using a phase-locked-loop or digital frequency multiplier to adjust the output frequency as required to maintain output stability.

4) Oven-Controlled Crystal Oscillator (OCXO). These devices are built inside a temperature-controlled enclosure for maximum temperature (and hence, frequency) stability. This enclosure is typically rather large (1-10 cm^3) and consumes large amounts of power for heating (1 W or more).

These categories are shown in Figure 1.2. It is clear from the figure that increasing the performance of a quartz-based device requires increasing the size, power consumption, and price of the device. Clever circuitry and manufacturing may modify the slope of this performance function somewhat, but it cannot be escaped entirely as long as the underlying technology is the same.

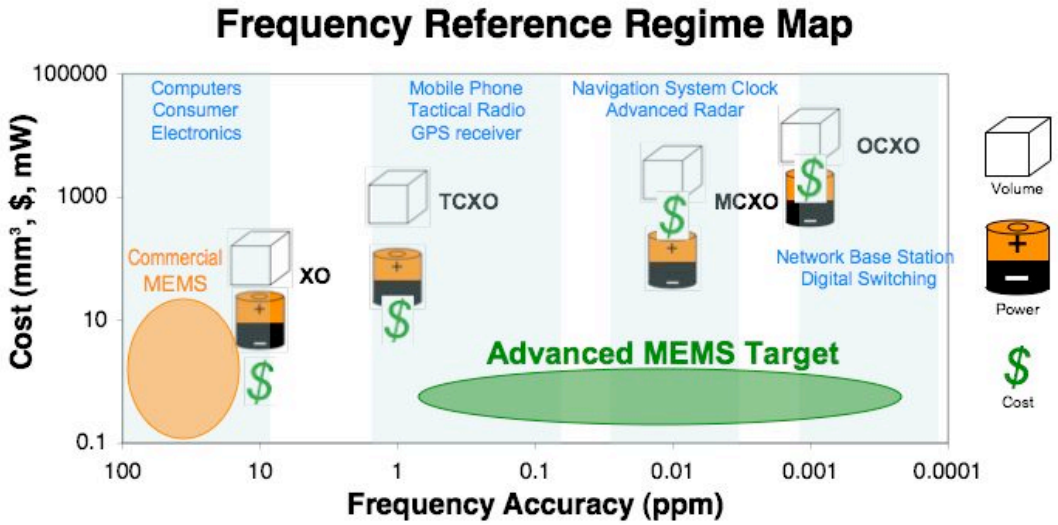

Figure 1.2: Frequency reference technology regime map
The horizontal axis value "Accuracy" combines several important measures of frequency reference performance and indicates how much the frequency output can be expected to deviate from its nominal value (i.e., smaller values are better). Accuracy is given in parts-per-million (ppm). Using silicon MEMS resonators instead of quartz crystals can enable high performance with low cost, size, and power.

It is the goal of this work to show that silicon MEMS resonators can not only replace quartz crystals, but also create new devices with superior frequency performance and orders of magnitude improvement in size, cost, and power consumption (Figure 1.2). Such devices can enable new technologies that are not possible with the limitations of quartz [8].

Certainly any industry that manufactures 10 billion units per year can be expected to continue doing so in the near term. However, as the 21st century begins, the era of quartz ends, for two reasons:

1) Miniaturization: the shrinking of technology requires ever smaller components and there are practical limits on the minimum size of quartz piece that can be used. New manufacturing and handling techniques for quartz have extended this limit for years, but it is impossible to keep up with the size reductions of digital technology, which uses batch fabrication techniques and follows Moore's Law [9]. A modern microprocessor chip might have 10 million transistors. To operate, it requires a single quartz frequency reference that is half the size of the entire chip!

2) Silicon compatibility: the progress of modern technology is inextricably bound up with the progress of silicon and complementary-metal-oxide-semiconductor (CMOS) integrated circuit technology. Devices that can be manufactured with silicon technology are promoted because they can be manufactured cheaply using the existing silicon batch fabrication capacity, and digital circuitry can be integrated into them directly, enhancing their performance and function. For example, automobile dynamic stability systems were impossible to deploy on a commercial scale until silicon MEMS-based inertial sensing systems were developed [10]. Optical projection systems are now made with an array of millions of separate mirrors on a silicon substrate, each smaller than the period at the end of this sentence [11]. Such devices can only be manufactured using batch fabrication technology, and silicon-based batch fabrication technology has the weight of the 30 years and trillions of dollars of CMOS development behind it. Quartz crystals are not silicon-compatible, and so they become simply the latest electronic technology to be knocked aside by the silicon juggernaught.

It should be noted that there are some efforts being made to integrate quartz and CMOS-compatible silicon to create frequency references [12, 13]. However, the cost of combining the two separate technologies outweighs the benefits and it seems likely to remain so.

The question, then, becomes: how can we make frequency references in silicon or CMOS-compatible materials? Silicon is not piezoelectric, so we cannot simply duplicate quartz technology. However, silicon is an excellent electrical and mechanical material and it is available in industrial quantities at extremely high purity. Researchers have been reporting on silicon-based resonant devices for over 20 years. One issue has prevented them from replacing quartz: frequency stability. A frequency reference is only as useful as its output is stable- if the output frequency varies, then it is not much of a reference! With the recent development of epitaxial silicon encapsulation technology ("epi-seal" [14]) it has become possible to consider designing a high performance silicon-based frequency reference.

This thesis describes the design and demonstration of the first stable silicon resonator suitable for high-precision frequency reference applications. By building on the silicon MEMS fabrication techniques developed previously [15-17], the design, fabrication, and operation of stable silicon MEMS resonators has been accomplished. Chapter 1 introduces the topic of stability in frequency references, and reviews prior work in silicon MEMS resonator research. Chapter 2 covers the fabrication of stable encapsulated silicon resonators. Chapter 3 develops the theoretical analysis of stability in silicon resonators. In Chapter 4, proposed solutions are analyzed, and Chapter 5 has experimental methods and results. Chapter 6 envisions directions for future research and development.

1.2 MEMS Resonator Development

MEMS resonators have been a topic of research for almost 40 years. Significant advances have occurred in the past 20 years, and commercialization efforts have begun in earnest in the last 5 years.

1.2.1 Research

The potential of integrating flexural-mode mechanical resonators with integrated circuits was recognized soon after integrated circuits began to become popular [18]. The first MEMS resonator is usually attributed to Nathanson [19] who created a “resonant gate transistor” (RGT) using electroplated gold in 1967. MEMS resonators have been an active area of research since then because they have many potential uses beyond frequency references, including: sensors [20-22] for mass (vapor, chemicals, proteins, etc.) [23, 24], pressure [25, 26], strain, force, and/or acceleration [27-30], temperature [31]; RF filters and mixers [32, 33]. Surface wave and bulk acoustic wave resonators were most common in the decades following the RGT because the fabrication was generally easier. As surface micromachining technology developed [34], more complex resonator designs were introduced in the late 1980's and early 90's [35-37]. Many of these designs introduced features in

MEMS resonator design, such as folded beams and comb drives, which are still in use today. A sample of various designs of MEMS resonators is shown in Figure 1.3.

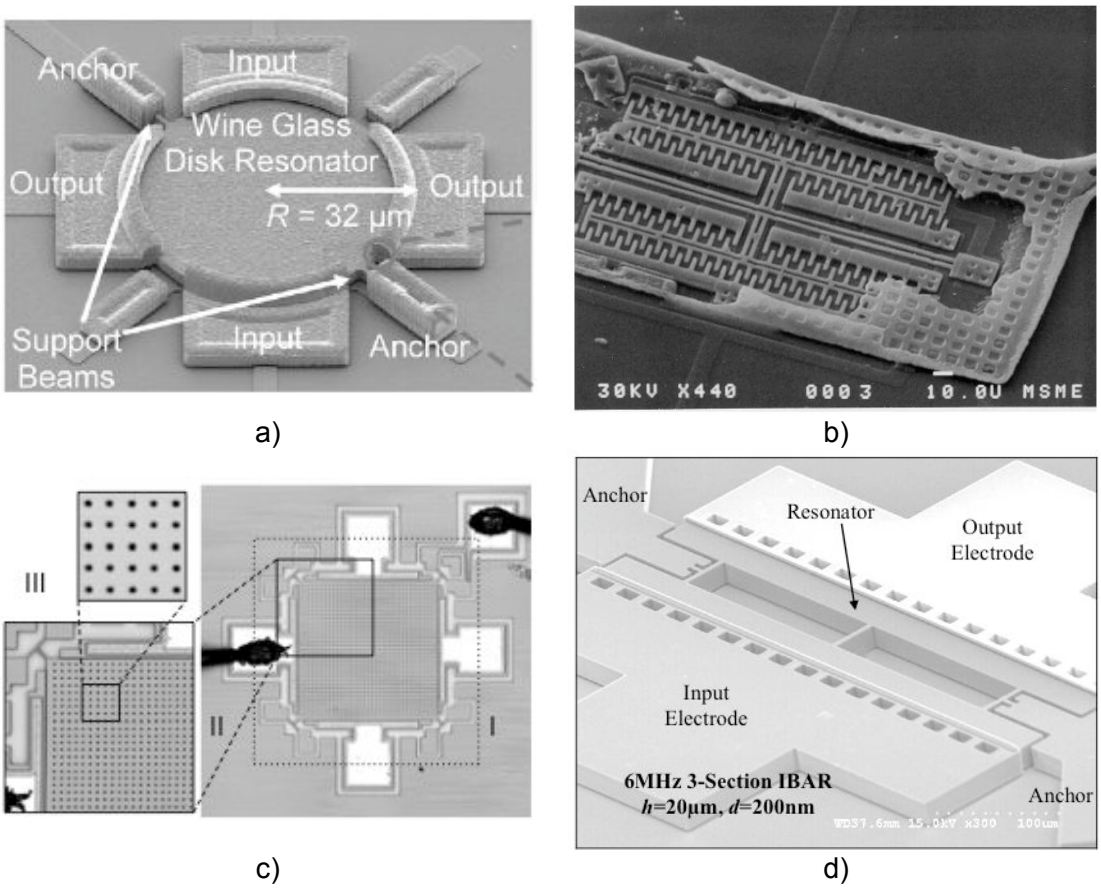

Figure 1.3: Examples of silicon MEMS resonators.
a) "Wine-glass" resonator [38]
b) Comb-drive tuning fork resonator with polysilicon encapsulation [39]
c) "I-bar" resonator, designed for high bias sensitivity [40]
d) Square bulk mode resonator [41]

As technology has improved, and the potential utility and value of MEMS resonators has improved, research in the area has increased. Figure 1.4 illustrates the trend by showing the number of research publications related to silicon resonators. A sharp increase is evident in 2003, corresponding to the start of several large research programs, including the program that supported this work[1].

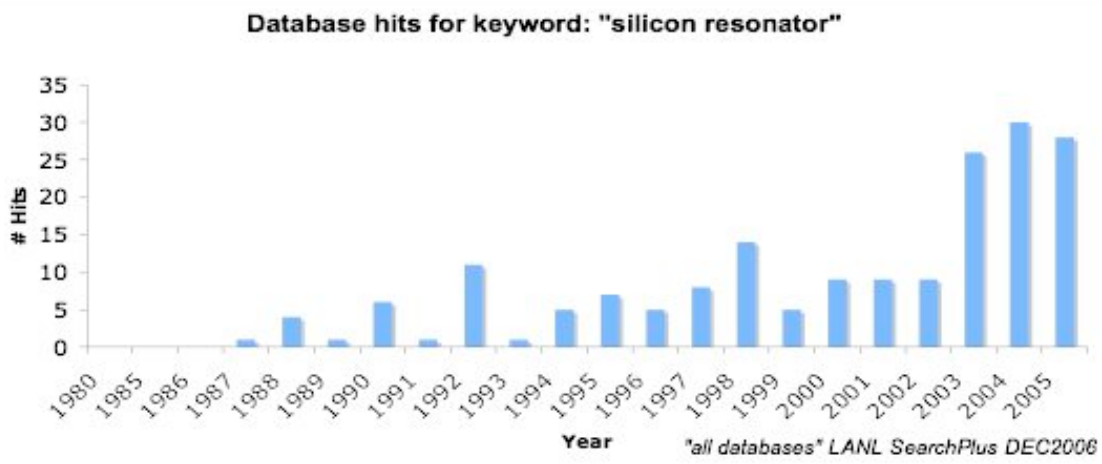

Figure 1.4: MEMS resonator research survey
The survey was performed by searching with the keywords "silicon resonator" in LANL SearchPlus with "all databases" selected, and the results restricted to each year of interest.

Recently, other investigators have approached the problem of using silicon MEMS resonators for frequency references. These efforts have either not reported frequency stability and focused on other aspects of resonator performance (e.g., phase noise, power handling) [42-46] or reported consumer-grade frequency stability [40, 47-49].

[1] This work was supported by the DARPA HERMIT program (ONR N66001-03-1-8942)

1.2.2 Commercialization

There are several companies actively engaged in commercializing silicon MEMS resonator technology for frequency references. They are concentrating on the high-volume consumer electronics markets which have relatively relaxed frequency stability requirements, indicated in Figure 1.2. A list of startup companies is given in Table 1-1. Of particular note is SiTime, Inc., which is commercializing the MEMS "epi-seal" fabrication technology used in this work for consumer applications.

Company		Core Technology	Year Founded
Discera	Discera, Inc.	Silicon MEMS	2001
Mobius	Mobius Microsystems, Inc.	CMOS	2002
SiTime	SiTime, Inc.	Silicon MEMS	2004
Silicon Clocks	Silicon Clocks, Inc.	SiGe MEMS	2005
VTI Technologies	VTI Technologies Oy	Silicon MEMS	2006

Table 1-1: Startup companies developing new frequency reference technologies

1.3 The Stability Problem

The stability of a signal is the deviation of the signal value from a target value over time. Stability is the primary performance characteristic of a frequency reference- a frequency reference is only useful over time scales where its frequency doesn't change much. Stability can be classified into three types based on the time period over which the signal is measured: long-term ("aging"), medium-term ("stability"), and short-term ("noise").

Stability measures are usually given in terms of normalized deviation from a target value, or "parts". In precision frequency measurements, the parts-per-million (ppm), or 10^{-6} (i.e., "1 part in 10^{6}") is commonly used.

1.3.1 Long-term stability

Long-term stability is characterized by changes in frequency over hours, days, or months [50]. It is also called aging or drift. In quartz devices, aging is ascribed to things like outgassing in the package that holds the quartz device; reflow of the metal electrodes; relaxing of solder joints, change in the quartz crystal under temperature cycling, etc [51]. Aging also has two types: fast, or "burn-in", and slow. It is typical for quartz product data sheets to specify an initial burn-in period (1 month is typical, see Appendix E [52]) during which the device will age rapidly as initial outgassing or solder reflow occurs [7]. In this case, the [slow] aging specification is valid after the initial burn-in period (Figure 1.5). Aging values are specified in fractional changes given as parts-per-million (ppm) or parts-per-billion (ppb) of the initial value. Extremely high-stability references may specify their drift as a fractional change with an exponent, e.g., "2×10^{-11} per year".

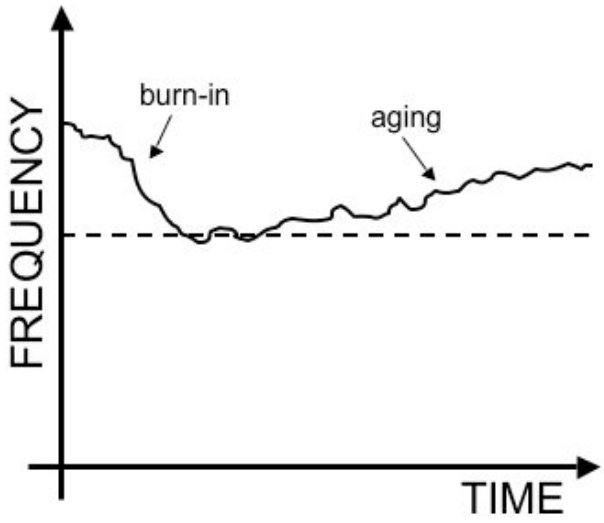

Figure 1.5: Long-term frequency aging or drift
The time scale is months or years.

1.3.2 Medium-term stability

Medium-term stability is characterized by changes over seconds to hours (Figure 1.6). Medium term stability is dominated by temperature sensitivity, and the term "frequency stability" typically refers to frequency stability against temperature. Other things can affect medium-term stability, such as acceleration, magnetic fields, or supply voltage fluctuations, but these are usually smaller effects that can be easily controlled or specified (do not operate device near magnetic fields, etc). However, temperature is a pervasive, unavoidable phenomenon, and temperature sensitivity is one of the most serious obstacles to stable frequency reference operation. Stability may be specified as a maximum ± deviation from a nominal value or a frequency range (maximum value minus minimum value). Temperature stability values are usually given in ppm or ppb over a temperature range.

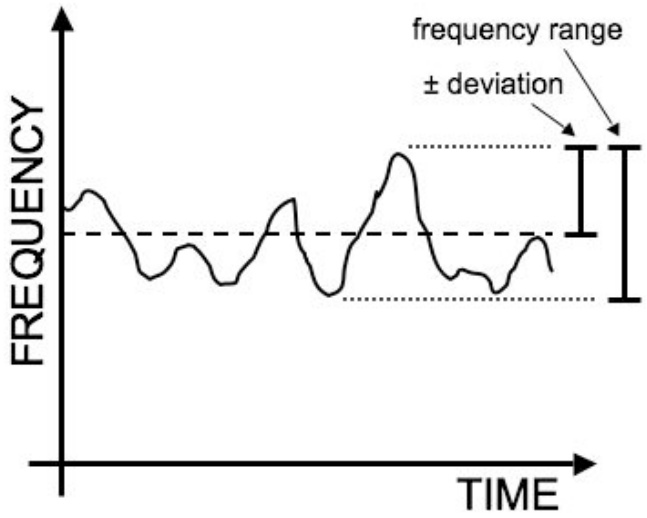

Figure 1.6: Medium-term frequency stability
The stability is the maximum variation from the nominal value. The time scale is minutes or hours.

1.3.3 Short-term stability

Short-term stability is noise- random frequency changes that happen in time periods of seconds or less. Noise in frequency signals can be characterized in the frequency domain, where it is called “phase noise”, and given in units of decibels with respect to the magnitude of the carrier frequency (dBc) in a one Hertz bandwidth at a certain frequency separation from the carrier. For example, reference oscillators for GSM mobile phones must have phase noise better than -130 dBc/Hz at 1 kHz offset from a 13 MHz carrier [38]. Figure 1.7 illustrates noise in the frequency domain.

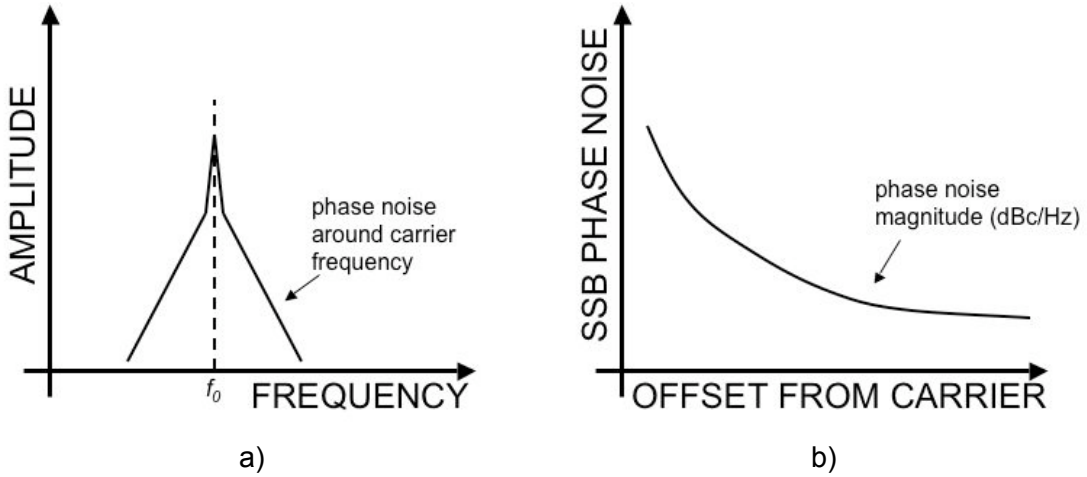

Figure 1.7: Short-term noise in the frequency domain
a) Manifestation of phase noise in the frequency domain. The sideband "skirts" are symmetric if the noise is randomly distributed.
b) Because of symmetry, phase noise is often presented as single sideband (SSB) noise, which is the ratio of power in one phase modulation sideband per Hertz bandwidth, at a frequency offset from the carrier frequency, to the total signal power (dBc/Hz).

Frequency noise can also be characterized in the time domain, where it is called “clock jitter”, and is given in ± time units, typically picoseconds, or as an RMS value. The jitter value represents the deviation from the time that the signal transition occurs versus the time that it "should" occur at the nominal output frequency (Figure 1.8).

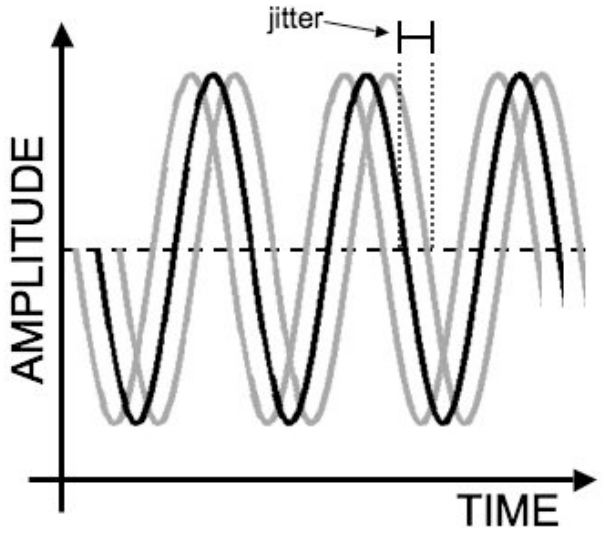

Figure 1.8: Short-term noise in the time domain
"Clock jitter" is the amount that the zero-crossing of the measured signal (gray lines) deviates from the time of the zero-crossing of the signal at the nominal frequency (black line). The value may be a ± value in time units representing a maximum deviation, or an RMS value if the noise is randomly distributed.

1.3.4 Stability Characterization

Frequency stability can be given as a "maximum deviation" value, as in Figure 1.6. It can also be described by the Allan variance of the frequency output [53, 54]. Allan variance, σ_y^2, is a "two-sample" variance of a time series measurement. It is computed as follows:

$$\sigma_y^2(\tau) = \frac{1}{2(m-1)} \sum (y_{n+1} - y_n)^2 \ , \qquad (1\text{-}1)$$

where the y_n are the individual frequency measurements, and m is the total number of measurements. The corresponding Allan deviation is:

$$\sigma_y(\tau) = \sqrt{\frac{1}{2(m-1)} \sum (y_{n+1} - y_n)^2} \ . \qquad (1\text{-}2)$$

In these equations, τ is the "averaging time". Each value of σ_y represents the variance of the signal when the measurements are averaged over τ seconds. The two-sample quantities are commonly used to compare oscillator stability performance

because the normal variance and standard deviation do not converge for typical oscillator measurements. An idealized plot of Allan deviation is shown in Figure 1.9.

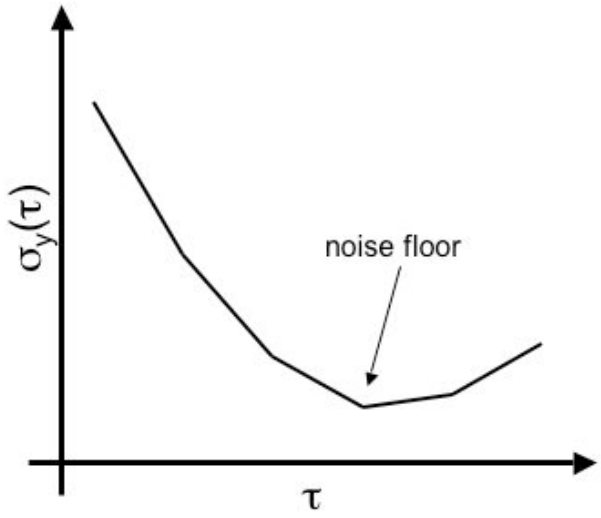

Figure 1.9: Ideal Allan deviation plot
Allan deviation plots are usually log plots of both quantities. Lower values of σ_y represent better stability. Larger values of τ represent longer averaging times. The left side of the curve represents random noise which can be removed by averaging. The right side represents long-term drift. The minimum point is the noise floor for the oscillator.

The minimum Allan deviation value is said to be the "noise floor" for a particular oscillator. This value represents the maximum medium-term stability, or minimum uncertainty value, of the frequency output. The slope of the line on to the left of the noise floor corresponds to certain types of random noise, while the increase to the right of the noise floor represents long-term drift. See Appendix C for a more detailed explanation of Allan deviation.

The frequency stability issues introduced by phase noise and jitter are generally much smaller than the contributions from temperature and other medium-term stability effects. Moreover, because they are often random effects, they can be removed by averaging. This is can be seen from a typical Allan deviation plot (Figure 1.9). The short-term noise sets the limit of stability on the left side of the Allan deviation plot, where the averaging time is short. Averaging is not an option in all

situations, and phase noise is particularly important when designing frequency references for RF applications.

1.3.5 Stability in Applications

Frequency stability has different significance in different applications. For example, for the frequency reference in a Global Positioning System (GPS) receiver, the long-term stability is not very important, because the time signal is updated from the GPS satellite signal every few minutes [55]. However, the short-term stability (noise) affects the precision of the resulting position and the averaging time required to achieve a given precision, while the medium-term stability affects the position accuracy when the satellite signal is unavailable, such as when driving through a tunnel. On the other hand, the atomic clocks used for global timekeeping, such as the NIST F-1 [56], produce a time signal that is calculated once a month. In this case, the long-term drift is most important and the short-term noise is relatively unimportant, as it can be averaged out over the long integration period.

To put some perspective on stability values, a typical consumer videocassette recorder might use an inexpensive TCXO frequency reference with an overall accuracy of 10 ppm. There are 2.6×10^6 seconds in a month, so we could expect the VCR clock to lose or gain up to 26 seconds in a month. Typically this loss or gain will be a continuous, monotonic process, as the VCR in the living room is in a relatively stable environment. If the VCR clock is not reset occasionally, you will begin missing the start or end of your favorite recorded television shows. On the other hand, a modern, high-end, expensive quartz-based wristwatch might have a yearly deviation of as little as 3 seconds, or 0.1 ppm [57]. However, the wristwatch time deviation at any given moment is likely to be greater than that, especially when the watch is not being worn or the weather is extremely hot or cold.

1.4 Conclusions

The size, cost, and power consumption of quartz crystal frequency references are simply too large for many future applications. A new paradigm for frequency

references is required to allow them to keep pace with technological evolution in other areas. Silicon MEMS resonators are a strong candidate for replacing quartz crystals, but if they are to be truly disruptive technology, their frequency stability must be improved by 4 to 6 orders of magnitude while maintaining advantages of small size, low cost, and low power consumption. This thesis presents a solution to silicon resonator frequency stability which meets these goals.

There is plenty of room at the bottom.
-Richard Feynman

Chapter 2 Fabrication of Stable Resonators

This chapter describes the MEMS fabrication process that was used for the resonators described in this work. The fabrication is described with an emphasis on the design choices which were made in order to ensure the long-term stability of the resonators. The silicon MEMS resonators described here are unique because they are fabricated using a microfabrication process that creates resonators that are effectively buried inside a silicon die in a small cavity filled with hydrogen gas. This allows the resonators to operate with unprecedented long-term stability. This process is called "epi-seal" [14] because the devices are encapsulated with epitaxially-deposited silicon. Epi-seal technology is an extension of "oxide-seal" technology developed previously [15, 58, 59] in which devices were encapsulated with deposited silicon dioxide.

2.1 Silicon Stability

The first design choice for a stable MEMS resonator is the material that will comprise the resonator structure. Silicon is chosen for this work not only because of the economic reasons given in Chapter 1, but also for long-term stability. The most important aspect of silicon as a material for stable MEMS resonators is that it is a crystalline material with a uniform, regular atomic structure. This means that in a high-purity sample there will be very few dislocations or cracks that would cause the

material to change under loads and stresses that are below the plastic deformation limit. In fact, crystalline silicon is strong but brittle; it fractures rather than deforming plastically, and the stress-strain curve is quite linear up to the fracture point [60, 61]. While no one has publicly postulated an "endurance limit" for silicon, below which the material would not experience fatigue, there is almost no evidence of fatigue of silicon at low temperatures (below ~600 K [62]), except when stressed by high moisture or oxygen atmospheres or in small structures with extremely high surface roughness [63-65]. The result is that a hypothetical pure smooth silicon bar, suspended in a stable, low temperature environment, deformed only by small amounts that create stresses well below the fracture limit, can be expected to undergo no significant material changes and behave in a consistent and predictable manner over time. This is in contrast to most metals, for example, which often have low yield strengths. Other sources of instability of a resonator involve external factors, such as physical contamination[2] or applied stresses. The challenge, then, is to fabricate a structure that recreates, as closely as possible, the hypothetical silicon device isolated in a stable environment.

[2] As discussed in Chapter 3, the resonator frequency is proportional to the square root of the inverse of its mass. The mass of the resonators considered here is on the order of 100 picograms. The mass of a single atomic layer of silicon on the resonator is on the order of 1 picogram. So physical contamination equivalent to a single atomic layer of additional mass deposition can change the frequency by hundreds or thousands of ppm!

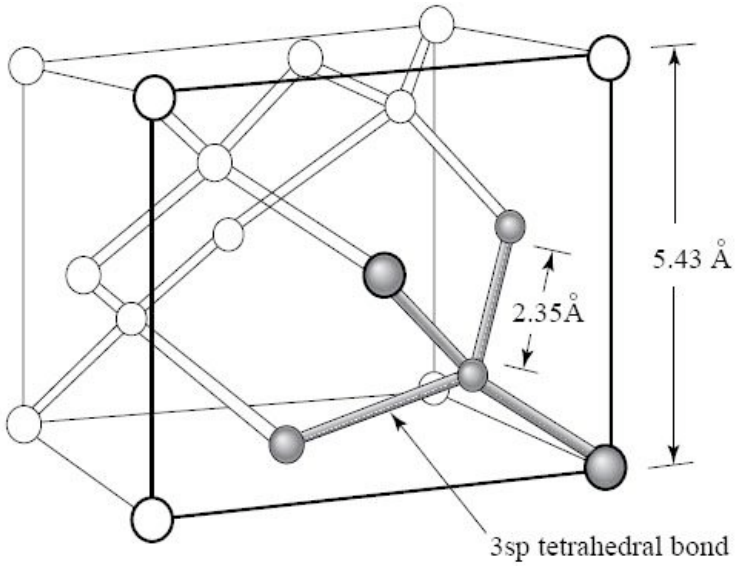

Figure 2.1: Silicon crystal structure.
Silicon has a diamond-type lattice and cubic symmetry. From [66].

2.2 An Overview of MEMS Encapsulation

Packaging of MEMS devices is essential for using them outside the laboratory. There are many different requirements for packaging, and the packaging may take many different forms [67]. Where the MEMS device has moving parts, those parts need to be protected from damage or contamination. Sensors may require a connection with the outside world, such as a putting a flow sensor in contact with the liquid or gas that is being measured. When MEMS devices need to interface with their environment through macro-scale components, such as a gas line, the packaging processes quickly becomes complex.

Resonators for frequency references, along with accelerometers and gyros, do not need any interface with their environment, and in fact, benefit significantly from *not* having any interface with their environment, so the packaging requirement is basically that they be sealed inside a mechanically robust enclosure with freedom to move. This kind of packaging is most often done by bonding a second silicon wafer, pyrex, or glass piece [68-75] over the device. Figure 2.2 shows commercial accelerometers packaged in this way.

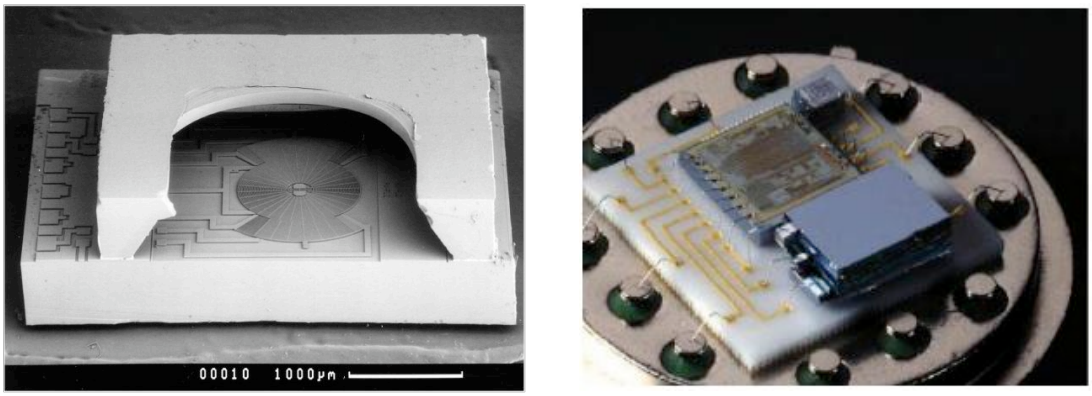

a) b)

Figure 2.2: Wafer-bond packaging.
a) SEM image of a commercial accelerometer packaged by bonding a glass cap over the top of the MEMS device (the cap has been broken for this image). The accelerometer with the bonded cap is then packaged in a standard injection-molded electronic package. (image courtesy Bosch RTC)
b) Photograph of a commercial accelerometer packaged by silicon-silicon bonding. The accelerometer proof mass is at lower right, and the control electronics are above. (Colibrys LTD)

However, with devices that do not need any macro-scale interaction with the environment, it is possible to do the packaging as part of the microfabrication process. This typically consists of depositing thin-film layers to encapsulate the MEMS device. Thin-film encapsulation has long been recognized for having advantages in size reduction, cost, and performance and so continues to be an area of active research [76, 77]. Because of the specific benefits for resonators, encapsulation has featured in some of the earliest surface-micromachined resonator work, such as the "vacuum envelope" [78] and "micro vacuum cavity" [79] from the late 1980s.

The basic process of thin-film encapsulation requires four steps (Figure 2.3):

1) deposit a sacrificial material to protect the MEMS device
2) deposit a structural layer, or frame, over the sacrificial layer
3) remove the sacrificial layer through openings in the structural layer
4) seal the openings in the structural layer to complete the enclosure

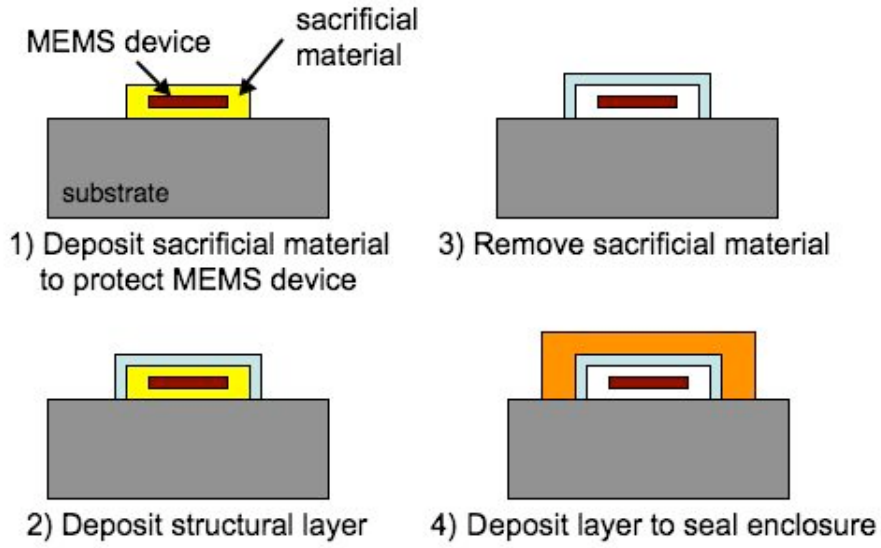

Figure 2.3: Thin-film encapsulation steps.

The main challenges in thin-film packaging are the following:

a) finding a suitable sacrificial material
b) depositing encapsulation films at sufficiently low temperatures
c) removing the sacrificial layer without harming the device
d) leaving a suitable environment inside the enclosure

Innovation in encapsulation technology has focused on these challenges. For example, while the most popular sacrificial material is silicon dioxide because of its easy availability and high etch selectivity to silicon, photoresists and other polymers have been used [80-82], although they may have problems with residual material remaining after step 3. Lebouitz, et al., [83] introduced the use of "permeable polysilicon" as the structural layer (See Figure 1.3b). This is a polysilicon that is deposited in such a way that it has a large number of pinholes in the film. This has the advantage of leaving only very small openings that need to be sealed in step 4 with a minimum of

deposition of the sealing material inside the cavity. Wet etches to remove the sacrificial layer in step 3 tend to cause stiction problems for delicate devices [84], so critical point drying [85, 86] and vapor-phase hydrofluoric acid [87, 88] have been used. Metals have been used for the structural and sealing materials because they have high resistance to diffusion and can be deposited at low temperatures by sputtering or electroplating [81]. Recently, high-angle sputtering has been used to deposit the sealing layer [89]. This reduces or eliminates secondary deposition on the encapsulated structure (see Section 2.5).

2.3 Epi-Seal Fabrication Process

The epi-seal process was designed with the goal of creating a clean enclosure for silicon devices with a low gas pressure and no contaminants or other processes which would affect the operation of the resonator after encapsulation. The process uses silicon dioxide for the sacrificial material, epitaxial silicon for the structural layer, vapor-phase hydrofluoric acid to remove the silicon dioxide, and epitaxial silicon to seal the openings in the structural layer. The epi-seal fabrication process is described in detail in Appendix B. A summary description is given here, corresponding to Figure 2.4. The fabrication of the devices described in this work was performed at the Stanford Nanofabrication Facility (SNF).

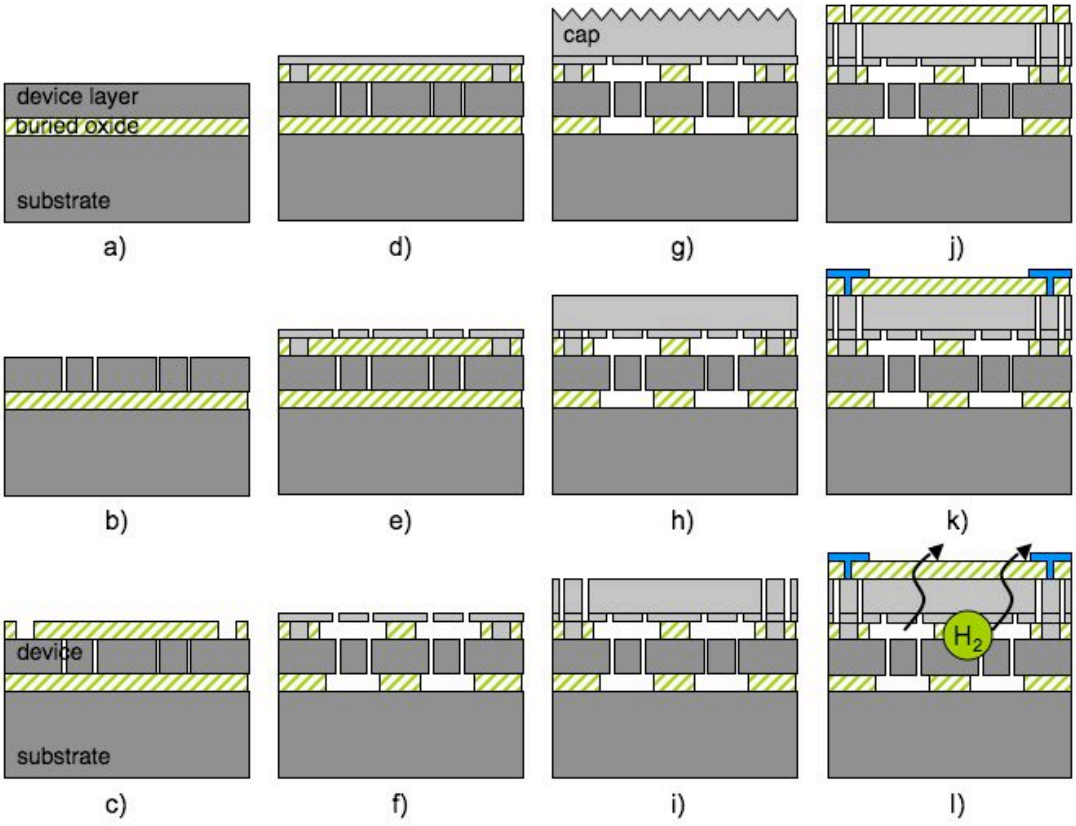

Figure 2.4: Epi-seal fabrication process.
Diagrams are cross-sections representative of a tuning fork resonator (See Chapter 3). See following text for a description of the steps, or Appendix B for details.

The epi-seal process begins with an SOI wafer with a 2 µm thick buried oxide layer and a 20 µm thick silicon device layer (a). Deep reactive ion etching (DRIE) is used etch the trenches that define the resonator structure into the top silicon layer of an SOI wafer (b). Next, the trenches of the unreleased resonator are sealed with a sacrificial layer of LPCVD oxide (c), and contact holes are etched into the oxide. These contacts provide electrical access to the encapsulated structures and mechanical support for the encapsulation layer. The silicon encapsulation layer is deposited in two steps. In the first step, a 2 µm "cap" layer of silicon is deposited on top of the sacrificial oxide (d) and vent holes are etched through the cap layer to expose the oxide (e). Vapor-phase hydrofluoric acid (HF) is then used to etch the sacrificial oxide and release the resonator structure (f). After etching the sacrificial oxide, the second part of the silicon encapsulation layer is deposited (g). This 20 µm thick "seal" layer

closes the vent holes and provides mechanical stiffness. This epitaxial silicon deposition is performed at high temperature (1000 °C) in a low-pressure reactor with the process gas dichlorosilane (DCS, formula H_2SiCl_2). Before the deposition, and high temperature bake step in H_2 is performed. This step breaks down the native oxide on the silicon and allows the silicon to reflow, smoothing out the surface features and leaving the silicon with very low surface roughness. After the vents are sealed, the DCS remaining inside the cavity quickly deposits on the silicon surfaces so the resulting gas environment inside the encapsulation is mostly hydrogen. Next, the wafer surface is planarized using chemical mechanical polishing (CMP) in order to eliminate the surface roughness of the thick epitaxial silicon and the topology over the encapsulated structures (h). At this point, the top surface of the wafer is nearly indistinguishable from an ordinary blank silicon wafer. Ring-shaped trenches are now etched into the encapsulation layer, creating isolated pillars of silicon in the encapsulation for electrical feedthroughs (i). LPCVD oxide is deposited to close the trenches and passivate the silicon surface, and contact holes are etched into the oxide (j). Finally, aluminum is deposited and patterned to make electrical connections and pads for electrical connections to the resonator (k). The final step is a low-temperature to anneal in a nitrogen ambient (l). During the anneal, the hydrogen gas remaining inside the encapsulated cavity diffuses out in a few hours. The larger nitrogen molecules are unable to diffuse into the cavity during this time [14]. The final pressure inside the encapsulation is ~ 1 Pa[3]. A SEM cross-section of a fabricated device is shown in Figure 2.5.

[3] The determination of the pressure inside the encapsulation is described in Chapter 3.

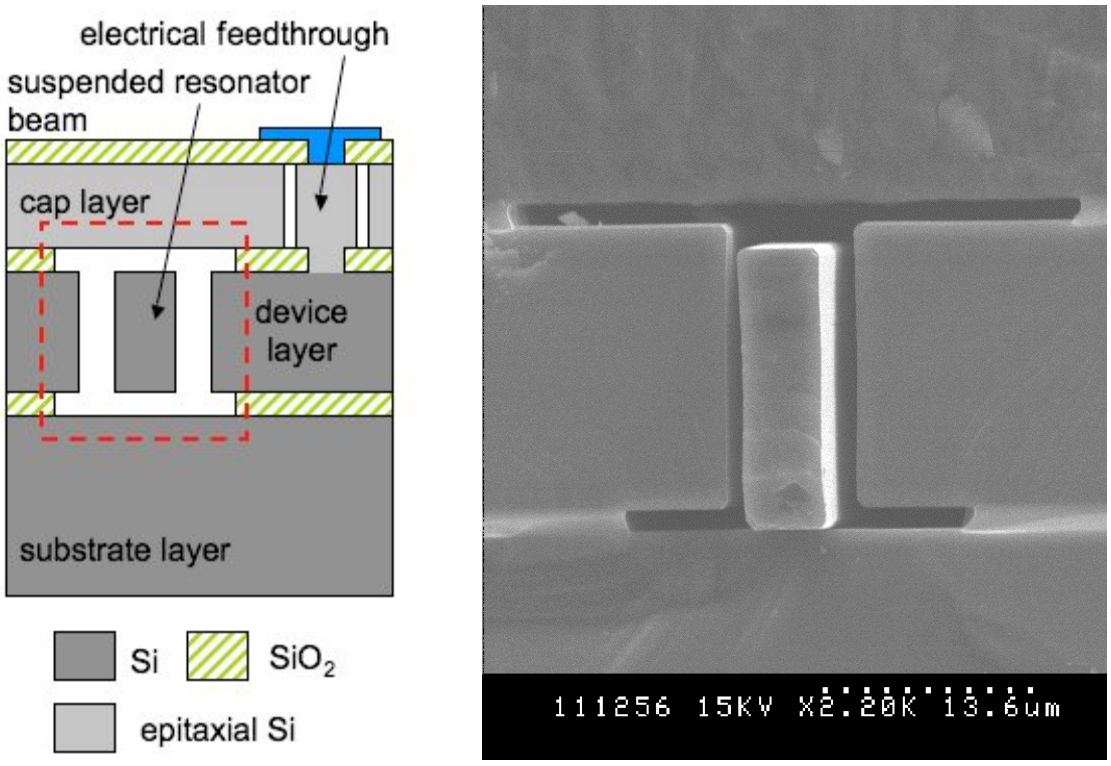

a) b)

Figure 2.5: Cross-section of an epi-seal device.
a) The key layers of the epi-seal device: substrate, device, and cap. The area highlighted in the dashed line in shown in the SEM at left.
b) A close-up SEM of an epi-seal resonator beam. The beam is resting on the floor of the cavity after being broken in order to take the picture. The epitaxial polysilicon cap is visible above the beam. The oxide layers are visible as lighter colored horizontal layers.

The oxide-seal process, mentioned above, essentially skips from step (f) to step (i) in Figure 2.4. This means that the cavity is sealed by an oxide deposition at 400 °C, rather than epitaxial silicon at 1000 °C. The deposition gases used in both processes are similar, but at the lower temperatures of the oxide deposition, the residual process gases inside the cavity do not deposit fully onto the structures inside the encapsulation. The remaining gas molecules (silane, SiH_4, and oxygen, O_2) are too large for easy diffusion through the cap, so the final pressure inside the oxide-seal encapsulation is much higher than with epi-seal, approximately 700 Pa.

2.4 Stability of Encapsulated Resonators

The advantage of the epi-seal process over previous encapsulation work is that the silicon resonators are encapsulated by epitaxial silicon deposited at very high temperatures (~1000 °C). At these temperatures, all residual moisture and contaminants, including any native oxide on the silicon resonators, are broken down and removed. The resonators are then sealed inside their encapsulated cavity by the silicon deposition. After the cavity is sealed, the remaining deposition gases inside the cavity quickly react, depositing silicon on the interior of the cavity, leaving only a pure silicon resonator inside a sterile, sealed environment. This is a good approximation for the ideal environment for high stability operation that was identified in Section 2.1, and so we expect stable resonator operation with little or no long-term drift. Figure 2.6 shows epi-seal resonator long-term test data from [90]. No long-term aging is observed, which is quite remarkable, and no burn-in period is observed either. Compare this to the drift evident in resonators encapsulated by oxide-seal shown in Figure 2.7. Further details of the epi-seal long-term testing can be found in [14, 90, 91].

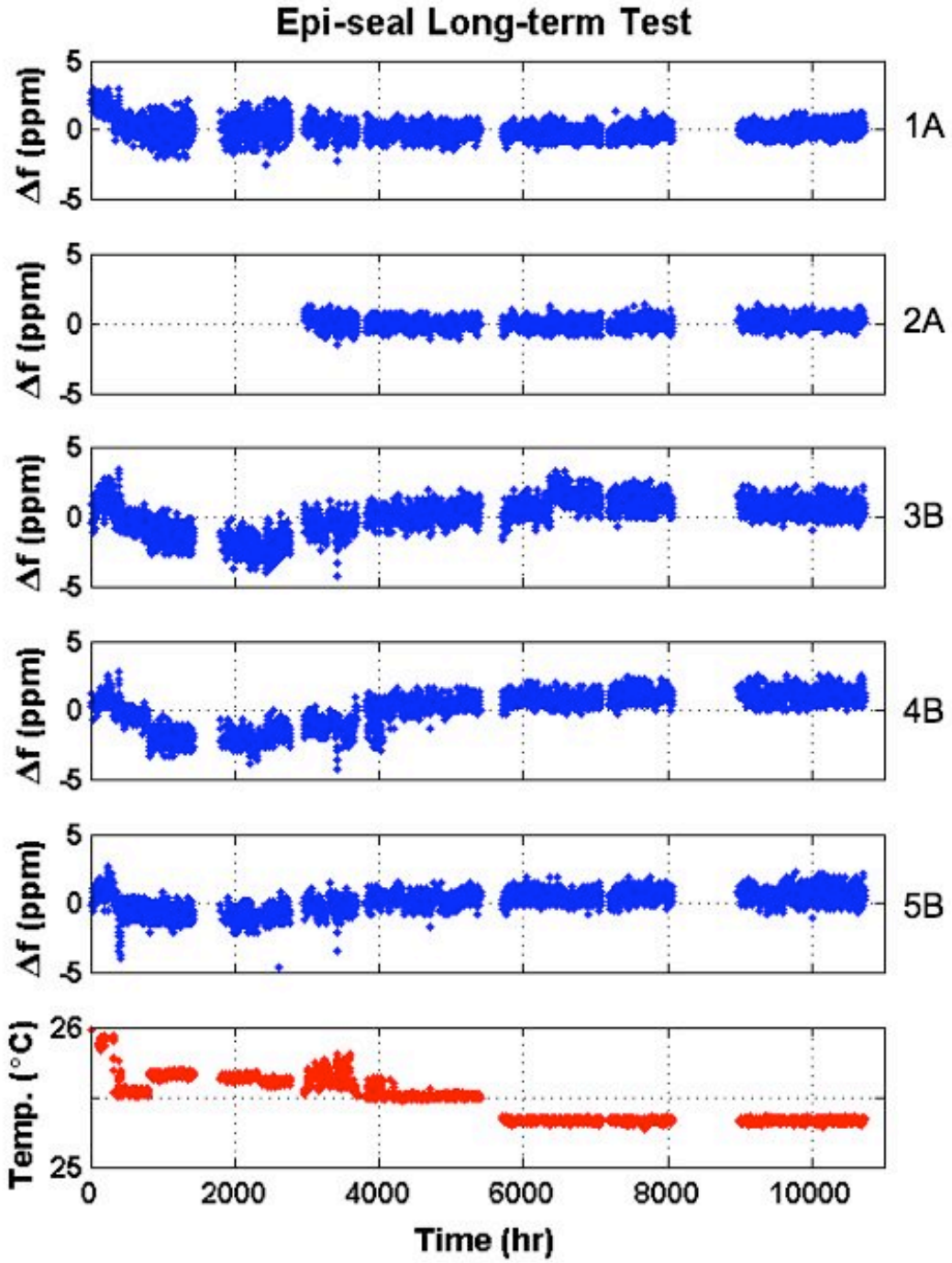

Figure 2.6: Long-term stability of epi-seal silicon resonators.
The resonators were placed in a temperature chamber set at 25 °C and measured every few minutes for over a year. No frequency drift was observed within the uncertainty of the measurement. The instability at the beginning of the experiment is attributed to electrical problems with the test setup. Resonators added after the problems were fixed do not show the initial instability. Data from [90].

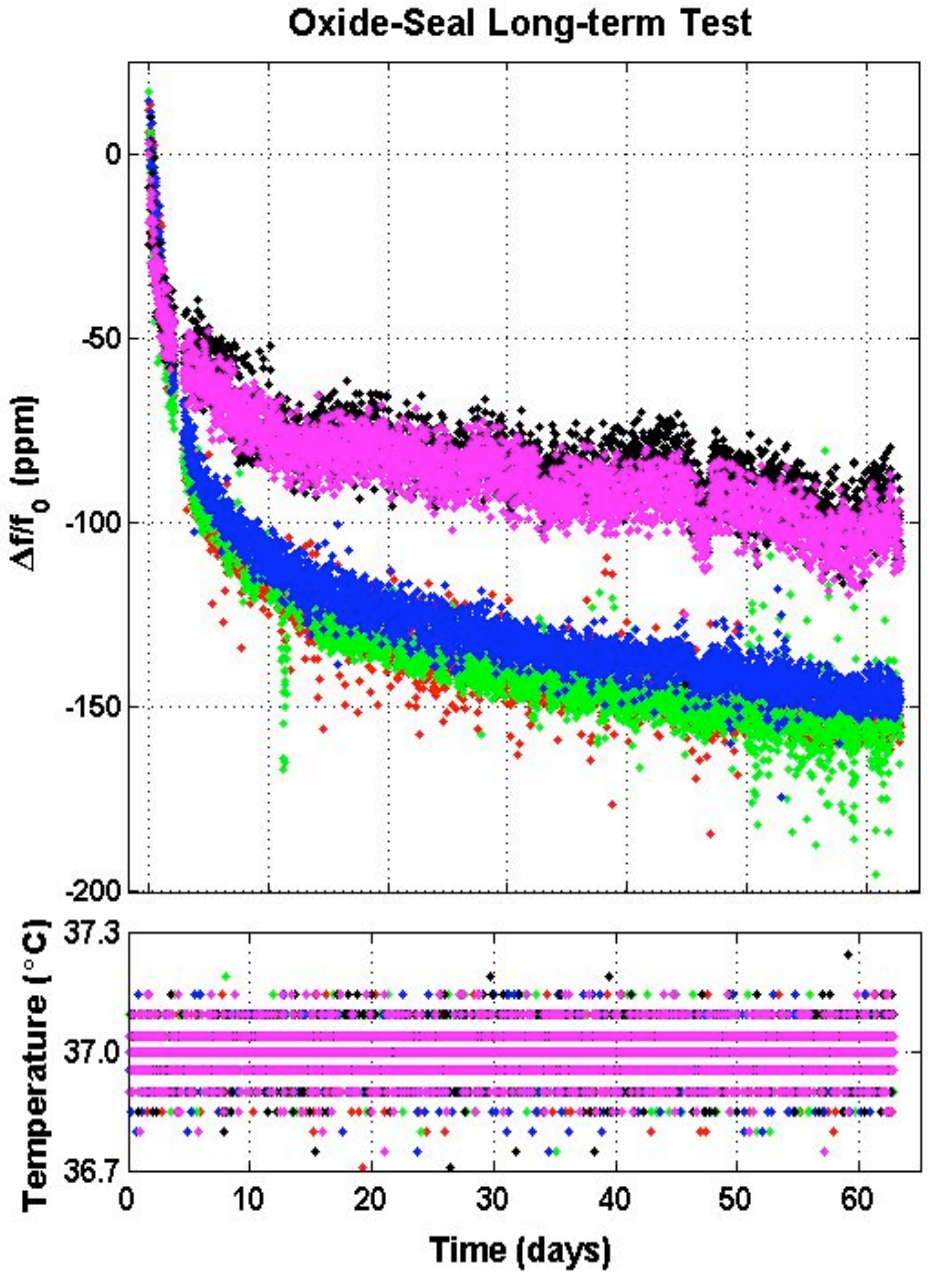

Figure 2.7: Long-term stability of oxide-seal silicon resonators.
The data from five separate resonators are shown in different colors. The resonators were placed in a temperature-controlled chamber and measured every few minutes for several weeks. Both burn-in and long-term drift are evident. [unpublished data courtesy of R. Melamud]

While the epi-seal process is more expensive and time-consuming than oxide-seal, it has been shown that encapsulating the resonators at lower temperature with a silicon dioxide deposition has adverse consequences for stability. It is suspected that

the lower temperature silicon dioxide deposition process leaves residual process gases inside the encapsulation after the cavity is sealed. Aging over a period of months can then be observed as the residual gases deposit on the resonator. Figure 2.7 shows long-term testing results from resonators fabricated in an oxide-seal process; both burn-in and long-term drift are clearly evident in these devices. It seems likely that the residual process gases remaining in the cavity after the cavity is sealed continue to react or deposit on the resonator after the fabrication has finished. Other researchers have reported some limited long-term stability data for silicon resonators that are packaged after fabrication using a commercial vacuum wafer-bonding process [49, 92]. The cavity pressures and the bakeout temperatures they report are comparable to the oxide-seal process, yet the reported drift is much lower, suggesting that controlling the composition of the gases remaining inside the encapsulation is essential for long-term stability. The epi-seal process ensures that the silicon resonators are encapsulated inside a hermetically sealed, well-controlled environment which enables reliable long-term operation.

2.5 Epi-Seal Limitations

The epi-seal fabrication process is an important advance for microfabrication of resonators. However, as currently implemented, it has three important limitations.

1) As discussed in detail in Chapter 3, the resonators described here are operated by electrostatic transduction. In electrostatic transduction, the width of the transduction gap between the electrode and the resonator is a key parameter in determining the performance of the device, and minimum width is generally desirable. In the epi-seal process, this gap is created in step (b) by deep reactive ion etching (DRIE) in silicon. The ratio of DRIE trench depth to width is limited to approximately 20:1 with the fabrication equipment available to us [93, 94]. This puts practical limits on the forces that can be applied by electrostatic actuation and hence the frequency of the resonators.

2) On the other hand, the maximum width of the trenches is also restricted. The deposition of the sacrificial oxide in step (c) must be thick enough to bridge the

trenches etched in step (b). The oxide thickness must be approximately 1.5 times thicker than the trench width, and oxide thickness is limited to 3-4 µm (see Appendix B). Therefore, devices in the cavity are limited to ~1.5 µm of displacement. That is not a serious limitation for resonators, which have displacements of nanometers or less, but accelerometers and other devices require more motion.

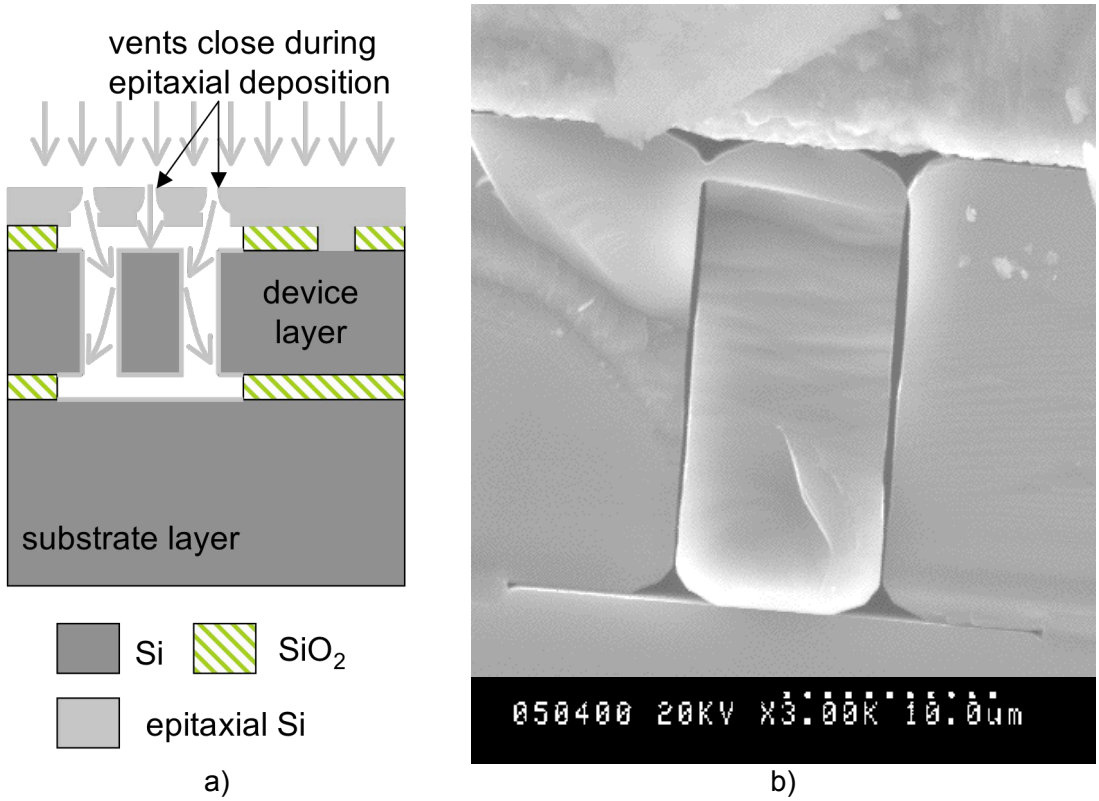

Figure 2.8: Process failure caused by excessive silicon deposition inside the cavity. This secondary deposition is sometimes called "redeposition". Compare this beam cross-section to Figure 2.5. The vent holes opened in step (e) (Figure 2.4) were larger than they should have been, so when silicon was deposited to close the holes, an excessive amount of silicon deposited on the structures inside the cavity.
a) Epitaxial deposition (step g). During deposition, some silicon is deposited on the structures inside the cavity until the vent openings have closed.
b) SEM cross-section of a resonator beam with excessive secondary deposition.

3) Another concern is secondary deposition inside the cavity in the sealing step (step g). As the vent holes are closed by deposited silicon, some silicon is inevitably deposited on the structures inside the enclosed cavity. Depositing additional silicon on the silicon devices described here is not a problem, but it does limit the types of

devices that can be encapsulated. Too much deposition can also cause failure of the fabrication process, as in the example shown in Figure 2.8.

Secondary deposition also exacerbates the problem of lateral dimension uncertainty[4]. In general, there is a significant possibility of error in the transfer of dimensions of the design as drawn to the final device through the lithography and etch steps of the fabrication process [95, 96]. These uncertainties are illustrated in Figure 2.9. See Appendix B for more description of the design and fabrication process.

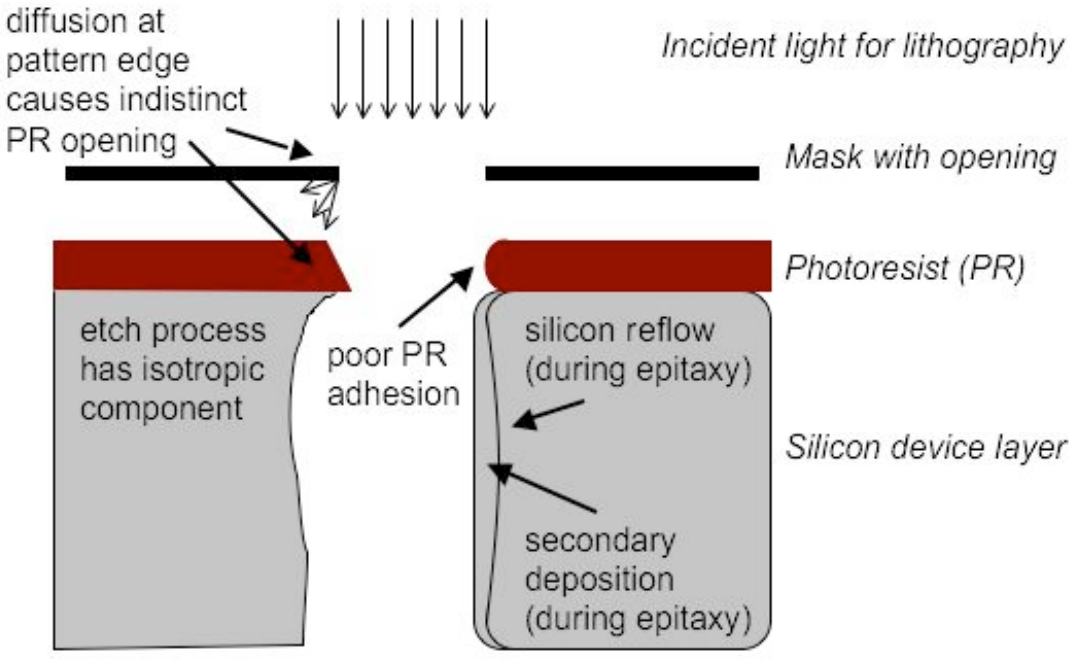

Figure 2.9: Sources of uncertainty in microfabricated lateral dimensions.
The lateral dimensions of fabricated devices are subject to uncertainty from a number of steps in the microfabrication fabrication process. In practice in epi-seal, the lateral dimensions were from -0.25 to +0.5 μm different from the intended designs.

An example of the results of DRIE processing at SNF is shown in Figure 5.10. Two parallel trench openings are drawn on the mask with width 1.5 μm. These trenches define a 5 μm wide beam structure between them. It is clear that the result is not quite a simple rectangular beam. The openings in the photoresist are slightly larger than drawn, and the trench that is created by DRIE is irregular, larger than the photoresist opening, and has scalloped sidewalls. During the epitaxial deposition for

[4] Uncertainty in lateral dimensions is an issue in microfabrication in general, not specific to epi-seal.

sealing, some additional silicon will deposit on these structures. In addition, during the high-temperature epitaxial deposition, the silicon re-flows [97], smoothing out the scallops and creating the rounded corners visible in Figure 2.5 and Figure 2.8. The result is that a significant variation in the actual lateral dimensions of epi-seal devices was observed, such that a typical rectangular structure might be between 0.25 µm less to 0.5 µm greater in width per side than designed. This sort of variation is not unusual for processing in a research fabrication facility.

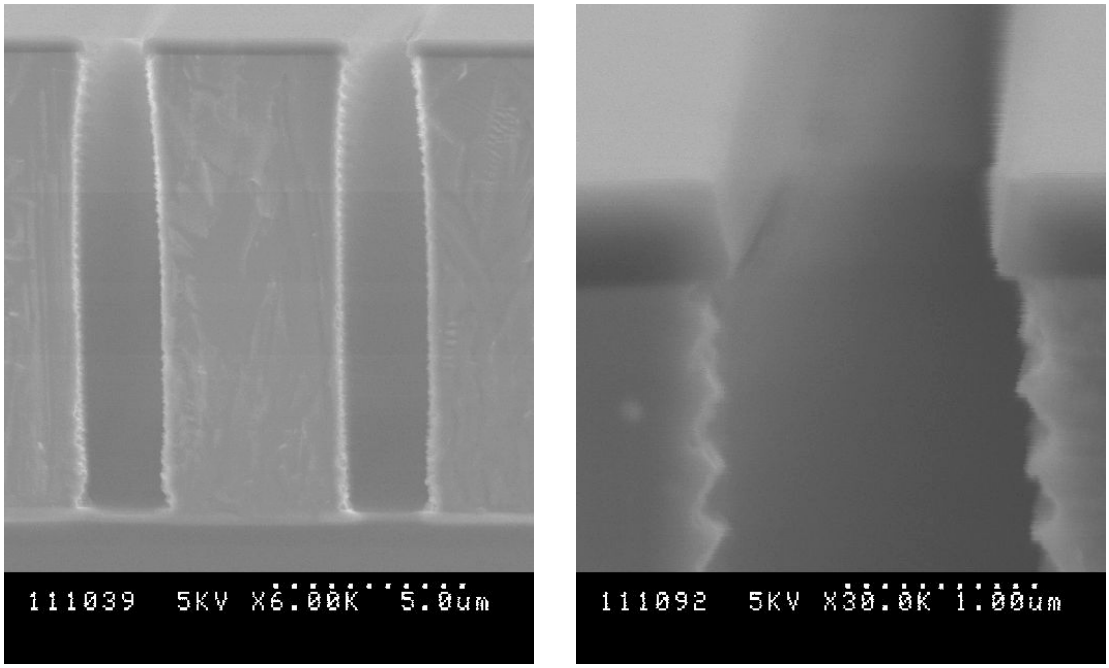

a) b)

Figure 2.10: DRIE test results.
These two trenches are etched by deep reactive ion etching (DRIE) in order to define a rectangular beam between them. The results are clearly not quite rectangular. This is typical of DRIE processing [93]. [SEM by G. Yama]
a) DRIE trenches. The trench openings were drawn 1.5 µm wide, 5 µm apart. The photoresist is visible on top of the silicon.
b) Close-up of a trench opening. The etch has undercut the photoresist and DRIE scallops are clearly visible.

2.6 Conclusions

The epi-seal fabrication process has tremendous advantages for silicon MEMS devices that require only small amounts of displacement inside a clean, robust, hermetically sealed environment. This perfectly describes the requirements for

resonators for high-stability frequency references. The results of long-term testing of resonators fabricated in an epi-seal process show that their long-term stability is as good or better than quartz crystals. The long-term resonator stability that is created by the epi-seal process makes it possible to focus on the other aspects of frequency stability.

2.7 Acknowledgements

The development of the oxide-seal and epi-seal microfabrication processes is an on-going project that began in 2001 in collaboration with Bosch RTC Palo Alto. Many people have contributed to the project, including Markus Lutz, Aaron Partridge, Gary Yama, the SNF staff, and all of the students in the HERMIT project (see Section ACK). The long-term drift experiments presented in Section 2.4 were performed by Bongsang Kim and Renata Melamud.

In mathematics you don't understand things. You just get used to them.
-Johann von Neumann

Chapter 3 Silicon Resonator Temperature Sensitivity

The medium-term frequency stability of the resonators (hereafter, "stability") is dominated by the temperature sensitivity of the resonators. In order to understand the temperature sensitivity, we must understand the operation of the resonators and develop models to describe their behavior. The specific physical device that we are considering is the double-ended tuning fork (DETF) (Figure 3.1). The DETF design is simple to analyze, yet has good performance. The coupling masses at each end of the tuning fork mechanically couple the two clamped-clamped beams so that they vibrate at the same frequency. Therefore, we can consider a single beam when describing the operation of the DETF.

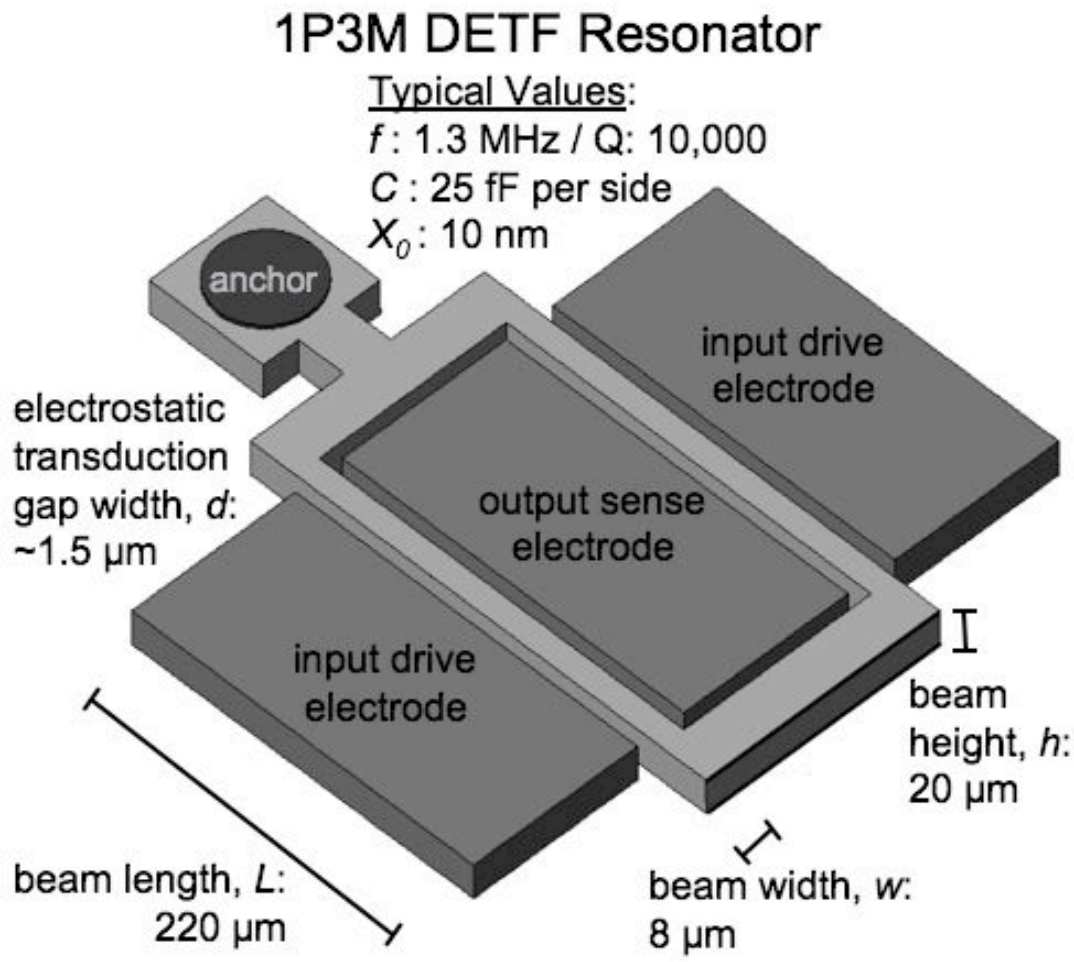

Figure 3.1: 1.3 MHz Double-Ended Tuning Fork
The experiments described in this work use the double-ended tuning fork (DETF) structure with the dimensions given here. The design is named "1P3M DETF" because it has a resonant frequency of approximately 1.3 MHz.

3.1 Electrostatic Transduction

The resonators considered here are flexural beams that are operated by electrostatics, so they are *transducers* which convert energy between the electrical and mechanical domains. Electrostatic transduction uses the attraction between electric charges to generate a mechanical force, or vice versa.

The resonator is actuated by electrostatic forces. If electric charges, Q, are constrained in separate mechanical structures, the structures will experience a force

pulling them together, F_E, which is proportional to the applied electric potential, V. [98, 99]. This is illustrated in Figure 3.2.

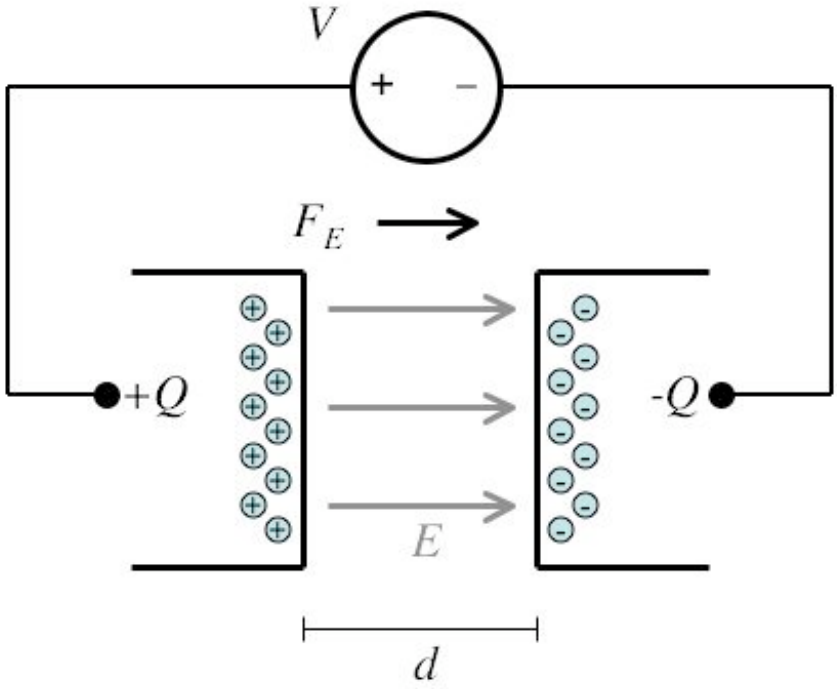

Figure 3.2: Electrostatic transduction
The attraction of charges confined in separate structures (a capacitor) creates a force attracting the two structures. Note that the force generated across a capacitive gap always acts to bring the plates of the capacitor together, regardless of the polarity of V.

We can analyze this capacitor system using the "parallel plate" model, which assumes a capacitor composed of two large[5] parallel plates of area A separated by a uniform material with dielectric constant ε. The capacitance, C, of this structure is:

$$C = \frac{\varepsilon A}{d} = \frac{Q}{V} \ . \tag{3-1}$$

The capacitor stores energy in the electric field, E, between its plates. The magnitude of the field is proportional to the amount of charge in the capacitor, which is proportional to the applied voltage. The energy stored in the system, U, is calculated by integrating (3-1) to find the total stored charge as a function of voltage:

[5] Large enough that we can neglect the fringing fields at the edges of the plates.

$$U = \int_0^V Q(V)dV = \frac{1}{2}CV^2 \ , \tag{3-2}$$

and the force attracting the plates together is the gradient of the energy function with respect to the direction of motion:

$$F_E = \frac{\partial U}{\partial x} = \frac{dU}{dd} = \frac{1}{2}V^2 \frac{d\left(\frac{\varepsilon A}{d}\right)}{dd} = -\frac{1}{2}\frac{C}{d}V^2 \ \text{, and so,} \tag{3-3}$$
$$|F_E| = \frac{1}{2}\frac{C}{d}V^2 \ .$$

The negative value of F_E indicates that the force is attracting the two plates together, in accordance with Coulomb's law. Note that F_E is independent of the polarity of the applied voltage V, and so the electrostatic force in a capacitor always acts to bring the two plates together. Because the direction of the force is always known, only the magnitude of F_E is normally used in analysis.

A cross-section of one of the resonator beams with electrical connections is shown in Figure 3.3. Two identical capacitors are formed by the structure: one between the input electrode and the beam, and one between the beam and the output electrode. A fixed bias voltage (V_b) is applied to the resonator.

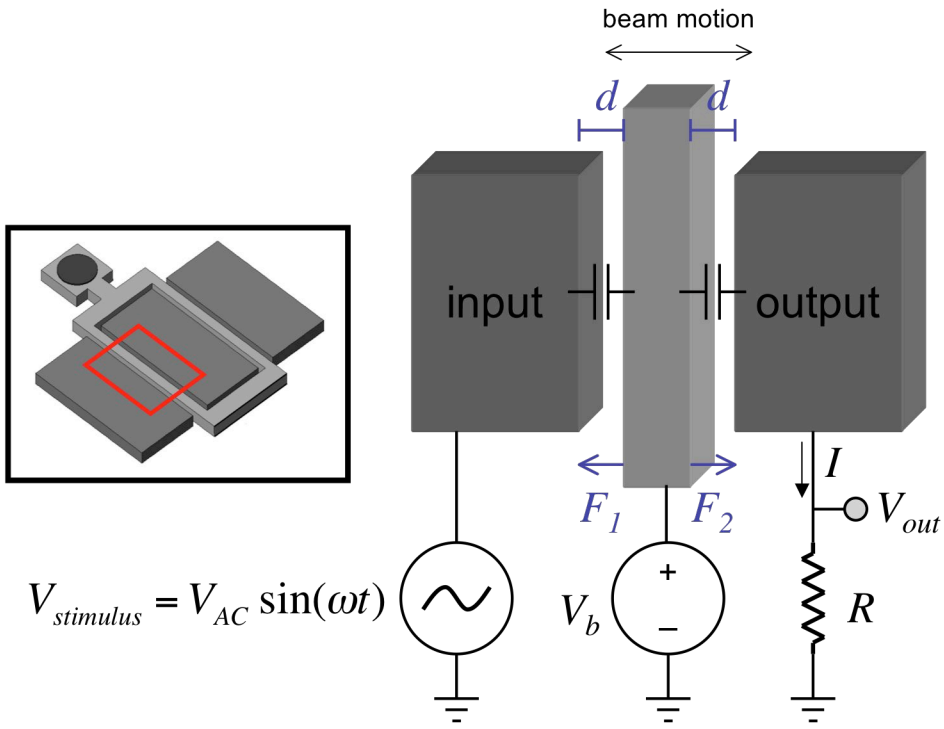

Figure 3.3: Resonator transduction

The input signal, a periodic voltage waveform referenced to zero (ground), is applied at the input electrode. The output is also referenced to ground. In the initial state, at time $t = 0$, the potential across both input and output capacitors is equal to V_b and beam experiences balanced forces pulling it toward each electrode ($F_1 = -F_2$). As the periodic input waveform, $V_{stimulus}$, is applied, the potential on the input side of the beam alternates between $V_b - V_{AC}$ and $V_b + V_{AC}$, and the force on the beam becomes unbalanced. The "input force", F_1, is:

$$F_1 = \frac{1}{2}\frac{C}{d}\left(V_b + V_{stimulus}\right)^2 ,$$
$$F_1 \approx \frac{1}{2}\frac{C}{d}\left(V_b^2 + 2V_b V_{stimulus}\right) \quad \left(V_b >> V_{AC}\right) , \tag{3-4}$$

while F_2 is:

$$F_2 = \frac{1}{2}\frac{C}{d}\left(V_b^2\right) . \tag{3-5}$$

Note that F_2 is acting on the beam in the opposite direction from F_1. The net actuation force that the beam experiences is the difference of F_1 and F_2:

$$F_{act} = F_1 - F_2 \approx \frac{C}{d}\left(V_b V_{stimulus}\right) . \tag{3-6}$$

The output from the resonator (the mechanical to electrical transduction) is the current generated by the time-varying value of the output capacitor. As the beam moves under the influence of the stimulus force F_{act}, the electrostatic gap width, d, of the output capacitor changes, while the bias voltage stays fixed. The charge stored in the capacitor is:

$$Q = CV . \tag{3-7}$$

The output current is the time derivative of the charge:

$$\begin{aligned} &\frac{dQ}{dt} = I_{out} = C\frac{dV_b}{dt} + V_b\frac{dC}{dt} \ , \ \frac{dV_b}{dt} = 0 \ , \\ &I_{out} = V_b\frac{dC}{dt} . \end{aligned} \tag{3-8}$$

The resonator output signal is typically measured as a voltage across a resistor (or a transimpendance amplifier, see Chapter 5):

$$V_{out} = I_{out}R . \tag{3-9}$$

The important consequences of resonator operation by electrostatic transduction are the following:

1) The resonator output signal level can be increased by increasing V_b, as per (3-8) and (3-9).
2) The magnitude of the force on the resonator beam is a sum of two forces. The net force is a function of V_b and $V_{stimulus}$, as per (3-6).
3) The operation of the mechanical resonator is based on two electrical capacitors and the force developed across the capacitor is a non-linear function of the displacement of the structure (3-3).

The importance of these points will become apparent when we model the behavior of the resonator in the following section.

3.2 Resonator Modeling

A "resonator" in this context refers to a mechanical system which has certain energetically preferred vibration frequencies. The preferred frequencies are determined by the modal shapes of the resonator, or modes. The resonators described here are flexural beams operated in the first mode (Figure 3.4), and "frequency", f_0, refers to the first mode frequency unless otherwise specified.

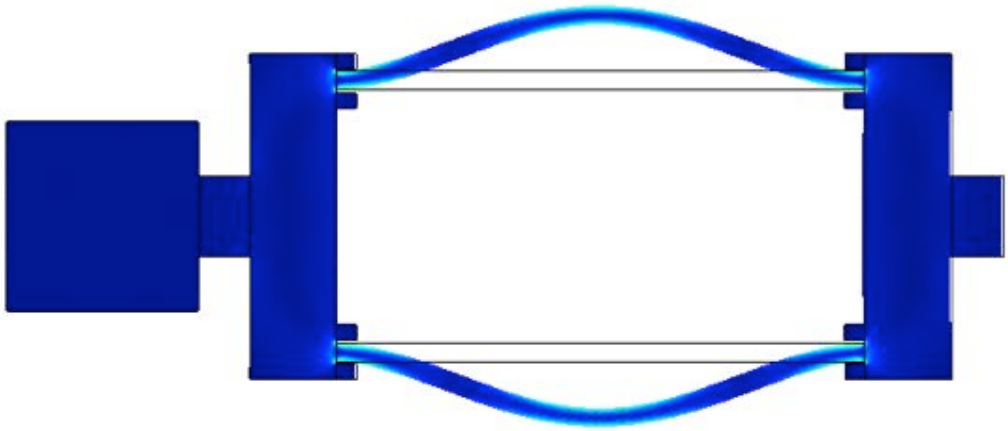

Figure 3.4: The first mode shape of the 1P3M DETF
The symmetric location of the input electrodes (see Figure 3.1) ensure that the beams are actuated out of phase with each other. The displacement shown here is greatly exaggerated for viewing. The other dimensions are to scale, with the dimensions from Figure 3.1.

There are several ways to model DETF resonators, and we will consider three of them in order to explain their observed behavior. These models are:

1) Mechanical Body – describe the behavior of a resonator beam as the vibration of a mechanical body subject to Newton's laws of Motion. This will allow us to explain the purely mechanical effects that define the resonant frequency of the beam.

2) Dynamic System – describe the resonator beam as a 2nd order spring-mass-damper system. This will allow us to consider non-mechanical influences on the beam motion.

3) Circuit Element – describe the resonator beam with an equivalent electrical circuit model. This is similar to the Dynamic model, but includes additional circuit elements. This will be used to describe the electrical effects that modify the measured response of the resonator.

3.2.1 Mechanical Body Model

The mechanical description of a flexural beam can be approached either with energy methods [98] or by solving the equations of motion for a differential element of the beam. The latter approach is more useful for this discussion, and a summary of the derivation is given here, following [100] and [101].

Consider a differential element of a vibrating beam, as shown in Figure 3.5. The uniform beam of length L has Young' s modulus E, second moment of area I, density ρ, and cross-sectional area A. It is acted on by a shear force V, moment M, and subject to axial load P. We wish to find and expression for the displacement of the beam, $v(x,t)$.

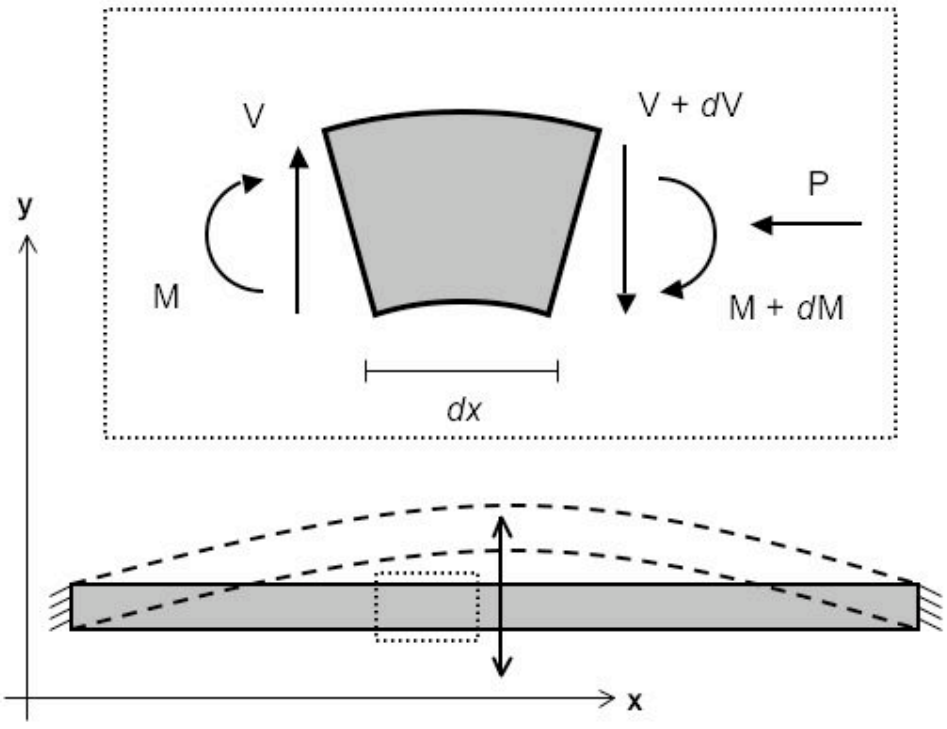

Figure 3.5: Differential element of a vibrating beam.

Let us initially disregard the axial load, P. We can balance the forces on the differential element and obtain a differential equation of the form:

$$\frac{-\partial^2 v(x,t)}{\partial t^2} = \frac{EI}{\rho A}\frac{\partial^4 v(x,t)}{\partial x^4} \ . \tag{3-10}$$

This formulation is called the *Euler-Bernoulli* beam equation. This equation is a function of position x and time t. It can be solved by separation of variables by writing $v(x,t)$ as:

$$v(x,t) = r(x)p(t) \ . \tag{3-11}$$

The expression for displacement as a function of position can then be written as:

$$\begin{aligned} &\frac{d^4 r(\xi)}{d\xi^4} - \beta^4 r(\xi) = 0 \ , \text{ where} \\ &\xi = \frac{x}{L} \ , \text{ and } \beta^4 = \frac{\rho A \omega^2 L^4}{EI} \ , \text{ for } \omega = 2\pi f \ . \end{aligned} \tag{3-12}$$

Rearranging the expression above for the mode constant, β, the natural frequency of the beam is given by:

$$f_0 = \frac{\beta^2}{2\pi L^2}\sqrt{\frac{EI}{\rho A}} \ . \tag{3-13}$$

The value of β is determined by solving Equation (3-12) with the appropriate boundary conditions. The solution for β is not exact for a clamped-clamped beam. For the first mode of a clamped-clamped beam, $\beta = 4.73$ [100].

Now consider the effect of the axial load P, where negative P indicates compressive loads. Equation (3-10) now includes an additional term:

$$\frac{-\partial^2 v(x,t)}{\partial t^2} = \frac{EI}{\rho A}\frac{\partial^4 v(x,t)}{\partial x^4} + \frac{P}{\rho A}\frac{\partial^2 v(x,t)}{\partial x^2} \ . \tag{3-14}$$

The equivalent expression for Equation (3-12) now has an additional term:

$$\frac{d^4 r(\xi)}{d\xi^4} + \pi^2 \alpha \frac{d^2 r(\xi)}{d\xi^2} - \beta_P{}^4 r(\xi) = 0 \ , \text{ where } \alpha = \frac{PL^2}{\pi^2 EI} \ . \tag{3-15}$$

The effect of P is to change the mode shape, which is reflected in a modified mode constant, β_P. The solution follows the same procedure as before, where the value of β_P

is determined by the boundary conditions of the beam, and again there is no exact solution for the clamped-clamped beam. The resulting expression for frequency is simply a modified Equation (3-13):

$$f_0 = \frac{{\beta_P}^2}{2\pi L^2}\sqrt{\frac{EI}{\rho A}} \text{ , where:}$$
$$\beta_P > \beta \text{ for positive } P \text{ (tension), and} \quad (3\text{-}16)$$
$$\beta_P < \beta \text{ for negative } P \text{ (compression).}$$

Plots of β_P for clamped-clamped beams are given in [100]. A useful approximate expression for the resonant frequency of clamped beams for absolute values of axial loads less than the buckling load is given by [102]:

$$f_P = f_0\sqrt{1+\frac{P}{P_b}\frac{\beta_1}{\beta_i}} \text{ , for } i = 1,2,3\ldots \quad (3\text{-}17)$$

where i is the mode number, P_B is the Euler buckling load for the beam, and the frequency f_0 is given by Equation (3-13).

It should be noted that the analysis is given in terms of an axial load, but it is actually the *strain* that the beam experiences which modifies its effective stiffness, and hence resonant frequency. The change in frequency of a clamped-clamped beam due to a change in strain can be approximated as [49]:

$$\Delta f = 0.15\frac{L^2}{w^2}\Delta S \text{ ,} \quad (3\text{-}18)$$

where S is strain of the resonator beam.

The result is that the resonant frequency of the clamped-clamped beam is a function of the beam geometry, the Young's modulus of the beam material, and any axial load (strain) on the beam.

3.2.2 Dynamic System Description

Another approach to understanding the behavior of resonators is to use a 2nd order system model with elements for energy storage, energy dissipation, and inertia. This is often given as the mass-spring-damper (*m-k-b*) model (Figure 3.6), whose behavior is expressed as:

$$m\ddot{x} + b\dot{x} + kx = F \text{ , with } F = F_0 \sin(\omega t) \text{ ,} \tag{3-19}$$

where F is a periodic force (with frequency ω) applied to the system. The physical analogies with the beam resonator are the inertia of the mass of the beam (mass, m), the mechanical restoring force of the beam (spring, k), and the energy dissipation due to the surrounding air or other energy loss mechanisms (damper, b).

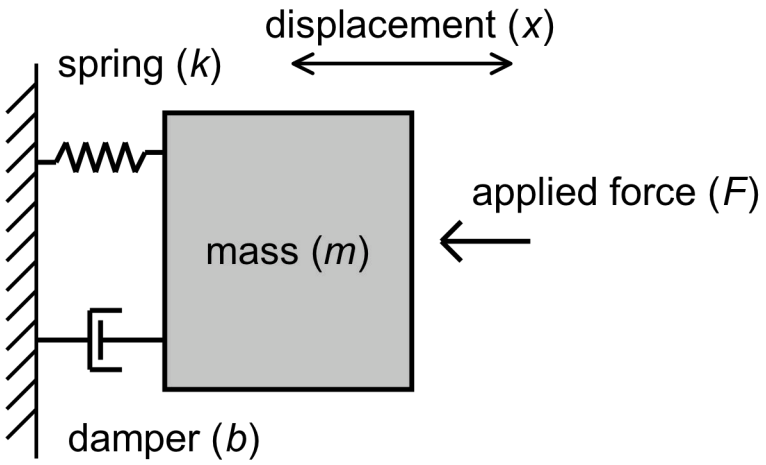

Figure 3.6: Mass-Spring Damper model

The solutions of (3-19) are well known and can be derived using standard differential equation techniques (for example, [98, 103]). The important characteristics of this system are the resonant frequency, f_0, the quality factor, Q, and the amplitude of motion at resonance, X_0. The solutions of (3-19) can be expressed as:

$$\frac{X(\omega)}{F(\omega)} = \frac{1/m}{-\omega^2 + j\omega\frac{b}{m} + \frac{k}{m}} \text{ ,} \tag{3-20}$$

$$f_0 = \frac{1}{2\pi}\sqrt{\frac{k}{m}} \text{ ,} \tag{3-21}$$

$$Q = 2\pi\frac{f_0 m}{b} \text{ ,} \tag{3-22}$$

$$X_0 = \frac{FQ}{k} \text{ .} \tag{3-23}$$

The frequency response of a second-order system (3-20) can be represented graphically, as in Figure 3.7. The amplitude of displacement increases dramatically at the resonant frequency. The effect of quality factor is to increase the peak amplitude and narrow the peak width, as seen on the plot. This frequency response plot describes the important characteristic of the resonator (amplitude, frequency, and Q) in a single plot, and measurements of actual resonators are often presented in this form. Usually, only the measurement near the peak is shown (e.g., Figure 3.9 or Figure 3.10), as the remainder holds little information.

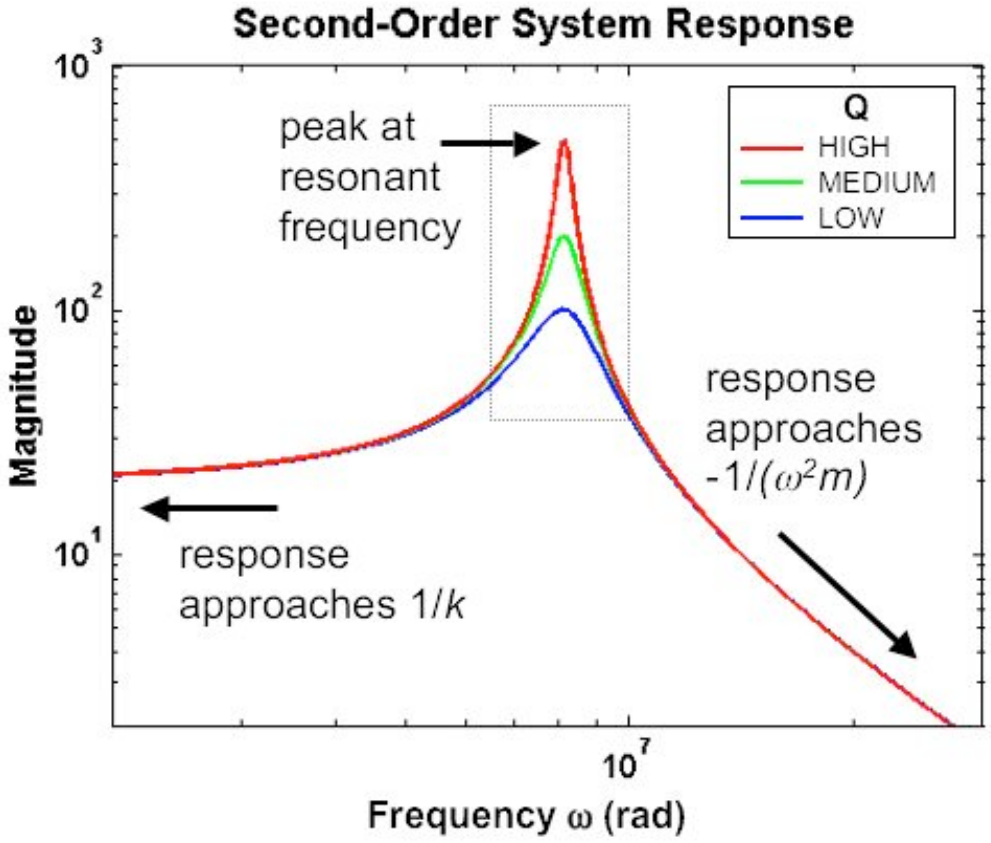

Figure 3.7: Dynamic System Model Frequency Response
Three simulated resonant systems with different Q values are plotted. Increasing values of Q give higher amplitude at resonance (3-23) and a "sharper" peak near the resonance frequency. The width and height of the peak are used to characterize the resonator.

We can see that the expression for resonant frequency (3-21) is similar to that derived from the Mechanical Body description (3-13). In fact, they are different representations of the same system parameter, so we should be able to make them

equal; the only question is what values to use for k and m. Notice that while k is the "stiffness" term, it is not possible to map the value of k directly to a mechanical property of the beam. The Dynamic System model is a second-order model, but the mechanical behavior of the beam has fourth-order components, as given by the Euler-Bernoulli beam equation (3-10). Therefore, some approximation has to be made when choosing values for k to represent the mechanical stiffness of the beam. The simplest meaningful k expression is derived from the maximum deflection, y, of a clamped-clamped beam deflected under a point load [104, 105]:

$$y = \frac{FL^3}{192EI} \ , \ k = \frac{192EI}{L^3} \tag{3-24}$$

For m, it seems obvious that we should simply use the mass of the beam, $m = L \times w \times h \times \rho$. This is not exactly correct, by a similar argument as for k, above. The dynamic model derivation assumes that the entire mass m is participating equally in the vibration displacement (and hence the energy storage as kinetic energy of the moving mass), but in the resonator beam, the displacement is distributed along the length of the beam (Figure 3.8). Therefore, the appropriate value of m for Equation (3-21) is the mass of the resonator beam reduced by a correction factor to account for the distributed displacement. Since the Mechanical Body model was developed using the true mode shape and distributed mass of the displaced beam, we can determine the value of the "mass correction factor" by setting the two expressions, (3-13) and (3-21), equal:

$$\frac{\beta^2}{2\pi L^2}\sqrt{\frac{EI}{\rho A}} = \frac{1}{2\pi}\sqrt{\frac{192EI}{m_{eff}L^3}} \ , \text{ for } m_{eff} = \mu_{cc} m \ . \tag{3-25}$$

We find that the mass correction factor, μ_{cc}, for the clamped-clamped flexural beam resonator is 0.384. A similar procedure can be used for other types of beams and other mode shapes. More complex approximations for k and m can also be used and other choices for k will lead to different values of μ_{cc} (e.g., [106, 107]).

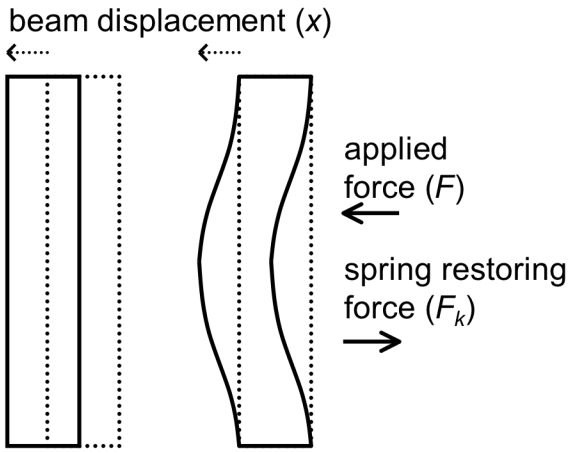

Figure 3.8: Beam displacement and spring restoring force
The beam mass displacement assumed by the Dynamic System model is shown at left. The actual clamped-clamped resonator beam displacement is at right. The electrostatic actuation force, *F*, is distributed along the length of the beam.

Now we have an expression for the frequency of the resonator in terms of a spring stiffness *k* and mass *m*. In the Mechanical Body description, the spring stiffness is due to the mechanical properties of the beam (elasticity, geometry, boundary conditions). However, both electrostatic actuation and mechanical deformation have significant dependencies on the magnitude of beam displacement. We can now modify the generalized *k* term in the Dynamic System model to include these effects by writing the stiffness as the sum of the electrical and mechanical components [105, 108-110]:

$$\begin{aligned} &k = k_0\left(1 + k_1 x + k_2 x^2 \ldots\right) \text{ , where:} \\ &k_0 = k_{m0} + k_{e0} \text{ ,} \\ &k_1 = k_{m1} + k_{e1} \text{ ,} \\ &k_2 = k_{m2} + k_{e2} \text{ .} \end{aligned} \qquad (3\text{-}26)$$

The original "elastic", or mechanical, restoring spring term is now the k_{m0} term. Note that because *k* is a coefficient of *x* in (3-19), k_2 is actually a third-order displacement term[6]. There are two important effects that are modeled by the generalized spring stiffness: electrostatic spring stiffness and non-linear displacement stiffness.

[6] Various authors use different numbering schemes when describing the higher order terms of *k*, either numbering from 0 or from 1. The reader is advised to be aware of the potential for confusion.

3.2.2.1 Electrostatic Spring Stiffness

When the beam is displaced from equilibrium by a force F, the elastic spring stiffness of the beam creates a restoring force, F_k, which acts to bring the beam back toward equilibrium (center), as in Figure 3.8. The magnitude of this restoring force is modeled as a linear function of beam displacement ($F_k = kx$).

However, when the beam is operated electrostatically, the beam displacement and the stimulus force are 90° out of phase[7] [110]. Therefore, a component of the electrostatic force is acting *in opposition* to the elastic restoring spring force. The restoring force is effectively reduced, and so the beam acts as though it has a reduced spring constant. Because the electrostatic force reduces the spring constant, this phenomenon is called "spring softening". The value of the k_e terms can be estimated by taking a Taylor expansion of the expression for the parallel plate electrostatic force (3-3) due to the bias voltage [105]:

$$F = -\frac{V_b^{\,2}}{2}\frac{\partial C}{\partial x} = -\frac{V_b^{\,2} C_0}{2d}\left(1 + \frac{2}{d}x + \frac{3}{d^2}x^2 + \frac{4}{d^3}x^3 \ldots\right), \tag{3-27}$$

where C_0 is the initial transduction capacitance and x is the beam displacement. The constant term represents the symmetric static force on both sides of the beam. The remaining terms give the relationship between force and displacement. The resulting electrostatic spring constant is:

$$\begin{aligned} k_{e0} &= -\frac{V_b^{\,2} C_0}{d^2}, \\ k_{e1} &= \frac{3}{2d}k_{e0}\,^{8}, \\ k_{e2} &= \frac{2}{d^2}k_{e0}. \end{aligned} \tag{3-28}$$

Because the displacement, x, is small for normal (low) values of V_b, the first-order term dominates, and the resulting "linear" expression for resonant frequency with both mechanical and electrical spring constants ($k = k_{m0} + k_{e0}$) is:

[7] This can be seen by expanding (3-20) to include the time-dependent driving force.

[8] Note that for symmetric electrostatic actuation structures like the DETF, the k_{e1} term should be neglected [106], [111].

$$f = \frac{1}{2\pi}\sqrt{\frac{k_{m0} + k_{e0}}{m_{eff}}} = \frac{1}{2\pi}\left(\frac{\frac{192EI}{L^3} - \frac{V_b{}^2 C}{d^2}}{m_{eff}}\right)^{1/2} . \tag{3-29}$$

So the linear electrostatic spring, which depends on the bias voltage, acts to reduce the effective spring constant. The practical result is that the resonator frequency is a function of the bias voltage. The ability to change the frequency of an electrostatic resonator by changing the bias voltage is often referred to as "frequency pulling" or "bias tuning". Frequency pulling in the 1P3M DETF is shown in Figure 3.9. Note that the magnitude of the mechanical spring, k_{m0}, is ~1000× greater than the electrical spring, k_{e0}, in the parallel plate model, so we can only affect relatively small changes in the resonant frequency through the bias voltage. We can estimate this effect by taking a derivative of (3-29) with respect to V_b:

$$\frac{df}{dV_b} = \frac{df}{dk_{e0}}\frac{dk_{e0}}{dV_b} , \tag{3-30}$$

$$\frac{df}{dk_{e0}} = \frac{1}{2\pi}\left(-\frac{1}{2m_{eff}}\right)\left(\frac{k_{m0} - k_{e0}}{m_{eff}}\right)^{-1/2} , \tag{3-31}$$

$$\frac{dk_{e0}}{dV_b} = \frac{2C}{d^2}V_b , \tag{3-32}$$

$$\left.\frac{df}{dV_b}\right|_{V_b=15} \approx \text{-600 Hz/V.} \tag{3-33}$$

This value depends on the bias voltage, and the parallel plate model approximations. More complex models for the electrostatic spring can be made by integrating the actual displacement of the beam [110]. Measurements of 1P3M DETF resonators typically show 100-200 Hz/V sensitivity to V_{bias}.

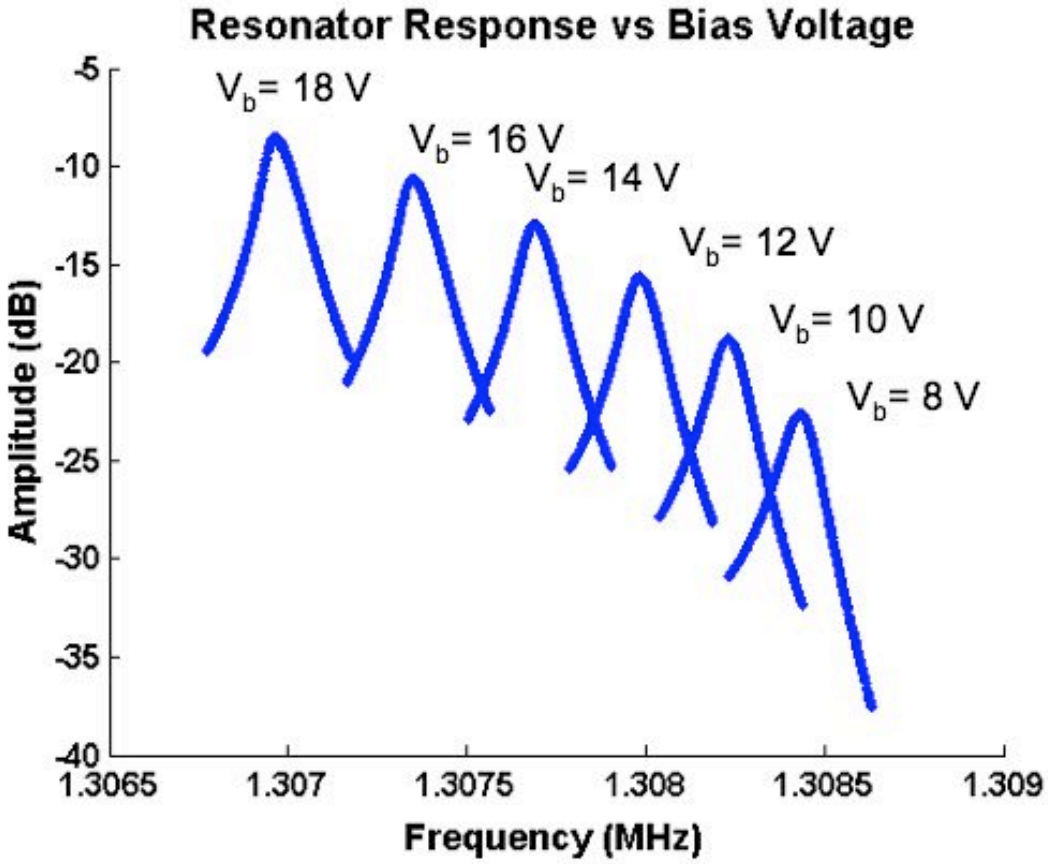

Figure 3.9: Frequency Pulling by Bias Voltage.
The frequency response of a typical 1P3M DETF to different bias voltages is shown. The resonant (peak) frequency decreases with increasing bias voltage. Compare this figure to the ideal response shown in Figure 3.7. Notice that the magnitude of the output increases as predicted by the expressions for electrostatic actuation, (3-8) and (3-9).

In deriving (3-29), we neglected the higher-order terms of (3-28) by assuming that the displacement was very small. However, the non-linear electrostatic terms do have consequences for the operation of our resonators, as discussed in the following section.

3.2.2.2 Non-Linear Effects on Resonant Frequency

The effect of the non-linear spring terms on the resonant frequency can be expressed as [105], where f_0' is the resonant frequency due to the non-linear spring:

$$f_0' = f_0\left(1 + \mathrm{K}X_0{}^2\right) \text{ , where}$$
$$\mathrm{K} = \frac{3}{8}k_2 - \frac{5}{12}k_1{}^2 \text{ , with } k_n \text{ defined in (3-26)}^9. \qquad \text{(3-34)}$$

The electrostatic non-linear displacement terms are given in (3-28). The mechanical non-linear behavior at these length scales can be estimated by considering the deflected beam as a triangle[10] [105]. The length of the two sides of triangle is greater than the length of the beam at rest, and so the deflected beam is experiencing axial tension. From the Mechanical Body model, we know that axial tension increases the resonant frequency of the beam (3-17). Using this simple "triangle deflection" model, we can estimate a value for the mechanical non-linear terms:

$$k_{m0} = \frac{192EI}{L^3} \text{ ,}$$
$$k_{m1} = 0 \text{ ,} \qquad \text{(3-35)}$$
$$k_{m2} = \frac{x^2}{2w^2}k_{m0} \text{ .}$$

The mechanical stiffness depends on the displacement of the beam, and serves to *increase* the stiffness, and hence frequency, of the resonator. Note that this effect is only present if the resonator beam is anchored at both ends; otherwise, there is no longitudinal tension in the displaced beam.

The change in resonant frequency due to the non-linear k_n terms depends on the operating conditions. Figure 3.10 shows a series of resonator measurements which illustrate these spring effects by increasing V_{AC} in order to increase the displacement of the resonator beam while keeping V_b fixed. When the bias voltage is high, the

[9] The symbol κ (lowercase kappa) is typically used in analysis of quartz resonators for the "A-f coefficient", (amplitude-frequency) which relates the change in frequency to the amplitude of the resonator displacement, X_0. However, in traditional quartz analysis, this frequency change is given with respect to the resonator rms driving current, I, rather than amplitude [112]: $\Delta f/f_0 = \kappa I^2$. Driving current is used rather than amplitude because I can be controlled in practical applications while X_0 is inferred (e.g., see the data in Figure 3.10). In this work, K (uppercase kappa) is used to relate change in frequency to resonator amplitude in (3-34). The analysis given here follows [105] which uses κ in a non-standard way. The analysis of non-linear behavior of silicon DETF resonators in [111] uses κ with the standard [quartz] meaning.

[10] The true mode shape is much more complex; this estimate is approximately 30% different from the "true" solution by FEM [105]. The higher-order terms for elasticity are also not considered in this approximation, but they are negligible for flexural resonators.

electrostatic non-linear effects (3-28) dominate, and the resonant frequency decreases with increasing displacement. When the bias voltage is low, the relative effect of the mechanical non-linear terms (3-35) is greater, and so the resonant frequency increases as the displacement of the beam is increased. Frequency change due to non-linear displacement effects is generally undesirable, and the resonators are usually operated in conditions that avoid extreme displacement.

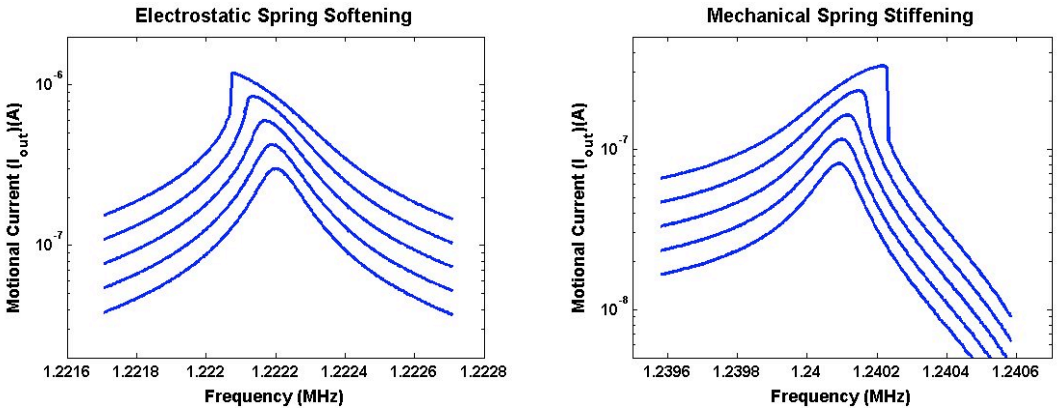

a) V_b = 90 V b) V_b = 15 V

Figure 3.10: Non-linear Effects on Resonator Frequency
The plots show the measured resonator response for different operating conditions (compare to the ideal response in Figure 3.7). The non-linear spring effects cause the resonant frequency to change as resonator beam displacement is increased. The data is the motional current, I_{out}, which is proportional to beam displacement (3-8). The magnitude of the driving stimulus force is controlled by the stimulus voltage V_{AC}. The "bending" of the response at large displacements is called "Duffing".
a) Frequency response when the electrostatic non-linear spring effects dominate (i.e., V_b is large and $k_2 < 0$). The resonant frequency decreases with increasing beam displacement.
b) Frequency response when the mechanical non-linear spring effects dominate (i.e., V_b is small and $k_2 > 0$). The resonant frequency increases with increasing beam displacement. Note that the resonator is a DA-DETF. SA-DETF resonators do not exhibit significant mechanical non-linear spring effects (see Section 3.4.4). [experimental data courtesy of M. Agarwal [111]]

With the Dynamic System model, we can easily add terms to the spring stiffness to account for the electrostatic actuation and non-linear displacement effects in a way that is very difficult to do with the Mechanical model.

3.2.3 Circuit Element Description

The resonator is an electromechanical element, and we cannot consider its operation without considering the electrical circuit that is used to operate it. For electrical design purposes, the resonator can be represented by a RLC equivalent circuit, which has the same properties and solutions as the Dynamic Systems model of Section 3.2.2. Using this equivalent circuit, we can model the behavior of the resonator using standard SPICE-based circuit simulation tools. The equivalent circuit values can be estimated from the measurement of a resonator using [38, 110, 113, 114] the following expressions:

$$R_x = \frac{V_{in}}{I_{out}}, \quad L_x = \frac{R_x Q}{\omega_0}, \quad C_x = \frac{1}{R_x Q \omega_0} \ . \tag{3-36}$$

The RLC circuit model of a 1P3M DETF resonator is shown in Figure 3.11, and the result of the simulation of the circuit is shown in Figure 3.12.

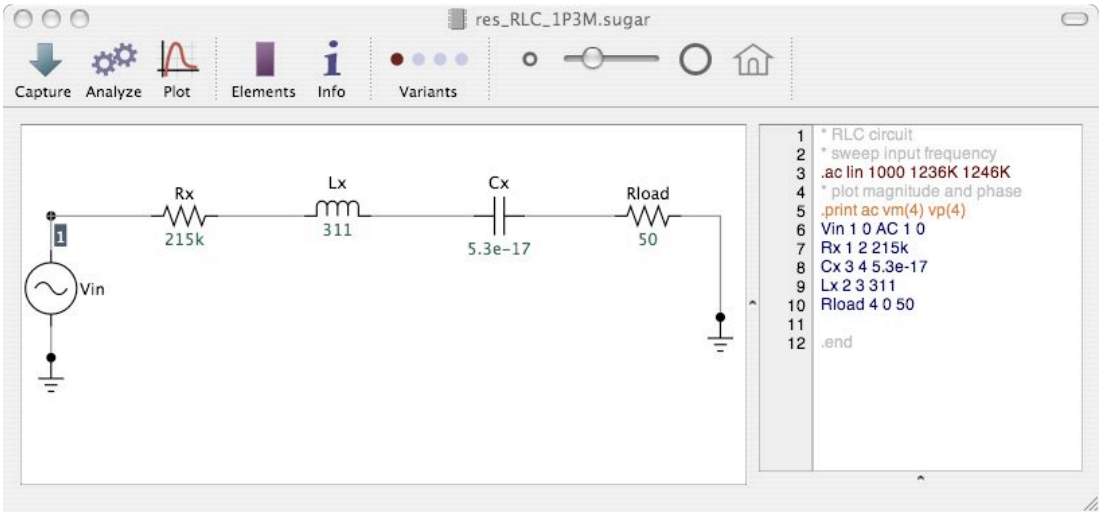

Figure 3.11: RLC equivalent circuit for a resonator
The SPICE netlist for the circuit is shown on the right. Note that the *Cx* value is for system modeling purposes, and is not the value of the transduction capacitors in Figure 3.3.

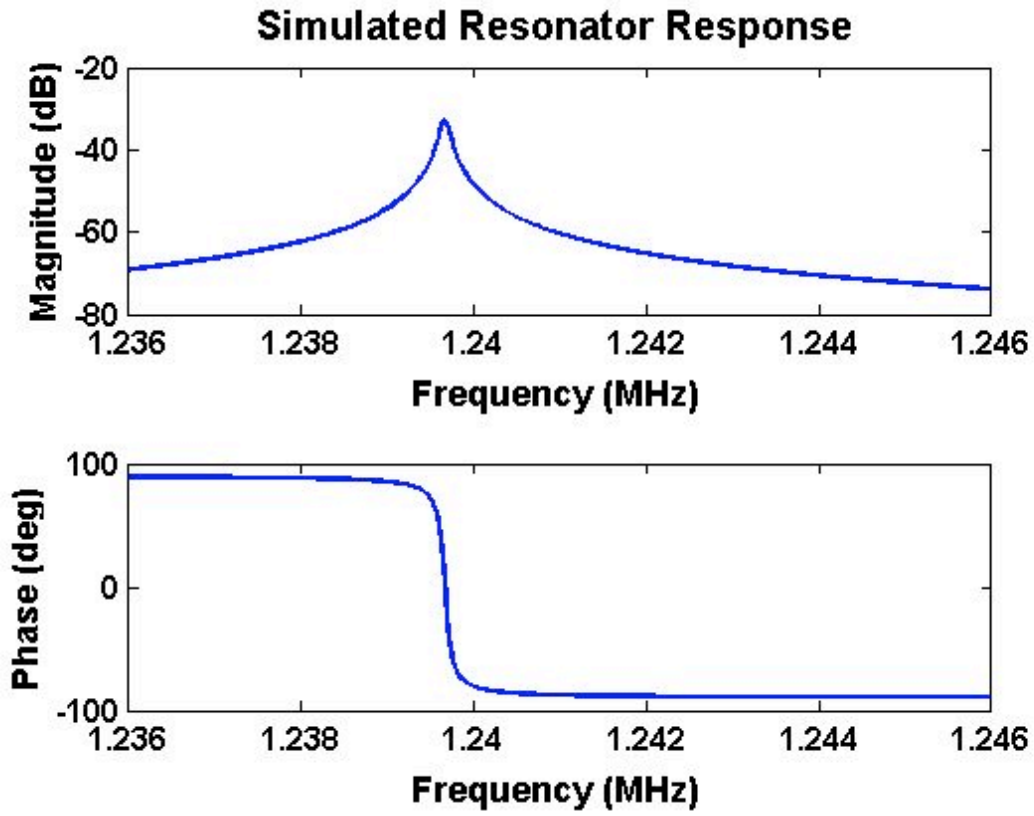

Figure 3.12: Ideal Resonator Response
The plot is the output from the SPICE simulation of the file in Figure 3.11. The response is as predicted by the standard second-order Dynamic System model.

When we operate the resonator, we measure the transduction response through the two capacitors shown in Figure 5.10. However, there always exists some additional capacitance between the input and output terminals, simply because they are separate conductors. In macro-scale applications, this "feedthrough" capacitance is typically negligible, but at the microscale, the feedthrough capacitance, C_{feed}, becomes significant. This is particularly true for epi-seal SOI devices. The silicon cap, the silicon device layer, and the silicon handle wafer all provide paths for feedback capacitance. In addition, the metal lines on top of the silicon die and the wirebonds contribute some capacitance. The resulting equivalent circuit is shown in Figure 5.10.

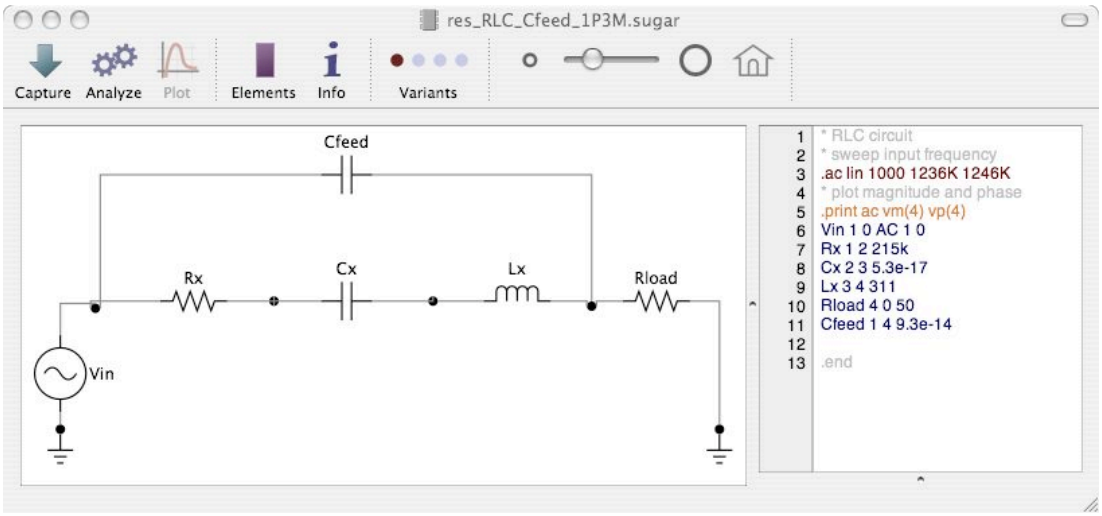

Figure 3.13: Equivalent circuit for a resonator including feedthrough capacitance
The SPICE netlist is shown at right.

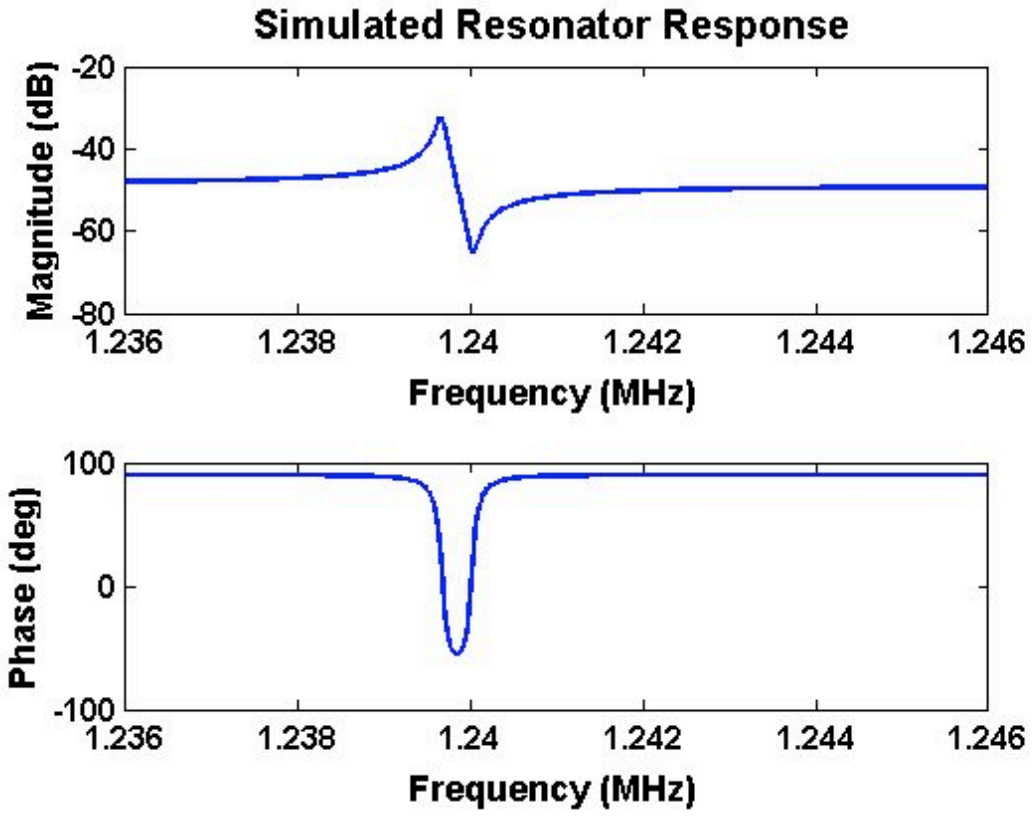

Figure 3.14: Resonator response with feedthrough capacitance
The plot is the output from the SPICE simulation of the file in Figure 3.13, which includes the feedthrough capacitance.

There are two important consequences of the feedthrough capacitance. First, the feedthrough capacitance determines the noise floor of the sweep measurement. From the circuit in Figure 3.13, we can see that C_{feed} will provide a signal path at all frequencies, and so determine the minimum signal level. Second, the electrical measurement of the resonator differs significantly from the ideal response shown in Figure 3.12. The effect of C_{feed} is to introduce an "antiresonance" peak, as shown in the simulated response from the circuit of Figure 3.13 (Figure 3.14). A typical resonator measurement is shown in Figure 3.15. The effect of the feedthrough capacitance is evident.

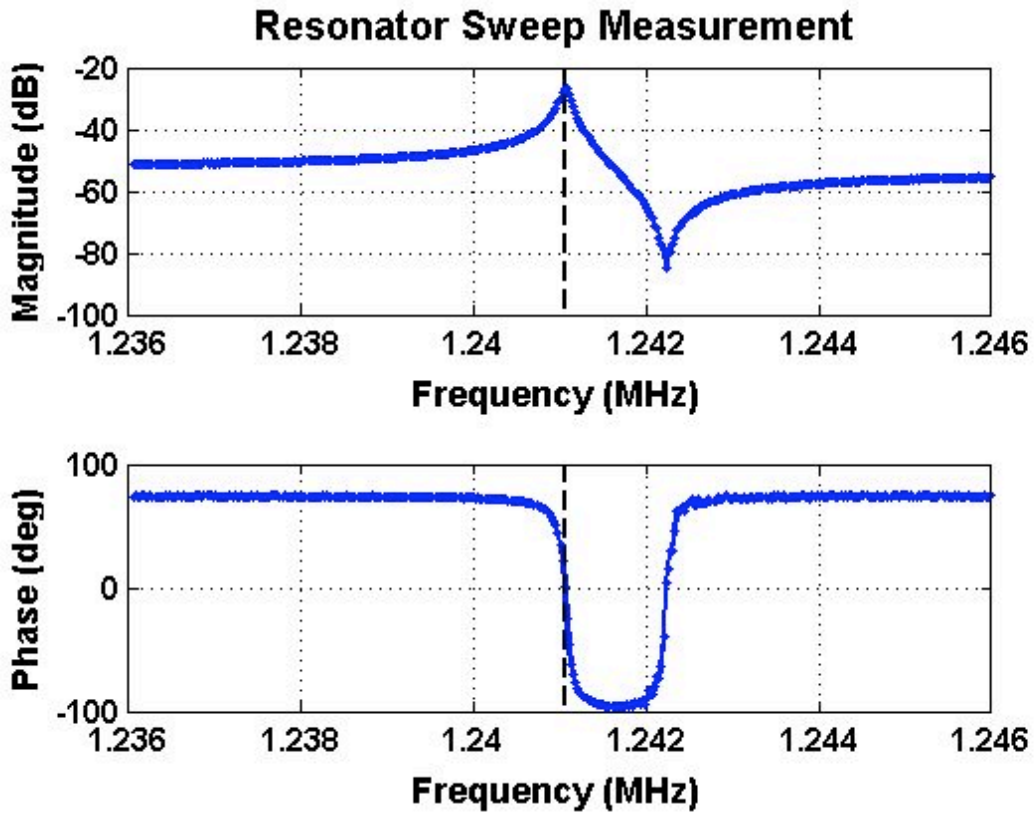

Figure 3.15: Measurement of Typical DETF Resonator
No feedthrough abatement techniques were used, and the effect of the feedthrough capacitance is strong. The measured resonance frequency (peak magnitude) is marked by the dashed line.

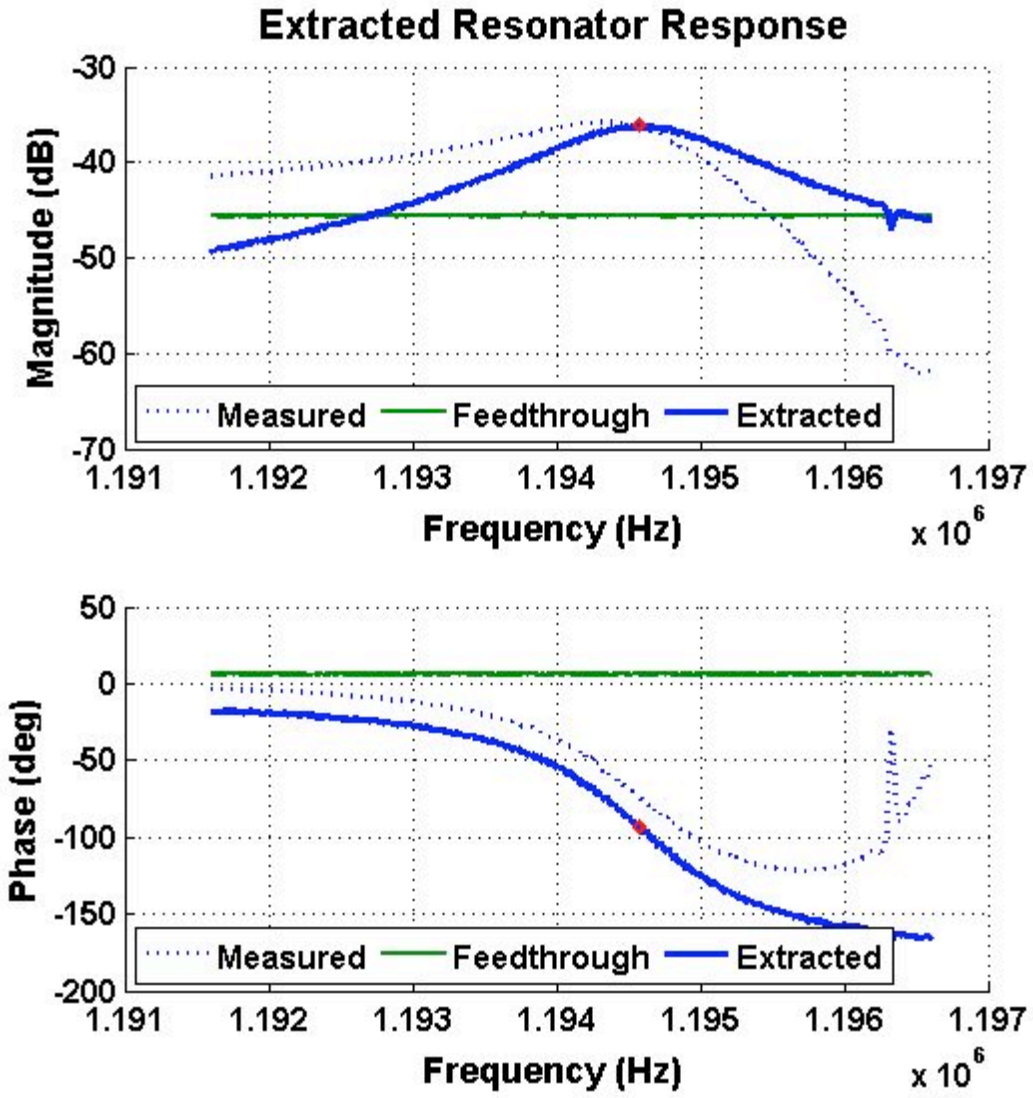

Figure 3.16: Resonator response de-embedded from feedthrough noise
The resonator measurement (dotted line) has a low, indistinct peak and phase shift much less than 180°, suggesting that the feedthrough capacitance is obscuring the resonator's true performance. When the feedthrough is subtracted, the apparent quality factor increases by 25%, and the resonant frequency shifts by 170 ppm. The high feedthrough level shown here is typical of measurements made on a probe station, where it is not possible to make an electrical connection to the substrate. When the resonators were packaged for temperature testing (see Chapter 5), the typical feedthrough level was reduced. MATLAB code for performing feedthrough de-embedding is discussed in Appendix D.

In a resonator measurement, the feedthrough capacitance can "drag down" the measured response peak, and change the measured resonant frequency or even obscure the resonator response altogether. Note that if we assume the circuit model from

Figure 3.13 accurately represents the resonator circuit, we can extract the resonator response from the total measurement by measuring the value of the signal level contributed by C_{feed} and then subtracting it from the measured response. Figure 5.10 shows an example of a resonator response extracted, or "de-embedded" from a measurement obscured by a high noise floor. However, as discussed below and in Chapter 5, in practice, the signal from the 1P3M DETF resonators was typically much higher than the noise floor established by the feedthrough capacitance, so de-embedding was not normally used.

3.3 Temperature Dependence of Quality Factor

The quality factor, Q, of a resonator is the ratio of energy stored in the beam to energy dissipated per vibration cycle. In the Dynamic System model, it is the inverse of the damping coefficient, b (3-22). A resonator with an infinite Q would continue to vibrate forever after being excited once (because it loses no energy), while a resonator with a low Q would quickly stop moving (because it loses energy with every vibration)[11].

$$Q = 2\pi \frac{E_{stored/cycle}}{E_{dissipated/cycle}} \tag{3-37}$$

The resonator Q is an important parameter for frequency reference design because it determines the motional resistance and the short term stability (phase noise). In micromechanical resonators, six mechanisms of energy loss or damping are usually identified: gas, anchor, surface, electrical, intrinsic, and thermoelastic dissipation (TED). When multiple factors contribute to damping, the individual Q values are added in an inverse sum [103], so that the smallest Q value dominates the total if the others are much greater.

$$\frac{1}{Q_{total}} = \sum \frac{1}{Q_{factors}} = \frac{1}{Q_{gas}} + \frac{1}{Q_{anchor}} + \frac{1}{Q_{surface}} + \frac{1}{Q_{electrical}} + \frac{1}{Q_{intrinsic}} + \frac{1}{Q_{TED}} \ . \tag{3-38}$$

[11] For example, a guitar string is a high-Q resonator. A door that you knock on is a low-Q resonator.

The Q mechanism(s) acting in a particular resonator can be inferred by observation of the Q under different conditions. In our encapsulated DETF resonators, the first four damping types are minimized, and TED dominates the final value.

Gas damping

Gas damping is the energy lost when the beam displaces gas molecules in the surrounding environment as it vibrates. For low-pressure environments where the gas molecules can be considered to be interacting primarily with the structure and not with each other (i.e., the mean free path of the gas molecules is much greater than the critical dimensions of the resonator and enclosure), the Q value for a flexural resonator is inversely proportional to gas pressure, p, and can be estimated by [18]:

$$Q_{gas} = \left(\frac{\pi}{2}\right)^{3/2} \frac{h\rho f_0}{p} \sqrt{\frac{RT}{M_0}} \quad , \tag{3-39}$$

where R is the universal gas constant and M_0 is the molecular weight of the gas (29 kg for air). In the epi-seal encapsulated resonators, the pressure inside the encapsulation is approximately 1 Pascal, and the estimated Q_{gas} for a 1P3M DETF is ~10 million. This is much larger than the measured Q of ~10,000, and so we conclude that gas damping has a minimal effect on the 1P3M DETF resonators. This was confirmed by opening the encapsulation to expose the resonators to atmosphere, then putting them in a vacuum chamber where pressure could be controlled and observing Q as a function of pressure [103, 115]. The Q of the 1P3M DETF resonators is independent of pressure at the pressure inside the epi-seal encapsulation (see Figure 3.17).

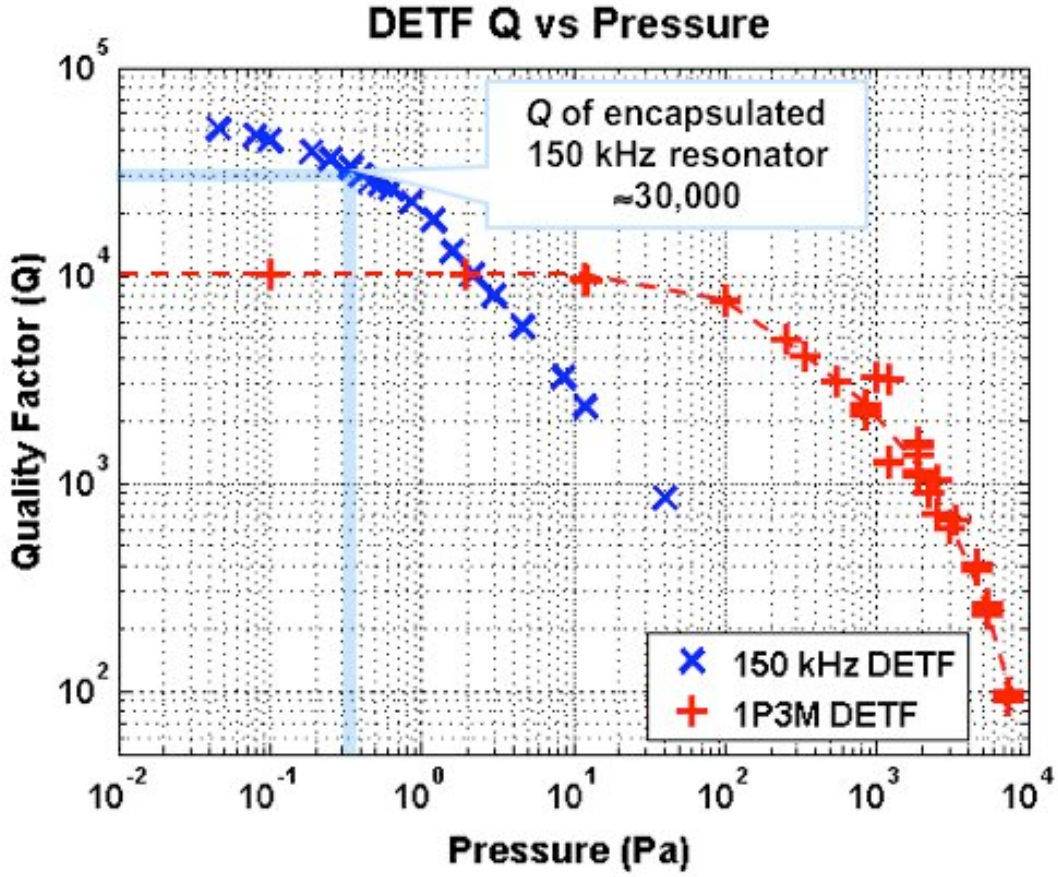

Figure 3.17: Pressure vs. *Q* for silicon DETF resonators
Measurements of *Q* versus ambient air pressure are shown for two DETF designs. The 150 kHz DETF is similar to the 1P3M, except that the arms of the tuning fork are longer (*L* is greater), so that the resonant frequency f_0 is lower. The encapsulation surrounding the resonators was opened, exposing the resonators to the atmosphere. They were then placed in a vacuum chamber, and their *Q* was measured as a function of chamber pressure. The *Q* value for the 1P3M design is ~10,000, regardless of pressure below approximately 10 Pa, while the *Q* value for the 150 kHz design has a significant dependence on pressure at all values. The light blue lines indicate the measured *Q* value of the 150 kHz design before the encapsulation was broken and the corresponding pressure inside the encapsulated cavity. Note that the pressure measurement is performed using air, while the gas in the encapsulated cavity is mostly hydrogen, so the equivalent pressure inside the cavity is approximately 4x greater than the pressure indicated on the plot [103]. At this pressure (~ 1 Pa), the *Q* of the 1P3M DETF is clearly limited by some mechanism other than gas damping. Data from [103, 115].

Anchor loss

Anchor loss, or support damping, refers to energy lost as the vibrating resonator launches acoustic waves in its supporting structure. The support structure is

not typically a good resonator, and so the energy in these waves is lost. While anchor loss in micromechanical structures is not fully understood and under active investigation [116, 117], the tuning fork design is well known to minimize anchor loss[12] by connecting two resonators to the same rigid support structure. The energy that would be lost in the support from one resonator is transmitted to the other resonator, and vice versa. The 1P3M DETF design takes advantage of this feature. Otherwise identical DETF designs with different length beams, and hence different resonant frequencies, have different Q values, indicating that the Q is not limited by the DETF anchor structure [103, 115] (for example, see Figure 3.17).

Surface losses

The properties of high-purity crystalline materials such as silicon are assured in the bulk volume of a structure but the surfaces represent discontinuities that may have lattice defects, layers of adsorbed contaminants, unterminated chemical bonds, and other non-ideal properties. Any of these deviations from the bulk material may cause energy loss [118]. However, these losses are typically only significant for resonators with sub-micron dimensions, and it is expected that the relatively low surface-to-volume ratio of the 1P3M DETF resonators studied here precludes significant Q effects due to surface losses. The comparisons of DETF designs with different beam lengths, whose surface area and surface-to-volume ratios are very similar, yet have very different Q values, suggests that surface losses are not significant.

Electrical damping

Both electrostatic actuation and sensing mechanisms can affect the measured Q of a resonator. As described in Section 3.2.2.1, in electrostatic actuation, a portion of the electrostatic forces are acting *against* the resonator motion, which effectively dissipates energy and reduces Q [110, 119]. In electrostatic sensing, the motion of the resonators creates electrical charge moving through a circuit of finite resistance (i.e., electrical current). If the electrical resistance is large enough, the energy dissipated by current flow can be significant, and the resonator Q will be reduced [103]. Both of these electrical effects are insignificant for the 1P3M DETF resonator designs, as

[12] As in the macro-scale tuning fork used for tuning musical instruments.

evidenced by the fact that the Q remains constant for different V_{bias} and V_{AC} levels (see Figure 3.9 and Figure 3.10).

Intrinsic losses

Intrinsic losses are energy losses due to relaxation of the material structure during deformation [103]. As discussed in Chapter 2, silicon is a brittle material with little or no plastic deformation before fracture, and so very low intrinsic material losses are expected. Silicon micromechanical resonators with Q values of 180,000 have been reported [106], so intrinsic losses should not be significant for silicon DETFs.

Thermoelastic dissipation

Thermoelastic dissipation (TED) is the energy loss that occurs when heat flows between hot and cold regions of the resonator. When the resonator beam flexes, part of it goes into tension, and part into compression. Temperature increases in the region in compression, and decreases in the region in tension in proportion to the strain rate[13] (Figure 3.18). When a temperature difference is present, heat flows between the hot and cold regions, and the mechanical energy that is transformed into heat is lost from the resonator (i.e., the system entropy increases), reducing the Q value. Energy loss due to TED is significant for the 1P3M DETF design and determines the Q of the resonators studied here.

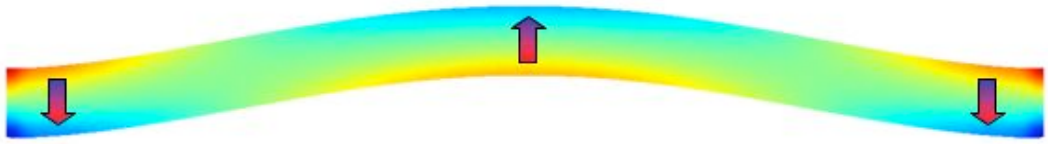

Figure 3.18: FEM Simulation of temperature distribution in a flexural beam.
Red is higher temperatures and blue is lower. The temperature profile follows the strain profile, and the temperature change is proportional to the strain rate. Heat flows across the beam from hot to cold regions (indicated by arrows), dissipating mechanical energy stored in the beam.

Thermoelastic dissipation was first described by Zener in the 1930's [120, 121], and TED in micromechanical silicon DETF resonators has been thoroughly

[13] This temperature change is analogous to the behavior of a volume of gas described by the ideal gas law, $PV = nRT$.

investigated [103, 115, 122-124]. A complete treatment of TED is beyond the scope of this work, but for simple beams, we can summarize by saying that the magnitude of energy loss is a function of the relative values of the mechanical resonant frequency, f_M (which is equivalent to f_0), and the frequency of the heat transport across the beam, f_T. The relationships are given in Table 3-1, and illustrated in Figure 3.19.

Relationship of mechanical and thermal frequencies (1rst modes in simple beam)	Effect on Q_{TED} for DETF resonators
$f_m = f_T$	Maximum heat energy will be dissipated as heat flows during every cycle of the resonator and Q_{TED} will be at a minimum.
$f_m < f_T$	Strain rate in the beam is reduced, and so the temperature difference between the hot and cold regions is reduced, causing less heat to flow, and less energy to be dissipated, leading to a higher Q_{TED}.
$f_m > f_T$	The hot and cold regions of the beam form and then disappear before heat flow occurs, so less energy is dissipated, and Q_{TED} is increased.
Table 3-1 Qualitative description of Q_{TED} in DETF resonators.	

For a rectangular flexural beam resonator we can estimate the Q due to TED using the simplified expression first identified by Zener [115, 120, 123]:

$$Q_{TED} = \left(\frac{f_M^2 + {f_T}^2}{f_M f_T} \right) * \frac{c_p \rho}{\alpha^2 T_0 E} \text{ , where}$$
$$f_M = \frac{\beta^2}{2\pi L^2} \sqrt{\frac{EI}{\rho A}} \text{ . and } f_T = \frac{\pi k_{th}}{2 c_p \rho w^2} \text{ .} \qquad \text{(3-40)}$$

where ω is the mechanical resonant frequency in radians, c_p is specific heat, k_{th} is thermal conductivity, ρ is density, and T_0 is the equilibrium temperature of the beam. The predicted Q_{TED} at room temperature for silicon DETFs with 8 μm wide beams is shown in Figure 3.19. Because of the Q inverse addition relationship (3-38), the Q_{TED} value should establish the approximate maximum value of Q for the resonator if the other contributions to Q are much larger than Q_{TED}. The predicted Q due to TED for the 1P3M DETF of approximately 10,000 agrees well with the measurements in Figure 3.17 and Figure 3.20.

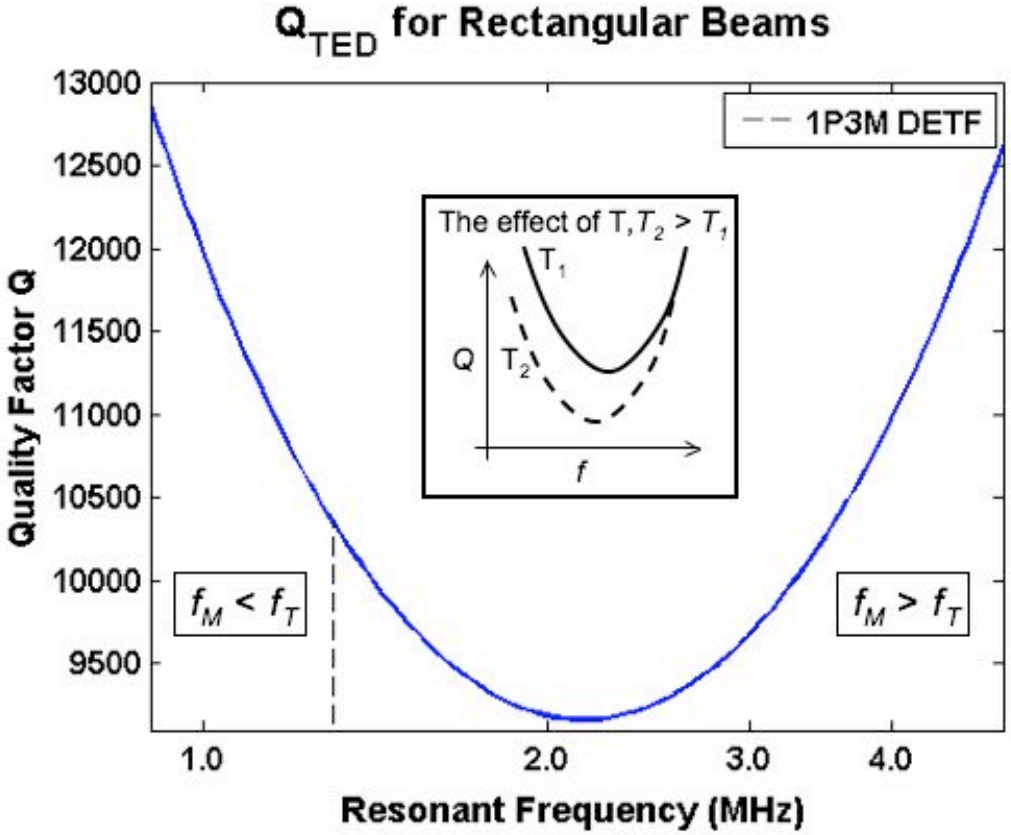

Figure 3.19: Q_{TED} as a function of resonant frequency
The plot shows the Q predicted by the simple Zener expression (3-40) for a rectangular silicon beam of 8 μm width. The resonant frequency corresponds to different beam lengths. Theory and measurements show that the Q value established by TED depends on the resonant frequency. The 1.3 MHz resonant frequency of the 1P3M DETF is the dashed line. By (3-38), Q_{TED} establishes the upper limit for the resonator Q if the other contributions to Q are much greater than Q_{TED}. The effect of increasing temperature on Q_{TED} is shown inset. Q_{TED} decreases with increasing temperature in a complex manner.

As TED is essentially an increase in the entropy of the system, Q_{TED} is inherently sensitive to the temperature of the resonator (T_0). In addition, the silicon thermophysical properties of heat capacitance (c_p), thermal conductivity (k_{th}), density (ρ), and thermal expansion (α), all have significant temperature coefficients [125-129]. The resulting mechanism of temperature dependence of Q_{TED} is complex. Qualitatively, an increase in temperature causes the Q_{TED} curve in Figure 3.19 to shift down as temperature increases and shift to the left as the thermal frequency decreases (see Figure 3.19, inset). The mechanical frequency also decreases ("moves left") with

temperature. While temperature only appears once in (3-40), it is implied in many other terms ($k_{th}(T)$, $\alpha(T)$, $E(T)$, etc.). The resulting relationship between Q_{TED} and T can be described as an inverse function of T:

$$Q \propto \frac{1}{T^{\gamma}} . \tag{3-41}$$

The coefficient γ is the "TCQ parameter". Typical γ values for the DETFs discussed here are 3 – 3.5.

The result is that the Q of a 1P3M DETF resonator is a strong function of temperature. A typical measurement of Q vs T is shown in Figure 3.20.

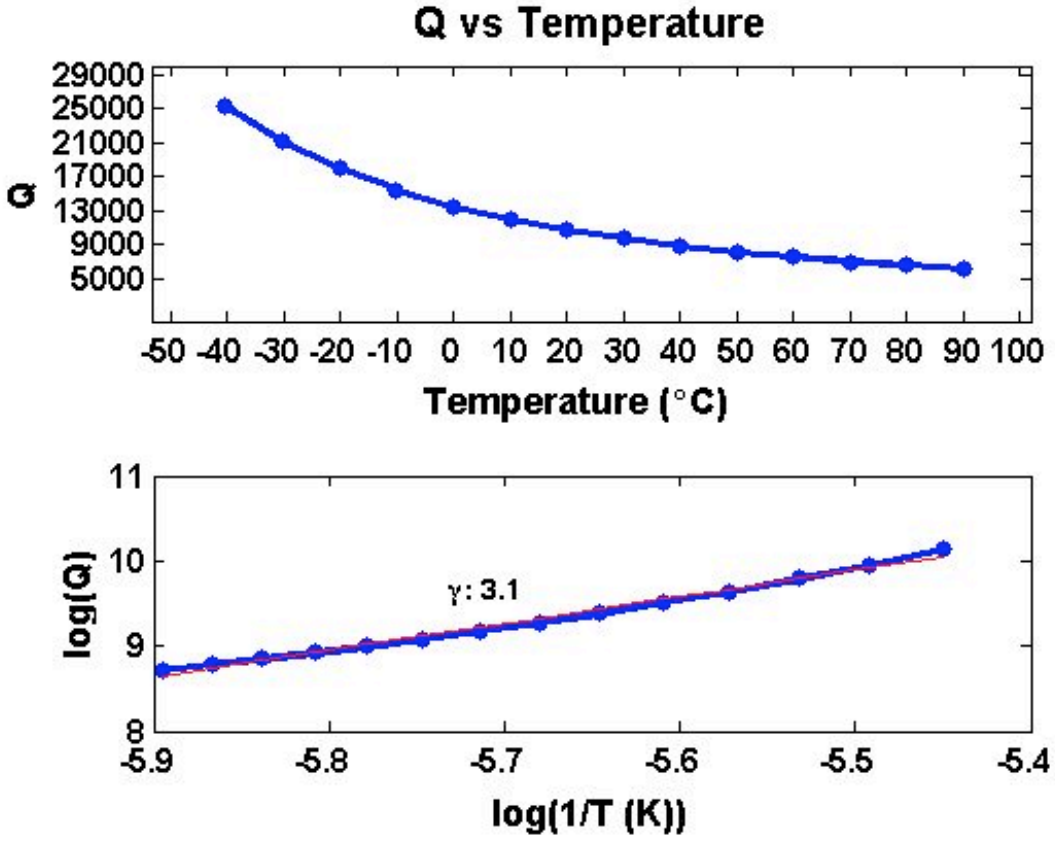

Figure 3.20: Measurement of Q vs T for a typical 1P3M DETF
The upper figure shows the Q as a function of temperature. The lower figure plots the same data on a log scale against the inverse of temperature in order to determine the TCQ parameter, γ.

It should be emphasized that this strong temperature dependence of Q is unusual behavior for resonators in general. The other terms of (3-38) do not usually

have a strong temperature dependence, except for Q due to gas damping when the resonator is operated in a closed volume, such that pressure increases with temperature. In this case, the TCQ due to gas damping is equivalent to $\gamma = 0.5$, which is much less than the TCQ due to TED [115].

3.4 Temperature Sensitivity of Resonant Frequency

Now that we have descriptions for the important aspects of DETF behavior, we can consider the temperature sensitivity of the resonant frequency of the resonator. In this section, the various mechanisms of this temperature sensitivity are discussed.

Frequency sensitivity to temperature is designated the Temperature Coefficient of Frequency (TCf). The TCf is often either nearly linear or considered over a restricted temperature range where is it linear, but the term "the TCf" is sometimes used to refer to a more complex expression with higher order terms. In the case of more complex TCf behaviors (such as considered in the following Chapters), it is conventional to refer to a "frequency-temperature response" or "*f-T* characteristic", rather than the TCf[14]. A typical TCf measurement of a silicon 1P3M DETF resonator is shown in Figure 3.21. The non-linear nature of the TCf can clearly be seen.

[14] When comparing high precision quartz resonators, the temperature behavior will sometimes be described by only by the third order coefficient of temperature.

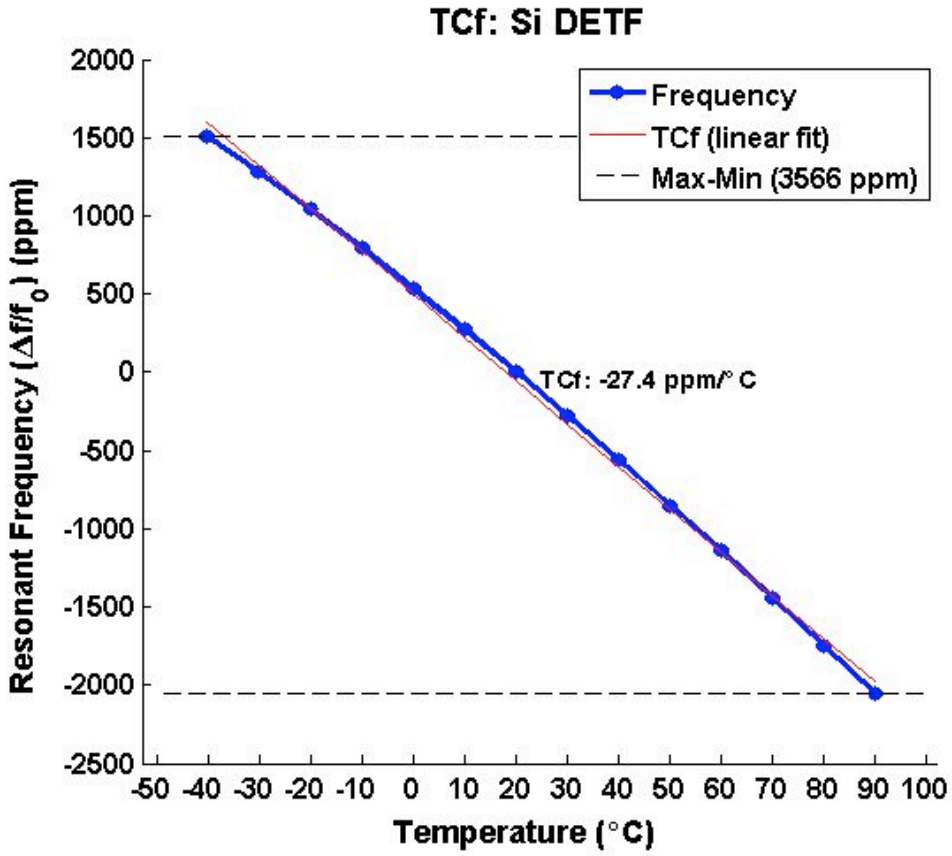

Figure 3.21: Typical silicon DETF resonator TCf measurement

3.4.1 Elasticity Change

The elasticity of materials is a function of temperature. In a simple material, the elasticity change occurs because the strength of the bonds between the atoms is a function of the distance between them. As the material heats up, it expands, and the distance between the atoms increases, and the strength of the bonds between them decreases (see Figure 3.22). This relationship is complex and non-linear; however, for small displacements of simple materials, we can consider the change to be linear. For silicon, the change in Young's modulus with temperature, the TCE, is approximately -63.7 ppm/°C at normal operating temperatures [130-133]. Silicon is a crystal with cubic symmetry (class m3m), and its thermal expansion is the same in all directions. Therefore, even though the Young's modulus of silicon is not the same in all

directions (see Appendix E), the *temperature-dependant change* in Young's modulus is the same in all directions.

We can predict the effect of the TCE on resonator frequency by taking a temperature derivative with respect to E of the mechanical expression for frequency (3-13). The derivative is evaluated at $\Delta T = T_0$, and the result is divided by the original expression for frequency to find the relative change:

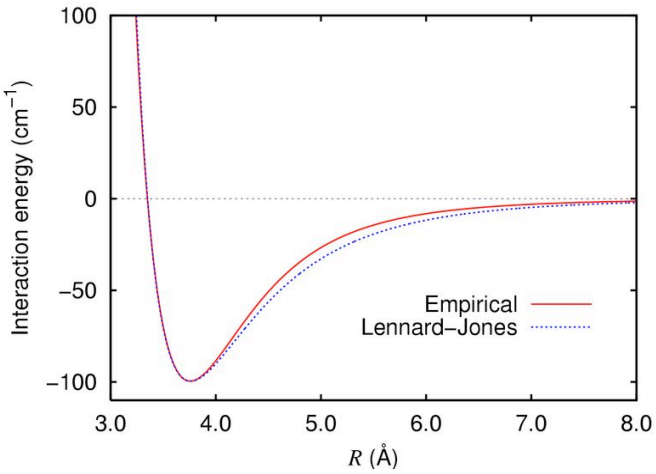

Figure 3.22: Atomic interaction force
The attractive forces between any two atoms can be modeled by the Lennard-Jones potential, which is a 6th order function of the distance, *R*, between two atoms. The true anharmonic quantum relationship, of course, is more complex, and the forces acting on a single atom in a structured crystal lattice is more complex still. The data shown here is for Ar_2. [134, 135]

$$f = \frac{\beta^2}{2\pi L^2}\sqrt{\frac{EI}{\rho A}} = CE^{1/2} \text{ , where} \tag{3-42}$$

$$E = E_0\left(1 + TCE \cdot \Delta T\right) . \tag{3-43}$$

$$\frac{df}{dT} = \frac{df}{dE}\frac{dE}{dT} \text{ , where} \tag{3-44}$$

$$\frac{df}{dE} = \frac{1}{2}C\left(E\right)^{-1/2} \text{ , and} \tag{3-45}$$

$$\frac{dE}{dT} = E_0 \cdot TCE \text{ . Thus,} \tag{3-46}$$

$$\frac{df}{dT} = \left.\frac{CE_0 \cdot TCE}{2E^{1/2}}\right|_{\Delta T = T_0} = CE_0^{1/2} \cdot \frac{TCE}{2} \text{ , and} \tag{3-47}$$

$$TCf_{TCE} = \frac{df}{dT}\frac{1}{f_0} = \frac{TCE}{2} \approx -31.9\,ppm/°C\ . \tag{3-48}$$

So we expect that increasing temperature to reduce the resonant frequency by TCE/2, approximately -31.9 ppm/°C at room temperature. This is true for higher order flexural modes as well[15]. This effect is, of course, temperature dependent, and different values of the higher order coefficients have been reported [130, 136, 137]. As we will see further on, this is the most significant manifestation of the effect of temperature on resonator frequency.

3.4.2 Dimensional Change

The dimensions of the resonator change with temperature due to thermal expansion. Silicon has an isotropic coefficient of thermal expansion (CTE, or α), at room temperature of approximately 2.6 ppm/°C [27, 125, 128], and that value increases with increasing temperature.

We can consider the effect of α on frequency by taking a temperature derivative of the mechanical expression for frequency (3-13), using a similiar procedure as for TCE:

$$f = \frac{\beta^2}{2\pi L^2}\sqrt{\frac{EI}{\rho A}} = C\frac{w}{L^2}\rho^{-1/2}, \text{ where} \tag{3-49}$$

$$w = w_0(1+\alpha\Delta T)\ ,\ L = L_0(1+\alpha\Delta T)\ , \text{ and } \rho = \rho_0(1-3\alpha\Delta T)\ . \tag{3-50}$$

$$\begin{aligned}\frac{df}{dT} &= \frac{\partial f}{\partial w}\frac{dw}{dT} + \frac{\partial f}{\partial L}\frac{dL}{dT} + \frac{\partial f}{\partial \rho}\frac{d\rho}{dT}\ , \\ &= \left(C\frac{w}{L^2}\rho^{-1/2}\right)\left[\frac{w_0\alpha}{w} - \frac{2L_0\alpha}{L} + \frac{3\rho_0\alpha}{2\rho}\right]_{T=T_0} = f_0\alpha\left[1-2+\frac{3}{2}\right].\end{aligned} \tag{3-51}$$

$$TCf_\alpha = \frac{df}{dT}\frac{1}{f_0} = \frac{\alpha}{2} \approx 1.3\,ppm/°C\ . \tag{3-52}$$

[15] TCf measurements of the 3rd order mode of the DETF resonators were performed by Suhrid Bhat (data unpublished). The TCf results were identical the usual 1st mode.

The effect of thermal expansion on the resonator frequency is $\alpha/2$, approximately 1.3 ppm/°C.

3.4.3 Stress

The effect of axial stress on the frequency of the resonator is a strong function of applied load, P, as reflected in the modified mode constant, β_P, (3-16). The TCf is:

$$TCf_P = 2\frac{d\beta_P}{dT} \; ; \tag{3-53}$$

i.e., the frequency sensitivity to temperature depends on the value of the temperature coefficient of axial load (TCP), which depends on the design and packaging of the resonator. For example, in this work, the 1P3M DETF resonator design had two variants, the single-anchored (SA-DETF) and double-anchored (DA-DETF), illustrated in Figure 3.23. In the SA-DETF design, the resonator is attached to the substrate only at one end, so there are no axial loads on the resonator beams[16]. In contrast, a DA-DETF is attached to the substrate at two points. A double-anchored resonator might experience temperature-dependent axial loads through differential thermal expansion of the resonator and the substrate. When epi-seal DA-DETF resonators were fabricated and mounted in electronic packages using a standard silver epoxy[17] (See Chapter 5), the expansion of the copper "paddle" at the base of the package with increasing temperature induced a compressive axial force on the resonator (Figure 3.24). The result was that the measured TCf of the DA-DETF resonators was 5-6× greater than that of the SA-DETFs (Figure 3.25).

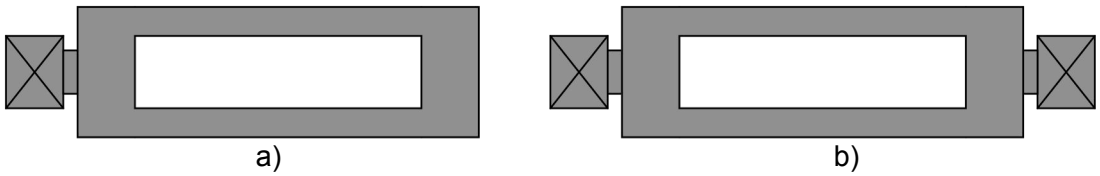

Figure 3.23: Single-Anchor versus Double-Anchor DETF
a) Single-anchor SA-DETF. The resonator is free to expand along its long axis.
b) Double-anchor DA-DETF. The resonator is constrained longitudinally.

[16] Except possibly from acceleration. The sensitivity of the 1P3M DETF design has been measured to be 0.0074 ppm per g along the axis of the beams [138].
[17] Die-attach silver epoxy H2OE, from Epotek, Inc.

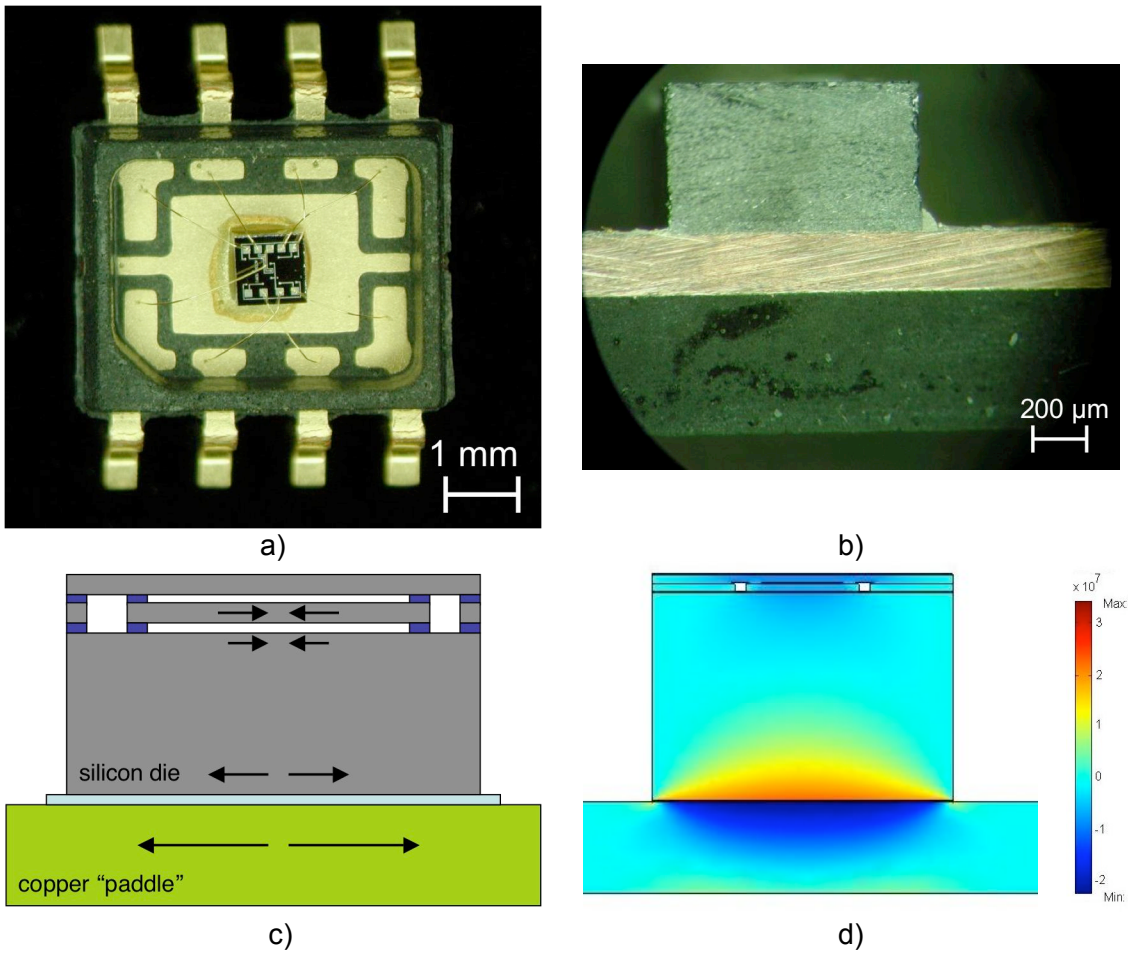

Figure 3.24: Axial compression induced by the electronic package
a) The resonator die mounted in a standard electronic package with epoxy.
b) A cross-section photo of the resonator die in the package. The package was cut with a diamond saw to produce this image. The resonator is too small to see at this scale, but it is located near the top of the silicon die. The resonator is attached to a copper “paddle” which is in the ceramic package. A bead of epoxy is visible at the lower right corner of the die.
c) Schematic illustration of the forces and strains induced by thermal expansion with increasing temperature. The arrows indicate strain directions and qualitative magnitude with increasing temperature. Notice that while the copper paddle in the electronic package is expanding with increasing temperature, the effect is to *compress* the resonator at the top of the silicon die, and lower its frequency.
d) FEM simulation result showing the stresses created by thermal expansion. The simulation assumes that the epoxy bonds the paddle and the die perfectly [simulation by R. Melamud]

The effect of temperature-dependent stress on frequency can be extremely large. For this reason, the stability experiments described in Chapter 5 were performed on resonators with designs such as the SA-DETF that isolated them from the substrate.

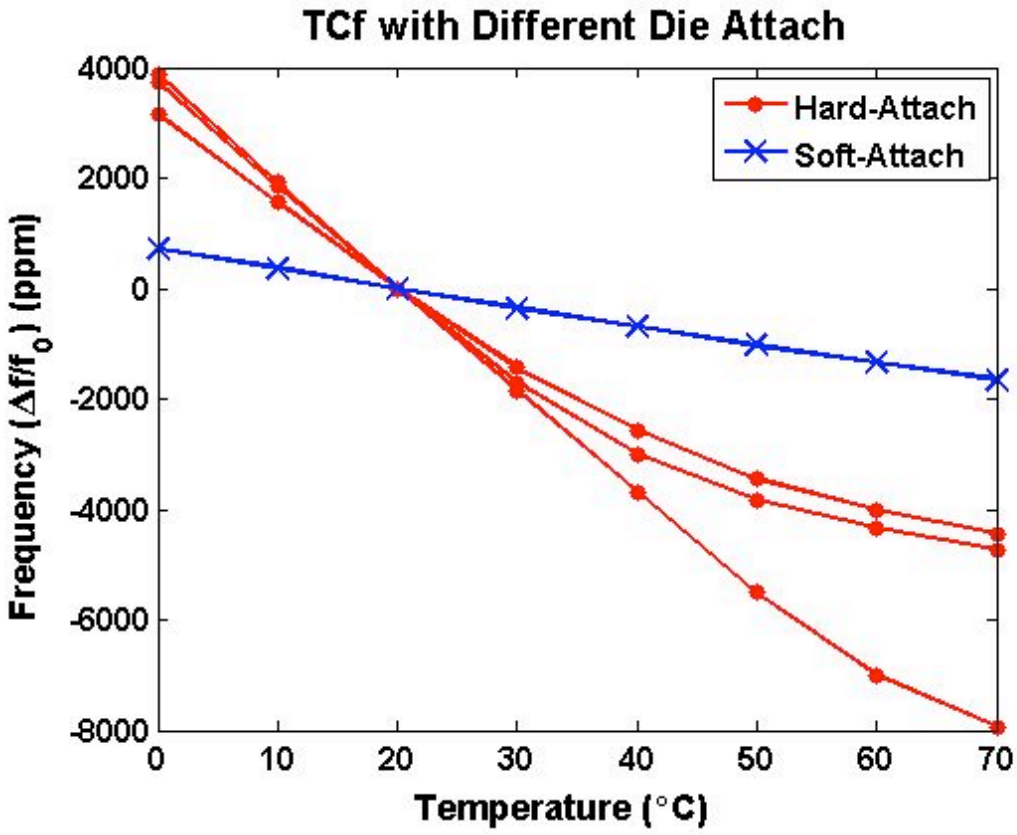

Figure 3.25: TCf measurements of packaged DA-DETF resonators. Measurements of three different samples mounted in packages with epoxy ("hard-attach") are shown in red. The expansion of the package couples stress to the resonator through the epoxy. The variation in the measurements reflects the different epoxy thicknesses (the dies are attached by hand). The most extreme TCf of the hard-attach measurements is nearly -200 ppm/°C. The reduction in slope at higher temperatures is due to softening of the epoxy. The blue line is a measurement of a resonator mounted in the package using photoresist instead of epoxy ("soft-attach"). The photoresist has a much lower Young's modulus than the epoxy, and consequently transfers much less stress from the expansion of the paddle into the resonator. The TCf value for soft-attach DA-DETFs is ~-34 ppm/°C, compared with ~-28 ppm/°C for SA-DETFs with no axial strain.

3.4.4 Electrostatic Stiffness

Now lets consider the effect of temperature on the electrostatic spring stiffness term. The linear electrostatic spring softening depends on the size of the gap, d, between the electrode and the beam, and the area A of the transduction capacitor (3-29). These values change with thermal expansion, by α. We can take the

temperature derivative of (3-29) to determine the effect of thermal expansion on the electrostatic spring term:

$$f = \frac{1}{2\pi}\sqrt{\frac{k_{m0} - k_{e0}}{m_{eff}}} \text{ , for } k_{e0} = \frac{V_b{}^2 C_0}{d^2} \text{ .} \tag{3-54}$$

$$\frac{df}{dT} = \frac{df}{dk_{e0}}\frac{dk_{e0}}{dT} \text{ ,} \tag{3-55}$$

$$\frac{df}{dk_{e0}} = \frac{1}{2\pi}\left(-\frac{1}{2m_{eff}}\right)\left(\frac{k_{m0} - k_{e0}}{m_{eff}}\right)^{-1/2} \text{ ,} \tag{3-56}$$

$$\begin{aligned}\frac{dk_{e0}}{dT} &= \frac{\partial k_{e0}}{\partial h}\frac{dh}{dT} + \frac{\partial k_{e0}}{\partial L}\frac{dL}{dT} + \frac{\partial k_{e0}}{\partial d}\frac{d\,d}{dT} \text{ ,} \\ &= \left(\frac{V_b{}^2 \varepsilon h L}{d^3}\right)\left[\frac{h_0\alpha}{h} + \frac{w_0\alpha}{w} - 3\frac{d_0\alpha}{d}\right]_{T=T_0} = k_{e0}(-\alpha) \text{ ,}\end{aligned} \tag{3-57}$$

$$TCf_{\alpha,k_{e0}} = \frac{df}{dT}\frac{1}{f_0} = \frac{k_{e0}}{4\pi^2 m_{eff} f_0{}^2}\alpha\Big|_{V_b=15} \approx 0.0025\, ppm/°C \text{ .} \tag{3-58}$$

The effect of thermal expansion on the frequency due to the electrostatic spring is quite small for normal operating voltages. Even for unusually high bias voltages (100 V), the effect is still << 1 ppm/°C.

3.4.5 Quality Factor

The quality factor of the 1P3M DETF resonators is a strong function of temperature. The displacement of the resonator at resonance is proportional to the Q (3-23), and the resonant frequency is a related to displacement through the non-linear spring effects (Section 3.2.2.2), so we expect that the TCf will be affected by the TCQ. The expression for resonant frequency as a function of the non-linear spring terms is given in (3-34) and the derivative with respect to T is straightforward if we approximate the change in Q with temperature at approximately -1%/°C. The amplitude of resonator displacement at resonance under the influence of the non-linear spring is X_c [105].

$$\frac{df_0'}{dT} = \frac{d(f_0)}{dT} + \frac{d\left(f_0 \mathrm{K} X_c^{\,2}\right)}{dT} \text{ , where } X_c = \frac{2}{\sqrt{3\sqrt{3}|\mathrm{K}|Q}} \text{ .} \tag{3-59}$$

$$\begin{aligned} &\frac{d\left(f_0 \mathrm{K} X_c^{\,2}\right)}{dT} = \frac{d\left(f_0 \mathrm{K} X_c^{\,2}\right)}{dX_c}\frac{dX_c}{dQ}\frac{dQ}{dT} \text{ , where} \\ &\frac{d\left(f_0 \mathrm{K} X_c^{\,2}\right)}{dX_c} = 2 f_0 \mathrm{K} X_c \text{ , } \frac{dX_c}{dQ} = -\left(3\sqrt{3}|\mathrm{K}|Q\right)^{-3/2}\left(3\sqrt{3}|\mathrm{K}|\right) \text{ ,} \\ &\text{and } \frac{dQ}{dT} \approx 0.01 Q_0 \text{ .} \end{aligned} \tag{3-60}$$

$$TCf_k = \frac{df_0'}{dT}\frac{1}{f_0'} = -2 f_0 \mathrm{K} X_c \left(3\sqrt{3}|\mathrm{K}|Q_0\right)^{-3/2}\left(3\sqrt{3}|\mathrm{K}|\right)0.01 Q_0 {f_0}'^{-1}$$

The result is less than -1 ppm/°C with a displacement of $X_c = X_0 \approx 10$ nm and $Q_0 = 10{,}000$. The precise value of dQ/dT is a complex function of material properties as discussed in Section 3.3. The overall effect is to decrease the resonant frequency as temperature decreases, introducing curvature to the plot of frequency versus temperature. However, change in frequency due to large displacements is undesirable because it introduces noise in the measurement (see Chapter 5), and the resonators are usually operated in a regime where the frequency contribution from displacement is small. To illustrate this, the resonator magnitude at each temperature step during the TCf measurement in Figure 3.21 is shown in Figure 3.26. The resonator frequency response during the TCf measurement does not show the "bending" behavior evident in the measurements of large displacements (with large V_{bias} and V_{AC}) in Figure 3.10., so the effect of the TCQ on the TCf is not expected to be large.

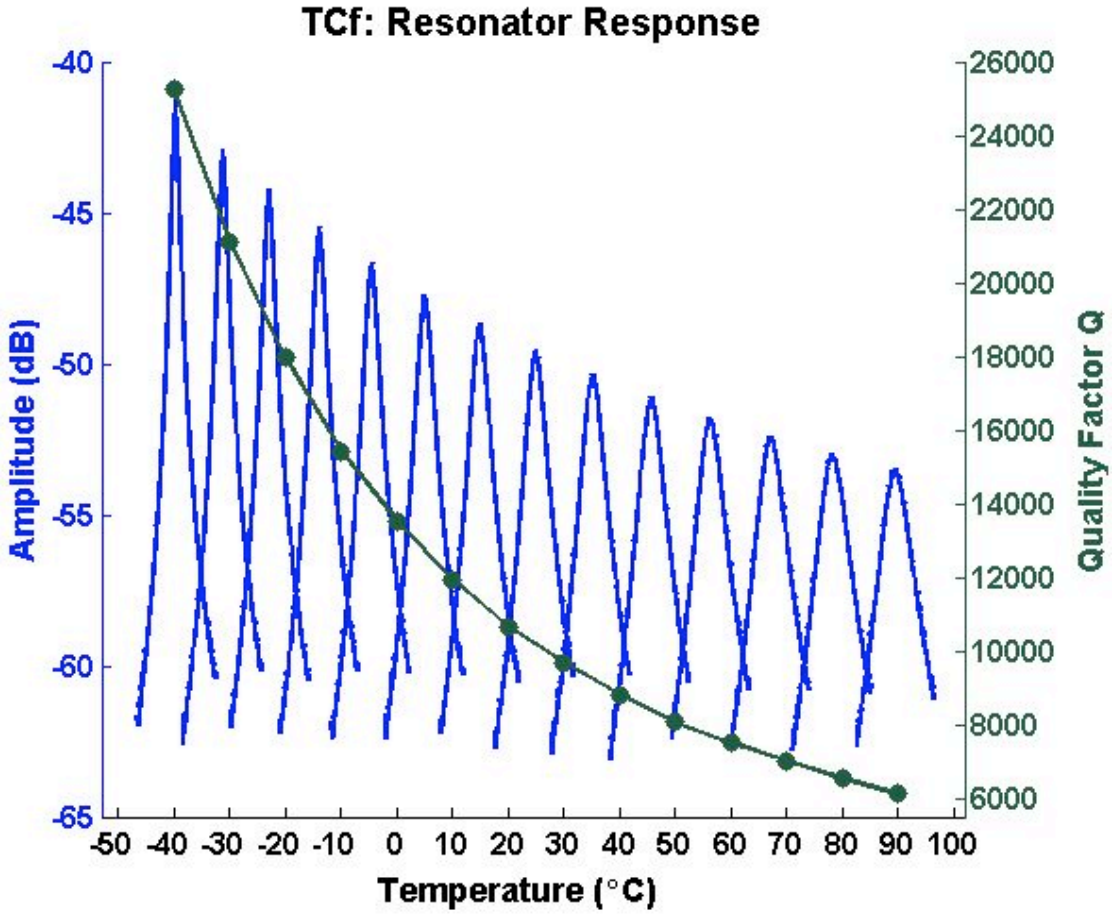

Figure 3.26: Resonator Respose to Temperature
The resonator frequency response at each temperature step is plotted. The resonator peaks do not exhibit visible "bending" indicative of extreme displacement (compare with Figure 3.10), and so the contribution to TCf from non-linear displacement effects is small.

3.4.6 Feedthrough Capacitance

The effect of the feedthrough capacitance on the measured frequency is negligible when the resonant signal level is much greater than the noise floor established by the feedthrough. The resonant frequency is the frequency where the resonator response has the maximum amplitude, as in Figure 3.15. Comparing Figure 3.12 and Figure 3.14 we can imagine how the antiresonance might "drag down" the right-hand side of the resonance peak and change the value of the measured resonant frequency. However, in practice, a) it is usually possible to increase the amplitude of the resonator signal (by increasing V_{bias}) to a level sufficiently greater than the noise

floor established by the feedthrough capacitance that the feedthrough has no effect, and, b) the feedthrough capacitance can be minimized by proper measurement techniques (see Chapter 5), so that the noise floor is quite low to begin with. As an example, the feedthrough capacitance in a typical device was measured at four temperatures. The average level of each measurement is basically the same (Figure 3.27), and there is no obvious difference between any of the measured noise levels (Figure 3.28).

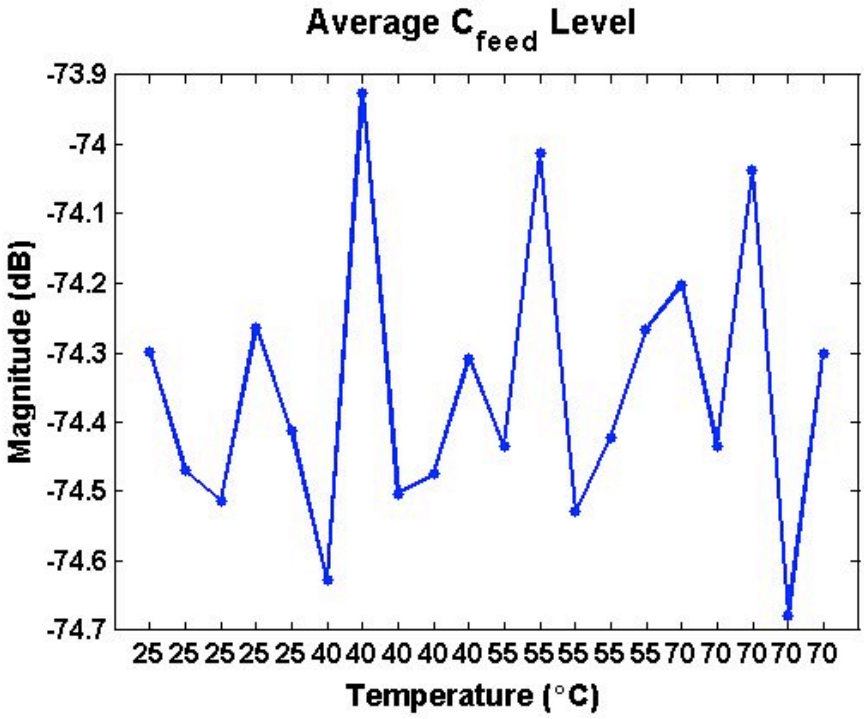

Figure 3.27: Average Level of Feedthrough Capacitance versus Temperature
Five measurements are taken at each temperature, shown in Figure 3.28. The average of each measurement is plotted here. No dependence on temperature is evident.

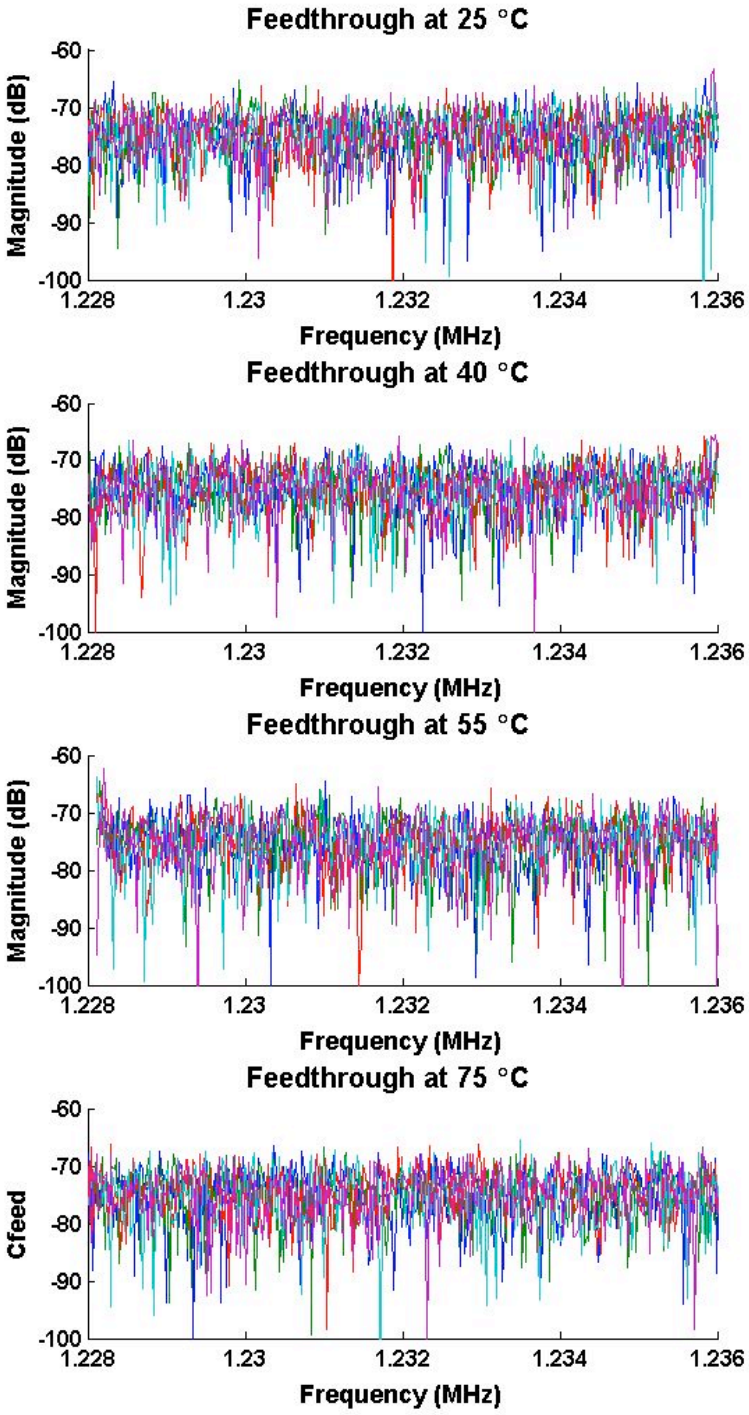

Figure 3.28: Feedthrough Capacitance at Different Temperatures
The feedthrough capacitance level is measured by performing a frequency sweep with the resonator bias voltage set to zero, so that the resonator beam does not move. Five measurements are taken at each temperature, and plotted together. All the measurements are similar and no dependence on temperature is observed.

3.5 Conclusion

Three models have been used to predict the resonant behavior of electrostatic MEMS DETF resonators, and a fourth used to explain the quality factor. These models identified five significant contributions to the resonant frequency with temperature dependencies, as well as the temperature dependence of quality factor, which in turn influences the resonant frequency through the higher-order dynamics. The temperature-dependent frequency components for a silicon SA-DETF resonator are listed in Table 3-2.

Effect	Symbol	Contribution to TCf (ppm)
Axial Load (strain-isolated designs)	P	0
Elasticity Change (n-type Si)	TCE	-31.9
Dimensional Change	α	+1.3
Electrostatic Spring Softening	k_{e0}	<< 1
Mechanical Spring Stiffening	k_{m2}	0
Quality Factor	TCQ/k_{e2}	(< -1, non-linear)
Total:		≈ **-30.6 ppm/°C** (at 25°C)

Table 3-2 Components of DETF TCf
The values are given for single anchored (SA) flexural resonators at room temperature. Double-anchored (DA) resonators will have non-zero TCf values for P and k_m. Note that all of the effects have higher-order temperature coefficients which are not considered here, but which will introduce curvature to plots of measured data, distorting the linear fit, especially over large temperature ranges.

The typical TCf measurement in Figure 3.21 (page 70) gives a TCf = -27.4 ppm/°C over a large temperature range centered on 25 °C. Numerous measurements of similar devices over the course of this work have produced results between -27 and -29 ppm/°C, and other researchers working with comparable silicon resonators report similar measurements [40, 49, 92, 139-141]. It is apparent from the figure that the linear fit to the data is not exact, and that the linear TCf result for each measurement depends on the temperature range that is measured and the TCQ of the resonator. Variations of ±1 ppm are not unusual.

The most important effect on frequency is the change in elasticity, the TCE. This effect is responsible for the widely quoted TCf value of "about -30 ppm/°C" for silicon resonators. Independent measurements of silicon TCE that have been reported over a period of several decades [[130, 132, 136, 137]] give TCE values between -52

and -107 ppm/°C, and it is quite possible that the true value is slightly lower than that used in this work (-63.7 ppm/°C, from [130]). Unfortunately, the other components of TCf, none of which are constant or even linear with temperature[18], cannot be quantified with sufficient precision to allow a value for TCE to be extracted from measurements of silicon DETFs described here.

Finally, it should be noted that the expressions for resonant frequency developed herein predict a frequency of 1.44 MHz for the 1P3M DETF with dimensions in Figure 3.1. However, FEM simulations (Figure 3.4) indicate that the coupling blocks do not provide a perfectly rigid anchor for the clamped-clamped resonator beam, and the frequency predicted by simulation is approximately 1.3 MHz at room temperature, which agrees with measurements.

3.6 Acknowledgement

Several people made important contributions to the understanding of the TCf of silicon resonators in the course of this work. Rob Candler thoroughly investigated the quality factor in micromechanical silicon DETF resonators and is responsible for the original 1P3M design. Bongsang Kim pioneered the work on the temperature dependence of Q_{TED}. Renata Melamud contributed greatly to the development of the analytical expressions for TCf presented here and led the investigations of stress in DA-DETF resonators. Manu Agarwal has investigated the non-linear effects in silicon MEMS DETF resonators. Jeff Li is responsible for the cross-sectioning the packaged devices.

[18] The silicon TCE at 25°C is -63.7 ppm/°C; at 125°C, the value is -74.6 ppm/°C.

It doesn't matter what temperature the room is, it's always room temperature.
-Steven Wright

Chapter 4 Temperature Compensation

The temperature sensitivity of frequency of silicon resonators, ~3000 ppm over a 100 °C range, is quite large compared to the stability requirements of high-performance frequency references (<< 0.1 ppm) or even low-performance frequency references (50 – 100 ppm) (see Figure 1.2). Clearly, some form of temperature compensation is required in order to use silicon resonators in practical frequency reference applications. In this chapter, a variety of methods for controlling the frequency-temperature (*f-T)* characteristic of silicon micromechanical resonators are examined and the design choices for a high-stability resonator are considered.

4.1 Frequency Tuning Methods

In general, any method that reversibly changes the frequency of a resonator can be considered for a temperature compensation scheme if it allows the frequency to be "tuned" in opposition to the changes induced by temperature. Every term in the expressions for resonator frequency (Chapter 3) is a candidate, as well as the temperature itself (ΔT). Some methods are passive and require no external power or control. Other methods are active and provide arbitrary frequency tuning capability.

4.1.1 Electrostatic Tuning

The "electrostatic tuning" or "bias pulling" effect in capacitive actuation (Section 3.2.2.1) is well known. Since the effective spring constant, and hence frequency, is a function of bias voltage in the parallel plate actuator, one can adjust V_{bias} based on a temperature sensor reading so that the frequency remains constant when temperature changes. The choice of what value of V_{bias} to use at each temperature is determined by a calibration step and stored in a lookup table, either as discrete points or as a function [140]. Results of better than 40 ppm *f-T* variation over 100 °C have been reported with the use of high-order calibration functions [40, 47].

Several researchers have reported designs that introduce separate control electrodes and voltages to tune the frequency, rather than using the bias voltage [142-144]. The phenomenon of electrostatic tuning is the same, but the bias voltage can be fixed (reducing complexity), and the structure geometry can be designed so that the frequency is an arbitrary function of control voltage, as opposed to a quadratic function of bias voltage for simple parallel plate spring softening. An alternative to a separate electrode is to mix the control voltage into the resonator stimulus signal, phase-shifted by 90° to match the electrostatic spring [145].

An interesting variation on this theme is the device described by Hsu [146]. In this design, the resonant beam was separated from the input electrode by gold posts. As temperature increased, the gold expanded, increasing the transduction gap, *d*, altering the electrostatic spring stiffness, and changing the frequency of the beam. Because the changing gap affected frequency in a non-linear manner, Hsu found that by choosing different V_{bias} values he was able to achieve different TCf values. The lowest value he reports is 0.24 ppm/°C. This method is interesting, but as it relies on large differences in thermal expansion coefficients, it suffers from material complexity issues, discussed in the next section.

Electrostatic tuning methods have the advantage of requiring little additional power and being relatively straightforward to implement. The resonator amplitude, and hence transfer function gain, is a function of bias voltage (see Figure 3.9), but this is usually acceptable for timing applications. However, bias pulling may require large

voltage swings and high voltages in order to tune the frequency of the resonator over large temperature ranges, and it requires a calibration step which can be time-consuming and costly. Bias pulling was considered for stabilizing the DETF resonators described herein; however, they are unsuitable because of the process limitations described in Chapter 2.5. The average sensitivity of the 1.3 MHz DETF resonator's frequency to bias voltage is approximately 100 Hz/V, so a swing of approximately 39 V would be required to compensate for a 3000 ppm shift in frequency. However, because the transduction gap in these resonators is large (see Section 2.5), the resonators must have a relatively low stiffness, and the range of bias voltages suitable for DETF operation is restricted: the bias must be high enough to generate a good signal, and low enough to avoid nonlinear operation or breakage.

4.1.2 Stress

A longitudinal tensile stress on a flexural mode resonator will increase its effective stiffness, and hence its frequency (3-15). A temperature-dependent stress can be created by a passive system using material combinations with different values of thermal expansion coefficients (α), for example [147, 148], or by thermal expansion of a trapped gas [149]. Stress can also be applied by an active transducer such as a capacitive actuator [150], or thermal actuator [151-153]. The advantage of passive "stress compensated" designs is that the compensation requires no external power or calibration. The primary disadvantage is poor repeatability and hysteresis. Most strong materials with large CTE values (i.e., metals) tend to have plastic deformation at low strains and poor adhesion to other materials. The temperature cycles required for useful resonator operation are large (at least 100 °C) and materials with large CTE values undergo large strains during these cycles.

An investigation into passive stress compensation was carried out during this work. DA-DETF resonators were fabricated with varying thicknesses of aluminum ($\alpha_{Al} \approx 23$ ppm/°C [154]) on top of them. The Al layer expanded with increasing temperature and put tensile stress on the silicon resonator ($\alpha_{Si} = 2.6$ ppm/°C [154]). The tensile stress acts to increase the frequency, while the silicon TCE acts to decrease

it. Promising initial results were achieved (see Figure 4.1[148]), but it quickly became clear that the sputtered Al layer was not performing reliably under thermal cycling. Figure 4.2 shows a test of the sputtered aluminum layer under repeated thermal cycling.

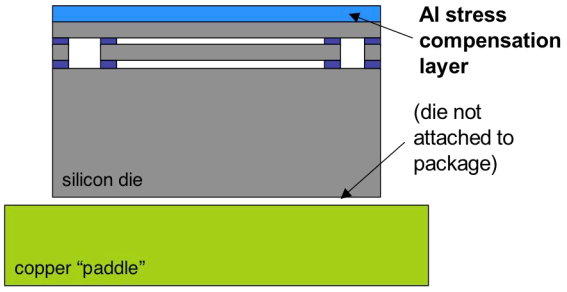

a)

Al Thickness (µm)	TCf (ppm/°/C)
0	-31
1.8	-22
5.6	-13
7.3	+16

b)

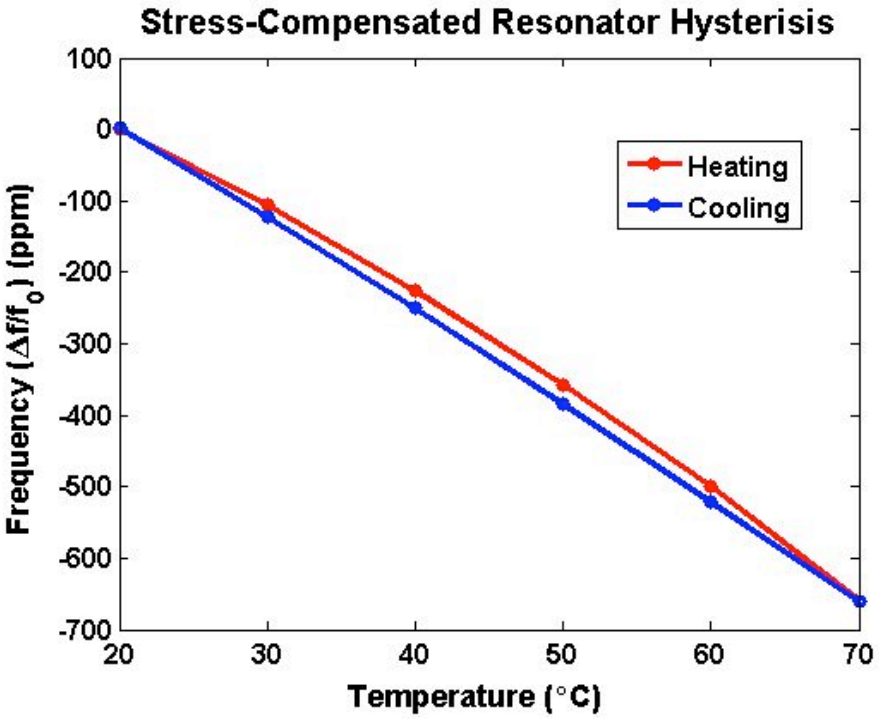

c)

Figure 4.1: Resonator stress compensation using an AL stress compensation layer
a) schematic of resonator die with Al compensation layer
b) TCf results with different Al thicknesses
c) a TCf measurement of a resonator with a 5.6 µm Al layer. The Al layer behaves differently during heating and cooling, causing the resonator frequency to be different. [unpublished data courtesy of R. Melamud]

From Figure 4.1 and Figure 4.2, we can see that the behavior of the Al layer is not repeatable enough for sub-ppm level reliability. In fact, Al is widely felt to be one of the worst materials for devices that are intended to be stable, and should be avoided if possible [155].

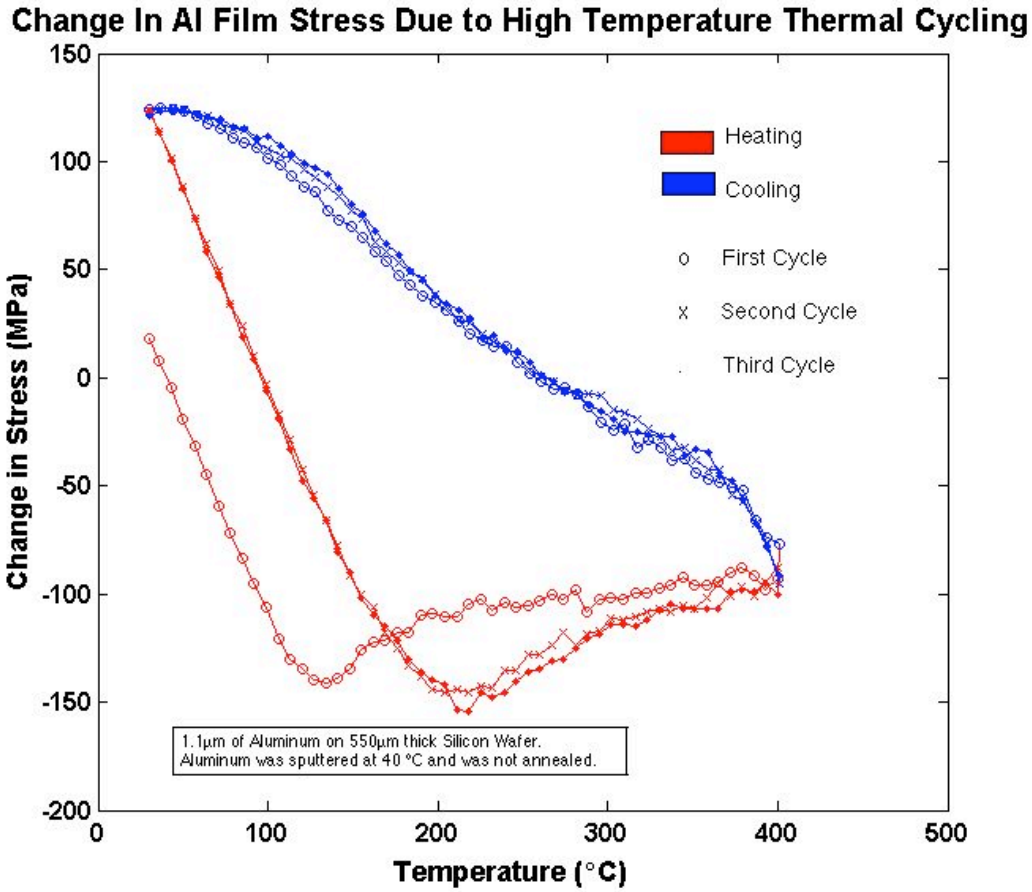

Figure 4.2: Sputtered aluminum under repeated thermal cycling
An Al film was sputtered on to a silicon wafer. The stress was determined by measuring the curvature of the wafer. [Figure by R. Melamud]

Several other material combinations were considered, and some were attempted. For example, it would be possible to reduce the thickness of the handle layer of the resonator so that the expansion of the copper paddle and epoxy were acting to reduce the TCf instead of increase it, but this mechanism relies on transmitting stress through the die attach epoxy, and the epoxy exhibits strong hysteresis and is difficult to apply with a constant thickness (see Chapter 3). Various other epoxies and polymers were used to coat the top of the resonator die, including

SU-8, cyanoacrylate, and several non-conductive die-attach epoxies. None were found to have well controlled (or documented) material properties, and deposition of uniform layers proved difficult. In general, multiple material combinations, especially when materials are selected for a large difference in α, are found to introduce fabrication complexity and reliability problems due to material interfaces, differential thermal expansion, diffusion, material hysteresis, etc.

4.1.3 Nonlinear Spring Stiffness (Displacement)

As discussed in Section 3.3, the resonators considered here have a strong temperature dependence of Q, and hence of displacement. It is also true that the electrostatic nonlinear spring causes frequency to decrease as displacement increases. Therefore, in resonators with a large TCQ and large displacement, we should be able to see a reduced TCf, and we should be able to tune this TCf value by changing the displacement, as in Figure 3.10. However, as discussed in Section 3.4.5, this non-linear effect is very small during normal operation, and at most we see a change in the curvature of the TCf measurement, rather than a dramatic reduction in the TCf. This effect is illustrated in Figure 4.3, which shows the TCf of a resonator at different bias voltages. Note that the highest bias voltage used in Figure 3.10 is 90 V, while the experiment shown here uses a maximum of only 25 V which is a more reasonable value for normal operation. The effect on TCf is measurable but quite small.

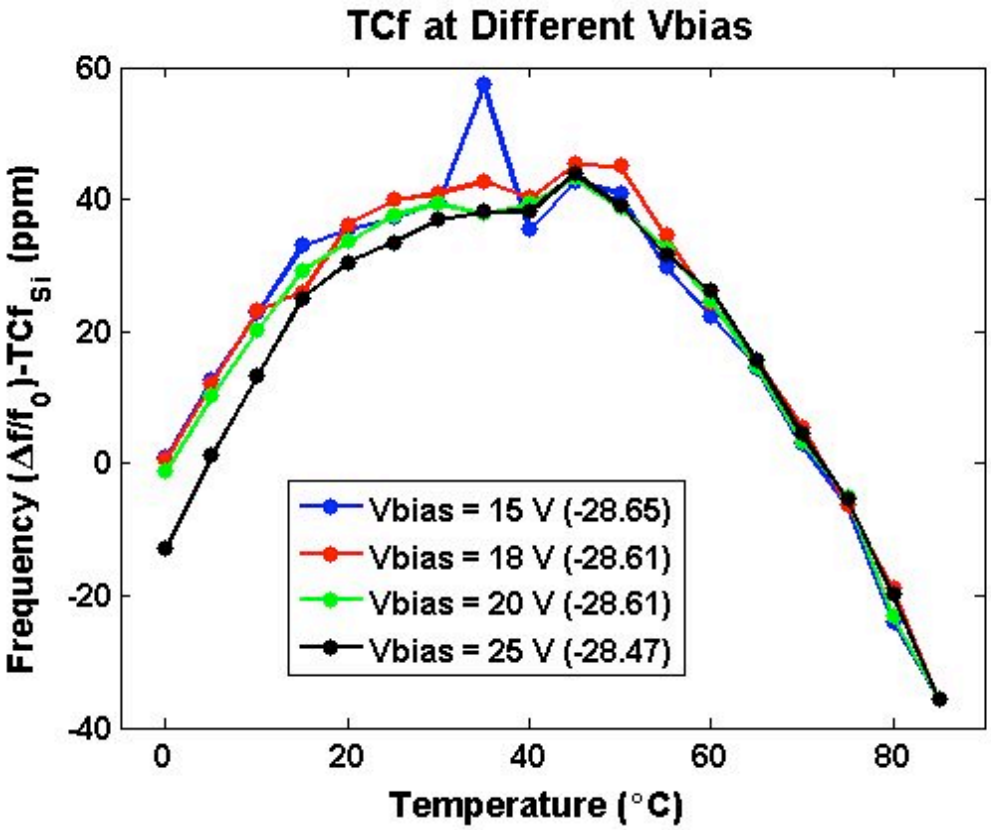

Figure 4.3: Comparison of measured TCf at different V_{bias}
The TCf data is shown with the "ideal" silicon TCf of -28 ppm/°C subtracted from each measurement so that the differences between measurements can be seen. As bias voltage is increased, the curvature of the TCf plot increases, especially at lower temperatures where the displacement is greatest. The TCf value from a simple linear fit to the data is given in the legend in (ppm/°C). Notice that the value is decreasing with increasing bias voltage.

Even though the bias voltage is restricted to 25 V, the resonator exhibits significant nonlinear behavior at low temperatures, where displacement is greatest. Figure 4.4 shows the resonator sweep measurement at 0 °C from the TCf measurement at 25 V shown in Figure 4.3. The "left-side" Duffing is clearly visible in the measurement, even at relatively low bias voltage, and the reduction in TCf is negligible. So it is impractical to use the electrostatic nonlinear spring stiffness to reduce the TCf. Moreover, increasing nonlinear behavior increases the phase noise of the oscillator output, which is undesirable.

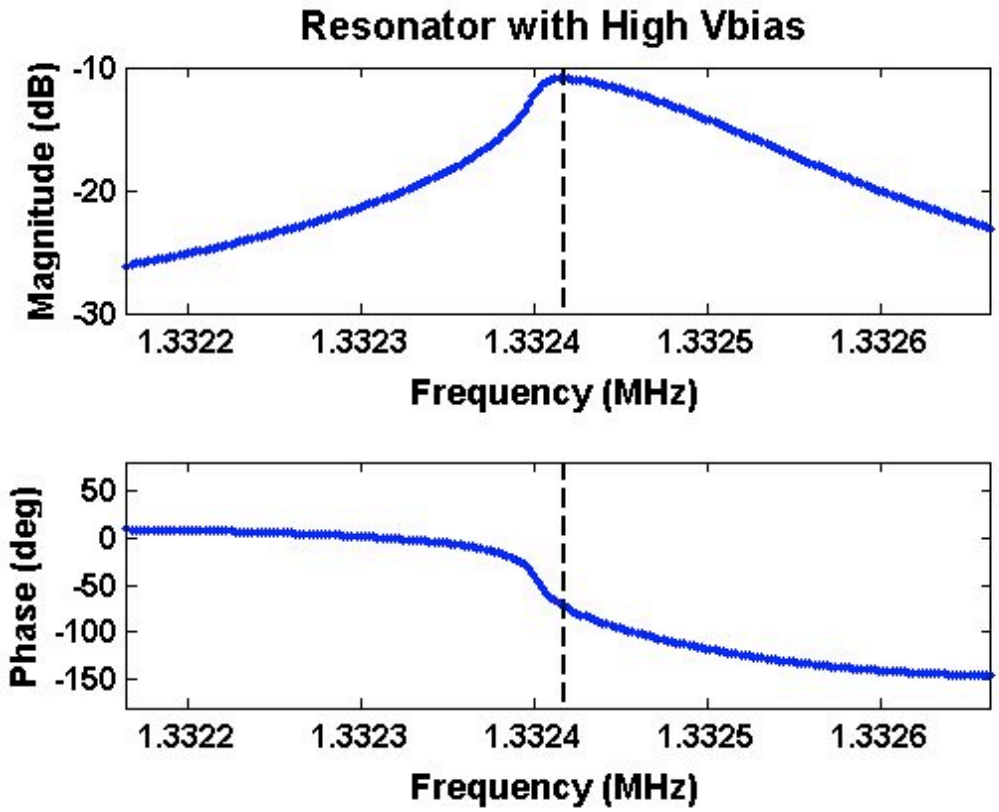

Figure 4.4: Resonator Frequency Response at High Bias
This is the measurement with V_{bias} = 25 V at 0 °C from the TCf measurement above (Figure 4.3). Even at this relatively low bias, the electrostatic non-linearity is clearly affecting the resonator, but the effect on the TCf is small.

4.1.4 Stiffness

The change in elastic stiffness of the resonator is the dominant factor in the TCf. The change in elastic stiffness is primarily due to the change in Young's modulus (E) with temperature, the TCE. Some anisotropic materials have a TCE that is a complex function of crystal orientation. Quartz (crystalline SiO_2) is the most common example and this is one of the most important reasons for its enduring popularity as a resonator material. If a resonator is cut from a piece of quartz at certain angles with respect to the main crystal axes, the resonator structure will have a dramatically different TCE than a structure of the same dimensions cut at a different angles, and hence the resonator will have a dramatically modified f-T response. In many cases the f-T response will have a quadratic or cubic form with local maxima and minima. The

existence of these so-called "zero-TCf cuts" is due to the complexity of the quartz crystal, which has a hexagonal crystal cell and forms crystals with 17 different faces [7] (Figure 4.5). When the first quartz zero-TCf cuts were discovered, they were kept secret by the companies that discovered them, but now there are many different published zero-TCf angles [156-158] and new ones are still being discovered, e.g. [159]. These angles are called "cuts" and identified with letters: AT, BT, SC, etc., as shown in Figure 4.6. The SC cut is the most common crystal cut used in the highest performance quartz devices.

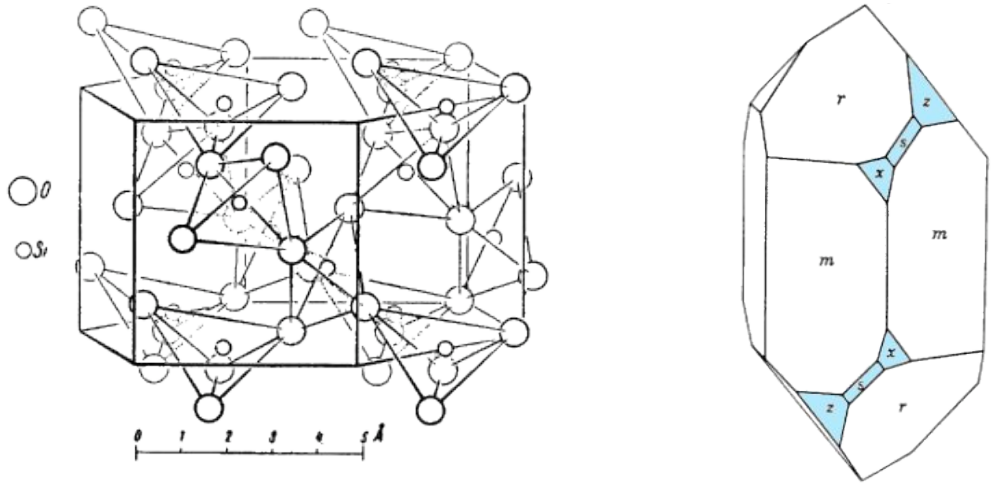

a) b)

Figure 4.5: Quartz crystal structure.
a) The unit cell for right-handed α-quartz. Compare this with the silicon structure in Figure 2.1.
b) Schematic of a crystal of right-handed quartz. Each of the 17 faces has an identifier. [160]

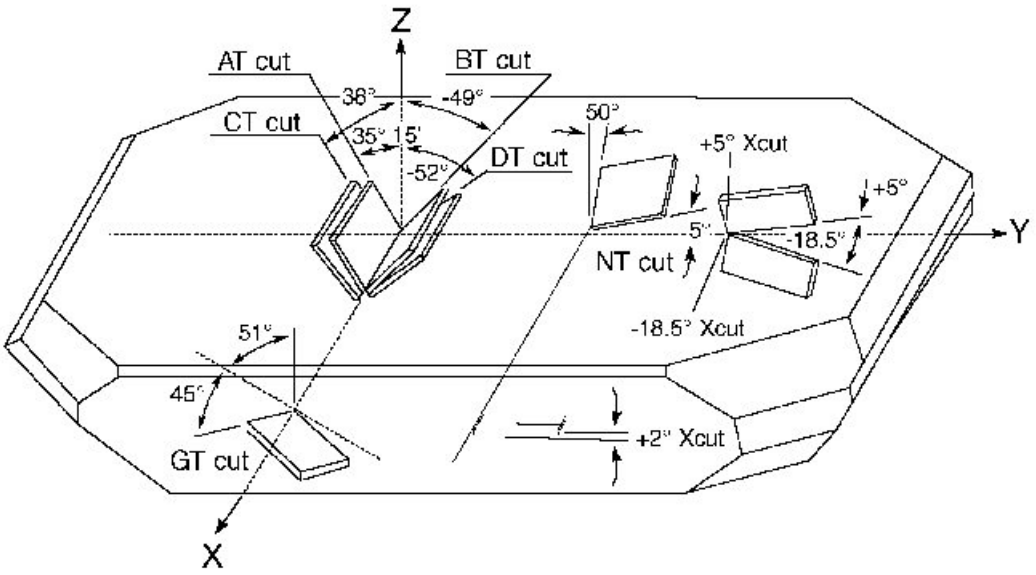

Figure 4.6: Different Quartz Resonator Cuts in a Quartz Blank.
A "Z-plate" quartz blank is shown. The top face of the piece is aligned with the z-axis (001). The angles with respect to the crystal axes for various cuts are shown [161].

The advantage of a higher-order *f-T* response for frequency stability is obvious. A properly cut quartz resonator will have a much smaller *f-T* range even without any further temperature compensation. Figure 4.7 shows the *f-T* curves for various quartz cuts. From the figure, we can see that the AT cut, for example, stays within approximately ±25 ppm over a large temperature range without any additional temperature compensation.

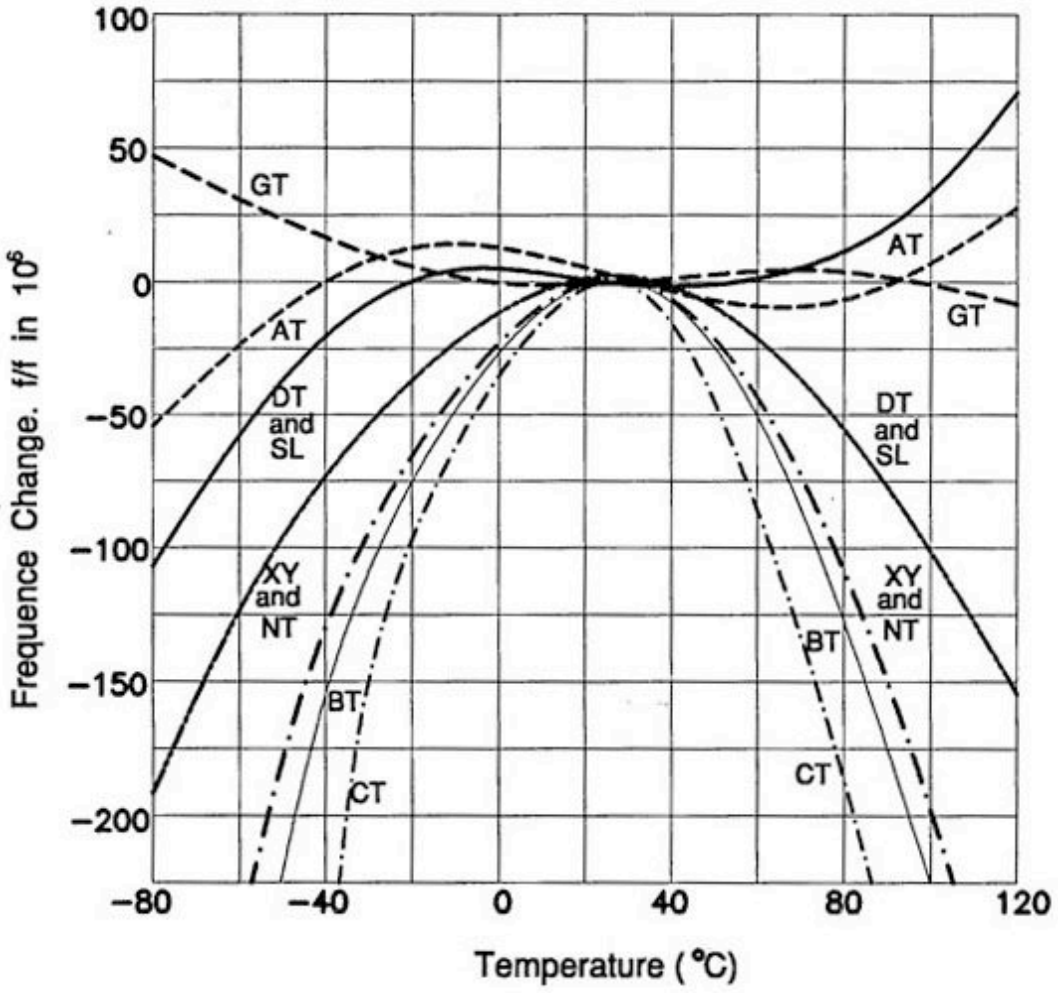

Figure 4.7: *f-T* curves for different quartz cuts.
From [162].

Silicon, although a crystalline material, does not have zero-TCf cuts. Its cubic crystal structure is too simple and the TCE is the same in all directions in the crystal [130, 132]. In addition, the flexural-type resonator creates nearly uniaxial strain which involves only a simple *E* component (see Appendix A), as opposed to a bulk-mode quartz resonator which operates in a high-order shear mode and creates strains in orthogonal directions, invoking a more complex elastic behavior.

However, it is possible to construct a composite structure of two materials with different TCE's so that the resulting structure has an "effective TCE". Amorphous silicon dioxide has a positive TCE [136, 163, 164] (Figure 4.8), and silicon and silicon dioxide can be easily combined in microfabricated structures.

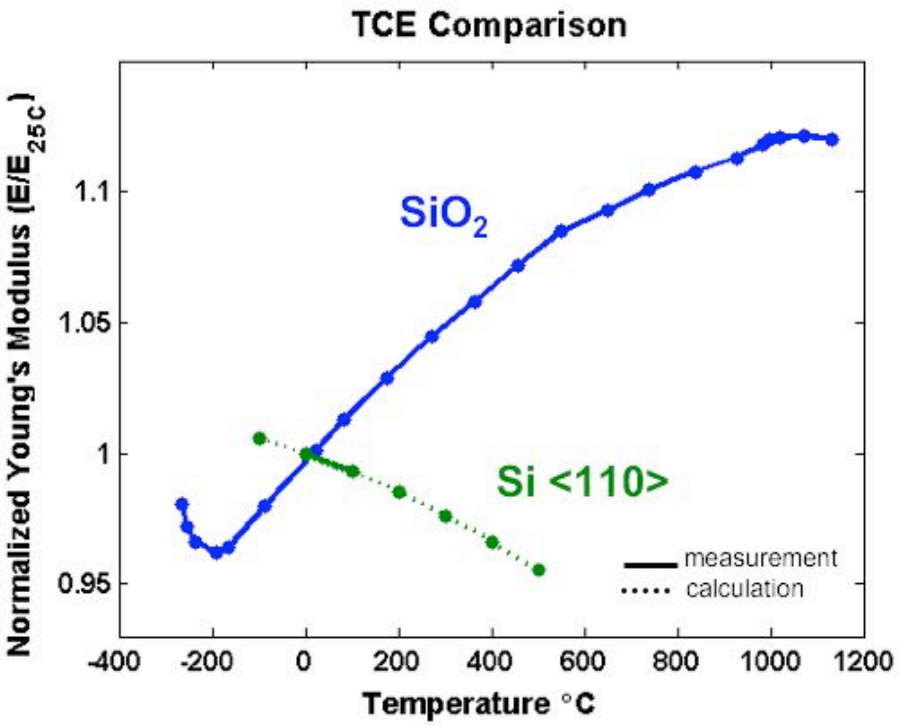

Figure 4.8: TCE of Silicon and Silicon Dioxide.
The SiO_2 data is from [163]. The Si data is from [130]. Silicon elastic behavior becomes less predictable near 600 °C [62].

The combination of silicon dioxide with other materials (including silicon) to create composite resonators with a reduced effective TCE has been reported previously in various permutations [165-171]. We have been investigating this combination for our DETF resonator. For flexural beams, the best design is the easiest one to fabricate, viz., a silicon dioxide coating on a silicon beam[19] as shown in Figure 4.9 [172]. The combination of silicon and thermally grown silicon dioxide appears to be an exception to the materials combination issues described in Section 4.1.2. The silicon dioxide forms a strong bond with the silicon it is grown from and the oxide is a relatively strong material with a low CTE. Testing is ongoing to determine the long-term stability of composite resonators.

[19] This technology is referred to internally as "Krispy Kreme" (a popular brand of donuts), because the silicon resonator is covered with a silicon dioxide "glaze".

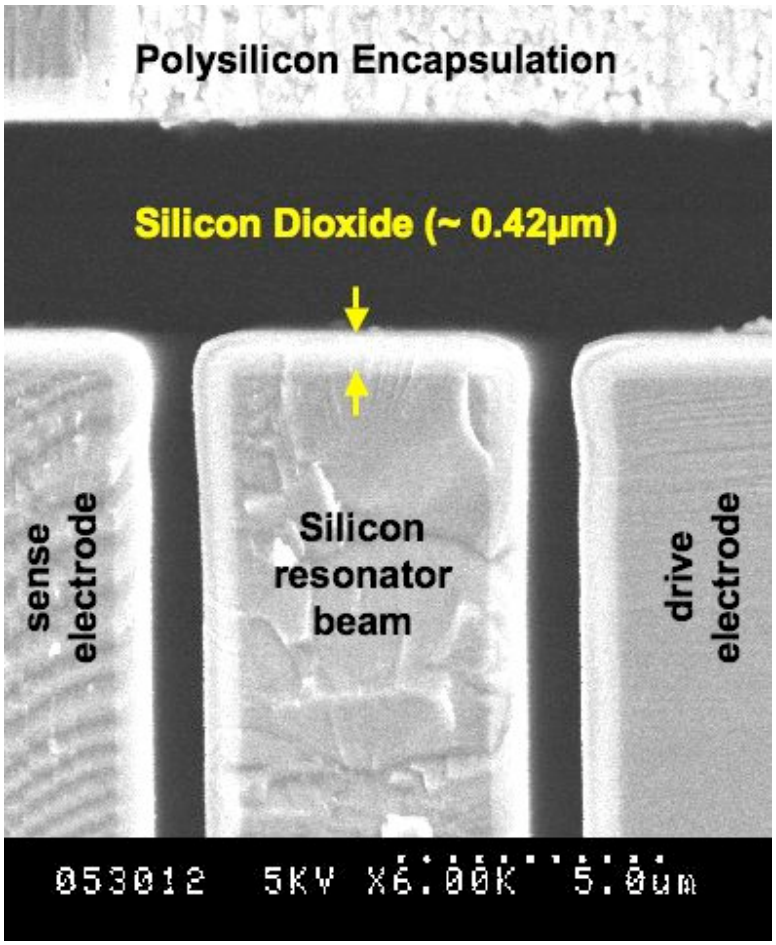

Figure 4.9: SEM of a Si/SiO_2 composite resonator beam.
Compare this with the SEM in Figure 2.5, which shows a silicon beam without an oxide coating.

The initial performance of Si/SiO_2 composite resonators is promising [173]. Due to the interaction between the higher order coefficients of elasticity and electrostatic softening, the resonators exhibit a quadratic *f-T* response with a local maxima, and the total frequency variation is reduced by an order of magnitude compared to pure silicon resonators (Figure 4.10). However, the total *f-T* range is still several orders of magnitude greater than the goal for high stability devices.

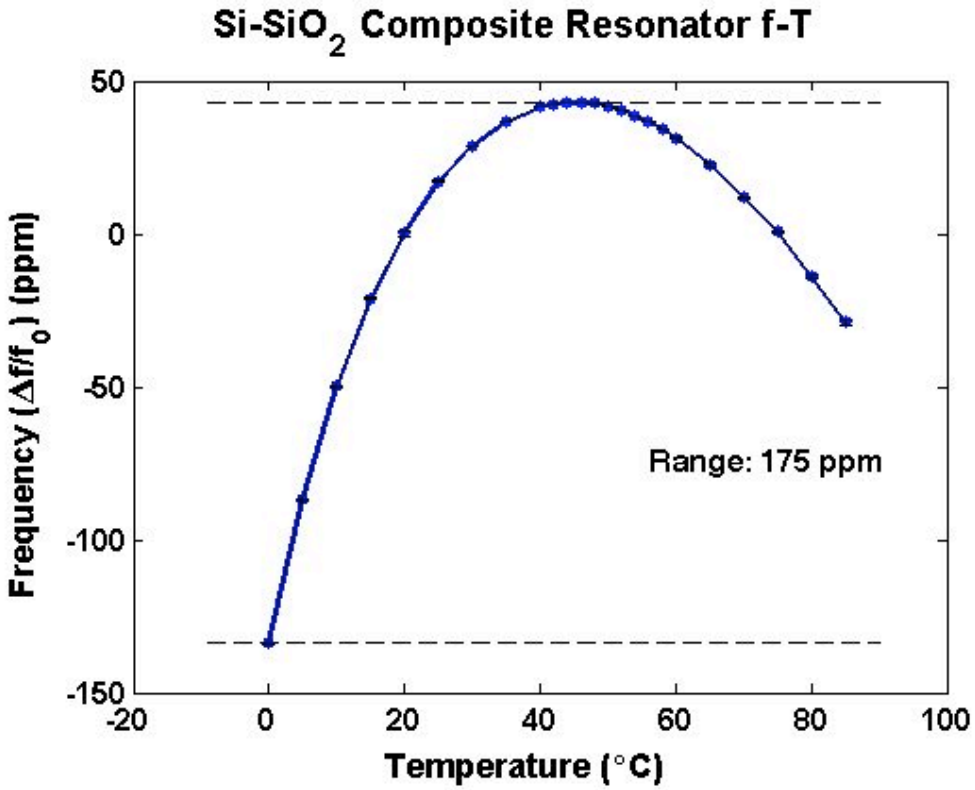

Figure 4.10: Typical *f-T* response of a Si-SiO_2 composite resonator

4.1.5 Temperature Control

The most straightforward method of controlling the frequency of a resonator with a high temperature sensitivity is to control the temperature of the resonator. This is in fact what is done in high-performance ovenized quartz oscillators (OCXO) (see Figure 1.2): the resonator is placed inside an insulated, temperature-controlled enclosure. This is called ovenization. Because heat pump efficiency is generally low, ovenization schemes typically do not include a cooling mechanism. The oven setpoint is chosen to be greater than the highest ambient temperature that will be encountered in operation, and the heating power is adjusted to keep the oven temperature constant as the ambient temperature fluctuates. Commercial macro-scale ovenized devices are relatively large because the insulation required for high thermal isolation requires space. Consequently, the power consumption and size requirements for high-stability devices are generally prohibitive for mobile and miniature applications.

The principle of ovenization can be applied to MEMS. A frequently-reported ovenized MEMS device is the "microhotplate" sensor [174-180], which is a heated platform suspended from a small number of supports which have minimized cross-sections for thermal isolation. Reported temperature stabilities and uniformities are usually measured in percent, and typically little effort is made to isolate the system from the ambient environment, as it is a sensor. “Micro-ovenization” for micromechanical resonators has been demonstrated using similar hotplate platforms [181, 182], but the fabrication and packaging of a micro-ovenized MEMS resonator with sufficient thermal isolation to achieve high levels of stability with reasonable power consumption along with all of the other aspects of frequency stability (see Chapter 2) is difficult.

4.1.6 Frequency Modification

An additional method for tuning frequency, which is not suggested by the analysis in Chapter 3, is direct modification of the oscillator output frequency without adjusting the resonator, either by circuit component tuning or frequency multiplication.

The TCXO class of quartz frequency references (see Chapter 1) is based on the design of oscillators with discrete components whose temperature coefficients are chosen to counteract the temperature coefficient of the quartz resonator. These components have their own complex temperature dependencies, but have the advantage of being passive and automatic. Modern TCXOs can achieve medium-level frequency stability performance.

Designs that use microcontrollers to implement complex frequency modification algorithms are categorized as MCXOs. In an MCXO system, the frequency is modified using a mixer or phase-lock loop (PLL). In the last decade, a new class of PLL circuits, called Fractional-N PLLs, has been developed, which make this technique even more useful [183, 184], and it is currently used in commercial frequency references [185]. However, frequency multiplication introduces noise in the

frequency signal, and MCXO oscillators are currently not suitable for high performance applications.

4.2 Compensation System Design

Several options are available for the design of a system for compensating frequency shift due to temperature. The passive effects (stress compensation, composite TCE, mechanical nonlinearity) have been demonstrated to reduce the *f-T* range, but with significant downsides such as fabrication difficulty and hysteresis. Moreover, all of these passive methods are attempting to moderate the effect of an inherently complex function, $f(T)=f(TCE_{Si}(T),P(T),\alpha(T),X_0(T))$ (see Chapter 3), by using a different complex function, such as $TCE_{Si\text{-}SiO2}(T)$, or $P(\Delta\alpha,T)$. This approach is inherently unable to produce high-stability results over a wide temperature range because the resulting *f-T* characteristic is the difference between *f(T)* and the compensating function, and the difference between these functions can never be zero. So even if a passive method can be implemented which [reliably and predictably] reduces the *f-T* range somewhat, an active method with the ability to tune frequency in an arbitrary manner will still be required to achieve high stability.

The active methods are electrostatic tuning, active stress compensation, frequency modification, and temperature control. Electrostatic tuning is difficult within the constraints of the epi-seal process, as described above, and may require unacceptably high voltages. Stress tuning is possible, but large forces are required, which implies large power consumption or high voltages and difficult mechanical designs. Frequency modification techniques introduce unacceptable levels of noise into the frequency output. Temperature control, however, has potential for arbitrary stability performance within the limits of thermal design and temperature sensing. Moreover, temperature control allows for the possibility of using a feedback control loop to stabilize the temperature of the resonator. All other methods require a calibration step and a look-up table or function. Finally, if a passive method is developed which successfully reduces the *f-T* range, it could automatically enhance the performance of a temperature-stabilized system without further design. So the

question becomes, how can we design a micro-ovenized resonator in the epi-seal fabrication process? Ovenization implies two things: thermal isolation, and temperature (heat) control.

4.2.1 Epi-seal Resonator Thermal Design

The goals for the thermal design of the micro-ovenized resonator are:

1) Achieve high thermal isolation of the resonator from the environment
2) Include heaters for heating the resonator
3) Avoid introducing any effects discussed above (stress, changing electrostatic gap, etc.) which might affect the frequency stability.

As described in Chapter 1, a typical ovenized quartz oscillator consumes up to 3 W of heating power in order to raise the temperature of the resonator 150 °C, implying a thermal resistance between the heater and the ambient on the order of 100 K/W. The desired power consumption for mobile applications is several orders of magnitude less, so our goal for thermal isolation of our design is ~10,000 K/W. The constraints on the design are simply that it must be compatible with the epi-seal fabrication process (Chapter 2) in order to benefit from the long-term stability provided by that process.

The thermal design problem is approached using an equivalent circuit method. The values for thermal resistance, R_{th}, for each heat transfer mechanism are developed using a 1-D Fourier equivalent circuit representation [186]:

$$
\begin{aligned}
&qR_{th} = \Delta T \text{ , where:} \\
&R_{th} = \frac{L}{k_{th}A} \text{ for conduction,} \\
&R_{conv} = \frac{L}{hA} \text{ for atmospheric convection,} \\
&R_{gas} = \frac{d}{k_{gas}A_s} \text{ for low-pressure convection, and} \\
&R_{rad} = \frac{1}{h_r A_s} \text{ for radiation.}
\end{aligned}
\tag{4-1}
$$

Here, q is the heat power (heat rate), R_{th} is the thermal resistance, k_{th} is the thermal conductivity of the material, k_{gas} is the thermal conductivity of the low-pressure gas, h

is the convection coefficient, and h_r is the radiation heat transfer coefficient. A is the cross-sectional area and A_s is surface area. The values used for modeling are given in Table 4-1.

Material	Thermal Conductivity, k_{th}, (K/m W)	Density, ρ, (kg/m^3)	Specific Heat, c_p, (J/kg K)
Silicon (Si)	150	2330	710
Silicon dioxide (SiO_2)	1.4	2240	1000
Aluminum	237	2700	798
Olin-260 Copper Alloy	260	8900	376
Die attach adhesive (Epotek H20E)	29	-	-
	Molecule Diameter (m)	Molecule Mass (kg)	
Hydrogen gas, H_2	2.80E-10	3.32E-27	

Table 4-1: Thermophysical property values used for modeling
Values taken from [96, 154, 187-189].

4.2.1.1 Convection and Radiation in Epi-seal

The environment inside the epi-seal enclosure consists of trace amounts of hydrogen gas at a pressure of ~1 Pa (see Chapter 2). At this pressure the mean free path (MFP, Λ) of the H_2 gas molecules can be estimated from the expression [190]:

$$\Lambda = \frac{1}{\sqrt{2} n_M \pi d_M^{\,2}} \,, \tag{4-2}$$

where n_M is the number of H_2 molecules per volume in the enclosed cavity (estimated from pressure measurements) and d_M is the effective diameter of the H_2 molecule. The MFP for the gas molecules at this pressure is >100 μm, which is much larger than the gap between the resonator structure and the walls of the enclosure, approximately 1.5 μm (see Figure 2.5). Therefore, we can estimate the thermal conductivity from the resonator to the surrounding enclosure by gas convection using a simple ballistic model where the gas molecules are assumed to interact with the structure and not with each other:

$$k_{gas} = \frac{1}{3} C v d \,, \tag{4-3}$$

where C is the heat capacity of the H_2 gas molecules, calculated using Boltzmann's constant, k_B, and the number of molecules per volume, n_M:

$$C = \frac{3}{2} k_B n_M \ . \tag{4-4}$$

The number of molecules per volume simply comes from re-arranging the Ideal Gas Law:

$$PV = NRT \ , \ n_M = \frac{P}{k_B T} \ . \tag{4-5}$$

Finally, the average velocity of the molecules, ν, is estimated as:

$$\nu = \sqrt{\frac{8 k_B T}{\pi m_M}} \ , \tag{4-6}$$

where m_M is the mass of the H_2 molecule and T is the average temperature of the gas. The result is that we expect a very low rate of heat loss from the resonator due to convection. The equivalent thermal resistance value (4-1) is $R_{gas} \approx$ 5.9e6 K/W.

Some energy is transmitted as radiation from the surface of the resonator to the surrounding encapsulation. We can estimate the heat flow by radiation from the resonator to the enclosure by considering the DETF structure enclosed in a cavity to be a series of parallel plates [186]:

$$q_{rad} = \frac{\sigma A \left(T^4 - T_0^{\,4} \right)}{2 \diagup \varepsilon_{Si} - 1} \ , \tag{4-7}$$

where σ is the Stefan-Boltzmann constant and ε_{Si} is the emissivity of silicon[20]. In this case, the radiation heat transfer coefficient, h_r, becomes,

$$h_r = \frac{\left(2 \diagup \varepsilon_{Si} - 1 \right)}{\sigma \left(T + T_0 \right) \left(T^2 + T_0^{\,2} \right)} \ , \tag{4-8}$$

and we can formulate a thermal resistance for heat transfer by radiation according to (4-1). The surface area of the DETF resonator with the dimensions given in Figure 3.1

[20] The spectral emissivity is a complex value, depending on wavelength and temperature. Here we use ε_{Si} 0.7, which is the "intrinsic" value at higher temperatures and longer wavelengths [191].

is 55,000 μm^2, and the equivalent thermal resistance, R_{rad}, is ~5.5e6 K/W for a temperature difference of 140 K.

The thermal resistances due to convection and radiation for the encapsulated resonator are both very large, so little heat will be lost from the resonator through these mechanisms, and we can proceed with the thermal design focusing on conduction as the primary mechanism of heat loss.

4.2.1.2 Non-Ovenized Resonator

We can gain some insight into the thermal design problem by first considering the equivalent thermal circuit model of a standard encapsulated SA-DETF resonator (such as Figure 3-1). The schematic cross-section of a non-ovenized SA-DETF resonator is shown in Figure 4.11 with its equivalent thermal model.

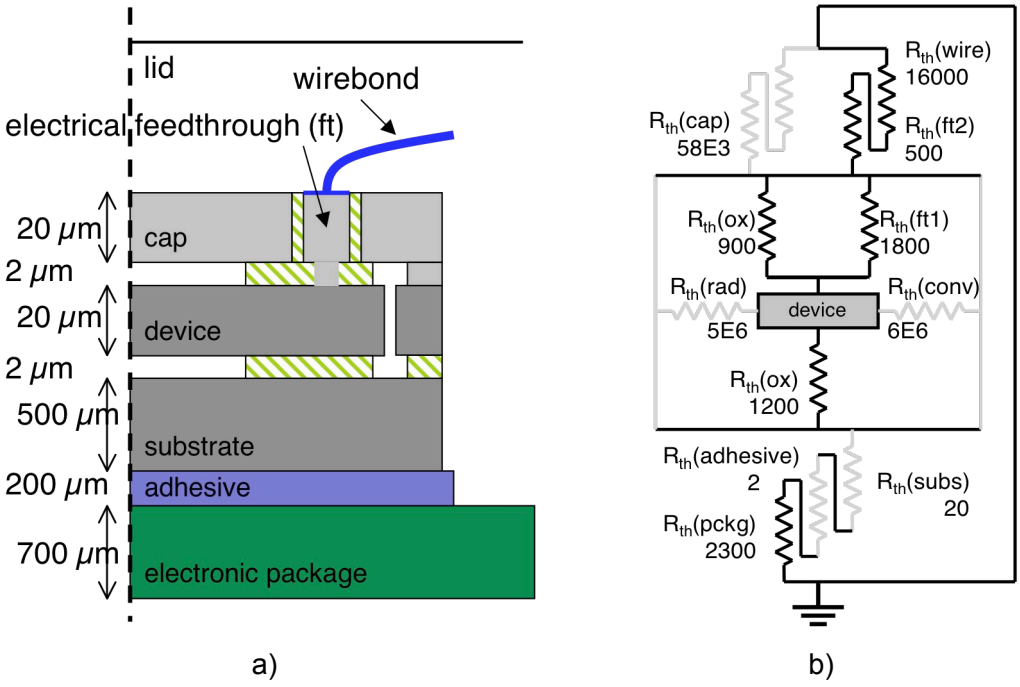

Figure 4.11: Thermal model for SA-DETF resonator
The silicon die is mounted inside an electronic package using conductive epoxy. The bottom of the package and the air outside the package lid are assumed to be at ambient temperature.
a) Schematic representation of the anchor of a SA resonator.
b) Equivalent thermal resistance circuit. Values are given in K/W. Elements whose values are large enough that they can be neglected for further analysis are gray.

The resistor network in Figure 4.11 can be simplified to the network in Figure 4.12a. The thermal resistance between an encapsulated structure and the outside environment is dominated by conduction through the anchor(s), and the conduction up through the wirebonds and down through the substrate are both significant.

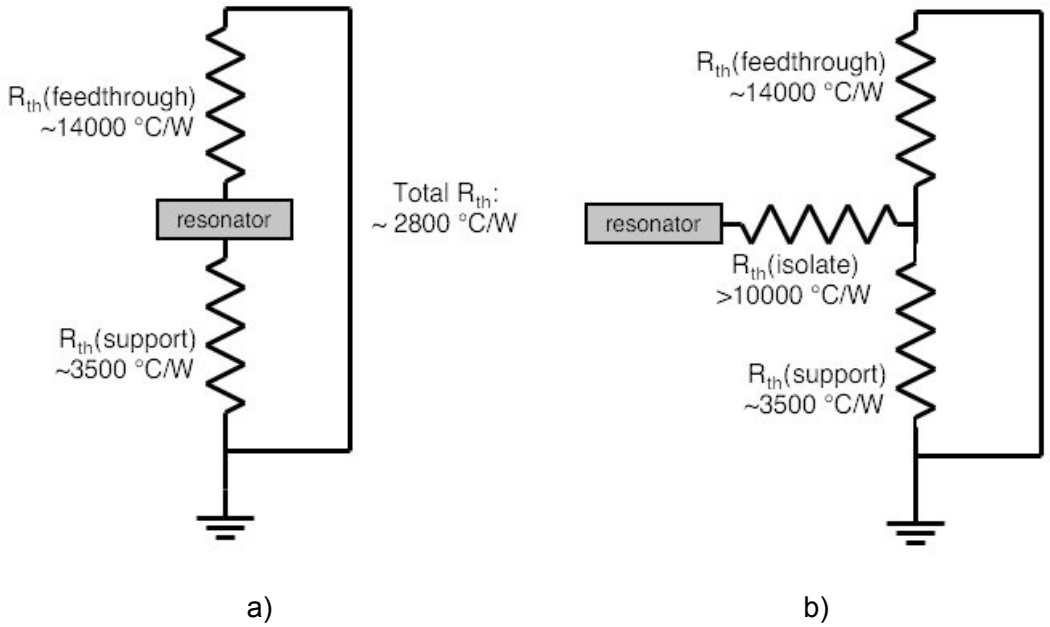

Figure 4.12: Simplified encapsulated resonator thermal models
a) Thermal isolation of the standard SA-DETF.
b) Desired thermal isolation for the micro-ovenized resonator.

The thermal isolation of the SA resonator is ~ 2800 K/W, which implies a heating power consumption of 50 mW for a 140 °C temperature increase, if heating power could somehow be applied to the resonator directly. In order to achieve our ovenization goals we need to include heating elements while increasing the thermal isolation further, to create the thermal circuit in Figure 4.12b.

4.2.1.3 Micro-ovenized Resonator

There are two basic approaches the thermal isolation when conduction is the primary mechanism of heat transfer, suggested by (4-1): reduce the thermal conductivity of the material or reduce the cross section and increase the length. The first approach implies finding materials other than silicon that are compatible with the epi-seal microfabrication process. Silicon dioxide, which is compatible with the epi-

seal process, has a thermal conductivity about 100 times smaller than silicon. Other investigators have fabricated thick layers of SiO_2 for thermal isolation [193], but the fabrication is quite difficult, and the performance is not particularly good because the dimensions of the oxide structures are relatively large. However, within the epi-seal process, we can fabricate silicon structures with cross-sections as small as 100 μm^2. So even though silicon has a high thermal conductivity, we can use microfabrication techniques to create a structure with a cross-section that is small enough that the silicon structure becomes a good thermal insulator. The answer, then, is to suspend the resonator from folded springs fabricated in the device layer. The springs serve three purposes:

1) thermal isolation
2) mechanical isolation
3) electrical heating

The spring-based resonator design is called the SR ("Spring Resistor") DETF, shown in Figure 4.13-15.

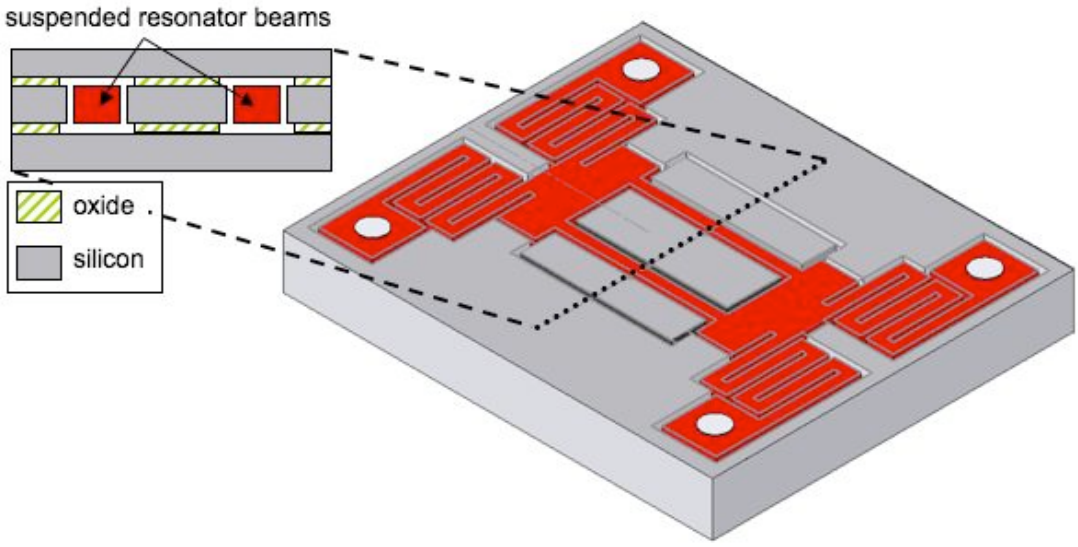

Figure 4.13: SR-DETF design
Cartoon schematic (not to scale) of the SR-DETF design. The tuning fork resonator in the center is identical to the tuning fork in the 1P3M DETF (Figure 3.1). The DETF is suspended from four SR springs.

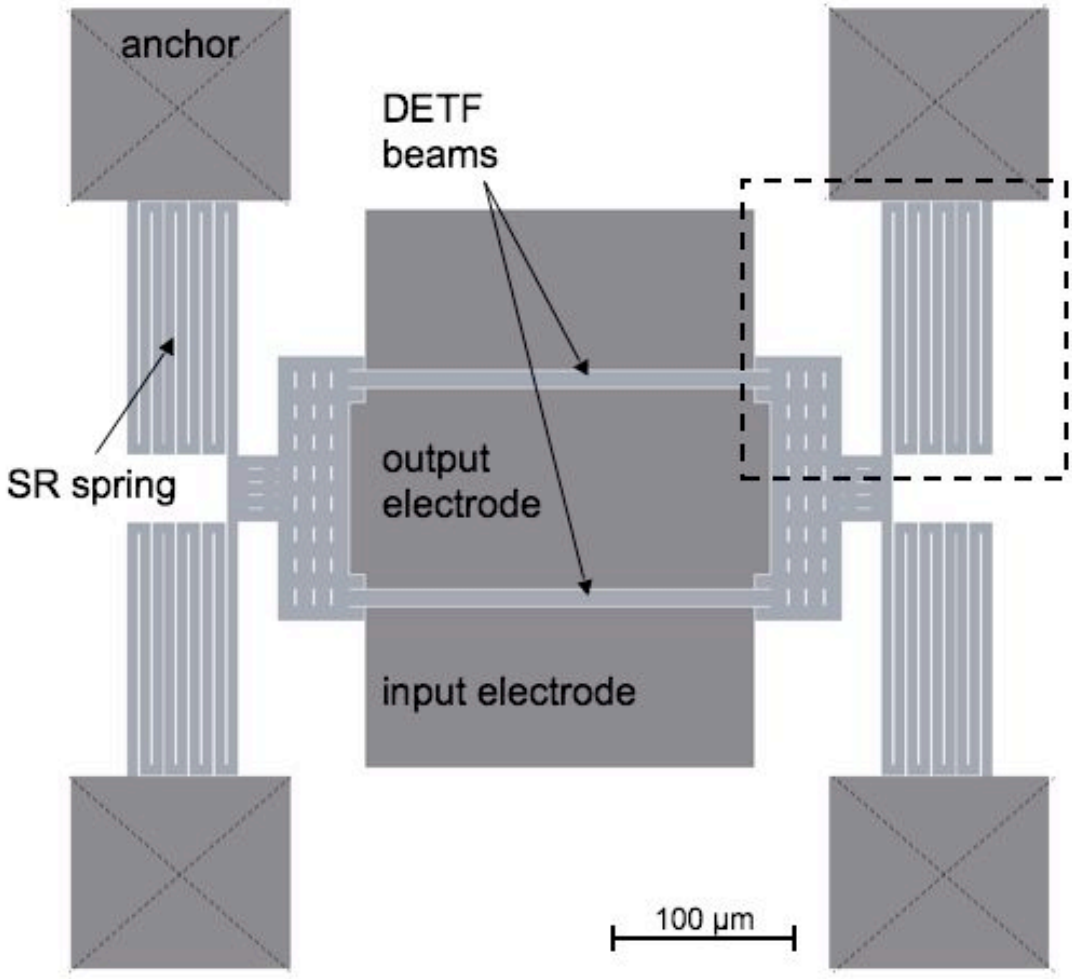

Figure 4.14: SR-DETF layout
This diagram shows the SR-DETF layout to scale in plan view. Darker areas are attached to the substrate, while lighter structures are suspended. The surrounding device layer material is not shown. The area inside the dashed line is shown in detail in the following figure.

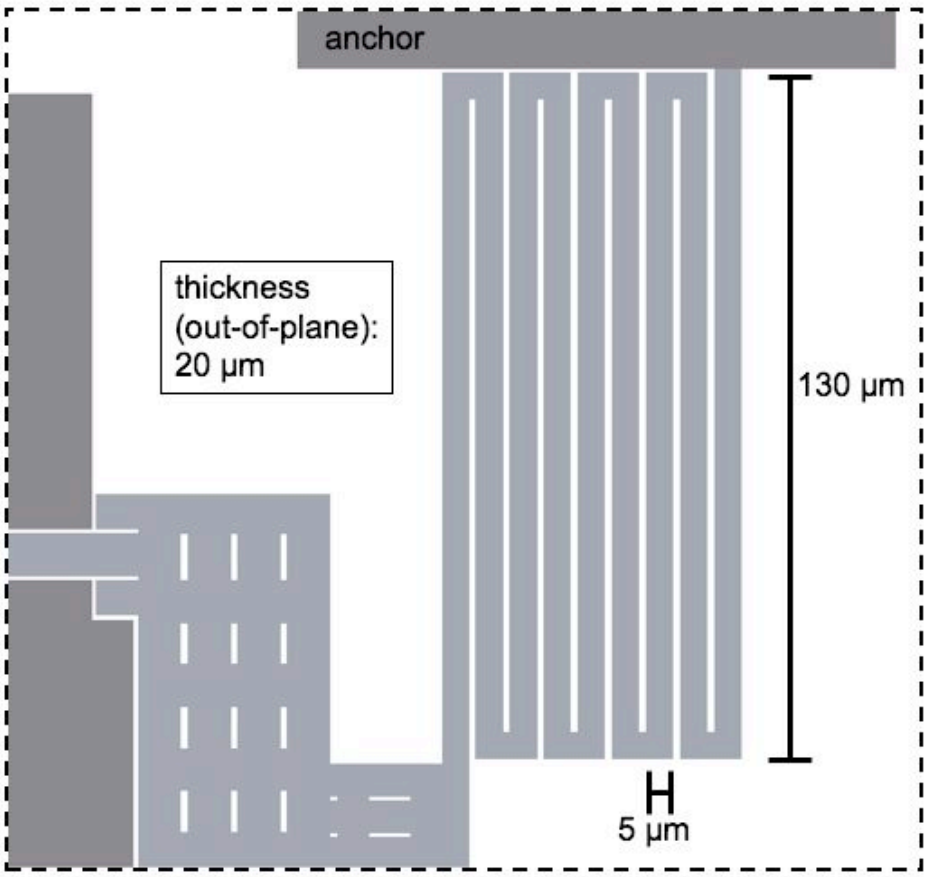

Figure 4.15: Detail of SR spring
The SR spring has 9 segments. The dimensions here are the dimensions as drawn for fabrication; the final dimensions may be slightly different due to the fabrication process (see Chapter 2 and Appendix B).

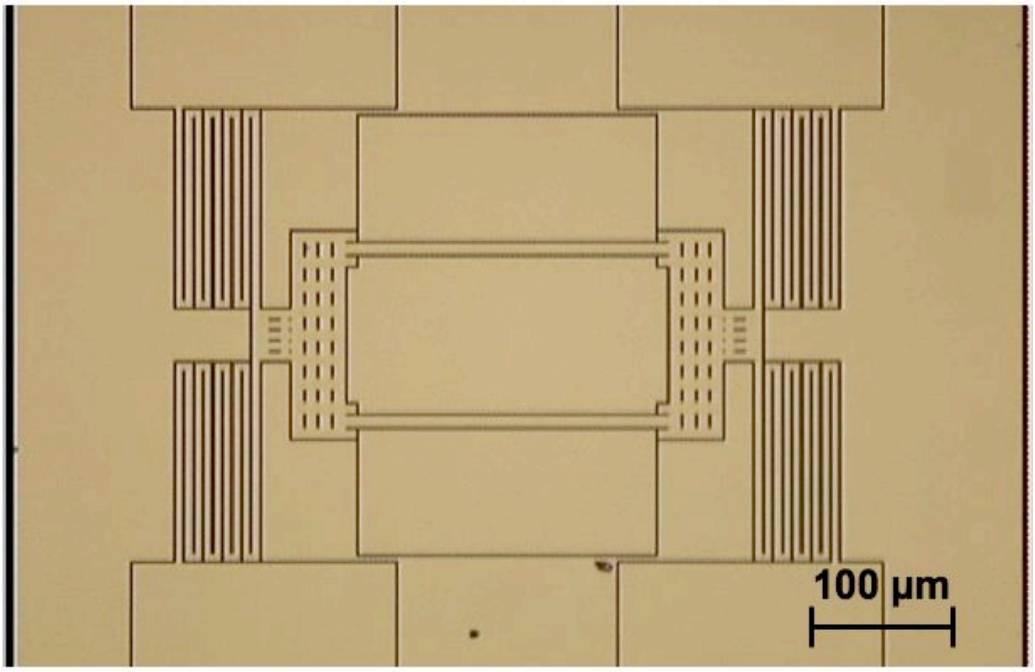

Figure 4.16: Photograph of SR-DETF resonator during fabrication
This is the view of the SR-DETF through an optical microscope during the microfabrication process, after the resonator shape has been defined but before the encapsulation layer has been deposited. This corresponds to step (b) in the process description in Chapter 2.

Thermal Isolation

The SR-DETF is supported by four folded (or serpentine) springs. Each spring is composed of 9 cantilever segments, each 5 µm wide, 20 µm tall, and 130 µm long. Each spring is designed to have a thermal resistance of $R_{th,SR} \approx 80{,}000$ K/W. As all four of the thermal resistors are connected to the resonator in parallel, the total thermal resistance between the resonator and the anchors is ~ 20,000 K/W.

Mechanical Isolation

The mechanical stiffness of the spring is an important design factor. The springs must be soft enough to avoid coupling any strain into the resonator which would affect the resonant frequency (see Section 3.2.1). The stiffness of the folded springs can be approximated as the sum of the stiffnesses of N individual cantilever segments, k_{seg}:

$$k_{seg} = \frac{3EI}{L^3} \ , \ k_{SR} = \frac{k_{seg}}{N} \ . \tag{4-9}$$

The spring constant of the SR springs along the axis of the DETF beams is ~ 6 N/m each, and the four SR springs are combined in parallel for a total stiffness of ~ 25 N/m. The combined axial stiffness of the two DETF resonator beams is ~ 250,000 N/m. So the majority of strain due any load applied along the axis of the beams will be born by the springs. TCf measurements of the SR devices confirm this; the typical linear TCf value for a SR device is -27 – -29 ppm/°C, indicating that axial strain due to differential thermal expansion does not affect the resonant frequency.

On the other hand, the suspension must be stiff enough to support the resonator. If the suspension is too soft, the device will deform or break under acceleration or vibration. Here, the scaling laws of microscale design work in our favor. The mass of the tuning fork is quite small (0.55×10^{-9} kg), and even under the worst case assumption of suspension by four unfolded springs (straight cantilevers), the vertical (out of plane) deflection due to gravity is only 20 nm. In-plane axial deflection with the folded springs (device turned on its side) is two orders of magnitude less. During the fabrication process, the released devices are processed on equipment which rotates the wafers at over 5000 rpm, subjecting them to an in-plane acceleration of up to ~1400 g, with no apparent damage[21].

Operational survivability is a separate question. No calibrated shock test facilities were available, but informal shock tests were performed by mounting an SR resonator on a temperature-stabilized fixture which was bolted to a large steel plate (~40 kg). The plate was then lifted to a height of 1 cm and dropped while the resonator was operated in an oscillator circuit. This applies a shock in the out-of-plane direction, where the SR springs are most compliant. The results are plotted in Figure 4.17. The resonator frequency was momentarily affected by the shock, but immediately returned to normal operation. This suggests that the DETF was jarred out of position, but did not touch the electrodes or fracture.

[21] The photoresist spin coat and develop steps are performed 3-4 times each during fabrication sequence following the release of the suspended structure. These steps involve rotation of the 100 mm diameter wafer between 2000 and 5500 rpm for durations of 60 seconds.

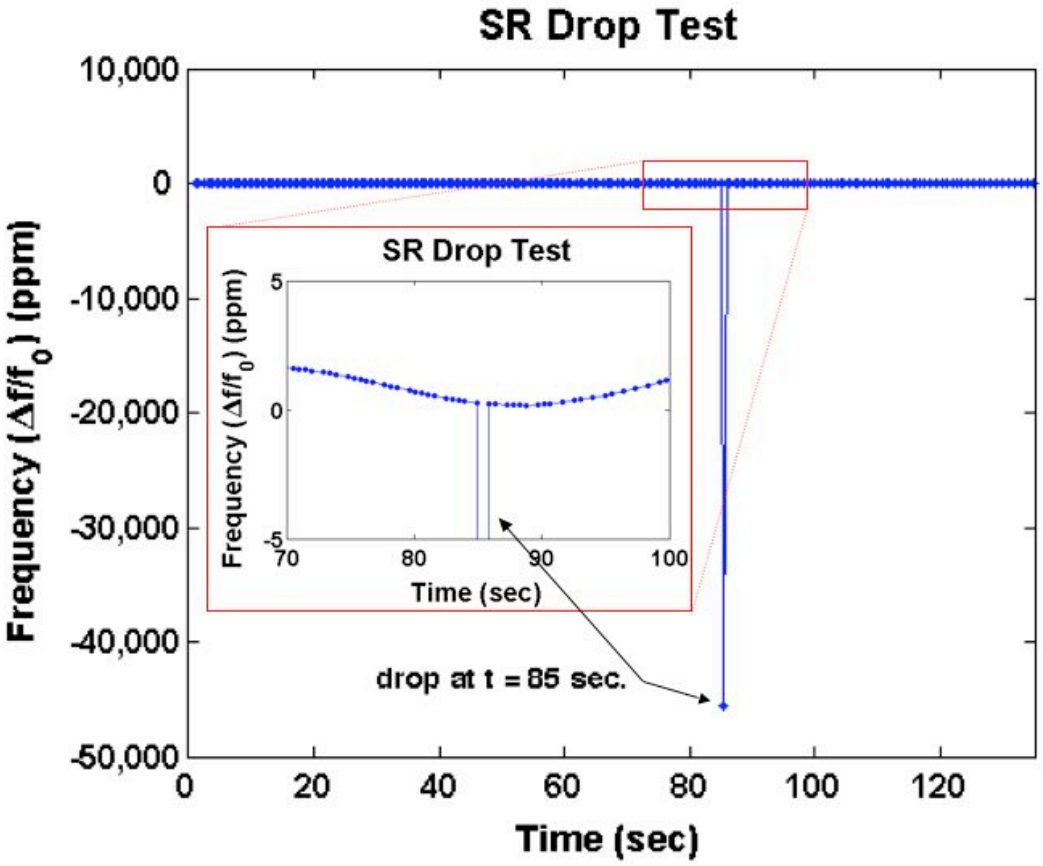

Figure 4.17: Shock test results
The resonator was mounted in a temperature-controlled fixture attached to a 40 kg steel plate. The plate was lifted 1 cm and dropped at time t = 85 seconds. The frequency at the time of the shock shifted by ~45,000 ppm, but immediately returned to normal operation (inset). The normal frequency pattern is due to the temperature fluctuation of the test fixture. The period of frequency measurement is irregular, but averages ~1 sec.

Electrical Heating

The final function of the SR springs is heating. The springs form simple electrical resistors, each with resistance R_e, which dissipate energy when an electric current, I_{heat}, flows through them. The energy is converted into heat as $P_{heat} = I_{heat}^2 R_e$ ("joule heating"). Referring to Figure 4.13, we must apply a heating current through two spring resistors in order to complete a circuit. Consider the case of a pair of resistors on one end of the tuning fork. The electrical circuit is simply two spring resistors in series (Figure 4.18).

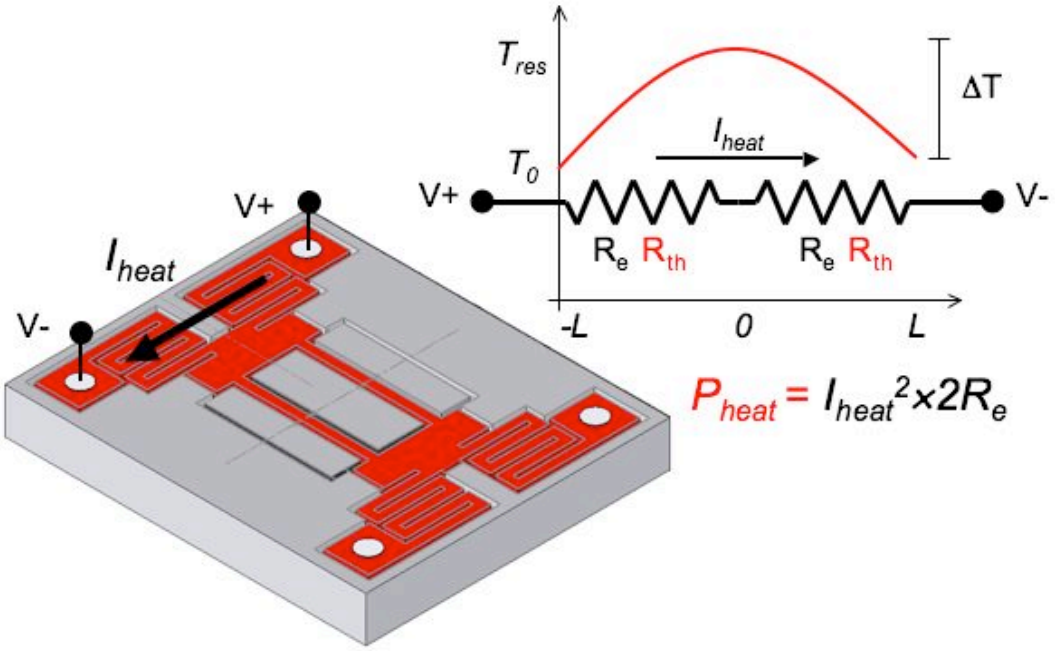

Figure 4.18: Joule heating circuit for the SR-DETF
Two SR springs at one end of the resonator are used for heating. They are connected in series electrically, but in parallel for thermal isolation calculations. The ideal temperature distribution across the two springs is shown at right.

We wish to determine the thermal isolation of the device when it is heated, so that we can determine the heating power required to achieve a given increase in temperature of the resonator.

$$\Delta T = P_{heat} R_{heat} \ . \tag{4-10}$$

For modeling, we assume that the anchors are perfect heat sinks at the ambient temperature. The expression for the temperature distribution in the heated springs is arrived at by integrating the 1-D heat equation [186] for a uniform beam. The temperature distribution is symmetric about the center, and the problem can be simplified by using the coordinates shown in Figure 4.18.

$$\frac{d^2T}{dx^2} + \frac{\dot{q}}{k_{th}} = 0 \ ,$$
$$T = -\frac{\dot{q}}{2k_{th}} x^2 + C_1 x + C_2 \ , \tag{4-11}$$
$$T = \frac{\dot{q}L^2}{2k_{th}}\left(1 - \frac{x^2}{L^2}\right) + T_0 \ .$$

where $\dot{q}$ is the heat generation per unit volume. The maximum temperature in this heating circuit occurs at the center of the resistor formed by two springs (at $x = 0$), which is where the resonator is attached:

$$T_{res} = \frac{P_{heat} L_{SR}^{\ 2}}{2V_{SR}\, 2k_{th}} + T_0 \ , \tag{4-12}$$

where V_{SR} is the volume of each SR spring and L_{SR} is the length.

We can re-arrange (4-12) to make an equivalent thermal circuit element for the heater:

$$T_{res} - T_0 = \Delta T = P_{heat} \frac{R_{th}}{4} \ . \tag{4-13}$$

So the effective thermal isolation provided by a pair of SR springs being used as heaters is $R_{th}/4$, approximately 20,000 K/W. A second pair of springs is connected to the other end of the DETF, providing a parallel conduction path, and we can approximate the total thermal isolation of the resonator in this case by considering the resistances in parallel:

$$R_{heat} = \frac{R_{th}}{4} \left\| \frac{R_{th}}{2} = \frac{R_{th}}{6} \approx 13{,}000 \text{ K/W.} \right. \tag{4-14}$$

With this level of thermal isolation, we can expect to achieve a 150 °C temperature increase above the ambient with only 12 mW of power. However, (4-14) is only an approximation, as the temperature distribution on the heaters and across the resonator is not accurately captured by the circuit element representation. Measurements and finite element simulations suggest that using the R_{heat} value from (4-14) in (4-10) overestimates the resonator temperature by about 20%. A typical measurement of the SR resonator frequency during heating is shown in Figure 4.19.

Note that the thermal isolation in actual devices is somewhat sensitive to the lateral dimension variations discussed in Chapter 2. From (4-1), the thermal resistance depends on w^{-1}. The width of fabricated devices can easily vary by 10%, which creates a nearly 10% change in the thermal resistance value of the SR spring, and corresponding increase in heating power. In operation, the observed values of the thermal isolation provided by the SR springs were greater than 10,000 K/W.

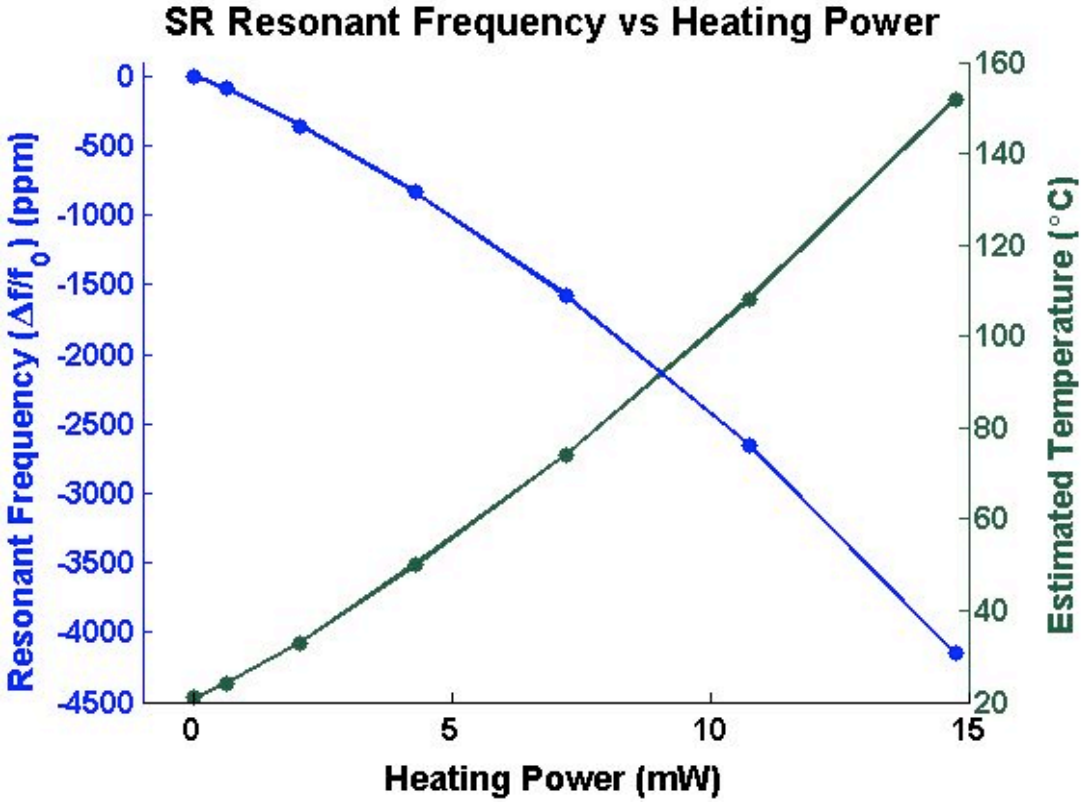

Figure 4.19: SR-DETF resonator heating
The heating power is applied to the SR springs on one side of the resonator (as in Figure 4.18), and the frequency is measured. The resonator temperature is estimated using the TCf value derived in Chapter 3, with the second order corrections for TCE given in [130]. The temperature estimate is slightly distorted by the temperature gradient across the resonator, as discussed in Chapter 5. The non-linear change in temperature with heating power is due to the decrease in thermal conductivity of silicon with increasing temperature.

Another consideration for heating is the dynamic response. A "thermal time constant", τ_{th}, can be identified for simple structures using a lumped element model:

$$\tau_{th} = R_{th} C_{th} \ . \qquad (4\text{-}15)$$

The time constant characterizes the exponential change in temperature during heating or cooling. During temperature control operation, a small thermal time constant allows the temperature controller to adjust the heating power of the resonator quickly. On the other hand, a small τ_{th} can be a disadvantage in situations where the temperature is fluctuating rapidly, as the resonator will respond to temperature changes at frequencies up to $1/\tau_{th}$ Hz. A larger thermal time constant can help to filter out the effect of high-frequency ambient temperature changes.

As with the estimate of resonator temperature, the lumped element expression of (4-15) is not strictly appropriate for this situation because the temperature distribution in the device is complex. However, we can approximate the dynamic behavior by using the total thermal capacitance of the resonator and the SR springs:

$$\tau_{th} = R_{heat}\left(4C_{SR} + C_{DETF}\right) \approx 15 \text{ ms}. \tag{4-16}$$

A discrete-element circuit model was used to investigate the dynamic thermal behavior. Because of the analogy between thermal and electrical circuits (heat flow/current, temperature/voltage) electrical circuit tools such as SPICE [194] can be used to investigate some heat transfer problems. The SR-DETF was modeled using half symmetry in order to take into account the different temperature distribution on the non-heated side of the resonator. In the SPICE model (Figure 5.10), the circuit capacitors are given an initial voltage that corresponds to the initial temperature distribution calculated from (4-11). The model indicates that the temperature change of the resonator can be characterized with a τ_{th} of 14.3 ms. This value is expected to be somewhat lower than the true value because the temperature distribution from (4-11) is only exact for the case of two heating springs with no resonator attached.

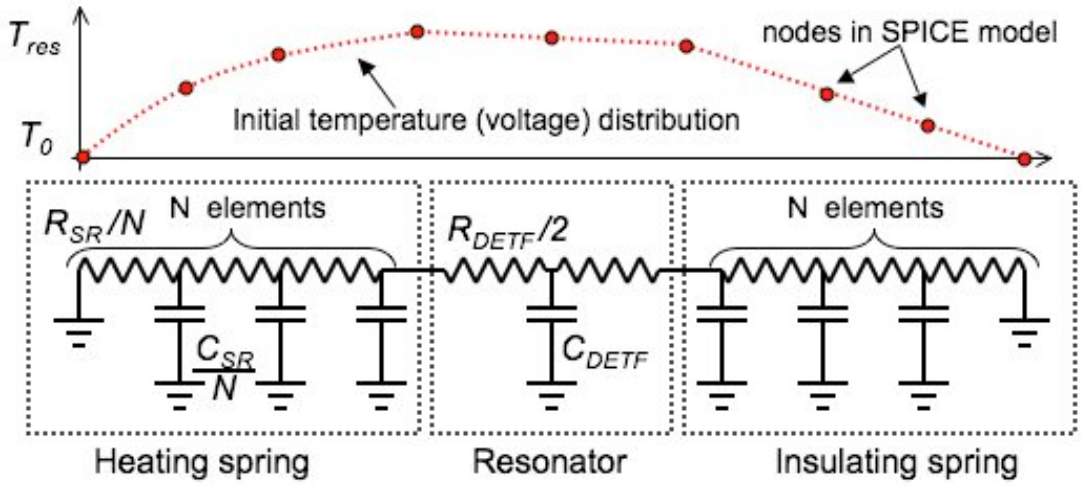

Figure 4.20: Circuit for SPICE model for dynamic thermal response
The discrete element model uses a large number (*N*) of small circuit elements to approximate complex behavior. A transient analysis was performed with the initial voltage on the capacitors determined by the ideal temperature distribution for the heater from (4-11), and linear temperature drops across the resonator and the other spring. The voltage as a function of time at the middle node represents the temperature of the resonator. Experimentally, N=70 nodes was required to achieve a converging solution.

A thermal time constant measurement was performed by connecting two springs of an SR-DETF in series with a small sense resistor. The voltage across the sense resistor was measured in order to monitor the current flowing through the SR springs. A periodic voltage signal was applied to the springs which alternately heated the device and then allowed it to cool (Figure 4.21). The result is shown in Figure 4.22. Note that this is a measurement of the *average* temperature of the heating resistors, not the resonator itself. The true dynamic behavior is characterized by multiple time constants due to contributions from the heating springs, the resonator, and the insulating springs.

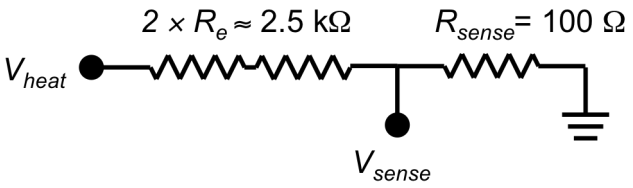

a)

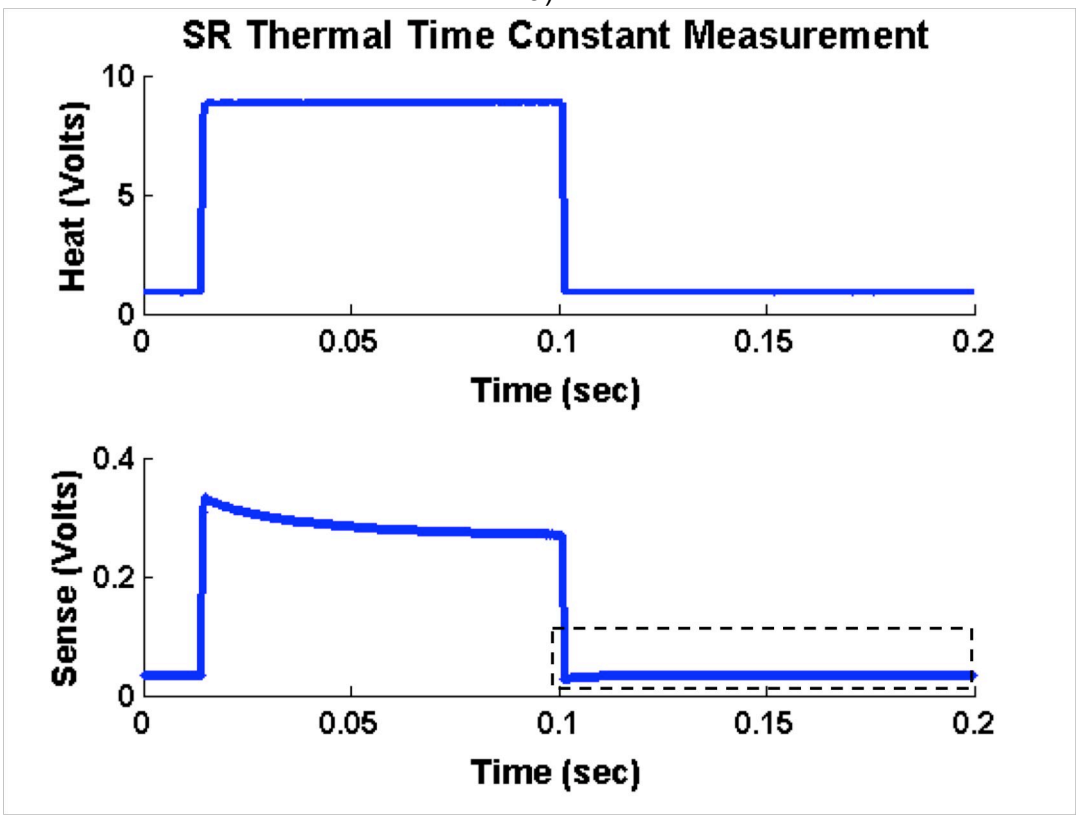

b)

Figure 4.21: SR Thermal Time Constant Measurement (Part I)

a) Two SR springs were connected in series with a 100 ohm sense resistor. The voltage measured across the sense resistor is proportional to the current flowing through the SR springs.

b) A periodic voltage pulse was applied to the heater circuit. The periodic heating voltage was chosen to have a 0.5 V DC offset so that the voltage across the sense resistor would not go to 0 V. The n-type silicon SR springs have a positive temperature coefficient of resistance (TCR), so the SR spring resistance increases as it heats up and decreases as it cools down. The cooling portion of the cycle is highlighted, and shown in detail in the next figure.

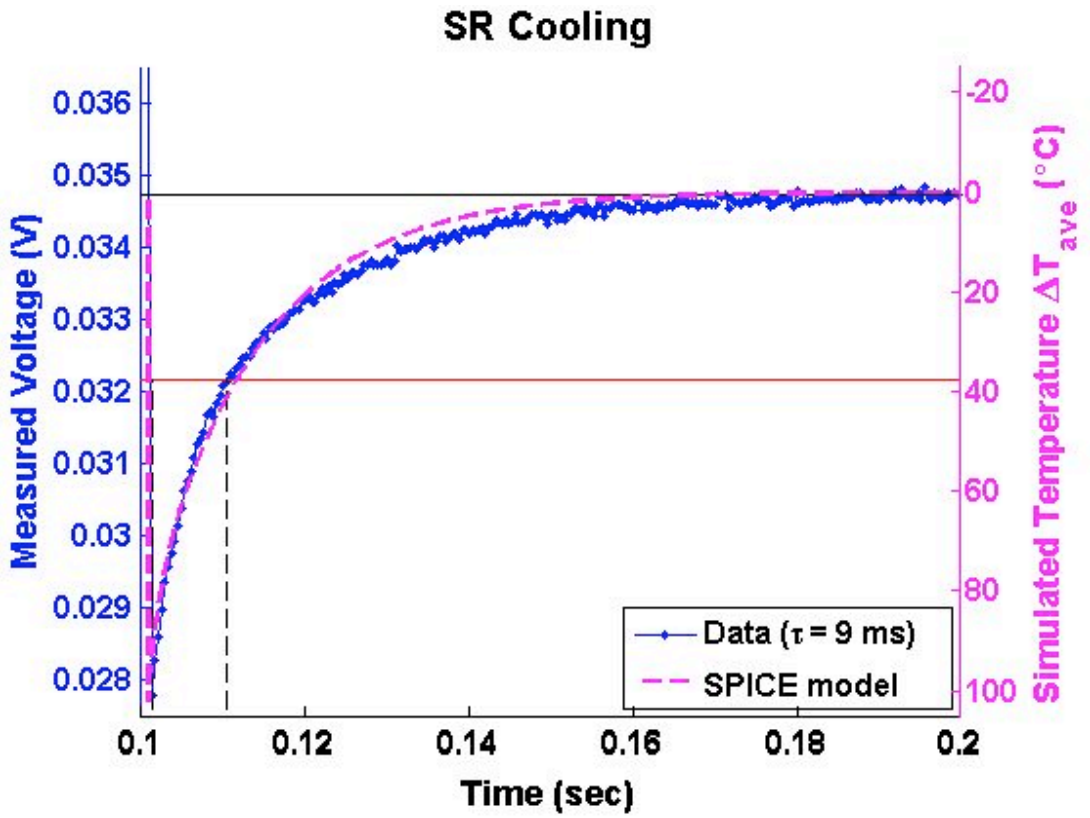

Figure 4.22: SR Thermal Time Constant Measurement (Part II)
Enlargement of the cooling portion of the waveform. As the SR springs cool, their resistance decreases and the current flowing through them increases. The thermal time constant is the time at which the temperature has fallen by 63% (red line) relative to its final value (black line). A SPICE model was used to simulate the dynamic temperature response. Note that this measurement (and SPICE result) reflects the *average* temperature of the SR springs, not the temperature of the resonator. FEM simulations indicate that the time constant of the resonator temperature is closer to 17 ms.

4.2.2 Resonator Temperature Sensor

Now that an ovenized resonator design has been identified, we need to consider the selection of a temperature sensor for the control system. If our goal for frequency stability is < 1 ppm, and our resonator has a frequency sensitivity to temperature of -30 ppm/°C, then our control system will have to be able to detect temperature changes *in the resonator* of at least 1/30 °C, and preferably 10x better than that. Three possible sensor types have been identified: a general-purpose external sensor, an internal silicon thermistor, and the quality factor of the resonator.

4.2.2.1 External Temperature Sensor

There are a large number of off-the-shelf temperature sensors with accuracies from ±1 °C to ±0.001 °C. Platinum resistance temperature detectors (Pt RTD), used in this work are capable of 0.002 °C resolution in a 6 Hz bandwidth. However, even the finest external temperature sensor is only reporting the temperature at a point outside the resonator die. The temperature reading at this point is subject to the influence of the surrounding material of the electronic package and circuit boards, external airflow, and the resonator heater.

In a steady-state case, of course, there would be no temperature difference between an external sensor and the resonator inside the encapsulation. So in addition to sensor resolution, the thermal capacitance of the structures between the sensor and the resonator are important. Even a simplified lumped-capacitance thermal model of the situation, as illustrated in Figure 4.23, can become complex, and the implications for frequency control depend on the final packaging of the resonator die and its environment. However, we can think about the performance of the external sensor by considering the thermal time constant, τ_{th}, of the structures between the sensor and the resonator.

There are three basic possibilities for an external temperature sensor: on the circuit board, in the electronic package, or on the resonator die itself. In the limiting case of a non-ovenized resonator with an ideal external sensor located directly on top of the encapsulation (e.g., a CMOS bandgap sensor fabricated on the wafer after the epi-seal fabrication is complete), the thermal resistance of the anchors and thermal capacitance of the resonator form the relevant thermal time constant. From the model in the previous section, the values are ~ 2800 K/W and 4.0e-7 J/K for a standard SA-DETF, which gives a thermal time constant of 1.1 ms. This suggests that significant temperature differences between the sensor and the resonator will not be sustained for more than 5 ms or so ($5\tau_{th}$). Also, there are no separate heat flow paths to the sensor and the resonator. If the system does not experience temperature fluctuations faster than 200 Hz, the temperature sensor should accurately report the temperature of the resonator within 5 ms.

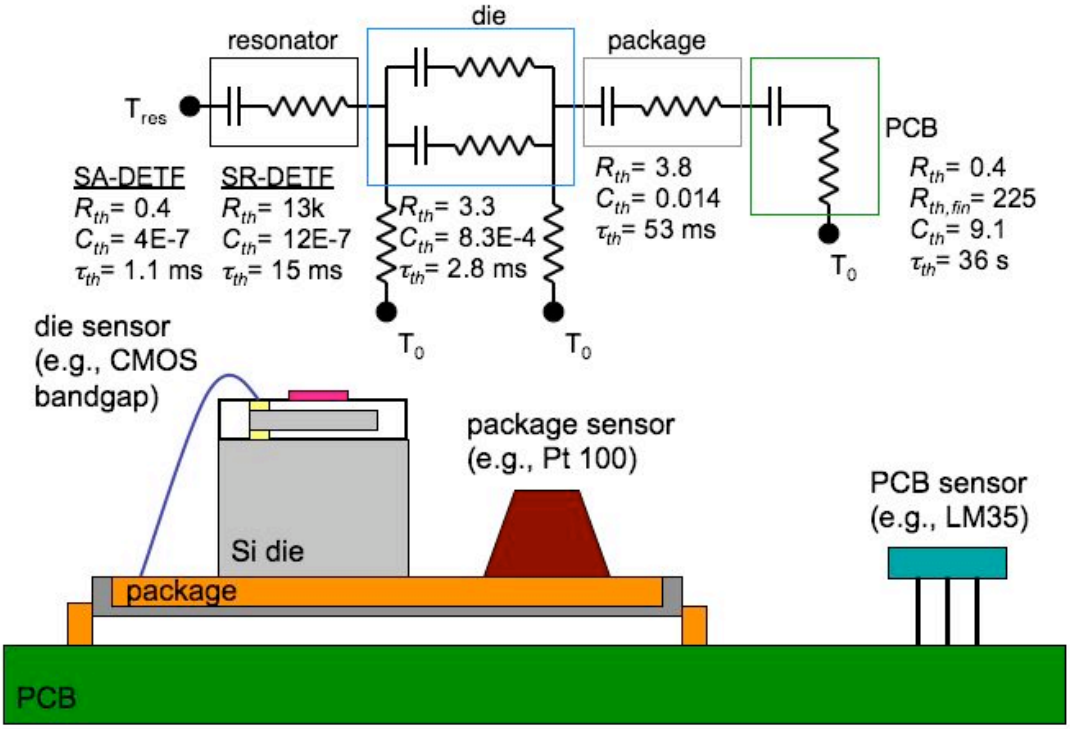

Figure 4.23: Lumped-Capacitance Model for External Temperature Sensors
Three external temperature sensor configurations are pictured:
sensor on the die
sensor in the electronic package
sensor on the printed circuit board (PCB)
This diagram approximates the experimental setup used in Chapter 5. Commercial applications would typically include additional packaging material around the silicon die and connections to other components on the PCB, complicating the thermal model. Note that the lumped capacitance model is not necessarily appropriate for the PCB, which has low thermal conductivity.

At the other extreme, a temperature sensor on the PCB is separated from the resonator by significant thermal elements and there are independent paths from the ambient to the resonator that bypass the sensor. The combined time constant for the PCB, the package, and the die is approximately 35 seconds, implying that significant temperature differences can be sustained between the PCB sensor and the resonator for up to 3 minutes, and even very slow temperature changes can create a difference between the sensor and the resonator. For example, during experiments discussed in Chapter 5, the ambient temperature can easily vary by 0.5 °C with a period of 100 seconds, implying a frequency error of 15 ppm, without considering phase and spatial effects.

In the intermediate case of a temperature sensor located inside the electronic package, the low thermal resistance and capacitance of the silicon die means that the time response is dominated by the package. The time constant of the resonator die and the package is 30 ms, and so when the resonator or the package is exposed to temperature changes, the resonator temperature may be different from the sensor for up to 150 ms. This intermediate case is the best that we can achieve in a laboratory setting, and is what was used in the experiments described in Chapter 5.

For all of the above cases, the SR-DETF design adds a large thermal resistance between the anchor and the resonator. For the SR-DETF, $\tau_{th,SR} \approx 15$ ms. With an external temperature sensor in the electronic package, the total time constant is 45 ms, and the RC cutoff frequency for temperature changes is 22 Hz.

For the micro-ovenized SR-DETF, there is an additional concern: the resonator is separated from the temperature sensor by a large thermal resistance, and the resonator will be heated internally, so there will be some temperature difference between the heated resonator and the external sensor. In this case, we can estimate the temperature difference from the "thermal voltage divider" of the resistance between the resonator and the sensor, and the sensor and the ambient temperature:

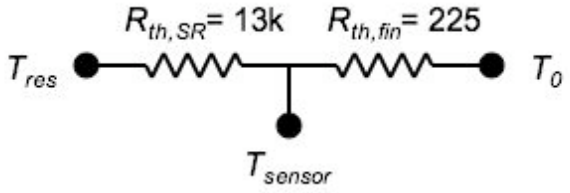

Figure 4.24: Thermal Voltage Divider

$$T_{sensor} = \frac{R_2}{R_1 + R_2}\left(T_{res} - T_0\right) . \tag{4-17}$$

We can estimate the thermal resistance of the PCB as a circular fin connected to the electronic package [186]. For the worst case of an ovenized resonator operating at 90 °C while the ambient temperature, T_0, is -55 °C, the temperature sensor mounted on the package will be 2.5 °C different than the resonator. This error is unacceptable for high-performance applications, and so an external temperature sensor is not

suitable for use with an ovenized device. With this sort of large temperature difference between the sensor and the resonator, feedback control is not possible, although if we interpret the readings from the external sensor carefully during experiments, we can still get some useful results using lookup tables, as discussed in Chapter 5.

Clearly, the performance of the external temperature sensor for frequency control depends heavily on the packaging of the resonator and sensor, and their surrounding environment. If they are buried together under a layer of plastic with a high specific heat, they are likely to see the same temperature most of the time. If the rate of change of temperature in the environment is small, then the frequency drift during 150 ms may be acceptable. If the device is used on a circuit board with many other components which are generating heat during operation, then the electronic package will likely be heated through the traces on the circuit board faster than the resonator, and so on. In general, high performance results using an external temperature sensor will be difficult to achieve and require a significant engineering effort for each specific instantiation.

4.2.2.2 Internal Thermistor

Another possibility for temperature sensing is some kind of temperature sensor attached to the resonator, inside the encapsulation. This would measure the temperature of the resonator directly. However, there are several difficulties with this idea:

1) Fabrication: the epi-seal process has an extremely high thermal budget and maximum temperature (~1000 °C). The thermistor material must be able to withstand these temperatures. Circuits (such as a CMOS bandgap sensor), are not possible. Implanted resistors are also ruled out.
2) Stability: the sensor must be in contact with the resonator structure but not affect its stability. The sensor materials must not outgas, creep, fatigue, etc. Metal thermistors (see Chapter 3) are out.

3) Self-heating: thermistors require a measurement current, which heats the thermistor, and hence the resonator, to some degree, reducing the accuracy of the measurement.

Given these constraints, the best possibility is some kind of silicon thermistor[22] (a modification of the SR spring geometry, perhaps). In fact, silicon has a strong temperature coefficient of resistance (TCR) and can be used to make reasonably good thermistors for -50 – 150 °C operation [195]. Lets consider the design of such a thermistor for the SR-DETF. The TCR for silicon is approximately 1%/°C [189][23]. We will measure resistance of the thermistor by passing a constant current through it and measuring the voltage drop, V_T, across the thermistor. This will cause some self-heating of the thermistor, creating a non-uniform temperature profile (as in the SR heaters in Figure 4.18), and introducing some bias to the measurement depending on the external temperature. In order to keep the measurement error small, lets limit the temperature increase from self-heating to 1 °C. The thermistor will be located on the SR-DETF resonator, which has a thermal isolation of 10,000 K/W (minimum), so the power dissipated in the thermistor, P_T, should be less than 0.1 mW to keep the self-heating bias reasonable. Lets choose a thermistor resistance value, R_T, of 10 kΩ so that the resistance change is measurable, but the resistor noise is not too large. The resulting measurement sensitivity is:

$$V_T = \left(P_T R_T\right)^{1/2}, \quad \frac{dV_T}{dT} = \frac{1}{2} P_T \left(P_T R_T\right)^{-1/2} 0.01 R_T = 5 \text{ mV/°C}. \tag{4-18}$$

We need [at least] 0.03 °C resolution, so we will need to detect < 150 μV changes in V_T in a reasonable bandwidth. This kind of measurement is not impossible, but it is challenging, requires careful attention to circuit design to minimize other sources of noise in the system, and does not offer much scope for improvement. Moreover, there are serious practical difficulties in implementing the thermistor with the SR-DETF. The thermistor has to be designed to be in thermal but not electrical contact with the

[22] Thermistor: a "thermally sensitive resistor", i.e., a resistor whose resistance changes with temperature.

[23] The TCR for silicon is a complex function of doping and temperature, but fortunately, the doping levels for maximum TCR in this temperature range (~ 1%/°C) are similar to those typically used for epi-seal resonators. See [189] for details.

resonator, and it is not clear how that can be accomplished in epi-seal. The electrical resistance of the SR springs is ~ 1 kΩ. From Figure 4.14, we can see that a 10 kΩ resistor (essentially a larger SR spring) would require more area than the resonator itself, and it would have a large thermal resistance and thermal time constant. We could use an SR spring as a thermistor, reducing R_T to 1 kΩ, which reduces the sensitivity by 1/3, requiring a measurement resolution of 50 μV. So using a silicon thermistor inside the encapsulation cannot be definitively ruled out, but it is not a promising approach.

4.2.2.3 Quality Factor

As discussed in Section 3.3, the quality factor of the silicon DETF resonators used in this work have a strong temperature dependence because it is dominated by Q_{TED} (Chapter 3.3). Therefore, we can use the resonator *Q(T)* response as a temperature sensor. The *Q* is an almost ideal sensor- it consumes no additional power, acts nearly instantaneously, and indicates the temperature of the resonator itself. *Q* is a non-linear function of temperature, but as the goal is to keep the resonator temperature stabilized, we can estimate its change at ~1%/°C (for $\gamma \approx 3$, see Section 3.3) from its room temperature value of ~10,000. This implies detecting a change in *Q* of 30, which is on the order of difficulty of detecting the μV changes discussed above. However, the advantages of no additional fabrication complexity, instantaneous response, and no additional power dissipation, mean that this method has significant potential and is the preferred choice for this system. In Chapter 5, we will discuss methods of making the *Q* measurement for high resolution resonator temperature sensing.

4.3 Conclusion

There are many ways to control the frequency of a silicon resonator and tune it in opposition to the changes created by changing ambient temperature. The best method, which has the potential to achieve the highest levels of frequency stability, is to ovenize the resonator and stabilize its temperature. It is possible to design and fabricate a MEMS resonator in the epi-seal process which includes elements for

thermal isolation, heating, and temperature sensing. The micro-ovenized resonator design is the SR-DETF, and the best temperature sensor available is the *Q(T)* signal. With these features, we can implement a control system which uses the signal from the temperature sensor to stabilize temperature, and thus frequency.

4.4 Acknowledgements

Chandra Mohan Jha contributed greatly to the characterization of the SR DETF resonators, in particular the finite element simulations and investigation of the thermal time constant.

In theory, there is no difference between theory and practice. But, in practice, there is.
-Yogi Berra

Chapter 5 Experimental Methods and Results

This chapter describes the results of experiments carried out to demonstrate the application of the analysis in Chapters 3 and 4 to frequency stability of silicon resonators. The early experiments with resonators were done using sweep measurements and external temperature sensors. Later experiments used oscillator circuits and advanced temperature sensing mechanisms.

This chapter includes a number of "frequency stability" plots. This is a plot of frequency versus temperature while the temperature compensation system is operating. The frequency is reported in parts-per-million (ppm) fractional change from a standard frequency (f_0), which is usually the resonator frequency at room temperature, or the frequency at the setpoint temperature. The frequency range (maximum-minimum) is the figure of merit for stability. Error bars are included, but the use of averaging several measurements generally reduces the error so that the error bars cannot be seen on the plots.

At the beginning of this project, some commercial ovenized quartz references parts samples were supplied by Corning, Inc.[24] While not the absolute top-of-the-line

[24] Subsequently, Corning sold its frequency reference business to Vectron, Inc. The Vectron part numbers are largely the same as the old Corning numbers.

part available at the time, the Corning C4550 OCXO (AT option) is a high-performance part, with a frequency stability of ±0.1 ppm (100 ppb) over a frequency range of -20 – 70 °C, while consuming up to 3 W of power. The data sheet for this part is in Appendix E. One of these oscillators was measured in the experimental setup described below, and the result is shown in Figure 5.1.

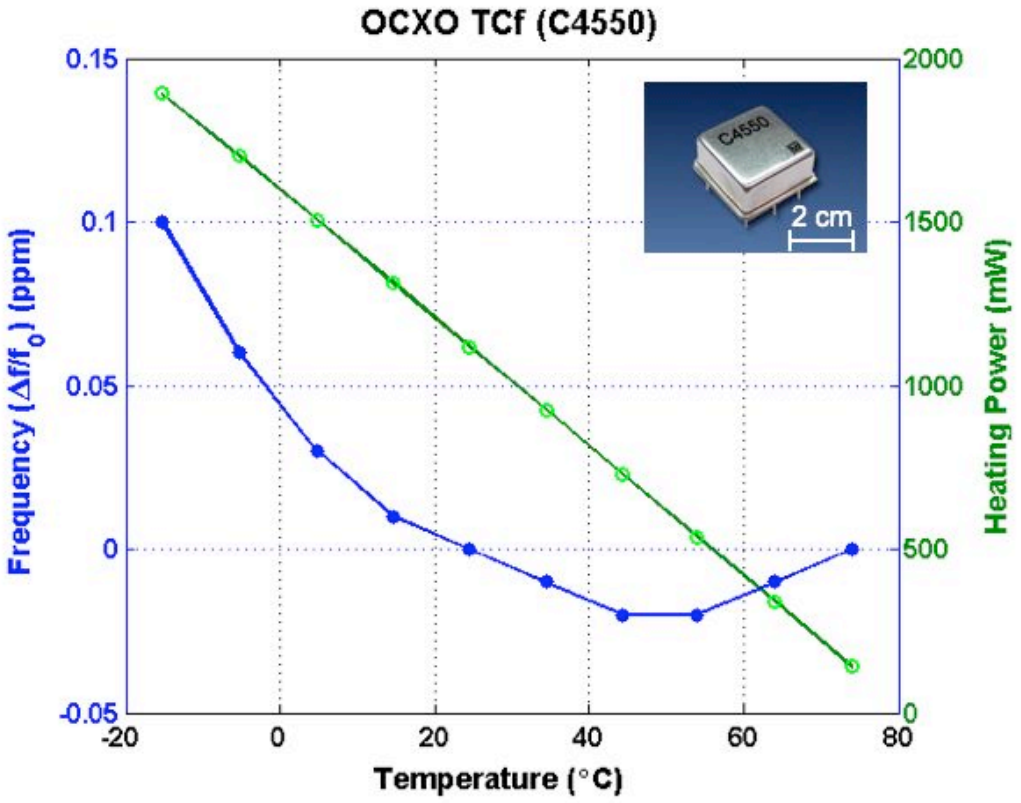

Figure 5.1: Frequency Stability of Corning C4550 OCXO.
The frequency at each temperature is the solid blue circles, and the power consumption is the open green circles. The commercial OCXO performed within its datasheet specifications. 100 frequency measurements are averaged at each point. The nominal output frequency is 10 MHz. Inset: the catalog picture of the C4550.

As we can see, high-performance frequency stability does not mean an absolute flat line on the graph of frequency versus temperature. We can always adjust the Y axis scale to see some variation. The question is, how tight is the frequency tolerance, and over what temperature range?

5.1 Experimental Setup

The experiments required three things: resonator measurement, ambient temperature control, and data collection.

5.1.1 Resonator Measurement

After fabrication, the resonators must be packaged in a robust manner suitable for repeated testing. The individual resonator dies were diced from the silicon wafer and mounted in an electronic package designed for prototyping[25]. They were attached to the package using conductive epoxy so that electrical contact could be made to the silicon substrate through the center pad of the package.

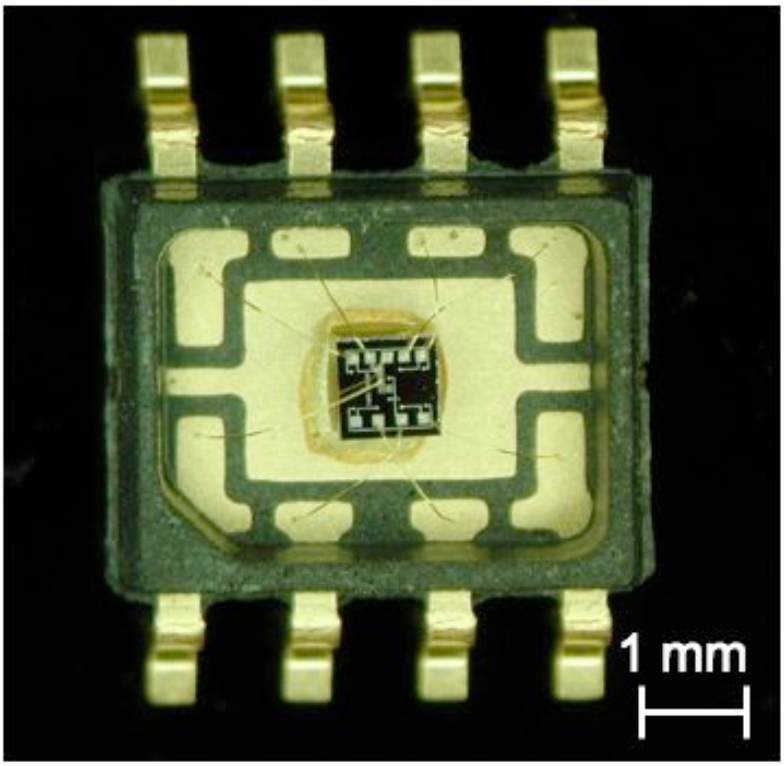

Figure 5.2: Resonator Die Attached in Electronic Package.
The package is the Spectrum Semiconductor SOIC-8 Open-Pak. Gold wirebonds are visible.

The resonators can be characterized using two basic methods: stimulus-response, or "sweep", measurement, and oscillation measurement.

[25] The Open-Pak products from Spectrum Semiconductor, Inc.

5.1.1.1 Sweep Measurement Setup

Resonators can be characterized by their frequency response, as discussed in Chapter 3. This type of measurement is very common, and instruments called Network Analyzers are sold specifically for this purpose. The Analyzer generates a periodic stimulus signal which is applied to the resonator. The stimulus signal is also recorded by the Analyzer and compared to the output of the resonator. The analyzer "sweeps" the frequency of the stimulus signal across the measurement range (the "span"), and the resonator response at each stimulus frequency is recorded. The measured amplitude is divided by the stimulus amplitude an presented in decibels in order to eliminate the effects of any frequency dependence of the stimulus [196]. This type of measurement is called a "sweep" or "stimulus-response" measurement. The sweep measurement setup used in these experiments is shown in Figure 5.3, and a typical sweep measurement result is shown in Figure 5.4.

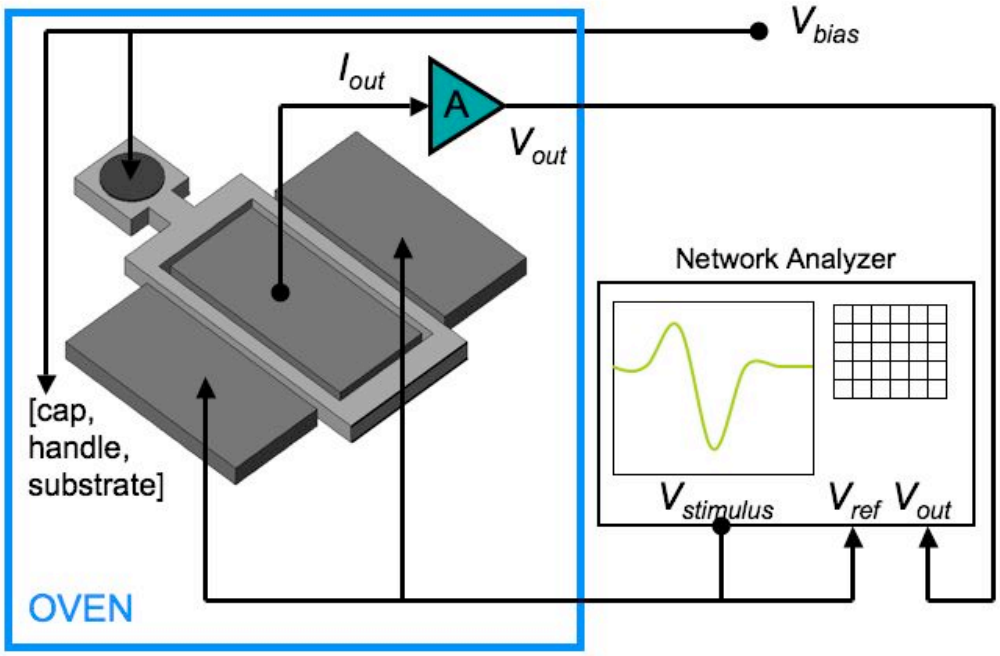

Figure 5.3: Sweep Measurement Setup Diagram
A transimpedance amplifier is used to amplify the small output current from the resonator into a larger voltage signal that can be more easily measured. Note the "ground" (V_{bias}) connection to the silicon die surrounding the resonator.

The resonant frequency of the resonator is the frequency at the maximum amplitude. The quality factor is computed as the resonant frequency divided by difference in frequency at the two points where the amplitude is 3 dB less than the peak (the "3 dB bandwidth", f_{3dB}) [103]:

$$Q = \frac{f_0}{f_{3dB}} , \tag{5-1}$$

as illustrated in Figure 5.4.

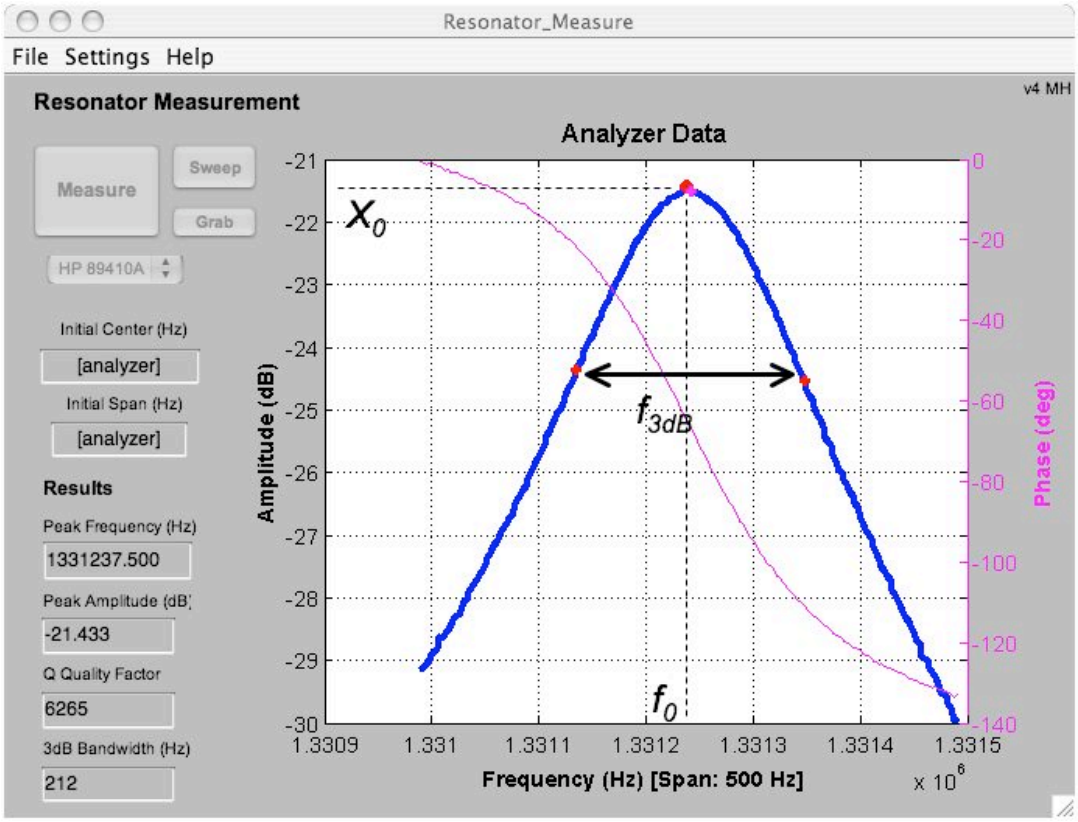

Figure 5.4: Typical Sweep Measurement
The data is captured from the analyer using the MATLAB program "res_meas.m" (see Appendix D).

For testing, the electronic package with the resonator was mounted on a printed circuit board (PCB) for connection to the cables and test equipment (Figure 5.5). The resonator test PCB included an amplifier for amplifying and buffering the resonator output. The amplifiers were JFET op-amps, chosen for their low current noise. They were connected in a transimpedance configuration, followed by a unity-gain buffer, to convert the resonator current output into a voltage level. A gain of 10,000 was

typically used. It was found that the amplifier could be located several feet away from the resonator without introducing significant noise into the measurement.

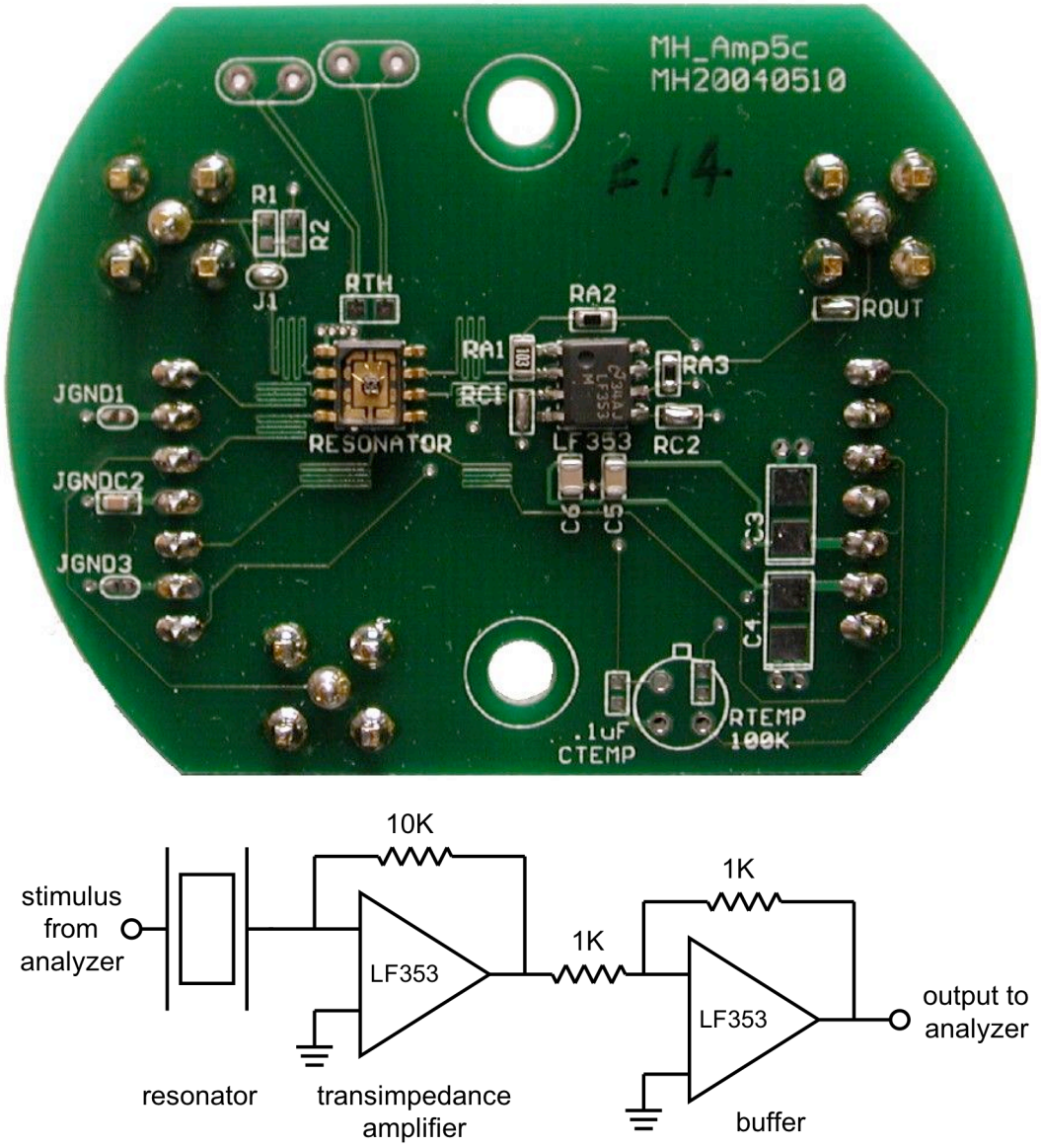

Figure 5.5: Resonator PCB and circuit diagram
(top) The resonator is mounted in an 8-pin dual-inline (DIP) package, soldered to the PCB on the left side. The PCB includes a dual amplifier (right center) for amplifying and buffering the resonator output signal, which is a pA current. The PCB is 2.4 x 1.8 inches.
(bottom) the circuit diagram for the sweep measurement circuit. For these relatively low frequencies, almost any low-noise op-amp is suitable. In later experiments, the resonator and the amplifier were mounted on separate circuit boards so that the amplifier could be located outside of the thermal test chamber.

The connection of V_{bias} to the silicon die surrounding the resonator (see Figure 5.3) is important for two reasons. The first is to reduce the feedthrough capacitance, discussed in Chapter 3. By connecting the feedthrough paths to ground or any fixed potential, the capacitance in these paths is discharged. The second reason is to avoid creating an electrostatic force between the resonator and the surrounding silicon encapsulation which might cause the resonator to be deflected or broken. This is especially important for ovenized SR devices, which are suspended by soft springs, and can be easily destroyed this way[26]. This electrical connection requires that the silicon die be attached to the electrical package with a conductive epoxy, and that the resonator design include a "ground contact"[27] structure, which is a opening in the surface passivation layer that allows electrical contact to the silicon encapsulation layer and device layer (see Appendix B for fabrication details). The difference is easily seen in the measurements. Figure 5.6 and Figure 5.7 compare similar resonators with and without the bias contact to the silicon die. The result with the bias contact much more closely approximates the ideal second-order system result (Chapter 3).

[26] Experimentally, a 12 V difference between the SR resonator and the surrounding encapsulation could cause the resonator to fail.
[27] "shield contact" is perhaps a more meaningful name for this structure.

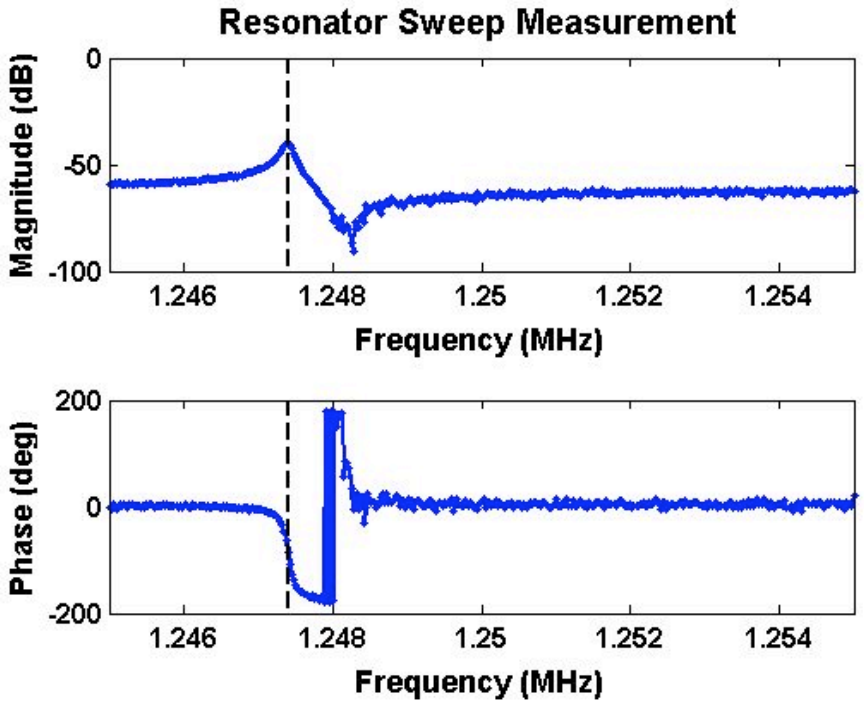

Figure 5.6: Resonator without Bias Contact
The feedthrough capacitance creates a strong “antiresonance” peak (see Chapter 3).

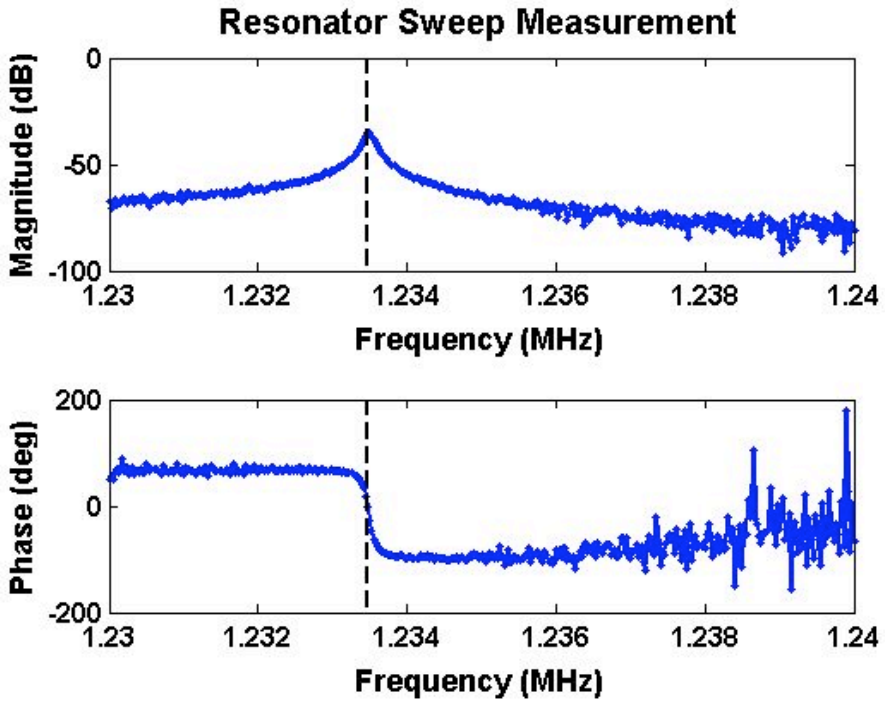

Figure 5.7: Resonator with Bias Contact
There is little evidence of feedthrough capacitance.

The sweep measurement provides a complete characterization of the resonator, but it has some important limitations. First, each measurement is quite slow. A single sweep might take from 90 to 180 seconds, depending on the desired resolution, and several sweeps are often needed to accurately identify the peak frequency. Second, the resolution of the measurement is limited by the number of datapoints available in each sweep, and is inversely proportional to the time of the measurement. Up to 800 datapoints are available on our analyzers. The 3dB bandwidth of our resonators is ~ 100 Hz, and generally a measurement span of 4× the 3dB bandwidth is required for a clean signal. This means that the frequency resolution will be 400 Hz/800 points = 0.5 Hz. However, a certain amount of noise is present in the amplitude signal, so that the point of maximum amplitude may be one of 3 or 5 points near the peak. Averaging several measurements, or increasing the IF bandwidth of the Analyzer, can reduce this noise, but at a cost of increasing measurement time. As discussed in Chapter 4, the resonator may be sensitive to temperature fluctuations as fast as 100 Hz, so the temperature of the resonator is likely changing during a long sweep measurement, adding uncertainty to the location of the "true" resonator peak.

The best results for sweep measurements were achieved by using 400 datapoints and averaging the results of 5 fast sweeps using the Hewlett-Packard 89410A Signal Analyzer. This requires about 60 seconds, and the frequency resolution is approximately 2 ppm for the 1.3 MHz resonators. This value can be improved by averaging; typically 5 measurements were used per data point, and the uncertainty in each measurement was reduced to < 1 ppm.

5.1.1.2 Oscillator Measurement Setup

A more efficient method of measuring the resonator frequency is to insert the resonator into an oscillator circuit and measure the frequency of the oscillator output. When oscillators were used for frequency measurement, a Hewlett-Packard 53132A frequency counter was used to measure the frequency of the oscillator output (Figure 5.8). The counter timebase is a quartz OCXO (Option 012) with a temperature stability of $< 2.5\times10^{-9}$ and long-term aging specification of $< 1\times10^{-10}$ per day and $< 2\times10^{-8}$ per year. The oscillator was custom-designed and built to meet the electrical specifications of the resonator. The oscillator circuits were kept outside of the thermal chamber to prevent the temperature coefficients of the circuit components from interfering with the measurement.

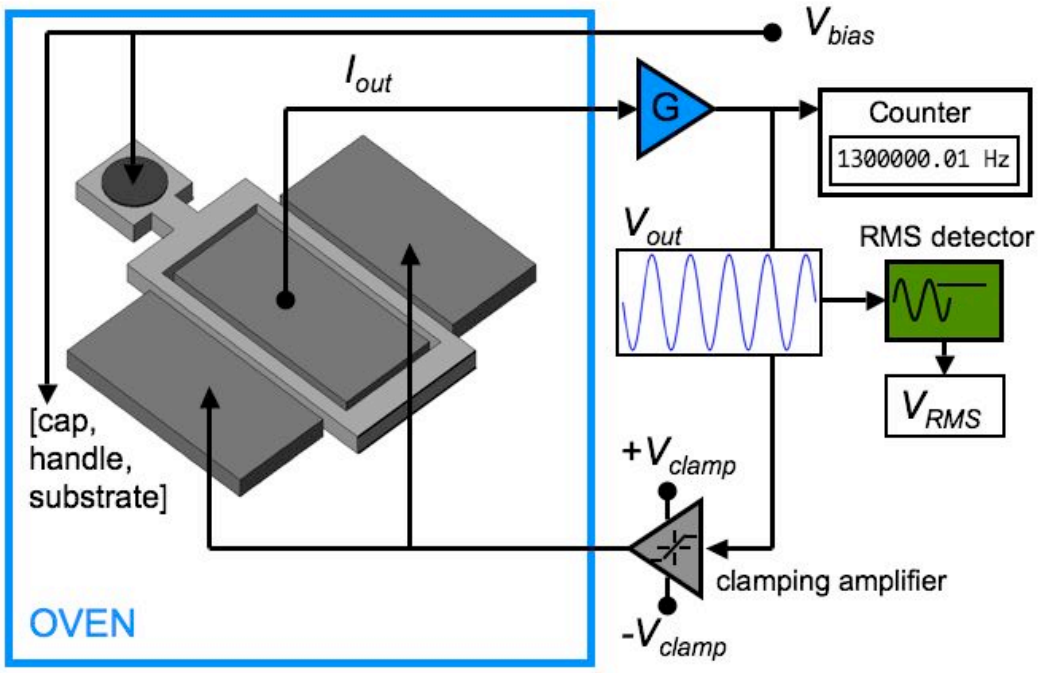

Figure 5.8: Oscillator Measurement Setup Diagram
A multi-stage amplifier ("G") amplifies the output from the resonator. This frequency of the sinusoidal signal is measured using an HP53132A counter. The signal is then fed to a clamping amplifier which limits the output to a level that can safely stimulate the resonator.

The output from the oscillator measurement is simply a number representing frequency and a timestamp, and any other quantities of interest (temperature, output amplitude, etc.). Because the measurement data was collected serially by a central computer, the rate at which the oscillator frequency was measured depended on the number of other measurements that were performed during each measurement cycle. When only the oscillator frequency was recorded, measurements could be taken 0.5 seconds apart (i.e., at a rate of 2 Hz). Typically, other quantities were recorded during each measurement cycle, and the measurement rate was 0.5 – 1 Hz (i.e., 1 – 2 seconds between measurements).

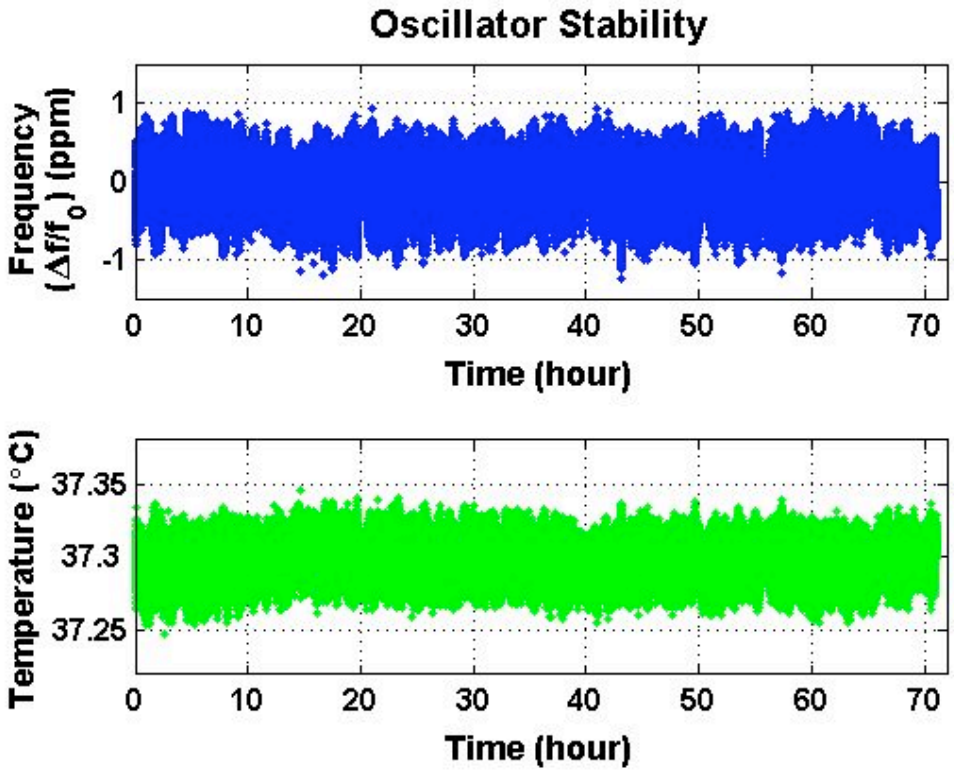

Figure 5.9: Oscillator Stability Test Data
The frequency and temperature data from the oscillator measurement setup. The resonator is a silicon 1P3M SA-DETF. The ambient temperature is held constant in order to establish the baseline stability of the oscillator measurement setup. f_0 for this measurement is 1312432 Hz.

The stability of the oscillator circuit and resonator determined the limit of frequency resolution of the oscillator measurements. Figure 5.9 shows the output from the oscillator with a standard silicon SA-DETF resonator measured for three days

while the ambient temperature was kept constant. The drift in frequency (linear fit to the data) was -3.4 × 10^{-9} parts per day. The Allan deviation of this data is shown in Figure 5.10. The noise floor was less than 0.05 ppm at τ = 10 seconds. The oscillator circuits are discussed further in Section 5.3.2.

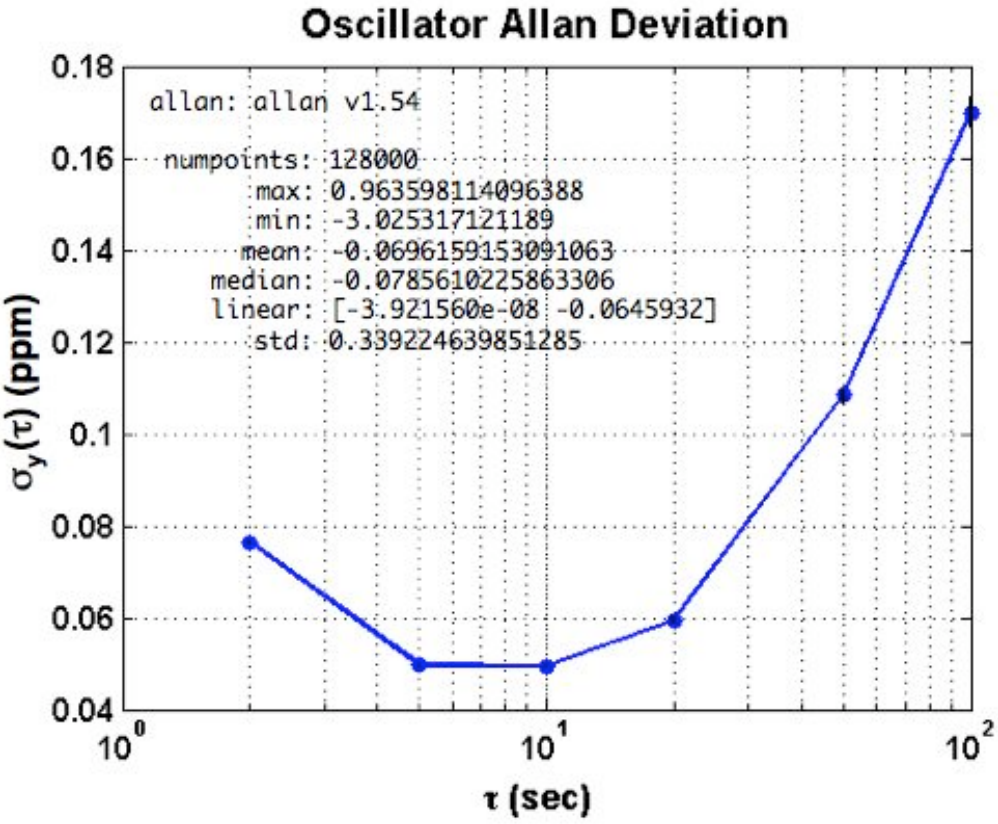

Figure 5.10: Oscillator Stability Noise Floor
The Allan deviation of the oscillator frequency data from Figure 5.9, given in ppm.

5.1.2 Ambient Temperature Control

In order to test the temperature response of the resonators, we need to control the ambient temperature. Themotron S-1 thermal test chambers (aka "Blue Ovens") were used for this purpose. They are capable of changing the chamber temperature from -55 °C to 100 °C in 15 minutes. The large test chamber can accommodate plenty of test equipment, different size circuit boards, multiple resonators, etc. The resonator circuit boards were mounted inside the chamber with a small fan to promote temperature uniformity.

a) b)

Figure 5.11: Thermal Chamber
a) A Thermotron S-1 “Blue Oven” thermal chamber.
b) A resonator mounted inside the thermal chamber for testing. A test PCB such as shown in Figure 5.5 is at the center of the image, underneath a small black fan.

The temperature controller for the thermal chamber is capable of maintaining the temperature within ±0.1 °C of the setpoint, on average, after ~30 minutes of stabilization time, depending on the temperature setpoint and the previous temperature. The chamber uses a PID controller, and the PID parameters are set by the manufacturer to provide the best performance over a wide temperature range. The chamber is heated using electrical heating resistors. The heat provided by the heaters can be smoothly adjusted by adjusting the heating current, and so the temperature control at elevated temperatures is good, generally better than ±0.1 °C. Cooling is provided by a mechanical compressor system which is cycled on or off to modulate heat removal. This means that the temperature fluctuation at low and intermediate temperatures can be larger than ±0.1 °C. In Figure 5.12, the oven temperature deviation is plotted over time for low, medium, and high temperatures.

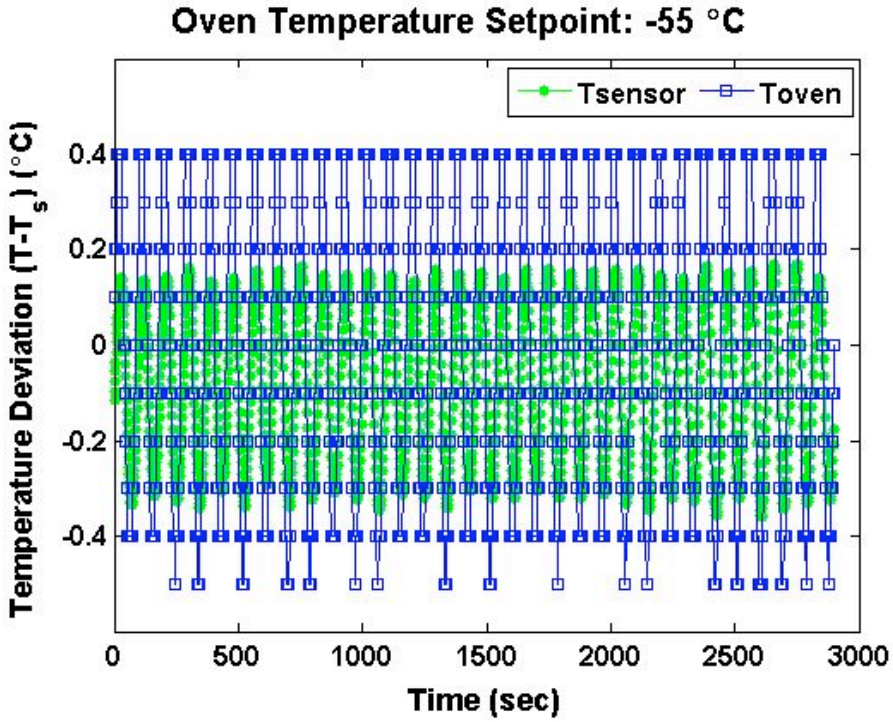

a) Oven Temperature Stability at -55 °C

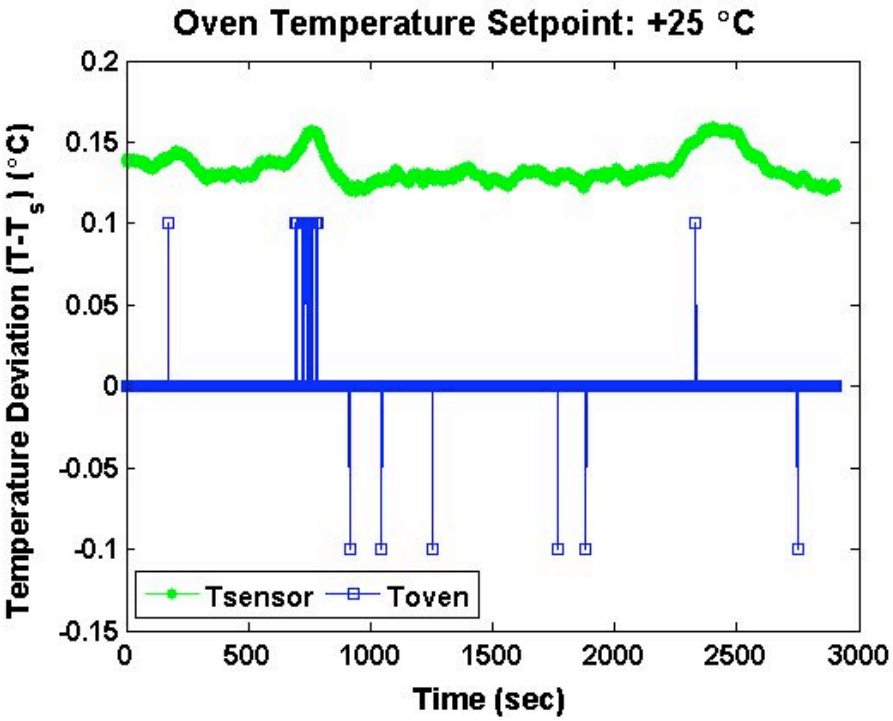

b) Oven Temperature Stability at 25 °C

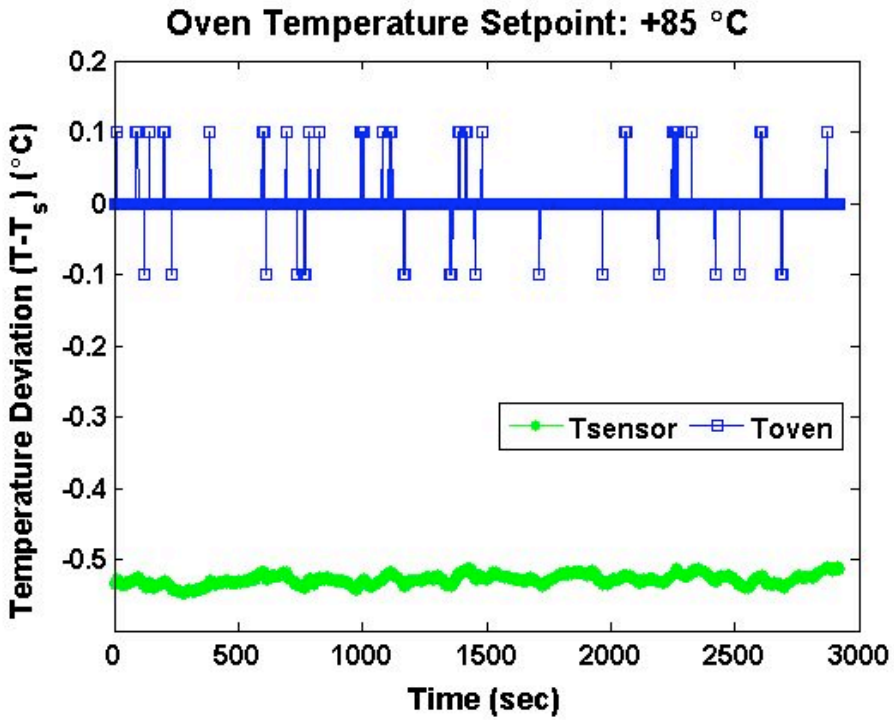

c) Oven Temperature Stability at 85 °C

Figure 5.12: Temperature Data During Thermal Chamber Stabilization
The temperature data is plotted of an offset from the temperature setpoint, *Ts*. The temperature was recorded *after* 30 minutes of stabilization time had passed. The temperature sensor data (Tsensor) is collected from a Pt RTD mounted on the test PCB. The thermal chamber temperature sensor (Toven) is a thermocouple hanging in space above the PCB. The resolution of the Toven sensor is 0.1 °C. The offset between the thermocouple and RTD readings is evident at high temperatures. The maximum deviation of the Tsensor readings for *Ts* = -55 °C is 0.53 °C. At 25 and 85 °C, the maximum deviation is almost identical, 0.040 °C.

A subroutine was written for the control software which monitored the temperature of the thermal chamber, using the output from the chamber's temperature sensor and the sensor on the resonator circuit board, and determined when the temperature of the chamber had stabilized to within a certain range of the setpoint. In general, the temperature during the experiments was varying by ~0.05 – 0.5 °C. As a result, at low temperatures (< 10 °C), the uncertainty of the high-precision stability measurements (~1 ppm) was dominated by the temperature instability, rather than the noise of the frequency measurement. In fact, by observing the resonator frequency, the thermal chamber itself (including the PCB and wires inside the chamber) was found to

have a very large time constant, so that 10's of hours were required for the oven temperature to return to within 0.01 °C of its previous value.

5.1.3 Experiment Control

The experiments described here required hours and days of time for temperature stabilization, as well as the logging of large amounts of data from multiple instruments. Clearly, some form of automation was required. The solution was to use standard personal computers running MATLAB [197], a general-purpose computational environment. LabVIEW, from National Instruments, is a popular program for interfacing with scientific instruments, and LabVIEW was used for some initial experiments. However, the complexity of the experimental setup quickly became greater than could be managed with LabVIEW.

A single computer controlled all of the laboratory instruments used in each experiment. The instruments were connected to the computer using GPIB (General Purpose Interface Bus) connections. GPIB is an IEEE standard for communication with scientific instruments. It is designed to be flexible and reliable in noisy environments, and the tradeoff is that it is relatively slow. Each command typically required at least 100 ms of bus overhead time. However, GPIB is robust and available on almost all scientific instruments.

During the experiments, the instruments were polled in serial. In the case of sweep measurements, the time required for each measurement was much greater than the GPIB command overhead time. However, for the oscillator measurements, the GPIB overhead and the instrument settling and integration times were on the same order, so the rate of data collection was affected by the use of GPIB.

A large amount of MATLAB code was written during the course of the work. Subroutines for measuring temperature, characterizing the resonators, analyzing data, etc., are listed in Appendix D.

5.2 Feed-Forward Stability Experiments

Feed-forward control uses a pre-determined set of calibration data (a "look-up table") to establish the output for a given set of inputs. Feed-forward control is relatively straightforward to implement, and can potentially outperform other methods of control. The performance of feed-forward for frequency stability depends on accurate ambient temperature measurement and calibration data.

5.2.1 AC Direct Heating

The first temperature-control experiments were performed on double-anchored DETFs. A resonator with a two anchors provides a natural path for a heating current- in one anchor, through the resonator, and out the other anchor. However, for electrostatic actuation, the resonator beam should be held at an elevated DC potential with respect to the electrodes. A heating current dissipating power in the beam will cause a voltage drop along the beam, disrupting the resonator actuation. The solution is to use an AC heating current. If the frequency, ω_H, of the AC heating current is higher than the resonant frequency of the resonator, the heating current will have no effect on the electrostatic operation. The DC bias is added to the AC heating signal as an offset, using a simple bias-T circuit, as shown in Figure 5.13.

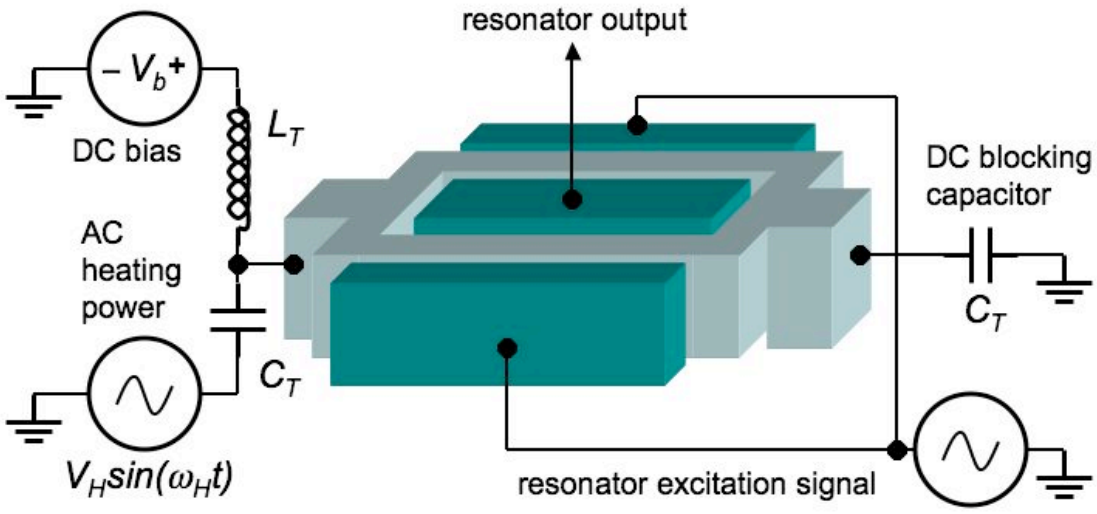

Figure 5.13: AC Direct Heating Circuit
The DA-DETF is connected to an AC heating power source while the bias voltage is applied as an offset on the AC heating signal.

It is important to choose ω_H such that the beam is not affected by what are essentially variations in the bias voltage. ω_H must be greater than ω_0 and should avoid exciting any additional modes or harmonics of modes of the resonator. Experimentally, ω_H = 5 MHz was found to give good results for the 1.3 MHz resonator. The values for the L_T and C_T components are chosen simply to create a highpass RC filter, with the resistance of the resonator, $R \approx 1$ kΩ. C_T was chosen to be 0.01 μF and L_T = 100 μH.

In Section 4.2.1.2, the thermal isolation of a resonator in the epi-seal encapsulation was estimated to be 2800 K/W per anchor. With two anchors, we expect to get half of that value. The function generator used to generate the AC heating current had a maximum power output of approximately 25 mW, so the experiment was limited to a temperature range of 35 °C. The results of the experiment are shown in Figure 5.14. The power consumption was very close to that predicted by the thermal model.

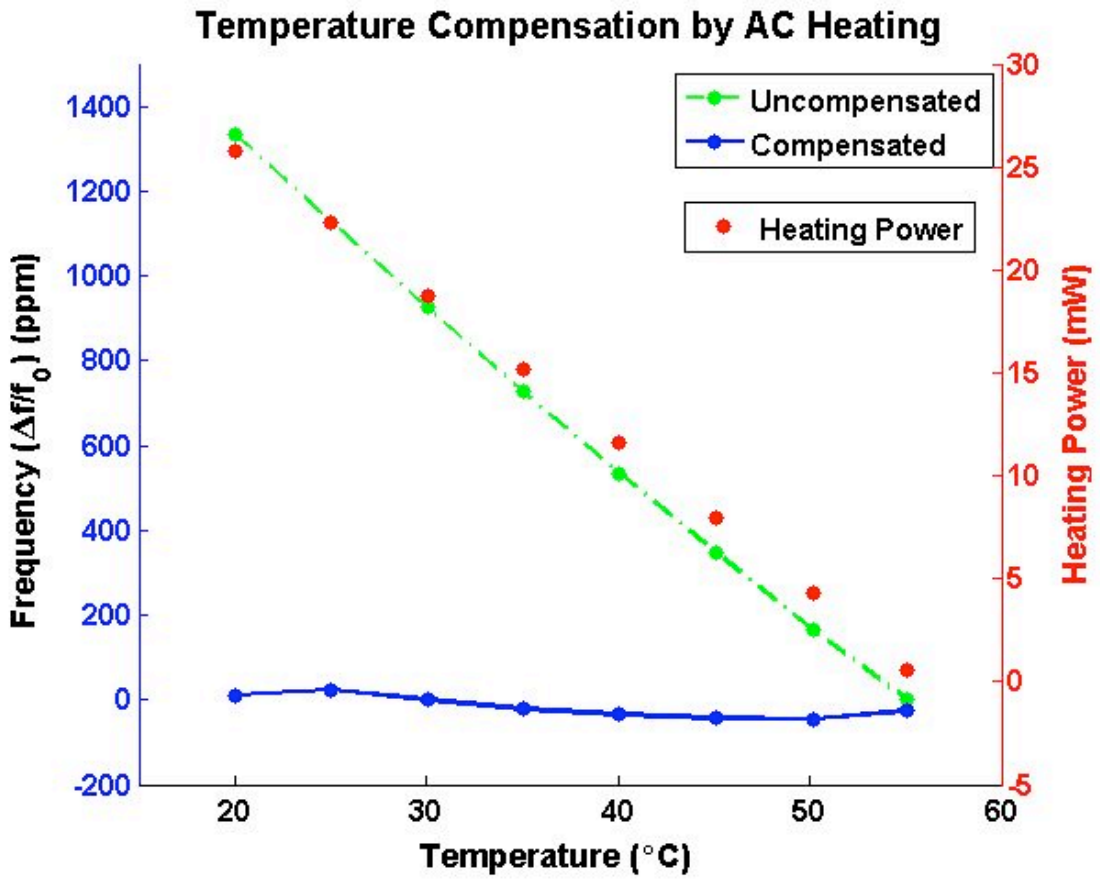

Figure 5.14: AC Direct Heating Results
A DA-DETF packaged with photoresist ("soft-attach") was used. Temperature was measured using an external temperature sensor, and power was applied according to the calibration data in order to keep the resonator temperature at the setpoint of 55 °C. The uncompensated resonator has a TCf in this range of -38 ppm/°C, or 1300 ppm over the termperature range. When temperature compensation was used, the frequency variation was reduced to 71 ppm, using 26 mW of heating power [198].

A discrete diode temperature sensor, the LM35, was mounted on the PCB and used to measure the ambient temperature. The control software applied heating power according to the data in a look-up table that was compiled manually. The results were promising, and the frequency variation was certainly reduced, but all aspects of the resonator operation need improvement from this point: temperature sensing, calibration, thermal isolation, resonator measurement, etc. Most of all, the AC direct heating method is cumbersome, as it requires generation and control of a high-power AC current source.

5.2.2 Calibration Data

A set of resonators with heating resistors embedded in the silicon die were fabricated. These devices were not ovenized, in that no attempt was made to thermally isolate the resonator, and consequently the power consumption was quite large, but the inclusion of separate elements for heating meant that the heater power could be delivered by a DC current, simplifying the measurement circuits and allowing for exploration of temperature control issues. The most important issue is the question of generating and using the calibration data for the feed-forward controller.

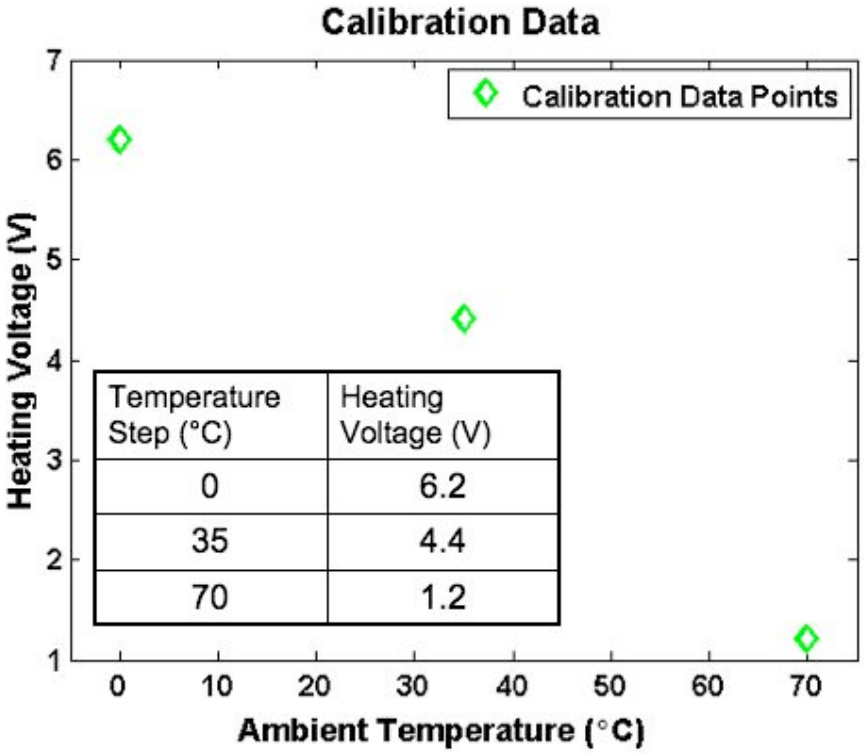

Figure 5.15: Typical Calibration Data
Only three calibration data points are shown in this example. Each point is the heating voltage value required to bring the resonator to its target frequency when the ambient temperature is at the indicated value. The target frequency is the frequency at the temperature setpoint of 75 °C.

The heating power delivered to the resonator is controlled by the heater voltage, V_h. The calibration data is simply a table of the appropriate V_h value to elevate the resonator temperature to the setpoint at a given ambient temperature. The heating power is, of course, $P_h = V_h^2/R_h$, but as discussed in Chapter 3, nothing in the system

is linear at the ppm level. The heater resistance, R_h, and the thermal resistance, R_{th}, and the resonator *f-T* characteristic all have complex dependencies on temperature, so that the shape of the calibration data is more complex than the V_h^2 relationship. A plot of a typical set of calibration data is shown in Figure 5.15.

Of course, during operation, the ambient temperature may not fall directly on the temperature points used for calibration. If we use linear interpolation between data points, we will have some error in the resulting V_h. The result from such an experiment using feed-forward with linear interpolation is shown in Figure 5.16.

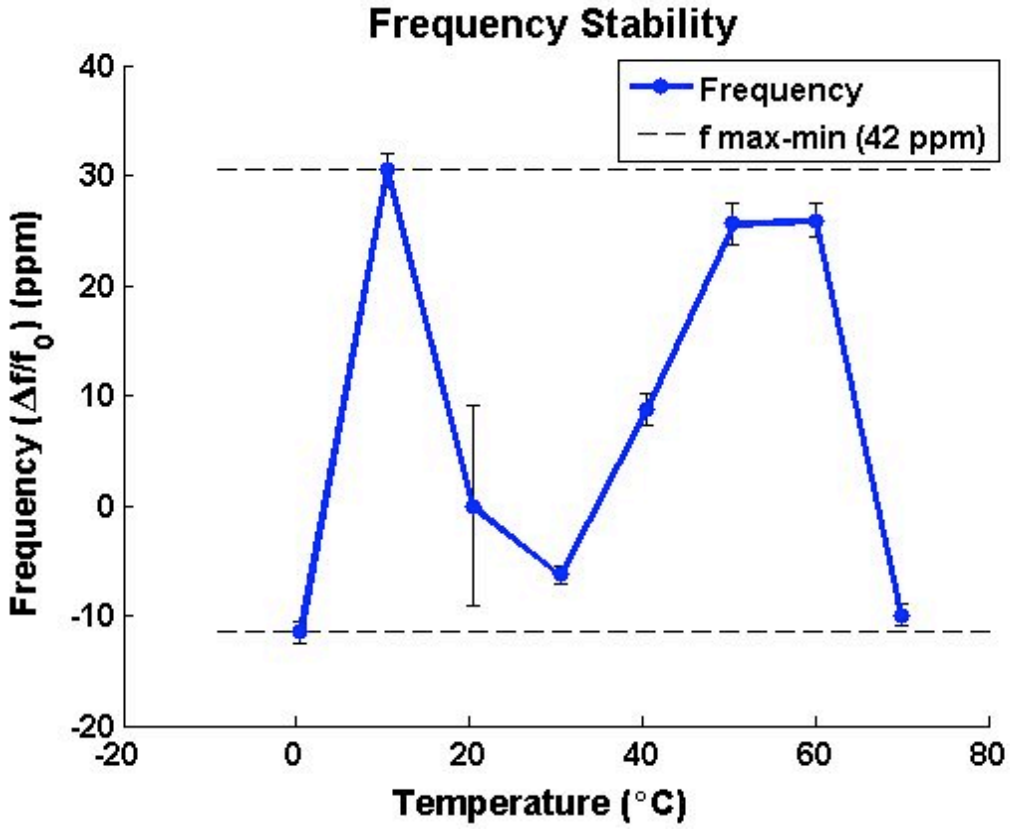

Figure 5.16: Frequency Stability using Linear Interpolation

The error from linear interpolation can be reduced by including more data points in the look-up table. For practical operation, this has a high cost, as each data point requires an hour to collect. It would be preferable if we could approximate the V_h calibration data with a polynomial function, as shown in Figure 5.17.

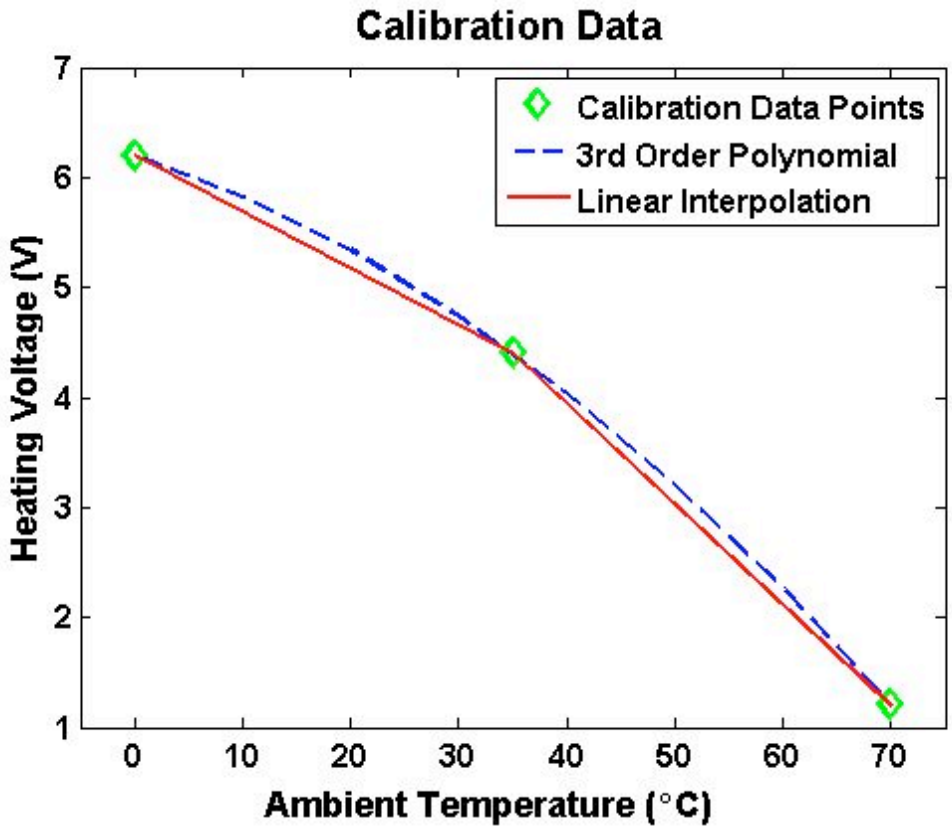

Figure 5.17: Calibration Data with Polynomial Fit
The polynomial fit clearly does a better job of estimating the "true" value between points.

Higher-order polynomial fitting functions should reduce the error in the estimates by more closely approximating the underlying behavior. Figure 5.18 shows the result of temperature stability experiments using increasing orders of polynomial fits to the same set of calibration data. The resulting *f*-*T* behavior when V_h is determined using a second-order polynomial fit clearly has a large third-order residual error. This residual error is reduced when the fit function is increased to third order, now a fourth-order residual error is evident. A fourth-order fit function reduces the residual frequency error further still, and now the residual error is not clearly defined. Further increasing the fit function order, to an 8th order function, does not significantly reduce the residual[28].

[28] In fact, further increasing the order of the polynomial fit will eventually *increase* the error for certain underlying functions. This is called Runge's Phenomenon.

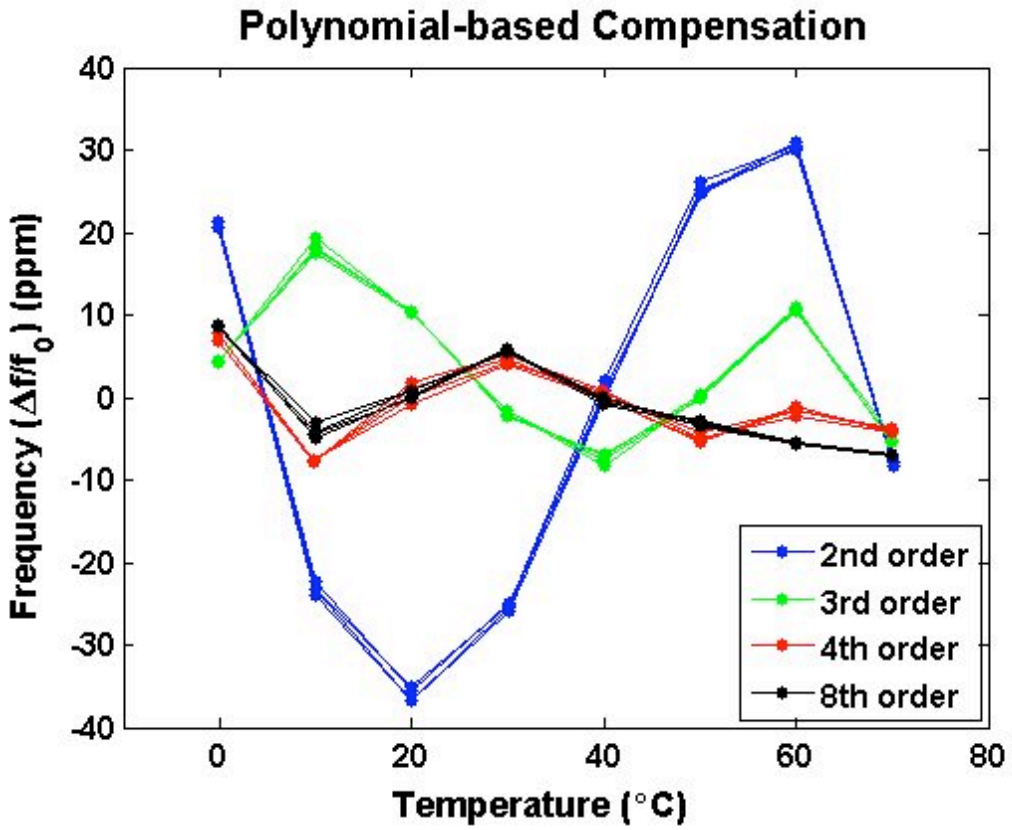

Figure 5.18: Frequency Stability Using Polynomial Fit to Calibration Data
The appropriate value of V_h is determined by fitting a polynomial function to the calibration data. As the order of the polynomial fit is increased, the residual error is reduced. Each data set includes two complete up-down temperature cycles. Five evenly-spaced calibration data points were used. The frequency range of the 8th order result is 18 ppm.

Another option for using the calibration data is spline interpolation. This method fits an individual function between each calibration data point, instead of using a single function for all of the points. With cubic spline interpolation, we can reduce the frequency error still further (Figure 5.19).

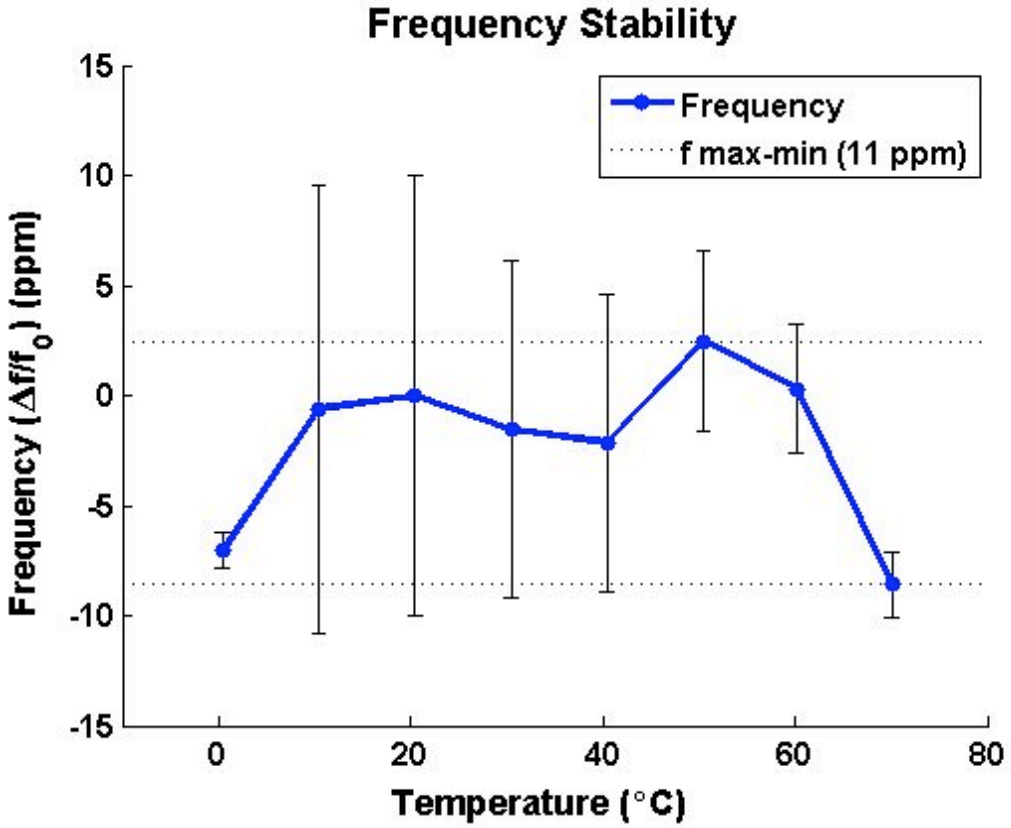

Figure 5.19: Frequency Stability using Spline Interpolation
The appropriate value of V_h is determined by cubic spline interpolation to the calibration data [199].

However, it is clear that, in order to achieve sub-ppm precision using feed-forward control, there is no substitute for simply increasing the number of calibration data points. When the calibration data was taken at 1 °C steps, and linear interpolation was used, the result was a frequency range of less than 1 ppm over a large temperature range (Figure 5.20).

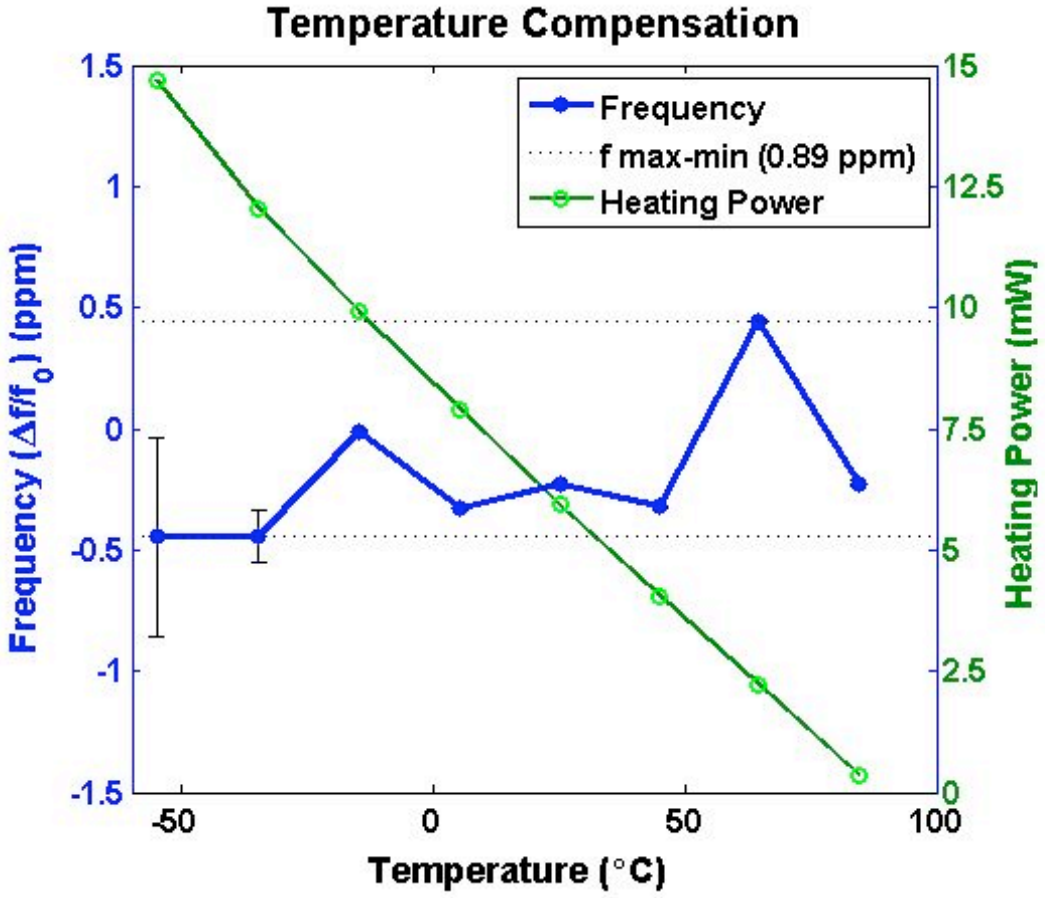

Figure 5.20: Frequency Stability with Precision Linear Interpolation
This experiment was performed using an ovenized SR-DETF, so the heating power consumption was minimized. The large error bars at low temperatures are due to the large temperature variations (see Section 5.1.2).

5.3 Feedback Experiments

It is possible to achieve sub-ppm stability using a feed-forward method with a large number of calibration data points. However, there is a limit on the number of data points that can be taken (the temperature step in the thermal chamber is limited to 1 °C), and the accuracy of the ambient temperature measurement is a problem. A solution is to implement a feedback controller which can adjust the heating voltage in response to changes in the temperature of the resonator. This requires an accurate sensor for the temperature of the resonator (not the ambient temperature). In Chapter 4, the resonator Q was shown to have a strong dependence on temperature, and so the amplitude of the resonator output can be used to indicate the resonator temperature. We also need to implement the temperature sensing and heating voltage control at a rate greater than, or at least comparable to, the temperature changes we are trying to counteract.

5.3.1 Sweep Amplitude

Q can be determined from a complete resonator frequency response measurement using the relationship (5-1). However, this requires performing a sweep measurement and then downloading the result from the analyzer. The result of Q measured this way can easily vary by ±5% due to amplitude noise at the 3dB points [103]. However, the amplitude at resonance, X_0 is proportional to Q (see Chapter 3). We can determine X_0 from a sweep measurement quickly, without downloading the entire data trace, and the sensitivity to amplitude noise is relatively small. Using the HP 89410A Analyzer with a fast sweep, and limiting the span based on the premise that the frequency will be relatively constant, we can perform measurements at a rate of 0.25 Hz. When the feedback system was implemented, the frequency variation was reduced to 4 ppm (Figure 5.21). This experiment demonstrates the viability of the *Q(T)* feedback system, but we will not be able to demonstrate sub-ppm stability with a control system rate of < 1 Hz.

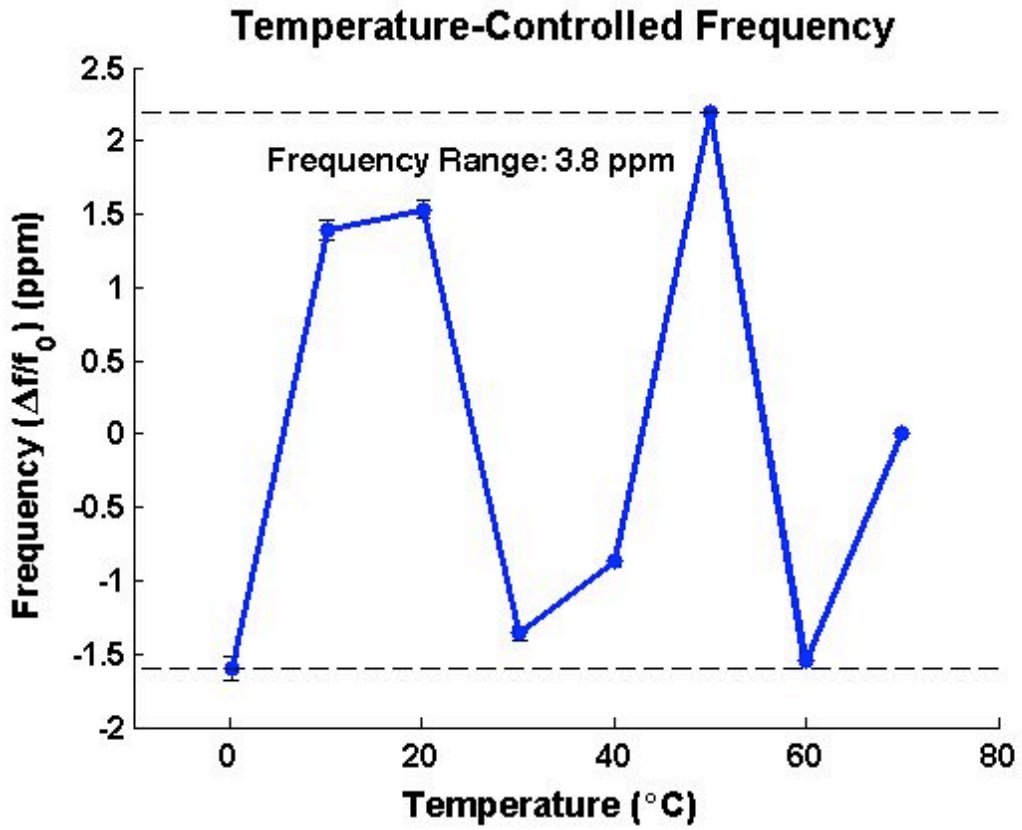

Figure 5.21: Frequency Stability using Amplitude Feedback
In contrast to the feed-forward experiments, there is no discernible residual error pattern, only random noise around the setpoint, which is characteristic of feedback control systems. A large number of data points (> 200) were averaged in order to get the low frequency uncertainty at each temperature step. This is evident in the small error bars at each data point.

5.3.2 *Q(T)* Operation

High-stability frequency results can only be demonstrated if the frequency can be measured with high accuracy at a reasonable rate. This requires that the resonator be operated in an oscillator circuit which produces a continuous output signal. An oscillator is simply an amplifier that feeds the resonator's output signal back to its input. The output of the oscillator a periodic signal, so the primary information that is available is simply frequency[29].

[29] Actually, phase relative to an arbitrary reference is the fundamental output signal. Frequency is the derivative of phase.

5.3.2.1 Measurement of *Q(T)* with Oscillator

The *Q* of a resonator is normally measured with gain-phase frequency-domain measurements or ring-down time-domain measurements. Neither method is suitable for high-resolution, high-bandwidth measurements required for control applications. Moreover, frequency references require oscillators, and neither gain-phase nor ring-down information is available from the oscillator output signal, which [ideally] consists of a sine wave at a fixed frequency. Therefore, we need to measure resonator *Q* indirectly.

As discussed in Chapter 3, the amplitude of the resonator output is proportional to *Q*:

$$X_0 = \frac{FQ}{k} \ . \tag{5-2}$$

The output transduction mechanism for our resonators is capacitive, so that if the beam displacement increases for the same frequency of vibration, the amplitude of the output signal, V_{out}, increases proportionally:

$$V_{out} \propto \frac{dC}{dt} \propto X_0 \ . \tag{5-3}$$

where C is the transduction capacitance. When the resonator is operated in an oscillator, the amplitude of the oscillator sine wave output reflects the resonator vibration amplitude. Therefore, if we can design an oscillator circuit that maintains a constant amplitude input signal to the resonator, then the amplitude of the oscillator output will directly reflect the resonator *Q* value. We can measure this amplitude with an RMS detector, whose output is a DC voltage proportional to the amplitude of the oscillator output. The output of the RMS detector, V_{RMS}, will be our temperature signal.

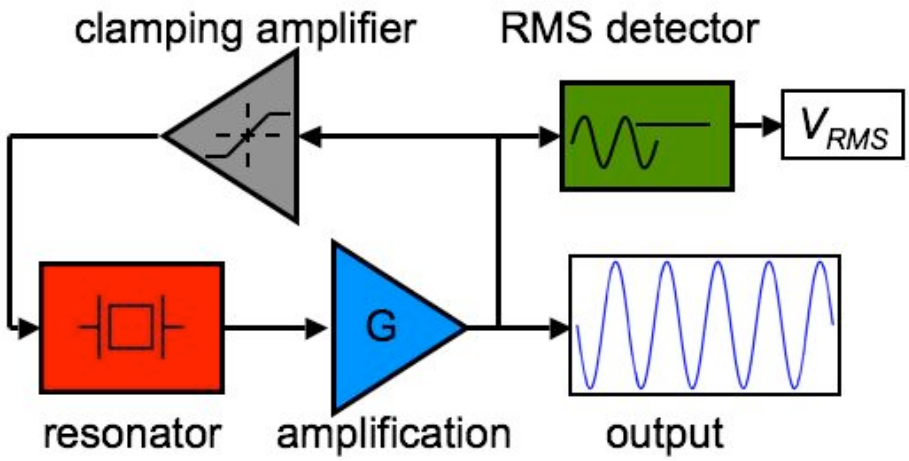

Figure 5.22: Oscillator Block Diagram for *Q(T)* Temperature Sensing.

The block diagram of the system is shown in Figure 5.22. A clamping amplifier with clamp levels set much lower than the lowest expected amplitude after the gain stage is used to hold the input voltage to the resonator at a constant level. The amplitude of the frequency output as measured by the signal analyzer and the V_{RMS} signal are shown in Figure 5.23, and the corresponding noise density is Figure 5.24.

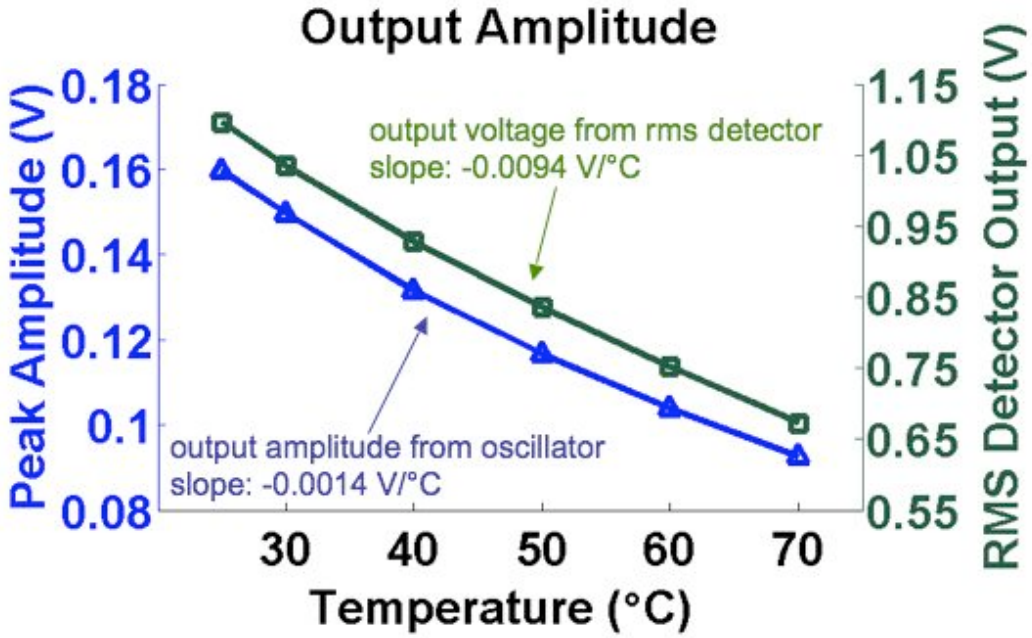

Figure 5.23: Temperature Signal Output from the Oscillator.
The amplitude of the frequency output is measured with a signal analyzer. The RMS detector output is a DC voltage level. The slope of the RMS output is ~ 10 mV/°C. From [200].

The frequency characteristic of the oscillator amplification stage is apparent in the noise plot. The resulting sensitivity and noise floor values for the output amplitude are 1.4e-3 V/°C and 5.26e-6 Vrms in a 1 Hz bandwidth, resulting in a temperature resolution of 0.0035 °C. This is a reasonably good temperature resolution and it indicates that the proposed method is functional.

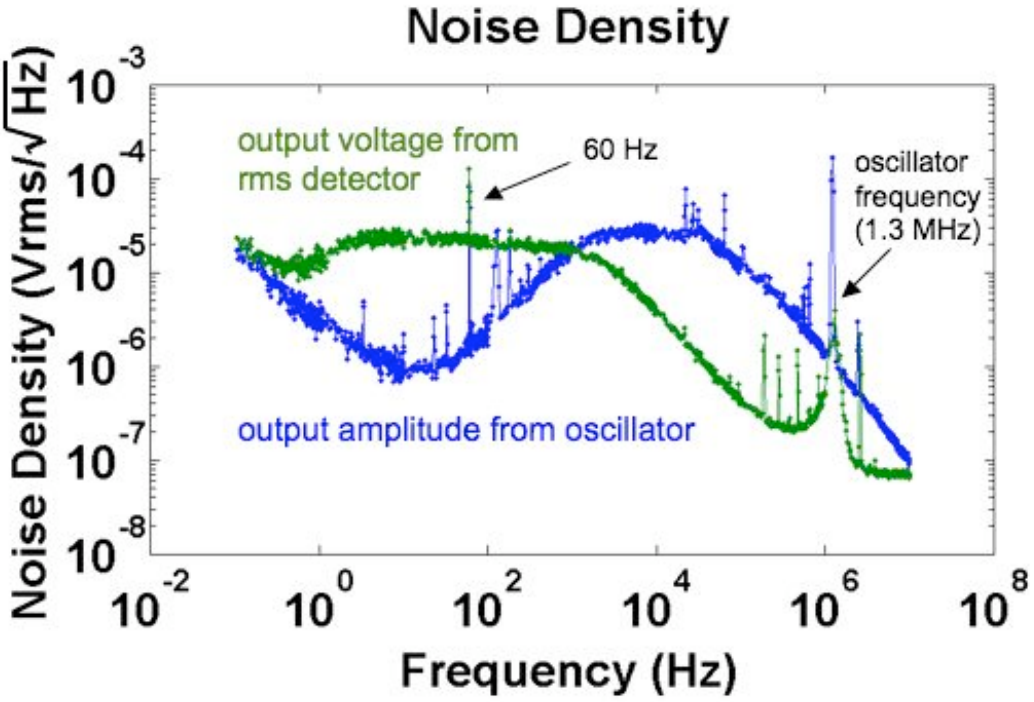

Figure 5.24: Noise Density for the *Q(T)* Oscillator Outputs. From [200].

However, use of a signal analyzer is impractical. Instead, the discrete broadband root-mean-square (RMS) level detector is placed at the output of the oscillator (Figure 5.22). The RMS detector output, V_{RMS}, is a DC voltage with a conversion gain of 7.5 V/V_{RMS} [201]. The RMS detector has a worse noise figure than the signal analyzer, especially at intermediate frequencies[30], but the increase in sensitivity due to the conversion gain more than compensates for it. The RMS detector output is also shown in Figure 5.23 and Figure 5.24, with a sensitivity of 9.4e-3 V/°C and a noise density of 1.16e-5 Vrms in a 1 Hz bandwidth. The resulting temperature

[30] Note that the RMS detector is a broadband device (designed for mobile phone frequencies) which is integrating signal amplitudes at all frequencies up to 2.5 GHz.

resolution in a 1 Hz bandwidth is 0.0017 °C. Even after doubling sensor bandwidth to allow the control system to operate reliably at 1 Hz, the temperature resolution is 0.0026 °C [200]. When the feedback control system is operating correctly, we can expect to keep the termperature of the resonator stabilized to the resolution of the sensor. With a temperature resolution of 0.003 °C and a silicon TCf of -30 ppm/°C, a frequency stability of 0.1 ppm is the limit of expected performance.

5.3.2.2 *Q(T)* Frequency Stability

Now that we have an oscillator and a signal representing the temperature of the resonator, we can implement a feedback system to stabilize temperature by keeping the *Q(T)* V_{RMS} signal constant. The controller was implemented in software as a PID controller, using experimentally chosen values for the coefficients.

The SR-DETF has four electrical contacts (at the anchors). In order to provide a variable heating current while maintaining a fixed bias voltage on the resonator, one anchor was used to apply V_{bias}. Two other contacts were used to apply a heating voltage from a power supply whose terminal were floating with respect to the circuit ground potential. This way, the bias voltage was maintained for arbitrary heating voltages, currents, and heating resistor values (which are never exactly identical because of variations in fabricated dimensions).

The SR-DETF is effectively double-anchored. If we heat the resonator using a pair of SR springs on one side, as in the example in Figure 4.16, a temperature gradient will occur along the resonator beams as heat flows out through the opposite pair of SR springs. The temperature gradient will be linear, as the resonator itself presents simple a thermal resistance. If we heat the resonator using a pair of SR springs on opposite sides of the resonator, a parabolic temperature gradient will occur along the length of the resonator, because it will participate in the heat generation. These cases are illustrated below in Figure 5.25.

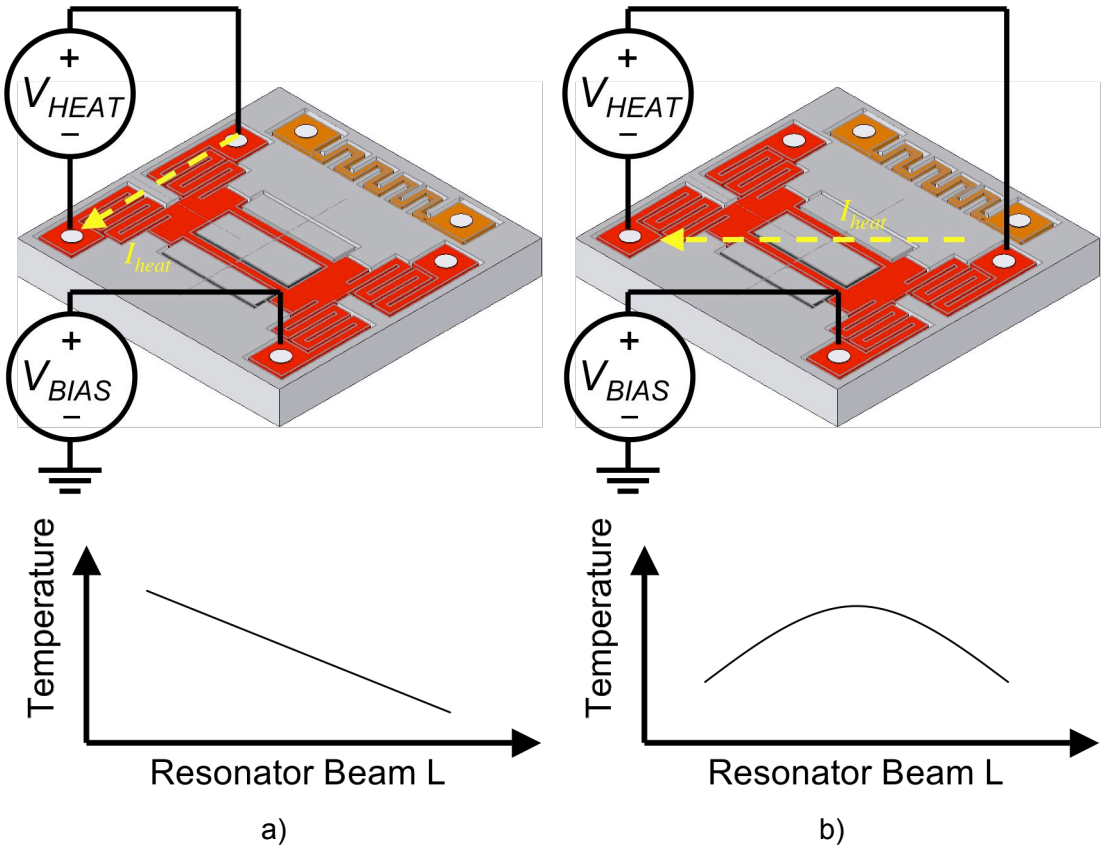

Figure 5.25: Two Cases of SR Heating
a) The heating current is passed through two SR springs on the same side of the resonator. The resulting temperature profile on the resonator beams is linear.
b) The heating current is passed through two SR springs on opposite sides of the resonator. The resulting temperature profile on the resonator beam is parabolic because heat is generated in the beam.

These temperature gradients cause problems because the resonant frequency and the quality factor respond differently to the two different gradients. For a linear temperature gradient, the elastic modulus varies along the length of the beam, and the frequency change due to the gradient is given by [202]:

$$\frac{f_{grad} - f_0}{f_0} = -\left(\frac{1}{3} - \frac{1}{2\pi^2}\right)\left(|TCE|\frac{\Delta T}{2}\right). \quad (5\text{-}4)$$

where ΔT is the difference in temperature between the ends of the resonator, and f_0 is the resonant frequency for the average temperature of the beam (equal to the temperature at the center of the beam). The resulting frequency change is relatively small- frequency changes by 10 ppm for ΔT = 150 °C. There is no closed-form

expression for the Q_{TED} of the resonator due to a linear temperature gradient, but the effect is relatively strong. We know that Q_{TED} is inversely proportional to T. Therefore, the change of T at lower temperatures will affect Q more than the change of T at higher temperatures (Figure 5.26), and $Q_{TED,grad}$ will increase relative to $Q_{TED,0}$ in a non-linear manner with increasing ΔT.

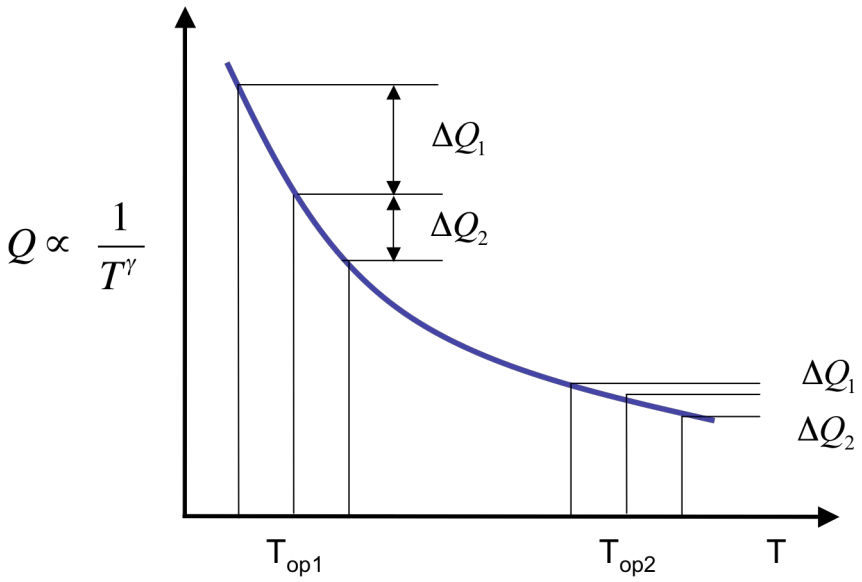

Figure 5.26: Change of Q_{TED} with Temperature
The same ΔT at lower temperatures changes Q less than the same ΔT at higher temperatures.

In the case of a parabolic temperature gradient, the frequency will be approximately the frequency we expect for the average temperature of the beam because of the symmetric distribution of temperature (and so elasticity) and stress. Again, there is no good way to estimate the effect on Q, however, it should be strong by the same argument as before.

The result is that for both cases, we see a significant error in the output frequency when we use $Q(T)$ to stabilize the resonator temperature. The error for the parabolic case is the least, with a residual error of approximately 50 ppm over the range of 0-70 °C.

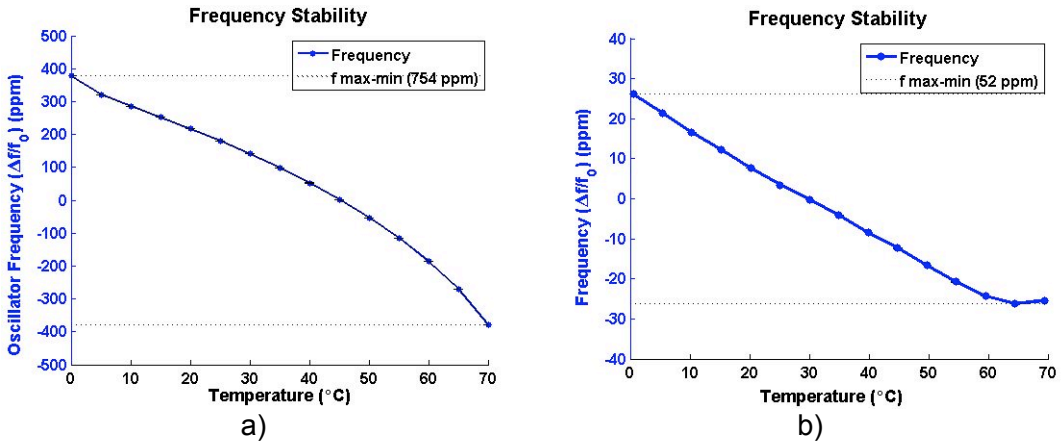

Figure 5.27: Frequency Stability for Two Heating Cases
a) Same-side heating case
b) Opposite-side heating
The heating cases correspond to the diagram in Figure 5.25.

So for the SR DETF, the heating mechanism creates temperature gradients in the device, which causes the *Q(T)* temperature signal to be imperfect and the frequency response to be unusual. However, we can still use the system if we implement a correction factor to account for these errors. This is not unlike using a Pt RTD, which has a non-linear, but well-known and reliable, temperature coefficient of resistance. When using an Pt RTD, the resistance is converted to temperature using this 3rd order function. Similarly, we can measure the frequency error as a function of heating power for the SR device, and use this correction function to correct the heating voltage. The temperature control system will now multiplex between two modes: in the first mode, the system is operated as usual to keep the *Q(T)* signal (V_{RMS}) constant. Periodically, the control system switches to the other mode, reading the heating power consumption and then adjusting the heating voltage according to the correction function to get the correct output frequency.

This multiplexing method, $Q(T,P_h)$, clearly has a number of disadvantages- the system will switch between two frequencies at some rate, with frequency noise and drift implications, and the correction function must be measured, much like the calibration data of the feed-forward methods, so much of the advantage of the feedback system is negated. However, the experiment was performed in order to

demonstrate the lower limits of the frequency stability of the system. The result of four stability measurements is shown in Figure 5.28.

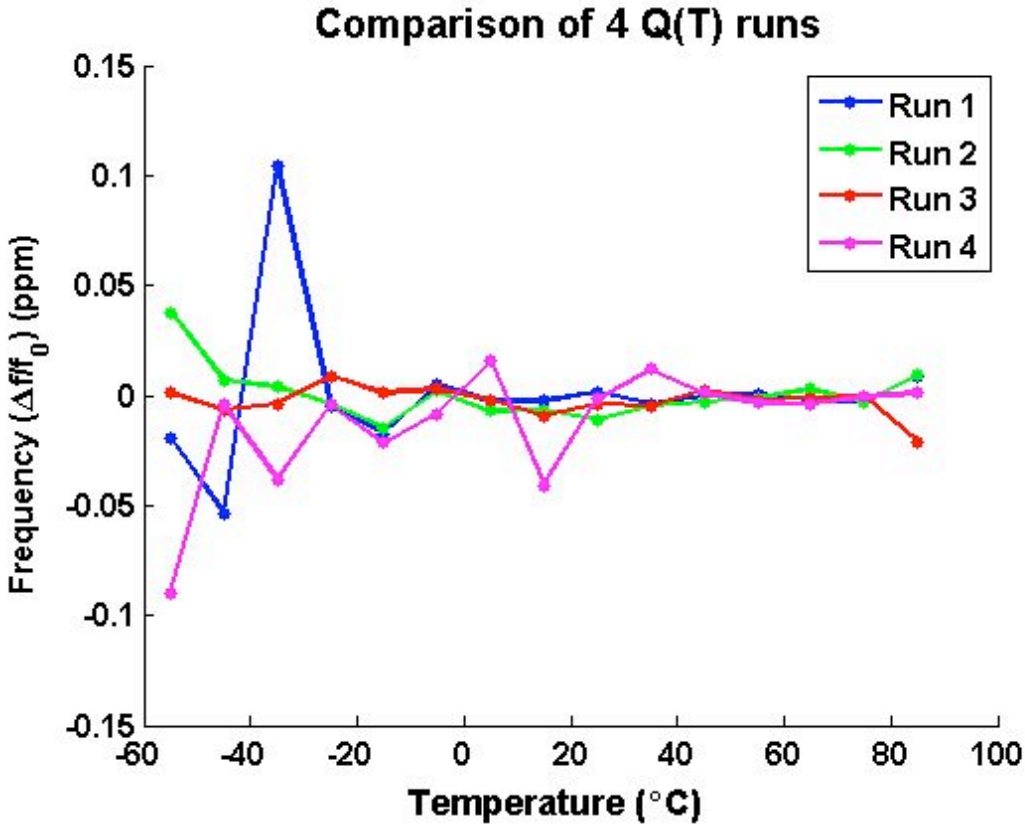

Figure 5.28: Frequency Stability with Feedback and Correction Factor
The results from four separate measurements are shown. The data plotted is the frequency after applying the correction factor.

In fact, some of the stability results above are better than the predicted limit of 0.1 ppm established by the temperature sensor. Run #3, for example, has a frequency range of only 0.03 ppm! However, these cases are just "luck", and not repeatable. The uncertainty comes from the uncertainty of the temperature sensor and the application of the correction factor, and the repeated results begin to approach the predicted limit of 0.1 ppm.

5.4 Conclusions

The frequency stability results achieved during the course of this work are summarized in Figure 5.29.

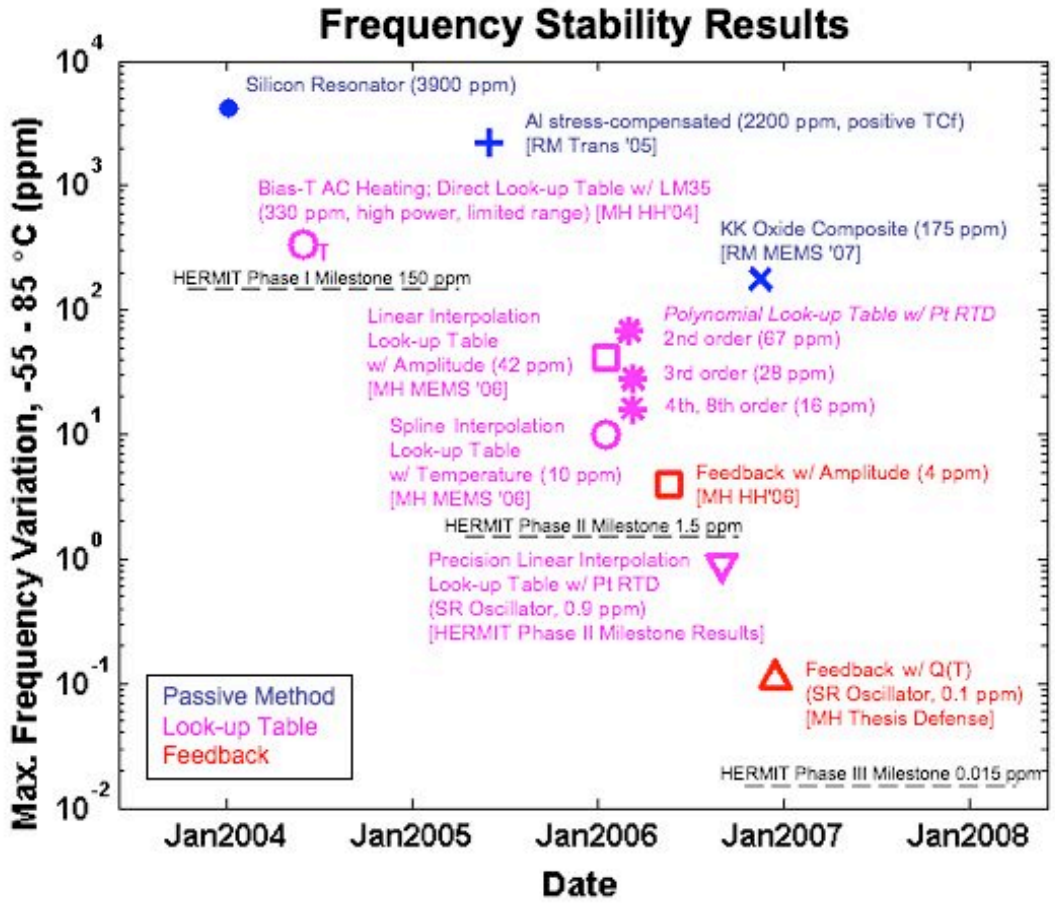

Figure 5.29: Frequency Stability Results
Uncompensated silicon resonators are shown at upper left. The milestones related to the research funding provided as part of the HERMIT project are shown in black.

While the final experimental results achieved here have significant caveats, we can compare the stability measurements to the OCXO measurement presented at the beginning of the chapter. The frequency stability is comparable, and in fact, the SR-DETF performance is within the datasheet specifications of the C4550 (if not the measured performance), over a greater temperature range (Figure 5.30). Moreover, the power consumption is not even a horse race- the SR DETF is using two orders of magnitude less power (~20 mW vs. ~2000 mW)!

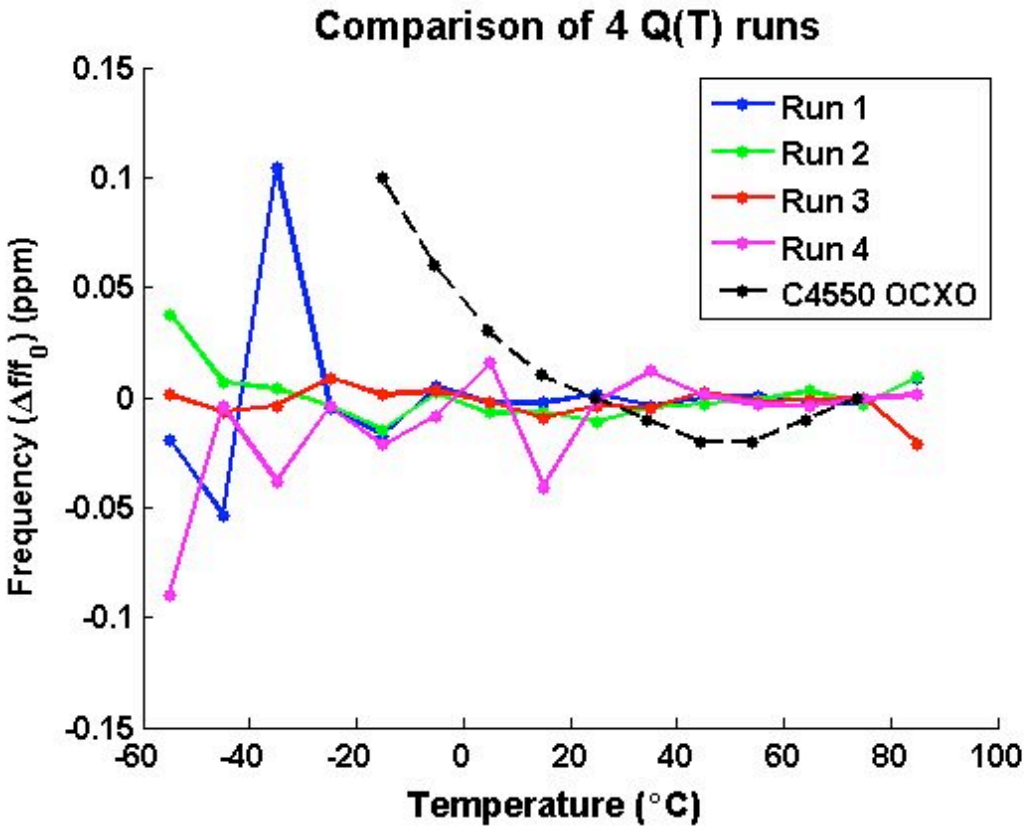

Figure 5.30: Comparison of SR-DETF and Commercial OCXO Stability
The SR-DETF performance is similar to the C4550 OCXO, but the power consumption (not shown) for the MEMS device is two orders of magnitude smaller than for the quartz part.

The limitations of the SR resonator design are easily rectified by removing the SR springs from one end of the resonator, and connecting a third spring to the other end, creating a single anchored SR (SA/SR) resonator. The *Q(T)* temperature signal of such a device would no longer be dependent on the ambient temperature, and no "correction factor" would be needed.

The limitation on the frequency stability with this temperature control system is the *Q(T)* temperature sensor. The *Q(T)* results shown here used resonators with $\gamma \approx 3$. Values of 4 are theoretically possible, which should create approximately 25% improvement in temperature sensitivity. As we can see from Figure 5.24, the noise in the *Q(T)* signal is limited by the electronic RMS detector and not the underlying amplitude signal. Improvements in circuit design could reduce the noise, and increase temperature resolution further; a 10x total improvement seems feasible.

5.5 Acknowledgements

The results presented here would not have been possible without an oscillator circuit. The design, fabrication, and testing of the oscillator circuits (custom designed for the requirements of the DETF resonators) used here was a difficult task, and would not have happened without the contributions of many people over a period of several years, particularly: Aaron Partridge, Manu Agarwal, Kwan Kyu Park, Harsh Mehta, Gaurav Bahl, Jim Salvia, and Hyungkyu Lee. Jeff Li and Hyungkyu Lee also made significant contributions to the instrument control code.

The future depends on what we do in the present.
-Mahatma Gandhi

Chapter 6 Conclusions and Future Directions

This thesis presents an investigation and demonstration of the suitability of silicon MEMS resonators for use as high-performance frequency references. It has been found that here are no fundamental limitations that prevent silicon MEMS from being used as frequency references, only engineering challenges. This chapter discusses some areas for future investigation.

6.1 Future Directions

The obvious disadvantage of the SR-DETF design is the fact that anchors are located at both ends of the resonator, which leads to temperature and current gradients across the device (see Chapter 4 and 5). The single-anchor SR design, SA/SR-DETF, shown in Figure 6.1, has been successfully designed and fabricated in an oxide seal process in order to test its feasibility. An epi-seal version is being fabricated and is expected to be ready for testing in Autumn 2007. The SA/SR-DETF uses the same SR spring design as the original SR-DETF, but uses only three springs (two for heating current, one for bias voltage), located at the same end of the DETF. This increases the thermal isolation while removing the current and temperature gradients across the resonator.

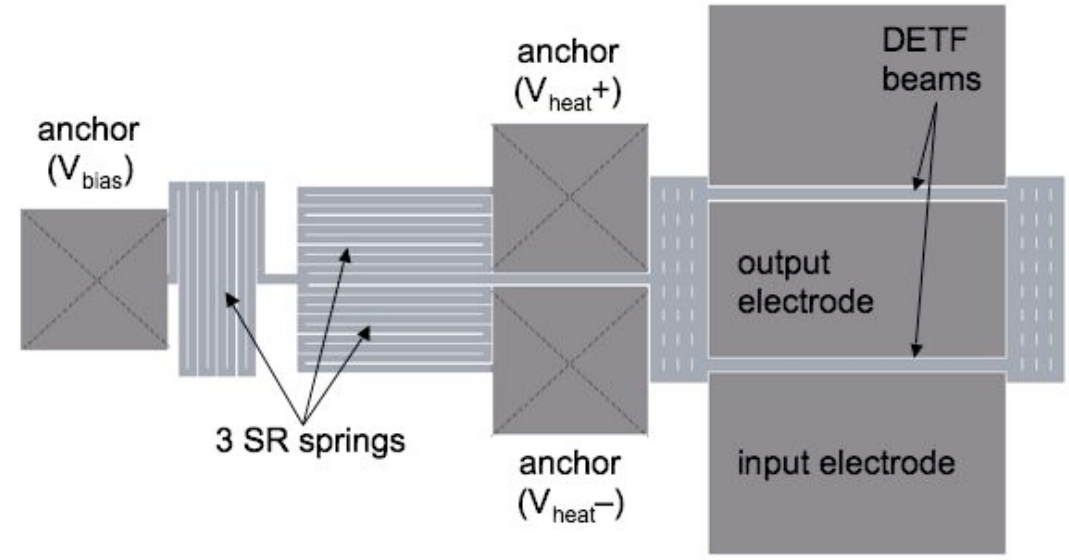

a)

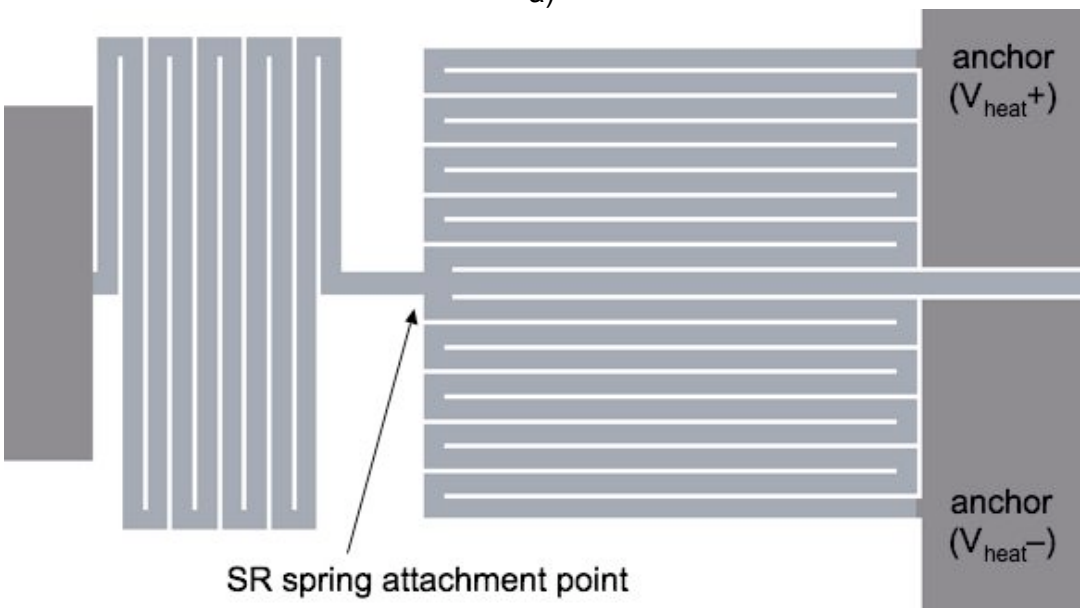

b)

Figure 6.1: Single-anchor SR DETF design (SA/SR-DETF)
The SA/SR-DETF design eliminates the temperature and current gradients across the resonator that are found in the SR-DETF. In addition, the separation between the SR heaters and the resonator should reduce the effect of any voltage gradient in the DETF. This SA/SR design has been successfully fabricated and tested in oxide-seal wafers, and epi-seal devices are expected to be ready for testing in Fall 2007.
a) SA/SR layout. This is the ST ("stem") version of the SA/SR.
b) Detail of SR spring attachment point.

In addition to heating the resonator from a single point, the heating springs are separated from the resonator by a long stem, which reduces the effect of the heating voltage gradient at the point where the SR springs are attached to the resonator. This effect is very small, and is expected to be important only for stability levels << 0.1 ppm.

The low heating power consumption of the SR-DETF depends on its thermal isolation, which is accomplished by suspending the DETF from mechanical springs. These relatively soft springs leave the device vulnerable to damage by shock and acceleration (see Chapter 4). Some optimized spring design is required to maximize thermal isolation and resistance to acceleration; possibly including non-rectangular spring geometries or modifications to the fabrication process to include out-of-plane spring elements. Possibly the electrodes could be suspended in a frame with the resonator; in this case, the entire structure would move together, reducing the effect of acceleration.

The temperature sensing mechanism is a universal challenge for any frequency reference. The method presented here, *Q(T)*, is an important development, but it has limitations. The most significant issue is noise- the output of the *Q(T)* sensor is an analog voltage. The measurement of an analog quantity can never be as precise and robust as the measurement of a digital quantity. The obvious digital quantity in this system is frequency, and if we had a frequency signal to use for temperature measurement, we could expect to achieve high temperature measurement performance. This is in fact what is done in some precision quartz references: two modes of the same resonator are excited simultaneously, and the beat frequency generated by mixing these two signals is the temperature sensor signal [203]. A similar approach has been demonstrated in silicon MEMS using two resonators [204, 205], but additional work is required to bring this method to epi-seal DETF resonators.

The most significant component of the temperature sensitivity of resonant frequency is the change in material elasticity, the TCE. If the TCE could be reduced, the stability of the system would improve dramatically. The composite Si/SiO_2 technology mentioned in Chapter 4 is promising, but the stability of the two-material

system has not been demonstrated, and it would be preferable to have a silicon-only solution. As discussed in Chapter 4, there are no known or predicted "zero-TCE" orientations for silicon flexural resonators due to the [relatively] simple elastic relationships for flexural modes in a cubic crystal. However, the shear wave propagation modes in bulk resonators present some additional possibilities [206], and it is not possible at this time to preclude the existence of a zero-TCE orientation for these and other more complex wave propagation modes. A further difficulty lies in exciting these modes, as silicon is not piezoelectric. Some recent work such as [207], which uses Poisson contraction of a second material layer to induce shear waves in bulk silicon, may be applicable.

6.2 Conclusions

In conclusion, it has been demonstrated that there are no fundamental barriers preventing silicon MEMS resonators from achieving high levels of frequency stability performance while maintaining the benefits of microscale design- small size, low power consumption, and CMOS compatibility. Referring to the regime map presented in Chapter 1, we can locate the results of this work at several orders of magnitude better than existing MEMS technology.

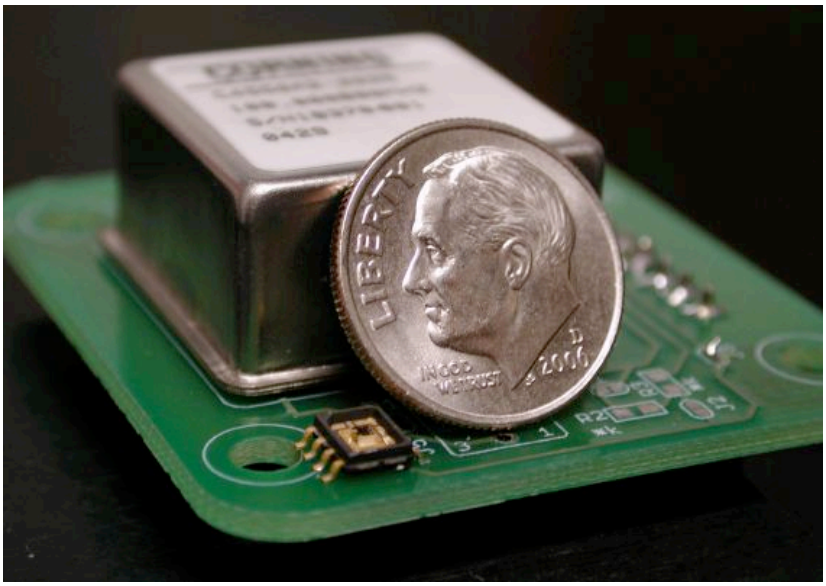

Figure 6.2: A packaged SR-DETF resonator and a commercial C4550 OCXO

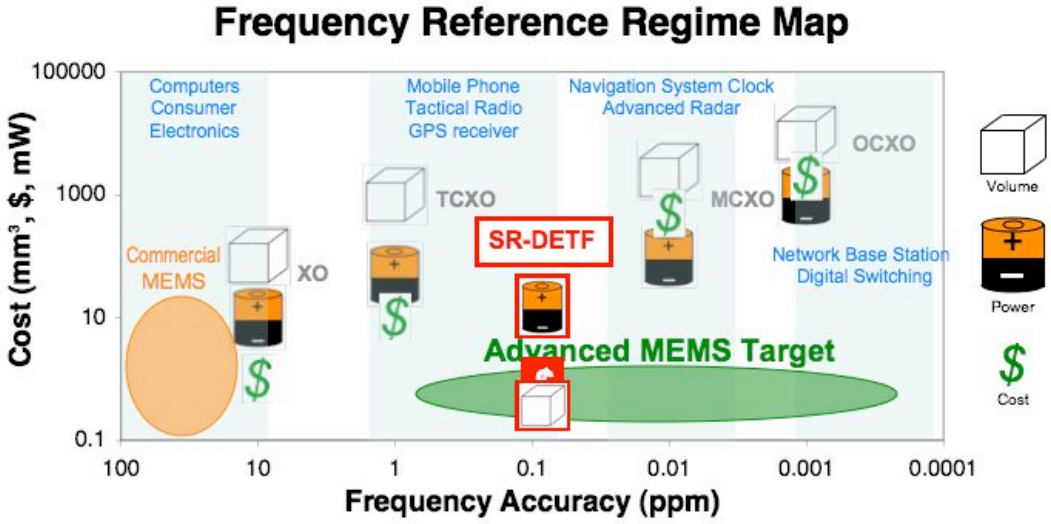

Figure 6.3: Frequency Reference Technology
The performance of existing quartz technology follows a typical inverse relationship between performance and price/size/power consumption. The MEMS resonators demonstrated in this work break out of this relationship and achieve good performance with dramatically lower cost.

Silicon has three significant advantages over quartz as a material choice for high-stability devices:

- The ability to withstand high temperature processing enables silicon devices to be fabricated in extremely clean conditions.
- The availability of a large and well-developed toolset for fabricating micro-scale silicon devices means that complex designs can be batch-fabricated in high volume and at low cost.
- The compatibility of silicon with CMOS circuitry means that silicon devices can be easily integrated with advanced control circuitry.

The only significant disadvantage of silicon versus quartz, the lack of a zero-TCf angle, is not enough to prevent silicon resonators from competing with, and eventually replacing, quartz as the technology of choice for future frequency references.

The wind does not break a tree that bends.
-Sukuma proverb (Africa)

A. The Elasticity of Silicon

The Young's modulus, or elastic modulus, (E), of a material is a key parameter for mechanical design. Silicon is a crystalline material with its atoms arranged in a regular crystal lattice structure (Figure A.1). The silicon crystal is anisotropic, so its material properties are different in different directions relative to the crystal lattice. In particular, Young's modulus varies by as much as 30% depending on the orientation of the structure, and there is no simple, single value for E, as many engineering formulas require. When designing mechanical structures in silicon, it is important to understand which crystal orientations are relevant to the structure and what corresponding values for elastic properties should be used for calculations. This appendix explains the elasticity (Young's modulus, Poisson's ratio, and shear modulus) of silicon for the MEMS designer.

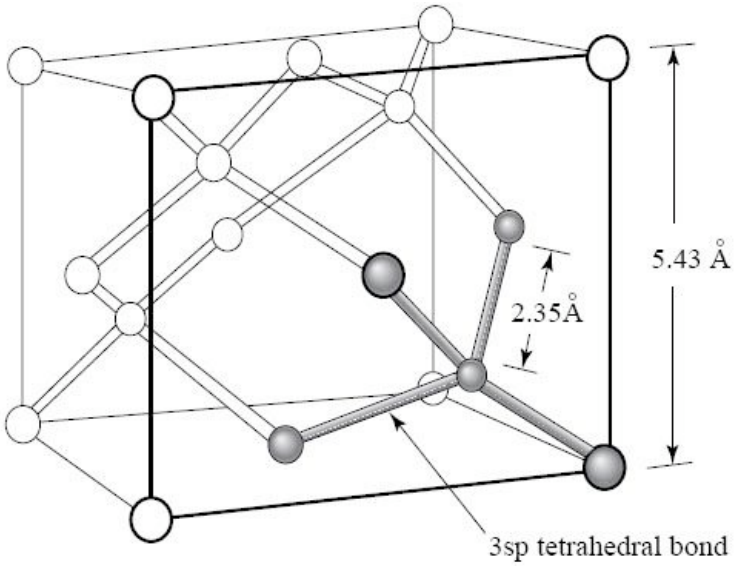

Figure A.1: Silicon Crystal Lattice
Silicon has a diamond-type lattice and cubic symmetry. From [66].

A.1 Crystal Orientation

In order to describe crystal orientation-dependent material properties, we first need to describe the crystal orientation. Crystallographic planes and directions are described by Miller indices, which are three-integer triples, corresponding to an XYZ coordinate system. The triple can describe either a direction, *uvw,* or a plane perpendicular to the direction, *hkl*. The *hkl* values are the reciprocals of the coordinates of the intercepts on the XYZ axes, multiplied by the lowest common denominator [99, 208]. Negative values are indicated by a bar. The important directions in silicon are shown in Figure A.2.

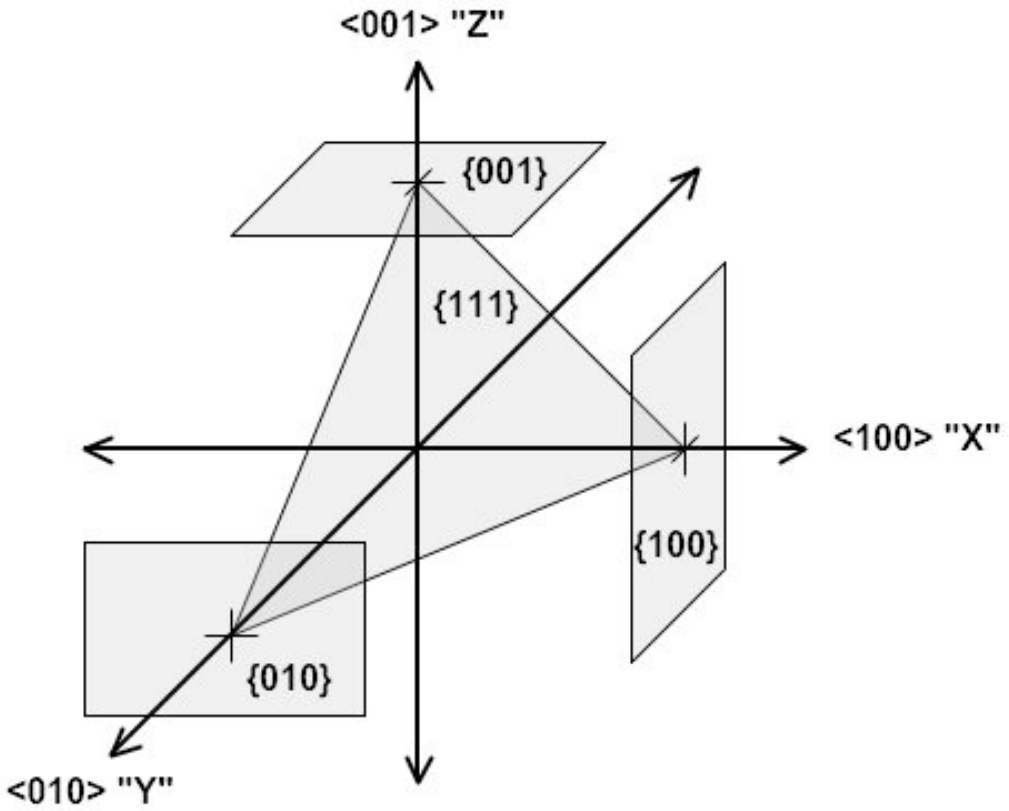

Figure A.2: Miller indices
The important planes for silicon are shown. The <100> directions are the XYZ axes for purposes of elasticity calculations.

In a crystal lattice with symmetry, certain directions are equivalent to one another. The silicon lattice has cubic symmetry, so directions and planes rotated 90° from each other are equivalent. Groups of equivalent directions or planes are called families. For example, in a cubic crystal, directions [100], [010], and [001] are the <100> family. Table A.1 lists the Miller indices notation. When referring to directions and angles within a crystal, the XYZ axes are aligned with the <100> directions.

Notation	Meaning
[*uvw*]	The direction vector given by *uvw*
<*uvw*>	The family of symmetric direction vectors equivalent to *uvw*
{*hkl*}	The crystal plane perpendicular to vector *hkl*
(*hkl*)	The family of planes equivalent to the plane perpendicular to vector *hkl*

Table A.1 Miller indices notation

A.2 Anisotropic Elasticity

Linear elasticity is the relationship between stress (σ) and strain (ε). Hooke's law describes this relationship in terms of compliance, S, or stiffness, C:

$$\sigma = C\varepsilon \text{ , and}$$
$$\varepsilon = S\sigma \text{ .} \qquad \text{(A-1)}$$

For isotropic cases, C is typically approximated by E. In a fully anisotropic material, there are four possible loads in each of three dimensions, and so a 4th rank tensor with $3^4 = 81$ terms is required to describe the elasticity (or any other anisotropic property). In this case, the elastic compliance/stiffness must be described with tensors, and Hooke's law is written with the subscripts which describe the orientation of the face and the vector, as in:

$$\sigma_{ij} = c_{ijkl}\varepsilon_{kl} \text{ , and}$$
$$\varepsilon_{ij} = s_{ijkl}\sigma_{kl} \text{ .} \qquad \text{(A-2)}$$

Fortunately, the combination of cubic symmetry and the equivalence of the shear conditions allows us to reduce the 4th rank tensor to a 2nd rank tensor with only 3 independent components. In addition, the four subscripts can be reduced to two, as given in Table A.2.

Face/Direction	Simplified Numeric Equivalent
xx or 11	1
yy or 22	2
zz or 33	3
yz or 23	4
xz or 31	5
xy or 12	6

Table A.2 Simplified subscripts for cubic symmetry*

The three independent components for cubic crystals are the 11, 12, and 44. The simplified tensor can be written as a 6×6 matrix:

* Many texts (such as [208]) use numbers instead of letters to indicate faces and directions, with X=1, Y=2, Z=3. The difference between this notation and the simplified equivalents must be inferred from context.

$$\begin{bmatrix}\sigma_1\\ \sigma_2\\ \sigma_3\\ \sigma_4\\ \sigma_5\\ \sigma_6\end{bmatrix} = \begin{bmatrix} c_{11} & c_{12} & c_{12} & 0 & 0 & 0\\ c_{12} & c_{11} & c_{12} & 0 & 0 & 0\\ c_{12} & c_{12} & c_{11} & 0 & 0 & 0\\ 0 & 0 & 0 & c_{44} & 0 & 0\\ 0 & 0 & 0 & 0 & c_{44} & 0\\ 0 & 0 & 0 & 0 & 0 & c_{44}\end{bmatrix}\begin{bmatrix}\varepsilon_1\\ \varepsilon_2\\ \varepsilon_3\\ \varepsilon_4\\ \varepsilon_5\\ \varepsilon_6\end{bmatrix} \text{ and}$$

$$\begin{bmatrix}\varepsilon_1\\ \varepsilon_2\\ \varepsilon_3\\ \varepsilon_4\\ \varepsilon_5\\ \varepsilon_6\end{bmatrix} = \begin{bmatrix} s_{11} & s_{12} & s_{12} & 0 & 0 & 0\\ s_{12} & s_{11} & s_{12} & 0 & 0 & 0\\ s_{12} & s_{12} & s_{11} & 0 & 0 & 0\\ 0 & 0 & 0 & s_{44} & 0 & 0\\ 0 & 0 & 0 & 0 & s_{44} & 0\\ 0 & 0 & 0 & 0 & 0 & s_{44}\end{bmatrix}\begin{bmatrix}\sigma_1\\ \sigma_2\\ \sigma_3\\ \sigma_4\\ \sigma_5\\ \sigma_6\end{bmatrix}. \qquad \text{(A-3)}$$

This matrix representation is given with respect to the XYZ axes (the <100> directions in a crystal). Stress and strain relationships can be calculated from this matrix for directions aligned with the XYZ axes using normal matrix operations (i.e., solving the simultaneous equations relating σ and ε). However, in order to calculate the stress/strain relationships in an arbitrary direction, the tensor must be rotated, which cannot be done using the matrix representation. See [208] for tensor transformations or [209, 210] for [relatively] simplified formulas for calculating rotated elasticity components. Once the tensor is rotated, the simplified 6×6 matrix can be written again with new components. Shortcut formulas exist for calculating the elastic properties in arbitrary directions for cubic symmetry, as discussed in Section A.5.

Finally, we can now ask, what are the elastic constants for silicon? Silicon is a very important economic material and it has been studied carefully. The resulting best values for the elastic constants are given in Table A.3.

C: 10^9 Pa S: 10^{-12} Pa	C_{11}	C_{12}	C_{44}	S_{11}	S_{12}	S_{44}
Silicon	165.7	63.9	79.6	7.68	-2.14	12.6

Table A.3 Elastic Constants of Silicon
Values for 298 K
References: [206, 209, 211-213]

Figure A.3 reproduces some plots from [209] showing the variation of Young's modulus and Poisson's ratio in the (100) plane.

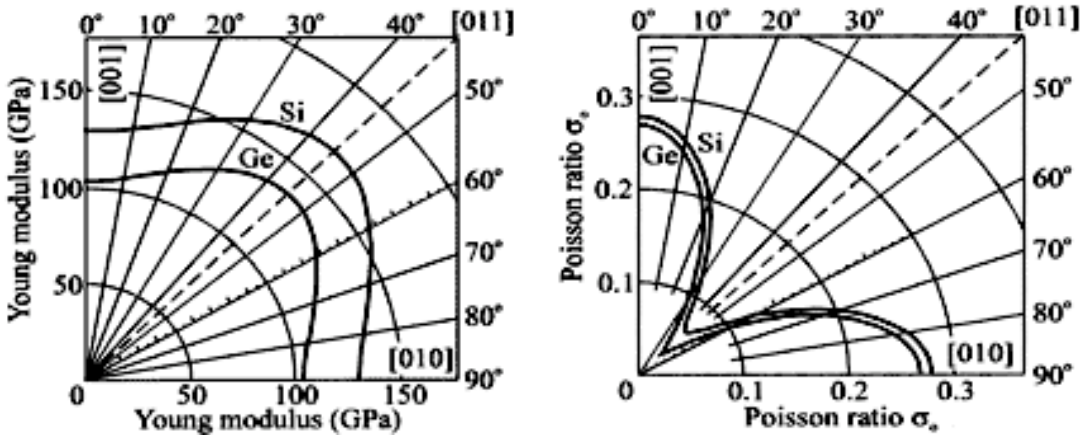

a) Young's modulus b) Poisson's ratio

Figure A.3: The variation of Young's modulus and Poisson's ratio in silicon and germanium
Values are for the (100), calculated using the constants in Table A.3. From [209].

A.3 Orthotropic Elasticity

We arrived at the matrix representation of the anisotropic elasticity tensor in (A-3) by simplifying the complete anisotropic 4th rank elasticity tensor. Because silicon has cubic symmetry, it is also possible to give the elastic properties in terms of *orthotropic* material constants. An orthotropic material is one which has at least two orthogonal planes of symmetry, and silicon, with cubic symmetry, can be described this way. Orthotropic elasticity is described with a matrix that looks quite similar to (A-3), except that the values for each entry are derived from the "fundamental" elasticity quantities of Young's modulus (E), Poisson's ratio (ν), and the shear modulus (G) in the axes of interest (x, y, z):

$$\begin{bmatrix}\sigma_{xx}\\ \sigma_{yy}\\ \sigma_{zz}\\ \sigma_{yz}\\ \sigma_{zx}\\ \sigma_{xy}\end{bmatrix} = \begin{bmatrix} \frac{1-\nu_{yz}\nu_{zy}}{E_yE_z\Delta} & \frac{\nu_{yx}-\nu_{yz}\nu_{zy}}{E_yE_z\Delta} & \frac{\nu_{zx}-\nu_{yx}\nu_{zy}}{E_yE_z\Delta} & 0 & 0 & 0 \\ \frac{\nu_{xy}-\nu_{xz}\nu_{zy}}{E_zE_x\Delta} & \frac{1-\nu_{zx}\nu_{xz}}{E_zE_x\Delta} & \frac{\nu_{zy}-\nu_{zx}\nu_{xy}}{E_zE_x\Delta} & 0 & 0 & 0 \\ \frac{\nu_{xz}-\nu_{xy}\nu_{yz}}{E_xE_y\Delta} & \frac{\nu_{yz}-\nu_{xz}\nu_{yx}}{E_xE_y\Delta} & \frac{1-\nu_{xy}\nu_{yx}}{E_xE_y\Delta} & 0 & 0 & 0 \\ 0 & 0 & 0 & G_{yz} & 0 & 0 \\ 0 & 0 & 0 & 0 & G_{zx} & 0 \\ 0 & 0 & 0 & 0 & 0 & G_{xy} \end{bmatrix} \begin{bmatrix}\varepsilon_{xx}\\ \varepsilon_{yy}\\ \varepsilon_{zz}\\ \varepsilon_{yz}\\ \varepsilon_{zx}\\ \varepsilon_{xy}\end{bmatrix},$$

where

$$\Delta = \frac{1-\nu_{xy}\nu_{yx}-\nu_{yz}\nu_{zy}-\nu_{zx}\nu_{xz}-2\nu_{xy}\nu_{yz}\nu_{zx}}{E_xE_yE_z}, \text{ and}$$

$$\begin{bmatrix}\varepsilon_{xx}\\ \varepsilon_{yy}\\ \varepsilon_{zz}\\ \varepsilon_{yz}\\ \varepsilon_{zx}\\ \varepsilon_{xy}\end{bmatrix} = \begin{bmatrix} \frac{1}{E_x} & -\frac{\nu_{yx}}{E_y} & -\frac{\nu_{zx}}{E_z} & 0 & 0 & 0 \\ -\frac{\nu_{xy}}{E_x} & \frac{1}{E_y} & -\frac{\nu_{zy}}{E_z} & 0 & 0 & 0 \\ -\frac{\nu_{xz}}{E_x} & -\frac{\nu_{yz}}{E_y} & \frac{1}{E_z} & 0 & 0 & 0 \\ 0 & 0 & 0 & \frac{1}{G_{yz}} & 0 & 0 \\ 0 & 0 & 0 & 0 & \frac{1}{G_{zx}} & 0 \\ 0 & 0 & 0 & 0 & 0 & \frac{1}{G_{xy}} \end{bmatrix} \begin{bmatrix}\sigma_{xx}\\ \sigma_{yy}\\ \sigma_{zz}\\ \sigma_{yz}\\ \sigma_{zx}\\ \sigma_{xy}\end{bmatrix} \quad \text{(A-4)}$$

The advantage of the orthotropic description is that the values can be used without a lot of tedious discussion of crystal orientation and tensor rotation; the elastic quantities for the orientation of interest are simply given, and the stress/strain relationships of interest can be calculated from the matrix. Of course, the orthotropic matrix cannot be rotated arbitrarily, but often that is not required. The elasticity quantities for a given orientation can be derived from the full anisotropic expressions using the expressions given in Section A.5. For example, the equivalent orthotropic stiffness matrix for silicon with three axes at [100], [010], and [001] is (for example [214]):

$E_{11} = E_{22} = E_{33}$ = 130 *GPa*,
$\nu_{12} = \nu_{23} = \nu_{31}$ = 0.28,
$G_{12} = G_{13} = G_{23}$ =79.6 *GPa*,

$$\begin{bmatrix}\sigma_1\\ \sigma_2\\ \sigma_3\\ \sigma_4\\ \sigma_5\\ \sigma_6\end{bmatrix} = \begin{bmatrix}165.7 & 63.9 & 63.9 & 0 & 0 & 0\\ 63.9 & 165.7 & 63.9 & 0 & 0 & 0\\ 63.9 & 63.9 & 165.7 & 0 & 0 & 0\\ 0 & 0 & 0 & 79.6 & 0 & 0\\ 0 & 0 & 0 & 0 & 79.6 & 0\\ 0 & 0 & 0 & 0 & 0 & 79.6\end{bmatrix}\begin{bmatrix}\varepsilon_1\\ \varepsilon_2\\ \varepsilon_3\\ \varepsilon_4\\ \varepsilon_5\\ \varepsilon_6\end{bmatrix} \qquad \text{(A-5)}$$

This is, of course, identical to (A-3) with the constants from Table A.3.

The most common use of the orthotropic expressions for silicon is to provide the elasticity in the frame of reference of a standard silicon wafer (see Section A.4), which is [110], [1$\bar{1}$0], and [100] (see Section A.4):

$$\begin{bmatrix}\sigma_1\\ \sigma_2\\ \sigma_3\\ \sigma_4\\ \sigma_5\\ \sigma_6\end{bmatrix} = \begin{bmatrix}194.4 & 35.2 & 63.9 & 0 & 0 & 0\\ 35.2 & 194.4 & 63.9 & 0 & 0 & 0\\ 63.9 & 63.9 & 165.7 & 0 & 0 & 0\\ 0 & 0 & 0 & 79.6 & 0 & 0\\ 0 & 0 & 0 & 0 & 79.6 & 0\\ 0 & 0 & 0 & 0 & 0 & 50.9\end{bmatrix}\begin{bmatrix}\varepsilon_1\\ \varepsilon_2\\ \varepsilon_3\\ \varepsilon_4\\ \varepsilon_5\\ \varepsilon_6\end{bmatrix} \text{ (in GPa).} \qquad \text{(A-6)}$$

When "orthotropic silicon" properties are used, it is essential to know what reference axes are used for the matrix. In general, use of the anisotropic matrix of (A-3) and the expressions given in Section A.5 is preferred, as the direction must be stated explicitly, so there is less chance for confusion. Moreover, the generalized shortcut formulas in Section A.5 are not applicable to the values in an orthotropic matrix.

A.4 Crystal Orientation of a Silicon Wafer

The crystal orientation of the silicon in a silicon wafer has significant effects on the electronic and IC fabrication properties of the wafer and so the crystal orientation is an important part of the wafer specification. The crystal orientation is specified in two ways. First, the orientation of the plane of the surface of the wafer is

given, for example, a “n-type (100) wafer” has the top wafer surface oriented in the (100) plane of the silicon crystal. The second part of the orientation information is given by the wafer primary flat. For the most commonly encountered wafers (p- and n-type (100) and (111) wafers), the primary flat is aligned with the [110] direction.

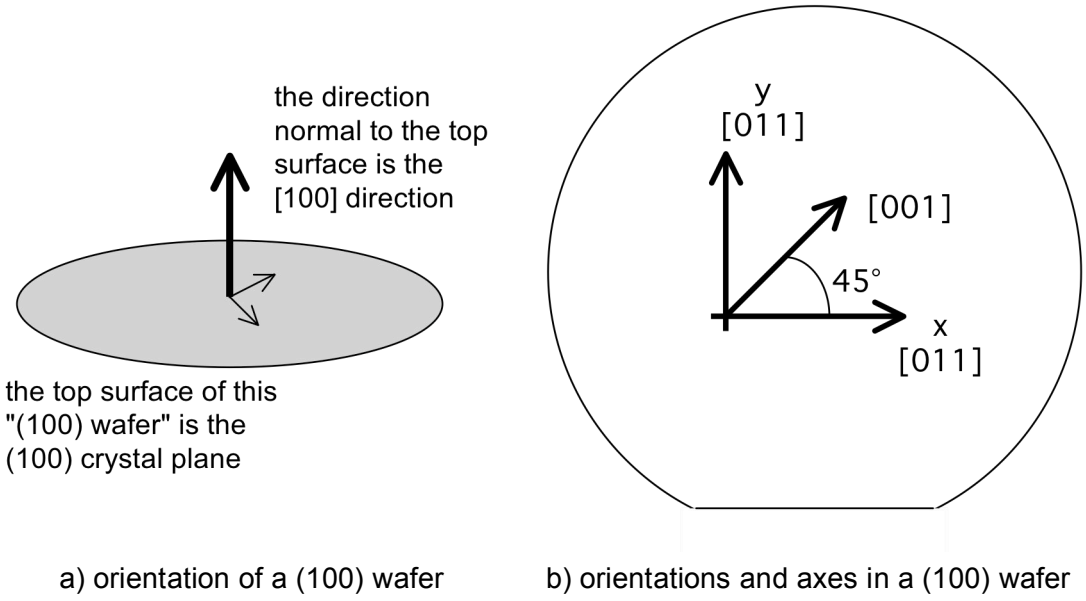

Figure A.4: Crystal orientation in silicon wafers
The (100) wafers are most common, as they are preferred for CMOS manufacture.

Most MEMS designs are drawn using a computer-based layout editor with an X-Y coordinate space and the layout is aligned with the axes in a left-right, up-down fashion. Most microfabrication tools use the primary flat of the wafer to orient the wafer for processing, and the conventional orientation is flat “down”, i.e., parallel to the floor when the wafer is held up vertically for examination, or toward the operator when inserted horizontally into processing equipment. This means that in the most common case of fabrication of a MEMS device, i.e., design aligned to the X-Y axes on a standard (100) silicon wafer, the X and Y axes of the design will be aligned with the <110> silicon crystal directions, as shown in Figure A.4. The Young’s modulus and Poisson’s ratio plots given in Figure A.3 apply to this situation. The example design in Appendix B is oriented this way.

A.5 The Elasticity Values of Silicon

The appropriate Young's modulus value for silicon depends on the crystal orientation of the structure and the type of loads that will be encountered. The book Roark's Formulas for Stress and Strain [104] is an excellent source for the equations of mechanical deformation in different structures which use the elasticity values described here.

Axial tension/compression

Use the appropriate E value for the direction of tension/compression. E can be calculated from the tensor in (A-3), or by using the simplified formula for cubic crystals [208]:

$$\frac{1}{E_{\alpha\beta\gamma}} = S_{11} - 2\left[\left(S_{11} - S_{12}\right) - \frac{1}{2}S_{44}\right]\left(l^2m^2 + m^2n^2 + l^2n^2\right). \qquad \text{(A-7)}$$

The terms l,m,n are "direction cosines": the cosine of the angle between the direction of interest ($\alpha\beta\gamma$) and X,Y,Z axes (the <100> directions). The most common cases simplify as:

$$\begin{aligned}
\frac{1}{E_{100}} &= S_{11}, \\
\frac{1}{E_{110}} &= S_{11} - \frac{1}{2}\left[\left(S_{11} - S_{12}\right) - \frac{1}{2}S_{44}\right], \\
\frac{1}{E_{111}} &= S_{11} - \frac{2}{3}\left[\left(S_{11} - S_{12}\right) - \frac{1}{2}S_{44}\right].
\end{aligned} \qquad \text{(A-8)}$$

For example, in a (100) silicon wafer:

- for "x or y axis" direction (parallel/perpendicular to flat), use E_{110} = 169 GPa
- for "off-axis" direction (45° diagonal to flat), use E_{100} = 130 GPa

Small deflection of a long, thin beam

This is basically axial tension and compression, so use the $E_{\alpha\beta\gamma}$ value for the direction of the neutral axis, as given above. Small deflection of a beam is defined as deflection less than 10% of the length of the beam. A beam should have length, L, greater than five times its width, w [215, 216]. For $L < 5w$, use the plate expressions

(below). The thickness of a beam should be small compared to the length; if the deflection criteria is satisfied then the thickness is usually as well.

Small deflection of a plate

For deflection of a plate structure (as opposed to a cantilever beam), use a "plate modulus" for the major axis of bending. The plate modulus is:

$$E'_{hkl} = \frac{E_{hkl}}{1 - \nu_{\alpha\beta}} \ . \tag{A-9}$$

Where $\nu_{\alpha\beta}$ is Poisson's ratio, the ratio of strain between two orthogonal directions α and β. Poisson's ratio can be computed for arbitrary directions in a cubic crystal with a relation similar to Equation (A-7) [212]:

$$\nu_{\alpha\beta} = \frac{s_{12} + \left(s_{11} - s_{12} - \frac{1}{2}s_{44}\right)\left(l_\alpha{}^2 l_\beta{}^2 + m_\alpha{}^2 m_\beta{}^2 + n_\alpha{}^2 n_\beta{}^2\right)}{s_{11} - 2\left(s_{11} - s_{12} - \frac{1}{2}s_{44}\right)\left(l_\alpha{}^2 m_\alpha{}^2 + m_\alpha{}^2 n_\alpha{}^2 + l_\alpha{}^2 n_\alpha{}^2\right)}. \tag{A-10}$$

Possion's ratio for silicon in the <110> direction in the (100) plane is 0.064, and it can be as high as 0.28 (see Figure A.3). The distinction between a plate and a beam is discussed above. The "I know it when I see it" rule is usually sufficient. For the (100) and (111) planes, the plate modulus is equivalent to the Biaxial modulus (below).

Thin film stress/strain calculations for a thin film membrane or bending substrate (incl. Stoney's equation calculations)

Some membranes have symmetric boundary conditions along more than one axis, such as a circular diaphragm or a free-standing wafer. Deformations of these structures can be computed using the symmetric Biaxial modulus B_{ijk} for the appropriate symmetric crystal plane, either (100) or (111). The (110) plane is not symmetric. The biaxial moduli are given by [217]:

$$B_{100} = C_{11} + C_{12} - \frac{2C_{12}^{\,2}}{C_{11}}\ ,$$
$$B_{111} = \frac{6C_{44}\left(C_{11} + 2C_{12}\right)}{C_{11} + 2C_{12} + 4C_{44}}\ . \qquad \text{(A-11)}$$

For silicon, B_{100} = 179 GPa. For the symmetric planes, the Biaxial modulus is equivalent to the plate modulus (A-9).

Stress concentration calculations or multi-directional polycrystalline situations

Use a Voigt or Reuss volume average for stress concentration calculations or estimates for multi-directional polycrystalline structures [218]. The Voigt average modulus, E_V (isostrain assumption), and Reuss average modulus, E_R (isostress assumption), values will give upper and lower theoretical bounds on the true value. For a cubic crystal, these values can be calculated as [219]:

$$E_V = \frac{\left(C_{11} - C_{12} + 3C_{44}\right)\left(C_{11} + 2C_{12}\right)}{2C_{11} + 3C_{12} + C_{44}}\ \text{, and}$$
$$E_R = \frac{5}{3S_{11} + 2S_{12} + S_{44}}\ . \qquad \text{(A-12)}$$

For silicon, E_V = 172 GPa and E_R = 164 GPa. Note that a volume average is what we would expect to measure with a nanoindentation test.

Hydrostatic loads

For calculating volume change due to hydrostatic (uniform pressure) loads, use the Bulk modulus, B, which for cubic crystals is given by [220]:

$$B = \frac{C_{11} + 2C_{12}}{3}\ . \qquad \text{(A-13)}$$

For silicon, B = 97.83 GPa. The symbol for Bulk modulus, B, should not be confused with the symbol for Biaxial modulus, B_{ijk}.

Shear Modulus

The shear modulus, G, (sometimes called "Rigidity modulus"), is a relationship between stress and strain in two orthogonal directions. This value is often used for estimating twisting under torque or shear loads. In an anisotropic crystal,

$$G_{ij} = \frac{1}{s_{ijij}} \,. \tag{A-14}$$

Expanded expressions for G in a cubic crystal are given in [209, 210, 221, 222]. The value of G is 79.6 GPa between the [100] direction and any other direction in the (100) plane. G is approximately 50 GPa between the [110] direction in the (100) plane (i.e., twisting a beam that lies in the plane of a wafer).

Doped Silicon

Most silicon wafers are not pure silicon; a certain amount of chemical impurities are usually added to control the wafer's electrical properties. This is called "doping". The effect of doping on crystalline elastic behavior can be predicted from the strain energy of the crystal [223]. The changes are negligible, typically 1-5%, and are usually ignored for engineering calculations [224, 225].

Finite Element Simulations

The detailed calculation of anisotropic elasticity can be tedious and the problem is well suited to solving by computer. However, it is important to note that most Finite Element Method (FEM) computer programs, including COMSOL and ANSYS, do not use the anisotropic elasticity formulas by default (this is intended to reduce the computation complexity for situations where the anisotropy is not important). Moreover, the "anisotropic" setting typically requires the user to enter the elastic constants from Table A.3.

A.6 Temperature Effects on Elasticity

The Young's modulus of silicon changes with temperature; this is called the temperature coefficient of Young's modulus (TCE). However, as with E, the temperature behavior of elasticity is more properly described by the temperature coefficients of the individual components of the elasticity tensor: Tc_{11}, Ts_{12}, etc. Several different values for these quantities are reported in the literature, and so the answer cannot be given definitively. However, the value of silicon TCE for axial loading situations is identical in all crystal orientations, and equal to approximately

-60 ppm/°C near room temperature. In this work, a value of -63.7 ppm/°C is used, following the values given by Bourgeois, et al.,[130], because those values agree most closely with recent experimental results (see Chapter 3), including those described in this work. The results from [130] are reproduced in Table A.4. Note that the temperature coefficients are not simple linear quantities. Using the results from Bourgeois, the TCE of silicon is about -64 ppm/°C at room temperature (25 °C), and -75 ppm/°C at 125 °C.

Elastic Constant Temp. Coeff.	p-type (4 Ω-cm, B)	n-type (0.05 Ω-cm, Ph)
	First order $\times 10^{-6}$/°C	
Ts_{11}	64.73 ± 0.29	63.60 ± 0.60
Ts_{12}	51.48 ± 1.5	45.79 ± 2.8
Ts_{44}	60.14 ± 0.20	57.96 ± 0.17
Tc_{11}	-73.25 ± 0.49	-74.87 ± 0.99
Tc_{12}	-91.59 ± 1.5	-99.46 ± 3.5
Tc_{44}	-60.14 ± 0.20	-57.96 ± 0.17
	Second order $\times 10^{-9}$/°C^2	
Ts_{11}	61.19 ± 1.1	60.51 ± 0.35
Ts_{12}	72.26 ± 5.1	75.70 ± 6.1
Ts_{44}	54.90 ± 1.7	57.31 ± 1.4
Tc_{11}	-49.26 ± 4.8	-45.14 ± 1.4
Tc_{12}	-32.70 ± 10.1	-20.59 ± 11.0
Tc_{44}	-51.28 ± 1.9	-53.95 ± 1.8

Table A.4 Temperature Coefficients of the Elastic Constants From [130].

Additional references for the silicon temperature coefficient of elasticity are: [27, 125, 130, 132, 133, 137, 163, 213, 226-228].

A.7 Summary

The appropriate Young's modulus values for silicon for a few common load cases are summarized in Table A.5.

Load Case	Appropriate Silicon *E* value
Axial or narrow beam bending loads <110> direction ("x or y axis") <100> direction ("45° off axis") Temperature Coefficient of *E*	 169 GPa 130 GPa -64 ppm/°C
Plate bending, ν = 0.064 for <110> in (100)	179 GPa
Thin film stress/strain, (100) plane	179 GPa
Shear load, twisting "x or y" <110> beam (***G***)	50 GPa
Stress concentrations	164 – 172 GPa
Hydrostatic loads	97.8 GPa

Table A.5 Young's modulus values for silicon

There are occasional cases where we need an "average" value for elastic properties, regardless of direction and crystal orientation. In these cases, the appropriate average values are based on Reuss/Voigt formulas, as discussed above. For average values, use E=168 GPa, ν=0.22, and G=66.5 GPa [220].

A.8 MATLAB Code for Elasticity Matrix Transformation

A MATLAB [197] function for transforming the silicon stiffness tensor to an arbitrary direction is reproduced here.

```
function [E,Cr] = Tc_transform(theta1,theta2)
%TC_TRANSFORM    Elasticity tensor rotation
% [E,Cr] = TC_TRANSFORM(THETA1,THETA2)
%
% TC_TRANSFORM rotates the stiffness tensor for silicon by THETA1 and
%  THETA2 around the z and y axis respectively and returns the Young's
%  Modulus value in the resulting x' direction.
% THETA1, THETA2 are in radians.
%
%
% M.A. Hopcroft
%  hopcroft at mems dot stanford dot edu
%

% Tensor rotation code taken from the script "Yangle.m". Comments fron Yangle.m:
```

```
%
% Author: Ville Kaajakari
% Date: 2.4.2003
% A Matlab script to calculate silicon Young's modulus and Poisson's ration in
% any crystal direction. For explanation please see the companion tutorial
% at http://www.kaajakari.net/~ville/research/tutorials/elasticity_tutorial.pdf
%
% You may modify this script to your own use and you may distribute this script
% unmodified.
%


% the 3 independent components of the stiffness tensor
%  in units of 10e9 Pa (values from Wortman and Evans, 1965)
c1111=165.7;
c1122=63.9;
c2323=79.6;

% Non-zero components of Si stiffness tensor in [100] coordinates
Cc(1,1,1,1)=c1111;
Cc(2,2,2,2)=c1111;
Cc(3,3,3,3)=c1111;

Cc(1,1,2,2)=c1122;
Cc(1,1,3,3)=c1122;
Cc(2,2,1,1)=c1122;
Cc(2,2,3,3)=c1122;
Cc(3,3,1,1)=c1122;
Cc(3,3,2,2)=c1122;

Cc(1,3,1,3)=c2323;
Cc(3,1,1,3)=c2323;
Cc(1,3,3,1)=c2323;
Cc(3,1,3,1)=c2323;

Cc(2,3,2,3)=c2323;
Cc(3,2,2,3)=c2323;
Cc(2,3,3,2)=c2323;
Cc(3,2,3,2)=c2323;

Cc(1,2,1,2)=c2323;
Cc(2,1,1,2)=c2323;
Cc(1,2,2,1)=c2323;
Cc(2,1,2,1)=c2323;


%%%% handle input arguments - set defaults

% default no rotation
if nargin < 2
    theta2 = 0;
end
% default
if nargin < 1
    theta1 = 0;
end


%%%%
```

```
% rotate to an arbitrary plane
% first rotation
[c1,Cc1]=trotate('z',theta1,Cc);
% second rotation
[Cr,Crot]=trotate('y',theta2,Cc1);


% By definitions
S=inv(Cr);
E=1/S(1,1);
v_angle1=-S(1,2)/S(1,1); % Between two (100)'-plane vectors
v_angle2=-S(1,3)/S(1,1); % Between (100)'-plane vector and [001]'-vector


% optional print result
fprintf('\n');
fprintf(1,'E: %.1f GPa\n',E);
fprintf(1,'Rotated Simplified Stiffness Tensor C (GPa):\n');
fprintf(1,'%.1f\t%.1f\t%.1f\t%.1f\t%.1f\t%.1f\n',Cr)
fprintf('\n');


%%%%%%%%%%%%%%%%
% subroutines
%%%%%%%%%%%%%%%%

function [Cr, Crot]=trotate(ax,theta,tensor);
% ax is the axis about which to rotate
%disp(ax)

% Rotation matrix
Q=rmatrix(ax,theta);

%Calculate new stiffness tensor in rotated coordinates
Crot=zeros(3,3,3,3);
for i=1:3,
    for j=1:3,
        for k=1:3,
            for l=1:3,
                for p=1:3,
                    for q=1:3,
                        for r=1:3,
                            for s=1:3,

Crot(i,j,k,l)=Crot(i,j,k,l)+Q(p,i)*Q(q,j)*Q(r,k)*Q(s,l)*tensor(p,q,r,s);
                            end
                        end
                    end
                end
            end
        end
    end
end

Cr=[
    [Crot(1,1,1,1) Crot(1,1,2,2) Crot(1,1,3,3) Crot(1,1,2,3) Crot(1,1,1,3)
Crot(1,1,1,2)];
    [Crot(2,2,1,1) Crot(2,2,2,2) Crot(2,2,3,3) Crot(2,2,2,3) Crot(2,2,1,3)
Crot(2,2,1,2)];
```

```
    [Crot(3,3,1,1) Crot(3,3,2,2) Crot(3,3,3,3) Crot(3,3,2,3) Crot(3,3,1,3)
Crot(3,3,1,2)];
    [Crot(3,2,1,1) Crot(3,2,2,2) Crot(3,2,3,3) Crot(2,3,2,3) Crot(2,3,1,2)
Crot(2,3,1,2)];
    [Crot(3,1,1,1) Crot(3,1,2,2) Crot(3,1,3,3) Crot(3,1,2,3) Crot(1,3,1,3)
Crot(3,1,1,2)];
    [Crot(2,1,1,1) Crot(2,1,2,2) Crot(2,1,3,3) Crot(2,1,2,3) Crot(2,1,1,3)
Crot(1,2,1,2)];
];

% fprintf(1,'%.1f\t%.1f\t%.1f\t%.1f\t%.1f\t%.1f\n',Cr)
%
% fprintf(1,'\n\n')
return


function Qm=rmatrix(ax,theta)
% determine the rotation matrix
%  http://mathworld.wolfram.com/RotationMatrix.html
%disp('rmatrix called')
if isequal(ax,'x') | isequal(ax,'X') | isequal(ax,'i')
    Qm=[1 0 0; 0 cos(theta) sin(theta); 0 -sin(theta) cos(theta)];
    %disp(ax)
elseif isequal(ax,'y') | isequal(ax,'Y') | isequal(ax,'j')
    Qm=[cos(theta) 0 -sin(theta); 0 1 0; sin(theta) 0 cos(theta)];
    %disp(ax)
elseif isequal(ax,'z') | isequal(ax,'Z') | isequal(ax,'k')
    Qm=[cos(theta) sin(theta) 0; -sin(theta) cos(theta) 0; 0 0 1];
    %disp(ax)
    %disp(Qm)
else
    disp('rmatrix error!')
end
return
```

Chaos is inherent in all compounded things. Strive on with diligence.
-The Buddha Siddhārtha Gautama

B. Epi-seal Fabrication User Manual

This appendix describes the epi-seal microfabrication process [14] with a goal of illuminating the issues relevant for a designer of devices in this process (a "user" of the process). This is not a Runsheet or a Design Rules document; this is a high-level explanation of the process for the user, a "User Manual". This document uses terms specific to silicon MEMS microfabrication. For a general background in MEMS fabrication, refer to Stanford course sequence E240/E341/E342, or [99]. This manual focuses on the epi-seal process, but the oxide-seal process [17, 59] is sufficiently similar that oxide-seal users can benefit from this manual as well.

B.1 Epi-seal Development History

The development of the oxide-seal and epi-seal fabrication processes has been subject of ongoing development work since 2001. The development cycle consists of "fab runs", which typically last from 3 to 8 months, including design, fabrication, and test. Each run is given a name. The Bosch Corporation[*] and Stanford University collaborated to produce preliminary results with the first three runs. These results were instrumental in securing funding from DARPA for further development in 2003 as

[*] The original concept for epi-seal was proposed by Markus Lutz of Bosch RTC [229].

part of the HERMIT program[**]. The epi-seal technology is considered mature for silicon resonators, and further development is focused on expansions and alterations of the encapsulation processes to include new materials and types of devices. Table B.1 lists the silicon encapsulation fab runs that have occurred to date.

Table B.1: Encapsulation Fabrication Runs

Run Name	Technology	Date	Results
Round 1 (R1)	oxide-seal	Summer 2001	No working parts. Learn about epitaxial silicon deposition.
Round 2 (R2)	oxide-seal	Spring 2002	First working resonators. Learn about testing resonators.
Round 3 (R3)	epi-seal	Fall 2002	First epi-seal resonators. Testing procedures improved (PCB).
Miniacc	oxide-seal	Fall 2003	First-generation design issues identified for new encapsulated piezoresistive accelerometer designs. Low yield.
Hotdog I (HD1) / Round 4	epi-seal	Fall 2003	Capacitive resonators established. High-yield, high-performance resonators. The quote "98% yield fab process" comes from this run. Pressure calibration established. Gold standard resonator performance established. Both polysilicon and SCS wafers produced. BK measures HD1 parts for 1 year to establish world-record resonator long-term stability performance. SiTime, Inc. founded on basis of HD1 results.
Miniacc2	oxide-seal	Summer 2004	Good results for second-generation accelerometers. First-generation piezoresistive resonators.
Hotdog II (HD2) / Round 5	epi-seal	Fall 2004	SR (ovenized) designs fabricated. Equipment problems cause significant yield issues. Approx. 60% yield on two wafers (one each polysilicon and SCS devices).
Hotdog III (HD3)	epi-seal	Spring 2005	Stress-compensated resonators demonstrated. Equipment problems cause significant yield issues. Approx. 30% yield on one wafer.

[**] DARPA Harsh Environment Robust Micromechanical Technology program (ONR N66001-03-1-8942) (http://www.darpa.gov/MTO/Programs/hermit/index.html)

Table B.1: Encapsulation Fabrication Runs			
Run Name	Technology	Date	Results
Green Tea I (GT1)	oxide-seal	Summer 2005	Resonators for piezoresistive sensing and heating, piezoresistive accelerometers. High yield on 8 wafers.
Green Tea Krispy Kreme (GTKK)	oxide-seal	Spring 2006	Re-work of some GT1 wafers to demonstrate feasibility of composite Si-SiO2 (Krispy Kreme) technology. Feasiblity established.
Hotdog IV (HD4)	epi-seal	Spring 2006	Designs for hermiticity investigations, crystal orientation, anchor damping. Equipment lessons from HD2 and HD3 are implemented. Equipment downtime caused significant fabrication delay. First wafers returned Spring 2007, testing ongoing.
Eclair I	epi-seal	Summer 2006	First-generation process for large-displacement inside epi-seal. Preliminary results promising.
Hotdog V (HD5)	epi-seal	Summer 2006	Designs for advanced ovenization, KK investigation. Good yield for two wafers. More wafers expected Spring 2007.
Slickshoes I	oxide-seal	Summer 2006	Investigation of alternative films for sealing (SiC). Decent resonator yield for one wafer to date; some epi-cap doping issues. Results ongoing.
Hotdog VI (HD6)	epi-seal	Spring/ Summer 2007	SR-SA/ST designs (ovenization), composite resonators (KK). Results ongoing.

B.2 Epi-seal Fabrication Process

The epi-seal process involves approximately 400 discrete fabrication steps. These steps are grouped by layout drawing layer and material deposition layer into "layers", listed in Table B.2. Each layer is described in terms of its design rules, fabrication challenges, and process steps. Figure B.1 is an overview of the process steps and the layers associated with each step. The following pages describe each layer with diagrams, photographs, and explanations of the process steps. The explanations and diagrams are given with reference to the design rules for Hotdog V. The details of each fab run are slightly different, so future design rules may differ from the explanations given here.

Table B.2: Encapsulation Design Layers			
Name (material layer)	Abbreviation (drawing layer)	GDS Layer #	dark/bright*
Alignment Marks 1	A1	33	bright
Buried Poly	BP	26	dark
Gasket	GA	9	bright
Definition	DF	10	bright
Differential Nitride	NT	13	dark
Contact Gasket	CG	55	dark
Vent	VT	12	bright
Alignment Marks 2	A2	34	bright
Insulation Trench	IT	42	bright
Contact Aluminum	CA	4	bright
Aluminum	AL	56	dark
Passivation Oxide	PO	50	bright
No longer used or unusual *The dark/bright drawing style reflects current practice. Epi-seal runs HD3 and earlier used EP (dark) instead of DF (bright) and CG bright/GDS 55 instead of CG dark/GDS 54. Oxide-seal runs have always used DF and CG bright/GDS 54.			

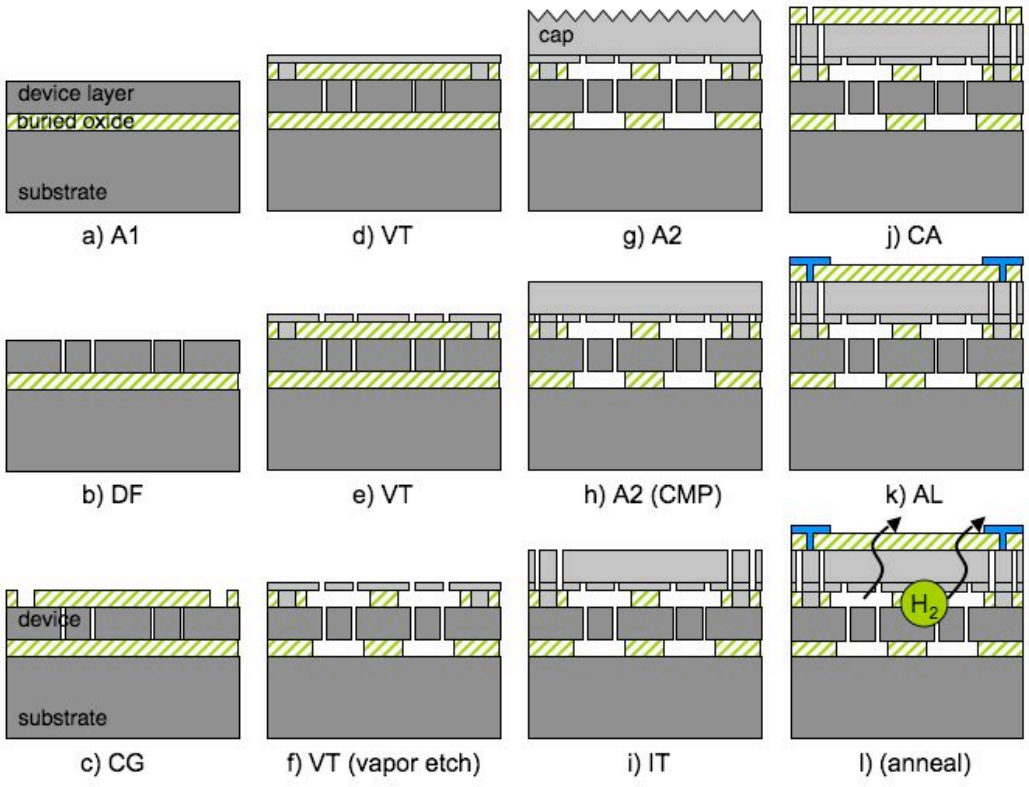

Figure B.1: Epi-seal fabrication steps and layers.

Starting Material and A1, BP, GA Layers

The processing begins with a silicon-on-oxide (SOI) wafer, which is a silicon wafer with layers of silicon dioxide and silicon on top of it (see figure below). The devices will be constructed from the top layer of silicon, the “SOI device layer”. The SOI buried oxide is a sacrificial material that will be etched away later in the process.

Normally, the SOI wafers are purchased with the top layers already present. However, it is possible to make custom SOI wafers ourselves in the fab, by growing oxide on a bare silicon wafer and then depositing silicon. This allows the designer to control where the sacrificial oxide is located (as opposed to being everywhere on the wafer). It also allows for precise control of the device layer thickness and resistivity. However, it increases fabrication time and complexity. When the custom SOI process is used, the buried oxide location is specified using the Gasket oxide (GA) drawing layer.

When the fab run uses standard SOIs, the GA drawing layer is not used, but the buried oxide layer is still referred to as the Gasket layer.

The Buried Polysilicon (BP) layer was used for custom SOIs made with *two* silicon device layers and *two* buried oxide layers. The BP layer was the lower silicon layer. This process has not worked well and BP has not been used since Round 3.

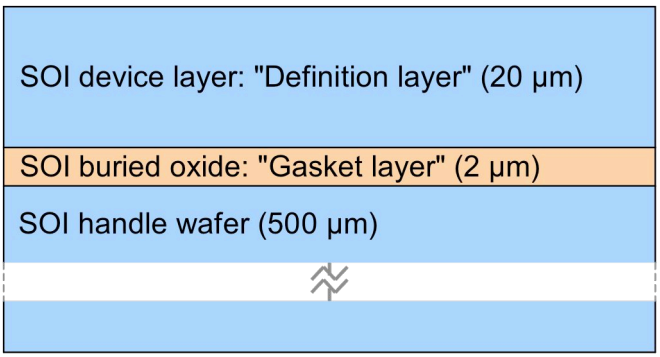

Schematic cross-section of a silicon-on-oxide (SOI) wafer. SOIs can be purchased with any combination of layer thicknesses. 20 µm is chosen for the device layer because it is the thickest layer that we can etch reliably in the DF etch step. The 2 µm buried oxide is chosen to be approximately the same thickness as the CG oxide, so that the two oxide layers will etch at the same rate.

Viewing a silicon wafer with a microscope in the fab.

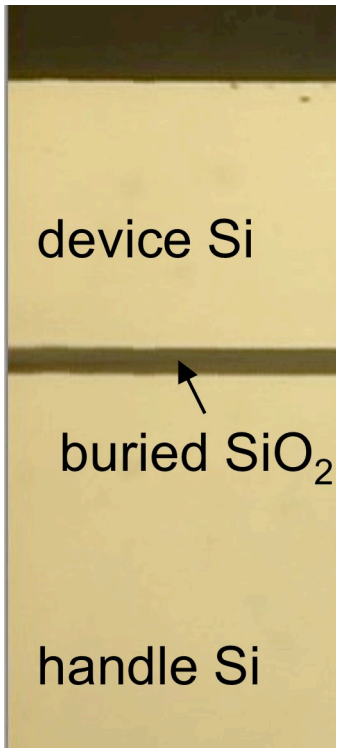

Optical microscope cross-section view of a standard SOI wafer. The buried oxide layer visible in the middle is 2 µm thick. The entire device layer is visible; only the top portion of the handle wafer is shown.

Starting Material and A1, BP, GA Layers

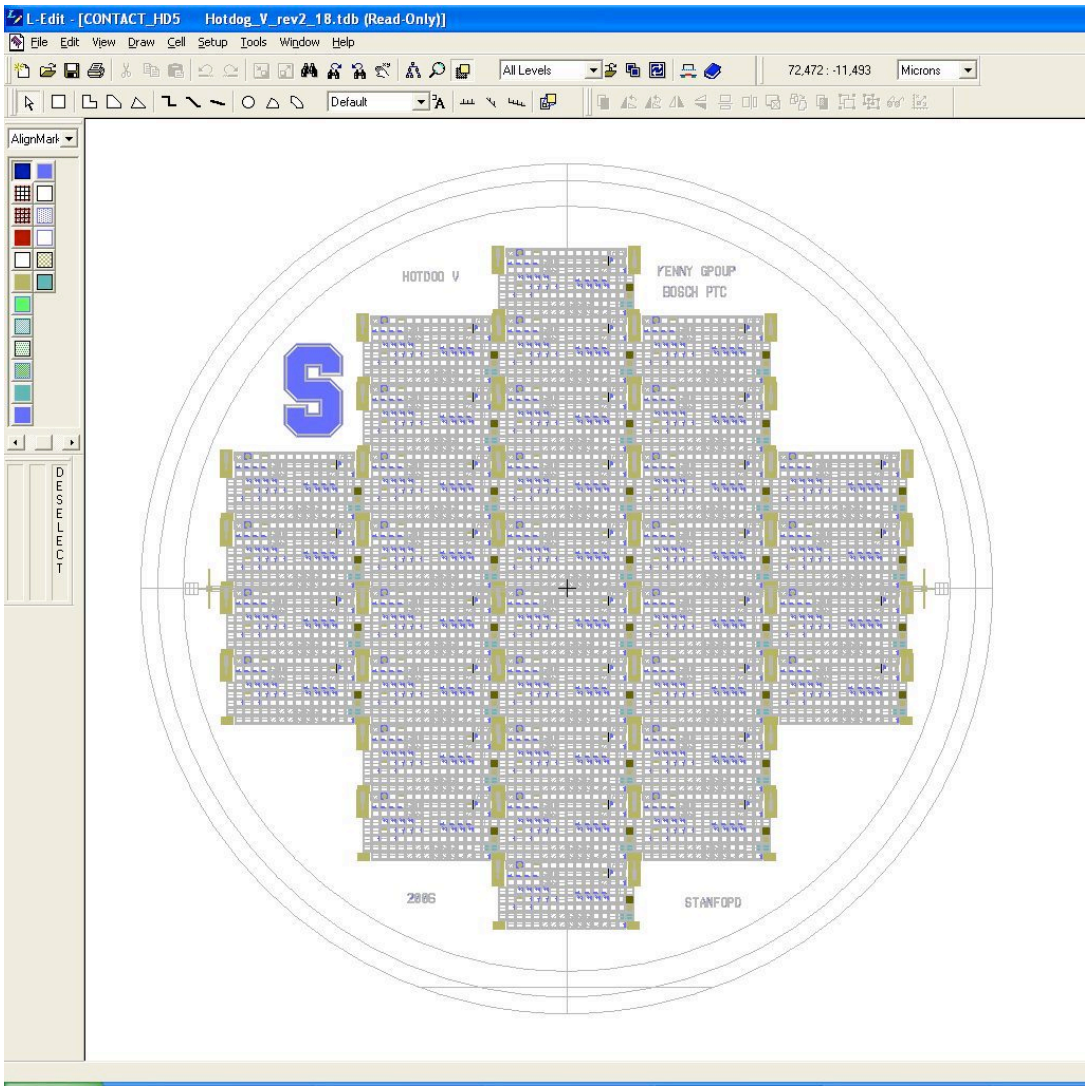

CAD layout file showing the final layout for the entire 4-inch (100 mm) silicon wafer. The wafer is divided into 34 rectangular exposure reticles. Each reticle is identical, and contains ~120 individual 1x1 mm design slots. These slots are divided among the users of a particular run.

The A1 alignment marks are in the brown rectangles at the edge of each reticle. The A1 alignment marks are the first features put onto a new wafer, and the reticles are aligned to the marks in subsequent processing steps.

Layer: Definition (DF)

The Definition (DF) drawing layer defines the shape of the structures that will be encapsulated. In the layout, this layer is where we draw the resonators, anchors, electrodes, etc.

The width of the DF trench is a key parameter for each fab run. The minimum trench width depends on the lithography and etch equipment capabilities. The CG layer deposition must be thick enough to seal the DF trench. The VT openings must be narrower than the DF trench. Typical trench widths are 1.0 – 1.5 µm.

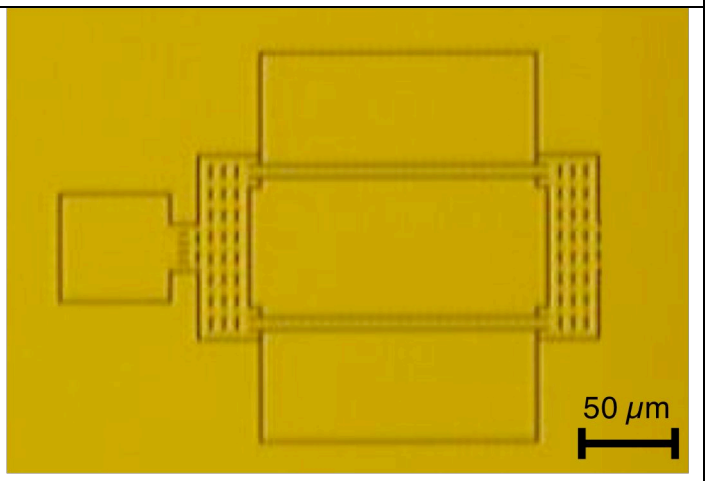

Optical microscope plan view of a 1.3 MHz SA-DETF resonator defined in SOI device layer by the DF etch.

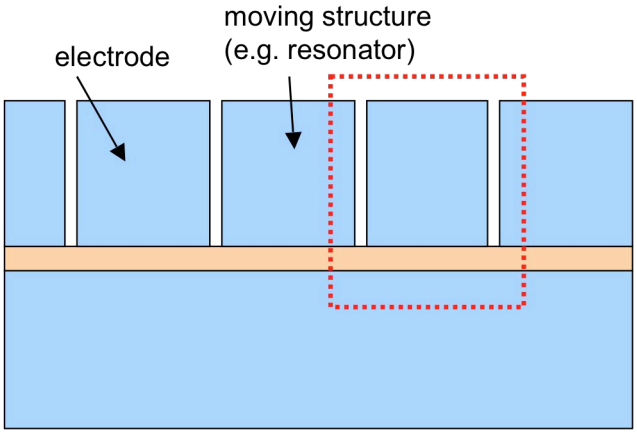

Schematic cross-section of DF etch in the SOI device layer. The ideal trench is a perfect rectangle with smooth vertical sidewalls.

The maximum width of a structure that will be released (meaning that the Gasket oxide will be etched away underneath) is an important parameter for each fab run. A resonator beam needs to be small enough to be released, but an anchor needs to be large enough that it will not be released.

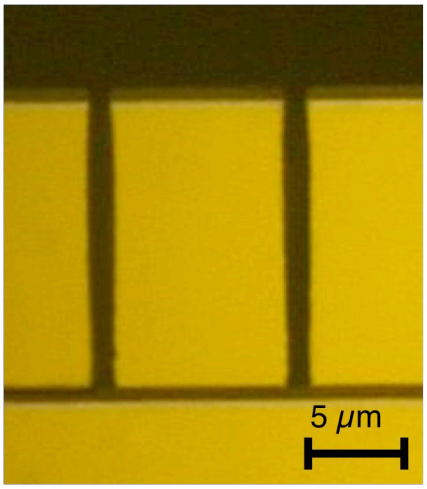

Optical microscope cross-section view of the DF trench etch. The etch stops at the buried oxide layer. The photoresist is visible on top of the wafer. The non-ideal shape of the etched trench is visible.

Layer: Definition (DF)

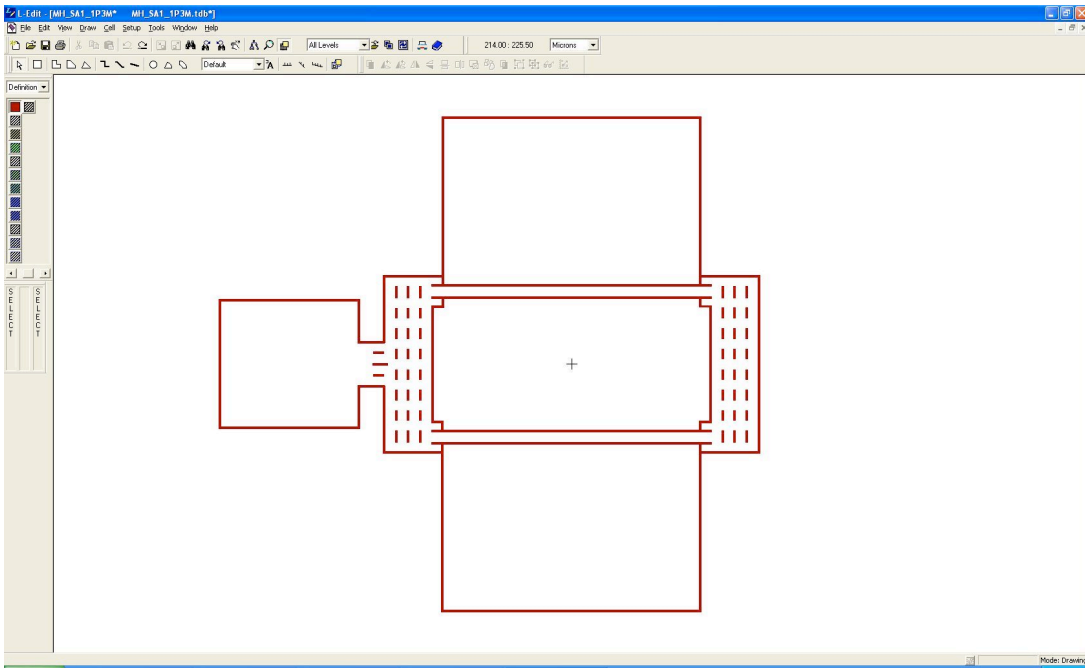

L-Edit layout file with only the Definition layer visible. The bright drawing style means that trenches will be etched where the lines are drawn. The small vertical lines are release holes to allow the Gasket oxide underneath the structure to be etched. This is how structures larger than the maximum width are released. Note that four-way intersections (crosses) are prohibited in the DF layer. This is because the opening at the center of a four-way intersection is larger than the width of the trench, and will not be sealed by the CG deposition. Three-way intersections and >90° corners are allowed.

Layer: Deferential Nitride (NT)

The Differential Nitride (NT) layer was proposed for stress compensated designs. It was a layer of silicon nitride on top of the device layer. It has not been used in fabrication to date.

Layer: Contact Gasket (CG)

The Contact Gasket oxide (CG) is the upper sacrificial material for the encapsulation. The Contact Gasket oxide is deposited on top of the wafer using the TEOS deposition process. The TEOS process is relatively high temperature (600 °C) and so it deposits a conformal layer that fills in the DF trenches. The CG drawing layer defines the openings in the Contact Gasket oxide for electrical contacts. It also defines the extent of the Contact Gasket oxide. The Contact Gasket oxide must cover the encapsulated silicon structures.

The thickness of the Contact Gasket oxide is determined by the maximum DF trench width:

$t_{CG} = w_{DF} \times \sqrt{2} \times 1.5 \approx 2w_{DF}$

This accounts for the larger trench width at 90° DF corners and the vertical/horizontal deposition ratio of the TEOS oxide (~1.5) [229].

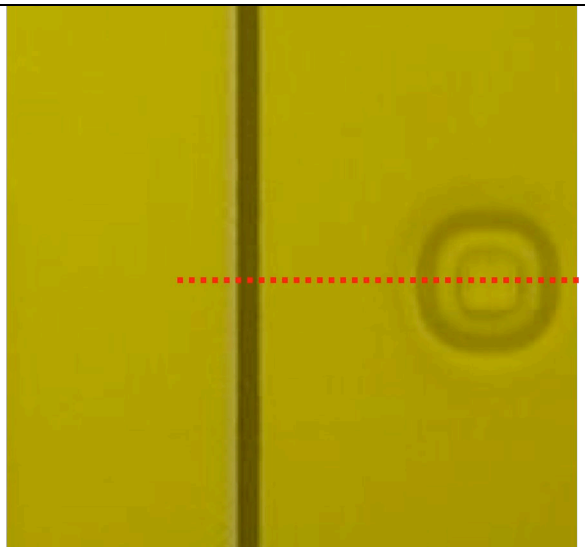

Optical microscope plan view of a contact opening in the CG layer (right side of image). The vertical line is a DF trench, visible through the CG oxide.

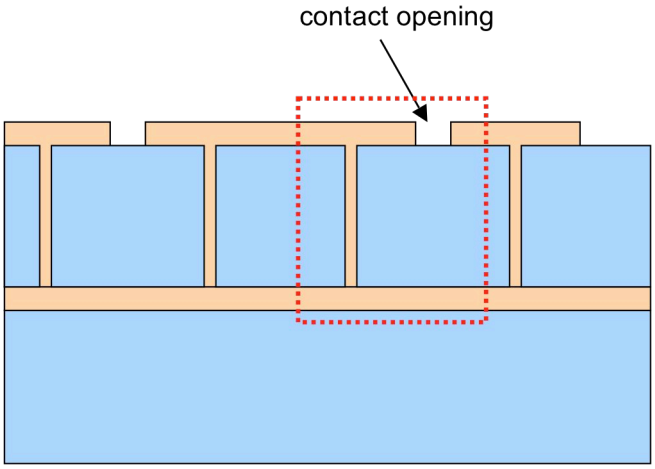

Schematic cross-section of CG oxide with contact openings etched in it. The oxide is shown as refilling the DF trench completely, but it actually leaves a keyhole opening in the middle of the trench (see cross-section image).

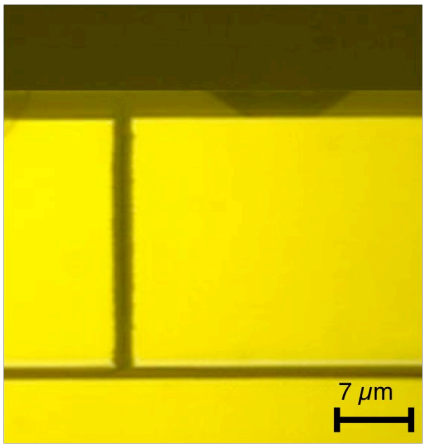

Optical microscope cross-section view of the CG layer with a contact opening and a refilled DF trench. Note the thin vertical gap (“keyhole”) in the oxide in the trench.

Layer: Contact Gasket (CG)

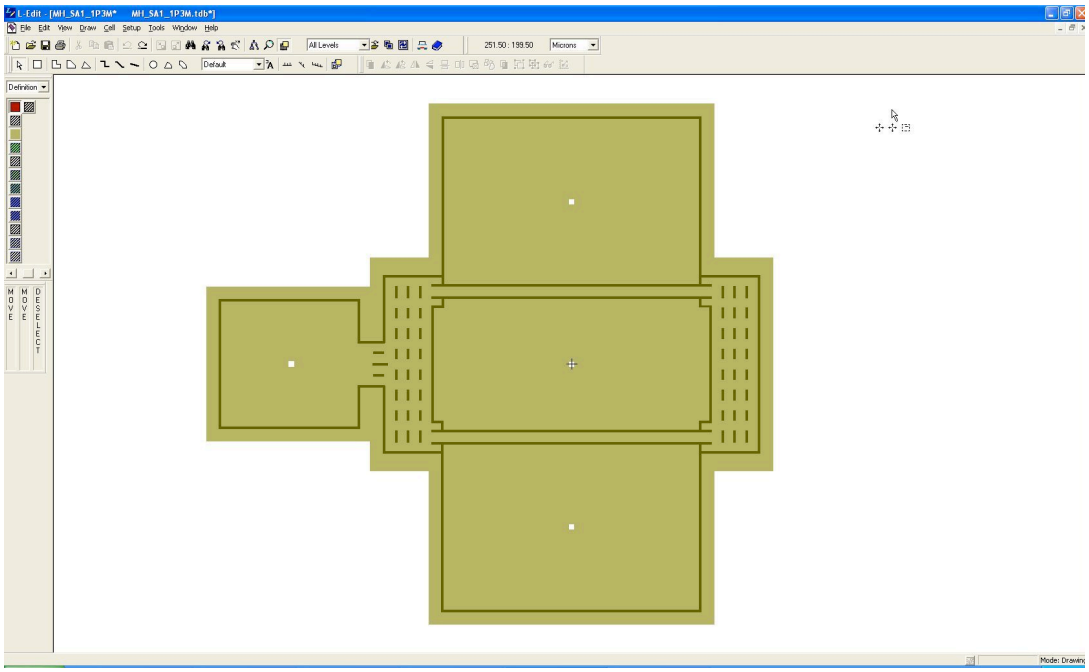

L-Edit layout file with the Definition and Contact Gasket layers visible. The CG drawing style is dark, so the oxide will remain where it is drawn. The CG (brown) must cover all of the DF trenches so that the resonator is isolated from the cap layer. The small openings in CG indicate where the electrical contacts will be. The oxide will be etched away in these openings and the silicon cap will be in contact with the silicon device layer.

Note that as of this writing, the upcoming Hotdog VI Design Rules are expected to use the opposite (bright) drawing style for CG, and to allow the Contact Gasket Oxide to cover the entire wafer instead of being limited to the area around the device. In this case, the figure above would have only small rectangles where the contacts are located.

Layer: Vent (VT)

The Vent layer (VT) is the first part of the silicon cap. The epitaxial silicon vent layer is deposited to cover the sacrificial Contact Gasket oxide. Then the vent openings ("vents") are etched through the silicon to allow the HF vapor to etch the oxide in the next step.

The vent openings need to be smaller than the minimum DF trench width because when the vents are sealed with silicon (IT layer), some silicon will deposit on the structures inside until the vents are closed.

Some fab runs have been using a thicker cap layer (up to 20 µm) in order to increase its mechanical strength. This is required for Krispy Kreme oxidation processes, where the oxidation will put stress on the cap and cause it to buckle.

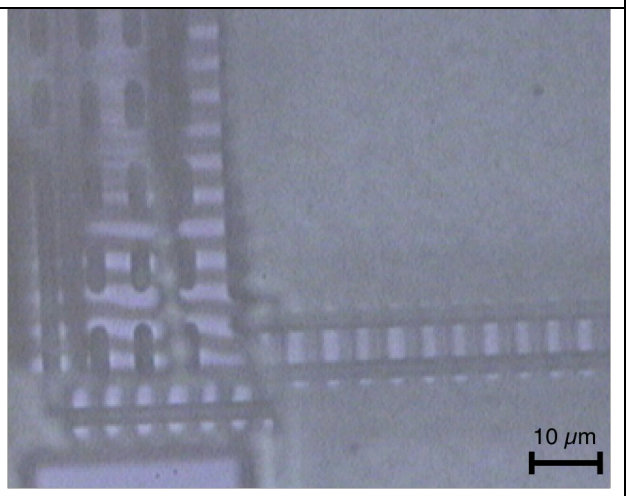

Optical microscope plan view of the vent openings over a resonator. The resonator is visible through the vents. The VT silicon layer is sometimes called "cap1".

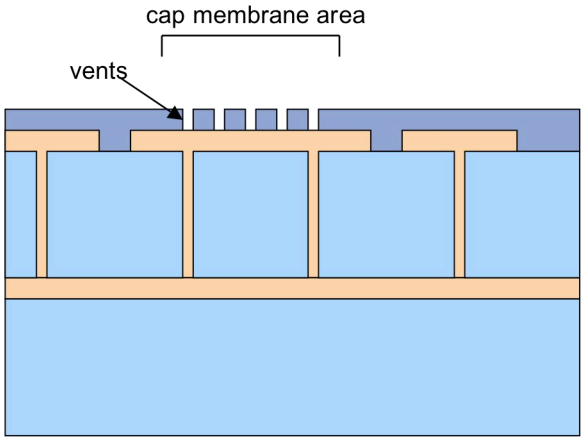

Schematic cross-section of VT silicon with vent openings. The sacrificial oxide will be etched underneath the vents, so the location of the vents defines the location of suspended cap membranes.

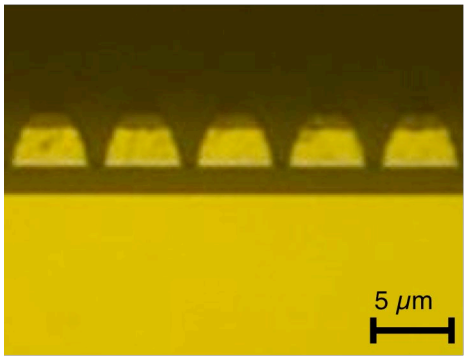

Optical microscope cross-section view of etched vent openings. The photoresist is visible on top of the cap layer.

Layer: Vent (VT)

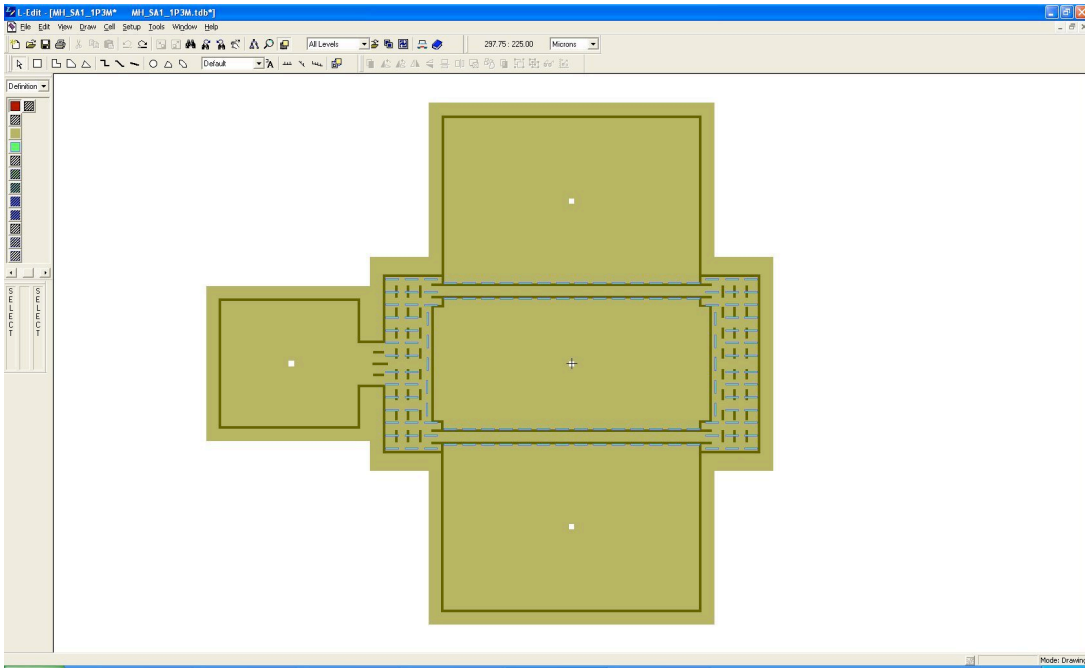

L-Edit layout file with the Vent layer visible (the VT openings are the small green rectangles over the body of the resonator). The VT openings must be near structures that are intended to be released (such as beams). They must be kept away from structures that will not be released (such as anchors). The VT drawing style is bright, so openings will be etched where lines are drawn. The size of the area covered by vents may be restricted in the Design Rules in order to limit the size of the suspended cap membrane.

Layer: Vent (VT) HF Vapor Etch

After vent openings are etched, the sacrificial oxide layers (Gasket and Contact Gasket oxides) are etched using hydrofluoric acid vapor. The HF vapor is used instead of liquid to avoid stiction problems when the liquid evaporates. The vapor etch is a timed etch, meaning that there is nothing to stop the vapor from etching too much oxide and destroying the devices, so the etch progress must be monitored carefully. Anchors need to have some oxide remaining after the vapor etch to connect them to the substrate. The minimum anchor size must be large enough to ensure that some oxide remains after the vapor etch.

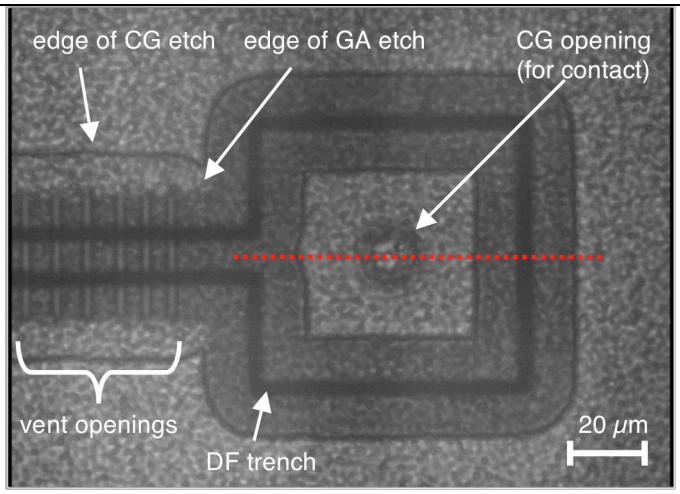

Infrared (IR) microscope plan view of the vapor etch result. Silicon is transparent to IR, so the microscope can see through the silicon layers and image the oxide layers. The structure is an anchor with a beam extending to the left. A square of oxide remains around the contact in the center of the image. Note that the separate edges of both the Gasket and Contact Gasket oxide layers are visible.

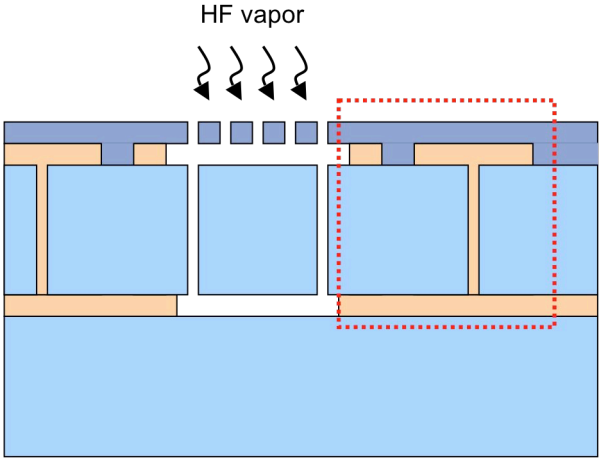

Schematic cross-section of vapor etching the sacrificial oxide. The sacrificial oxide is etched underneath the vents, creating a suspended cap membrane.

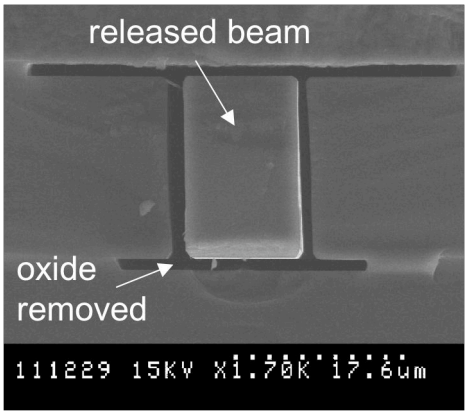

SEM cross-section view of the results of vapor etch. The upper Contact Gasket oxide etch is wider because the vents exposed the oxide. The lower Gasket oxide layer is etched only where the Defintion trenches allow the HF vapor to penetrate. [SEM by R. Candler]

Layer: Vent (VT) HF Vapor Etch

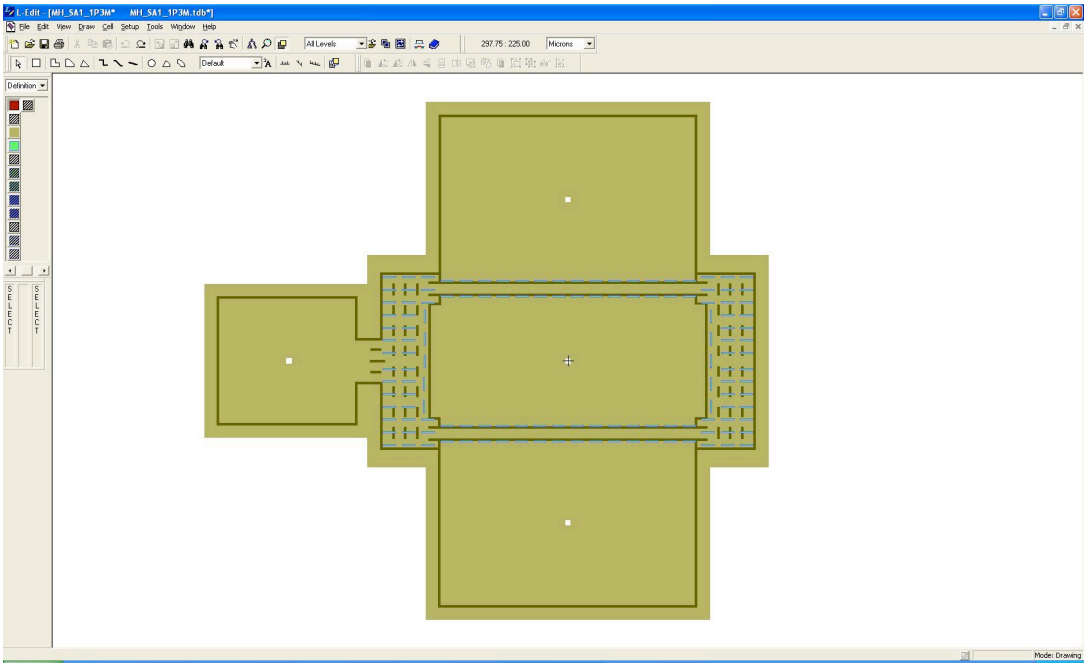

L-Edit layout file with the Definition and Vent layers visible. The VT openings must be near structures that are intended to be released (such as beams). They must be kept away from structures that will not be released (such as anchors). The VT drawing style is bright, so openings will be etched where lines are drawn.

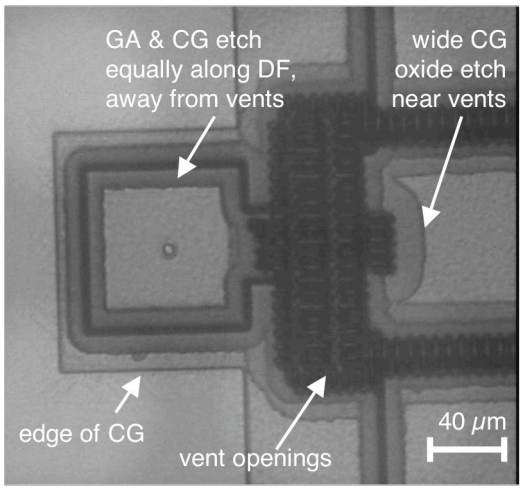

During the vapor etch step, the HF vapor will travel along the DF trenches, through the “keyhole” opening (see CG) and etch the oxide near the trenches. This means that structures that are far from the vents will experience some vapor etching may be released.

Layer: Insulation Trench (IT), CMP, A2

The Insulation Trench (IT) layer is the second part of the silicon cap. The epitaxial silicon "seal" layer (sometimes called "cap2") is deposited to seal the vent openings. The first 2 µm of silicon closes the vents, and usually ~25 µm of silicon is deposited to give the encapsulation mechanical strength. After the thick silicon deposition, the wafer surface is rough. It must be made smooth by chemical-mechanical-polishing (CMP). Typically ~5 µm of silicon is removed during polishing.
After CMP, the IT trenches are etched to create vias through the silicon cap.

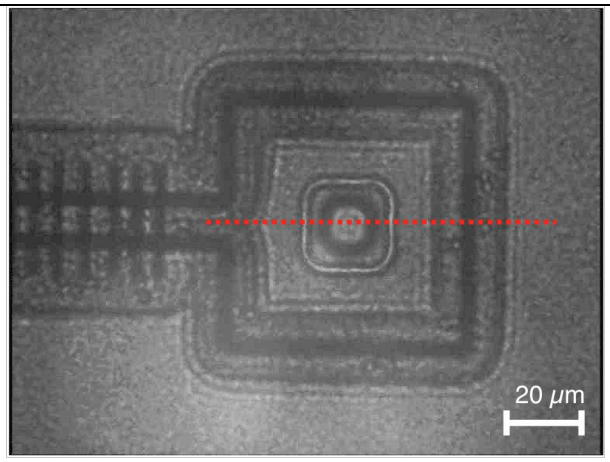

IR microscope plan view of the IT trench ring around a contact. After CMP, new alignment marks (layer A2) are etched on top of the wafer using the IR microscope to align A2 to A1.

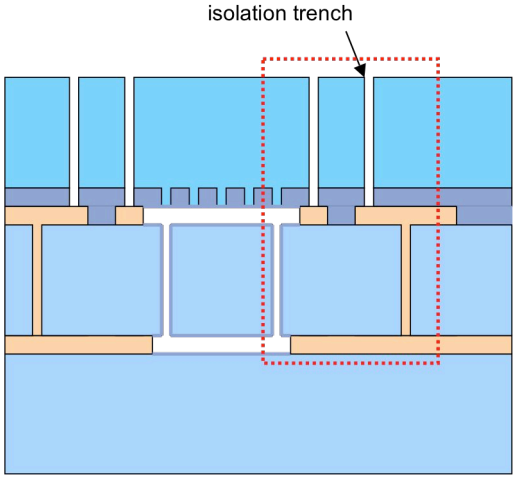

Schematic cross-section of the IT deposition. Note that Krispy Kreme oxidation processes use thicker cap layers (both seal/cap1 and cap/cap2) for mechanical strength.

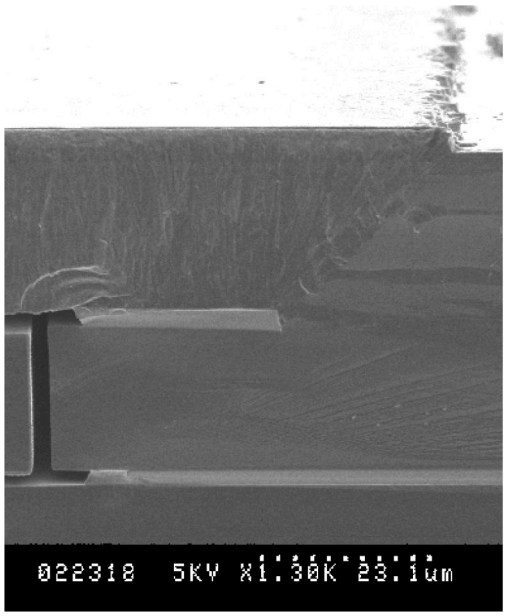

SEM cross-section view of the deposited silicon cap layer. The edge of the CG layer is shown. Note that the epitaxial silicon forms polysilicon where it is deposited on the Contact Gasket oxide, and single-crystal silicon when it is deposited on silicon.
[SEM by B. Kim]

Layer: Insulation Trench (IT), CMP, A2

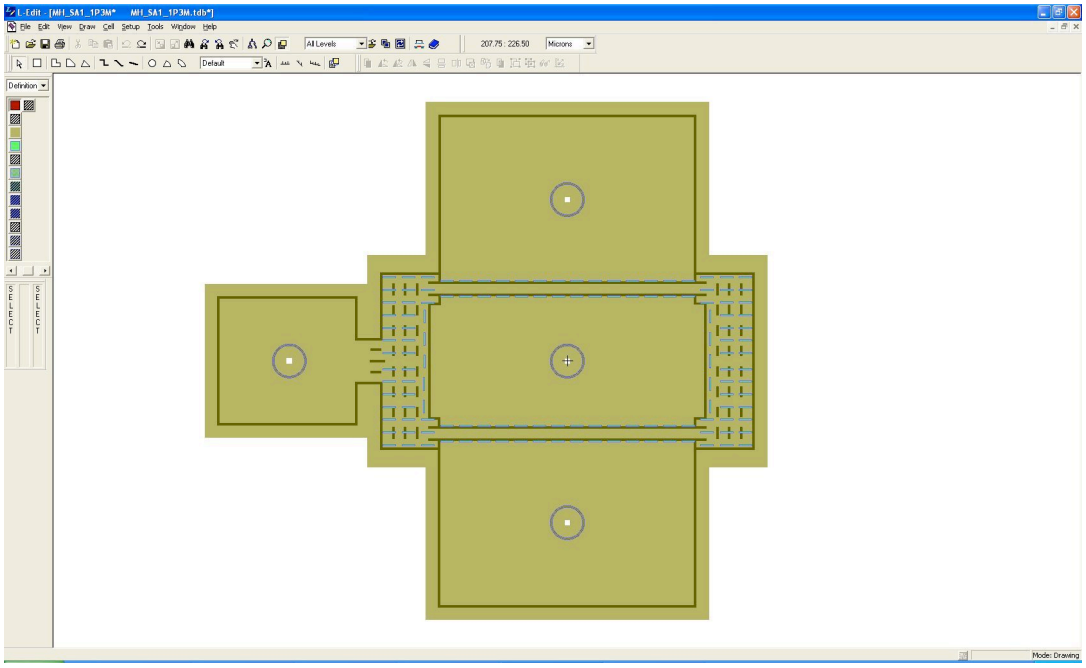

L-Edit layout file with the Insulation Trench layer visible. The IT trenches are the rings around the contacts. The IT drawing style is bright, so the lines indicate where trenches will be etched. The IT trenches must be drawn over CG oxide that will remain after the vapor etch. Otherwise, the trench etch would open the encapsulation. Intersections are typically prohibited in the IT layer, to reduce the required CA oxide thickness (see CA).

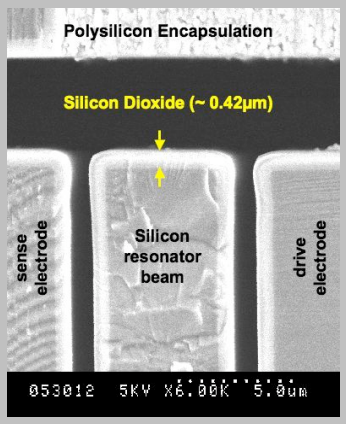

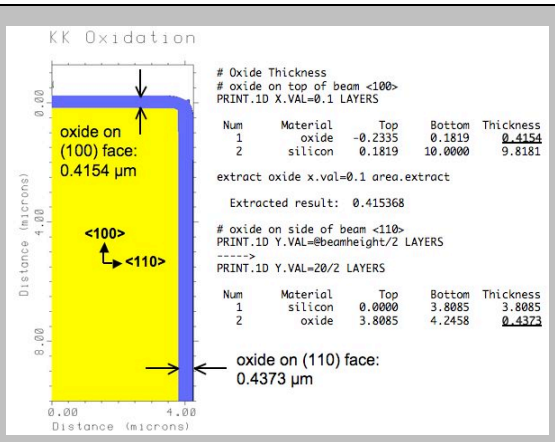

SIDEBAR: KK For Krispy Kreme (KK) composite resonator fabrication, a thermal oxidation step is performed *before* the cap2 silicon layer is deposited, while the vents are still open. In this case, thermal oxide grows on the silicon structures inside the encapsulation. The SEM cross-section above (left) and TSUPREM4 simulation (right) depict this result. After the KK oxidation, the oxide is removed from the surface of the wafer, and the process continues with the deposition of the seal/cap2 layer.

Layer: Contact Aluminum (CA)

The Contact Aluminum (CA) layer is the final oxide layer deposited on top of the encapsulation for electrical electrical passivation. The CA oxide layer must be thick enough to seal the IT trenches. The IT trenches are typically drawn with no intersections, so that the CA oxide can be thinner (the √2 term can be eliminated from the expression for oxide thickness given in the CG description):

$t_{CA} = 1.5w_{IT}$

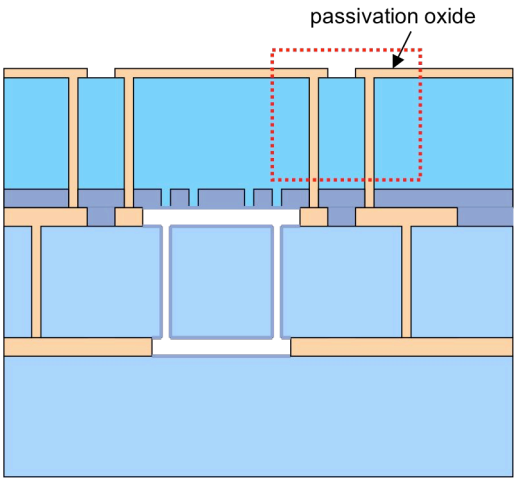

Schematic cross-section of the CA layer deposition and etch. The CA oxide does not typically fill in the IT trenches, as implied by the diagram.

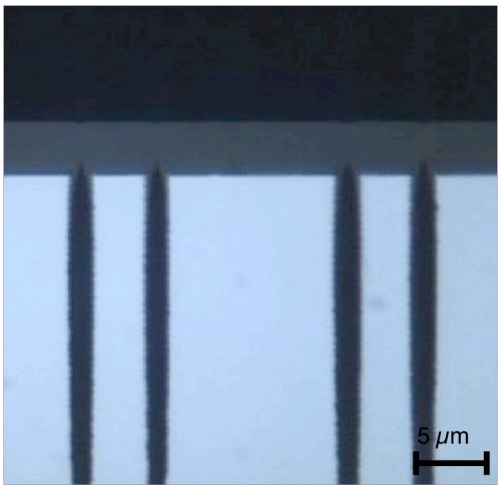

Optical microscope cross-section view of the CA oxide layer sealing IT trenches. A low temperature oxide (LTO) deposition was used. This deposition is not conformal, and the trenches are not filled in, as opposed to the CG oxide deposition.

SIDEBAR: Oxide-seal

In oxide-seal processes (as opposed to epi-seal), the cap consists of only one layer of epitaxial silicon deposition, equivalent to the Insulation Trench layer. The VT layer is omitted, and VT openings are combined with the IT trenches on one drawing layer (basically skipping steps d-f in Figure B.1). The long-term stability of oxide-seal resonators is worse than that of epi-seal resonators. However, the oxide-seal process is easier to fabricate and more flexible. Recently, some experiments have been proposed using other films, such as Silicon Carbide or Silicon Nitride, to seal the encapsulation in an oxide-seal type process.

Layer: Contact Aluminum (CA)

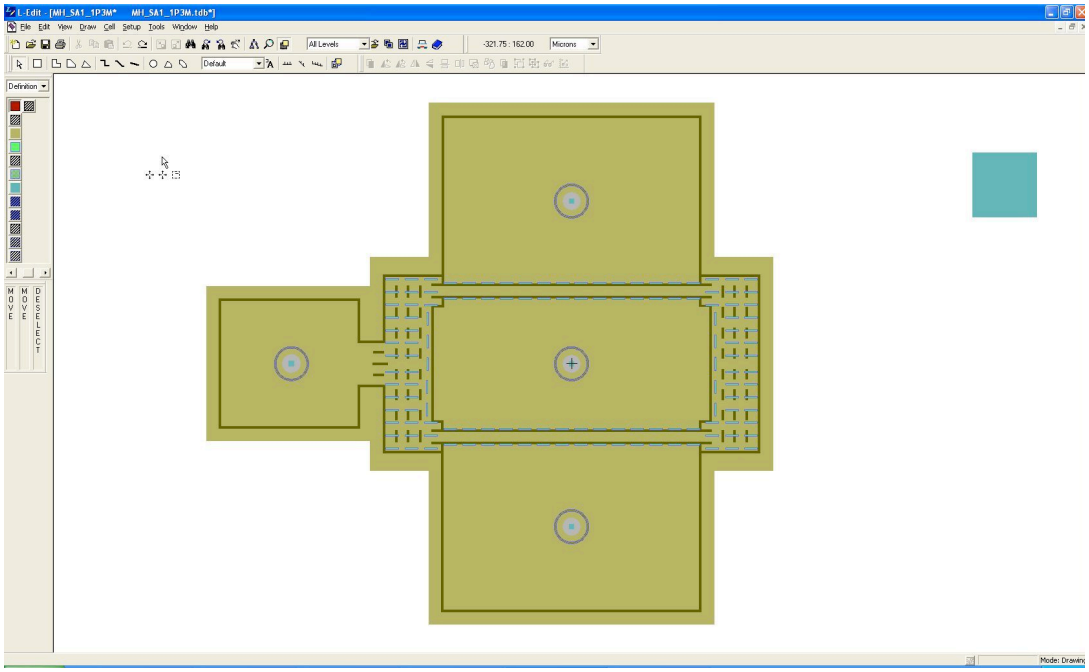

L-Edit layout file with the Contact Aluminum layer visible. The CA openings are at the center of each contact. The CA drawing style is bright, so the rectangles indicate openings that will be etched in the CA oxide layer. The large etch opening at upper right is a “ground contact”. It will create an electrical contact to the silicon in the cap and device layers. This electrical connection is important for reducing the feedthrough capacitance for capacitively actuated devices.

Layer: Aluminum (AL)

The Aluminum (AL) layer is the metal that makes electrical paths and bond pads. 1% Al/Si is usually used to prevent silicide formation at the contacts, but other metals (Ti, W) can be used.

The metal deposition must be thick enough to make a good connection over the step from the top of the CA oxide to the bottom of the "pit" of the CA etch opening. Typically 1.5 µm metal thickness is used.

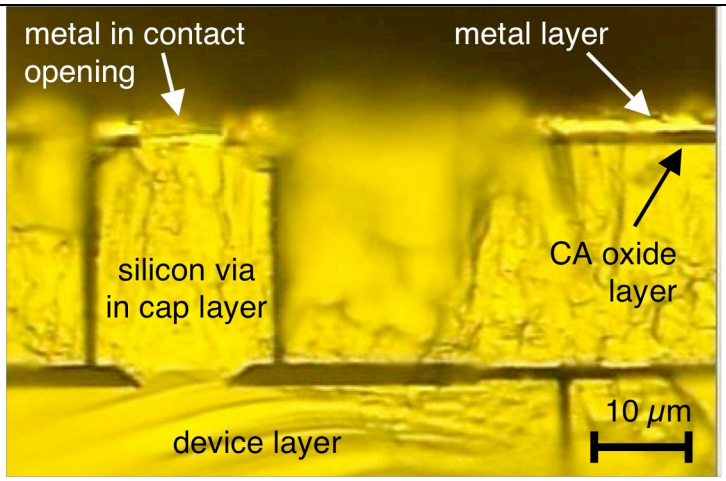

Optical microscope cross-section of a silicon via with deposited metal on top of the CA oxide.
The polysilicon cap does not break cleanly, so some regions in the picture are out of focus.

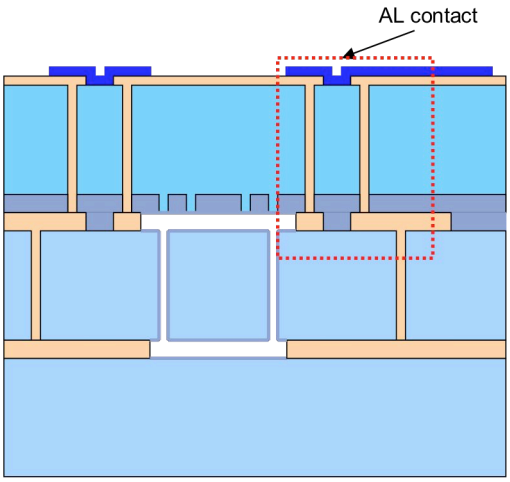

Schematic cross-section of the Al metal deposition. The metal layer includes electrical traces, bondpads, and labels.

Metal bondpad locations should be chosen with probing and wirebonding in mind- e.g., put inputs on one side and outputs on the other, with respect to the orientation of the package bondplan (see Process Finish section).

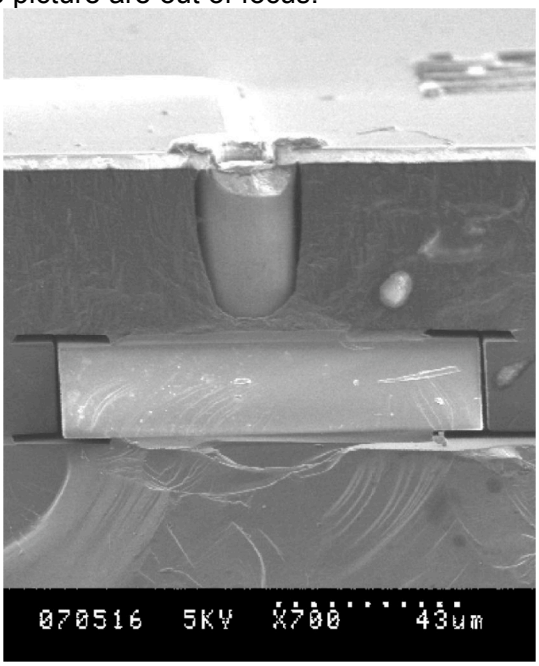

SEM cross-section view of a contact. The round via created by the IT trench etch is at the center of the image. The Al metal layer is visible on top of the via. [SEM by B. Kim]

Layer: Aluminum (AL)

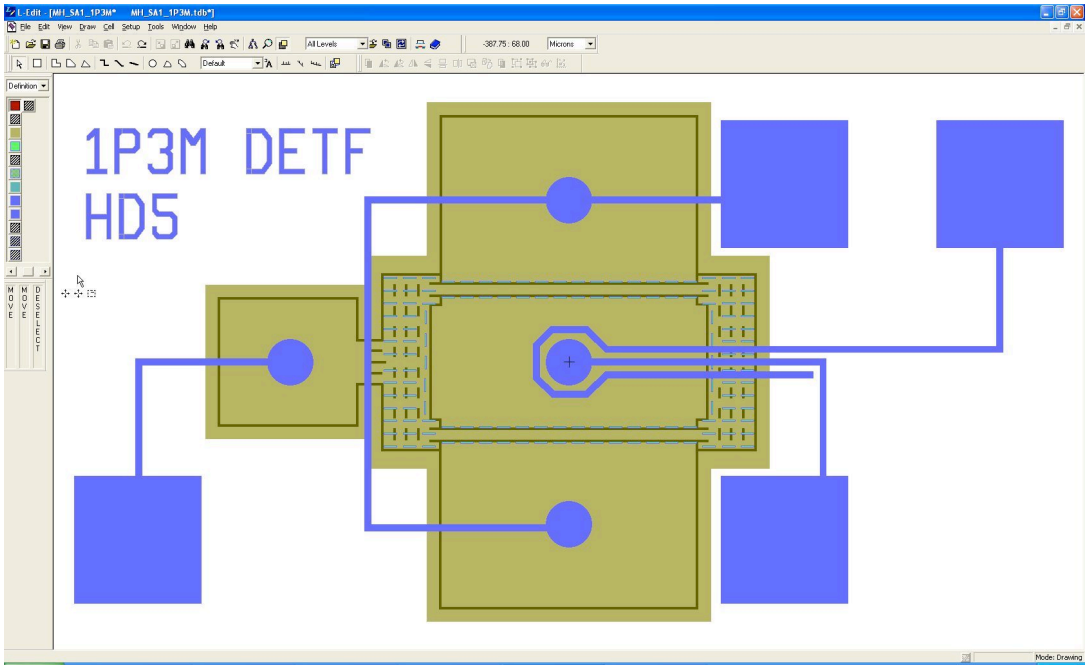

L-Edit layout file with the Aluminum layer visible. The AL layer is drawn dark, so the lines here indicate where the metal will remain. When the fabrication is finished, only the metal layer will be visible on top of the cap. It is customary to use metal to label each device so that it can be identified easily during testing.

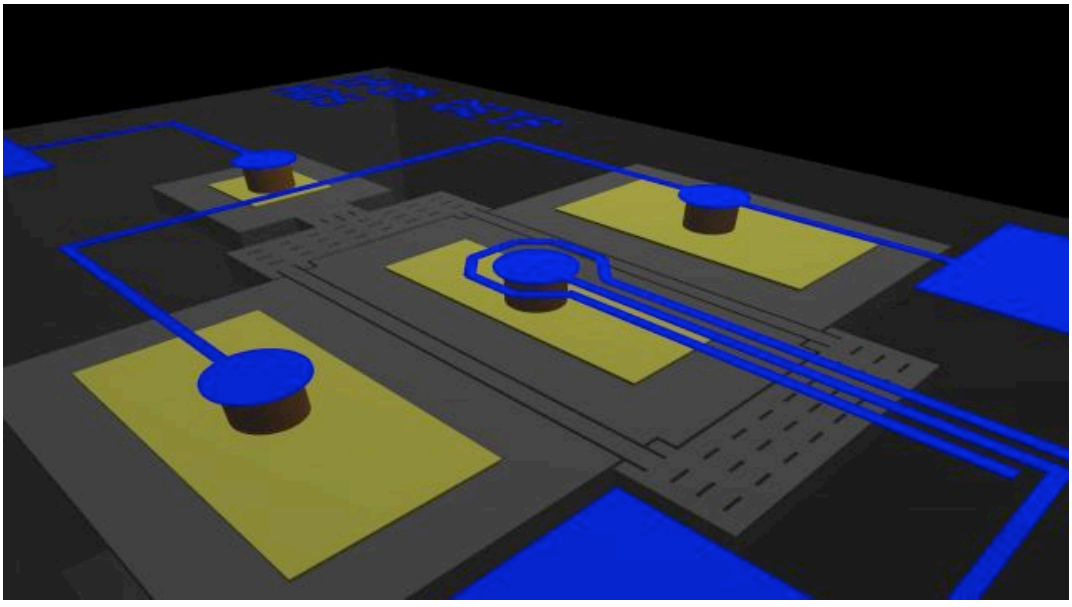

Rendering of a fabricated SA DETF. The cap layer, surrounding device layer, and handle wafer substrate are shown as a transparent box.

Process Finish

The final processing step is to anneal the wafers in a nitrogen ambient until most of the H_2 gas inside the cavity has diffused out. Then the wafer is ready to be tested. After the wafer is tested on the probe station, it is diced into individual dies. The dies are then mounted in electronic packages and wirebonded.

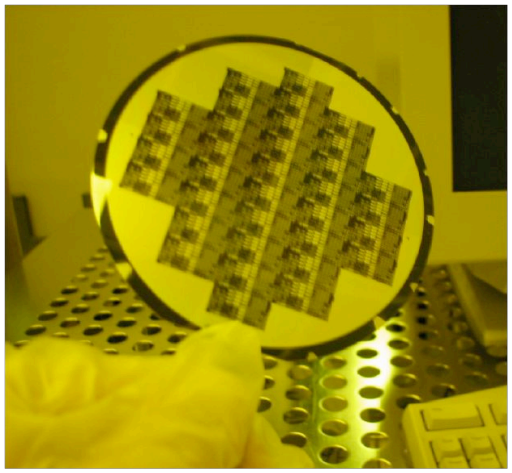

A finished 4” (100 mm) wafer at the end of the epi-seal process.
[photo by B. Kim]

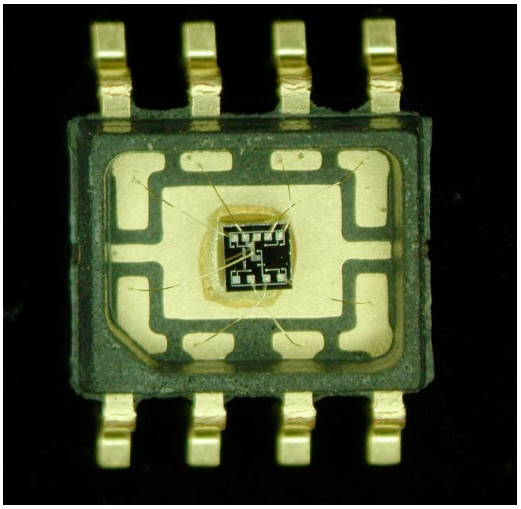

An epi-seal resonator packaged in a 8 pin OpenPak DIP package. Gold wirebonds connect the bondpads on the die to the pins of the package. The die is ~1 x 1 mm.

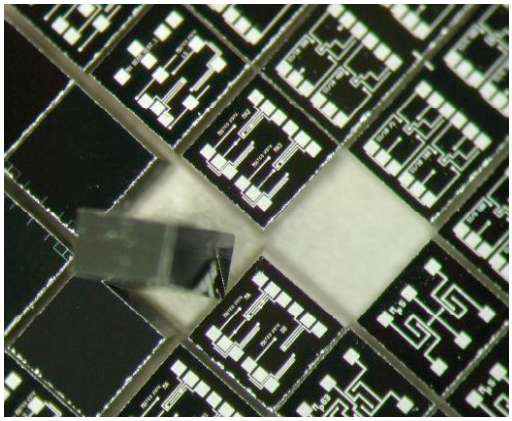

Optical microscope view of silicon die after dicing. Each die is approximately 1 x 1 mm.

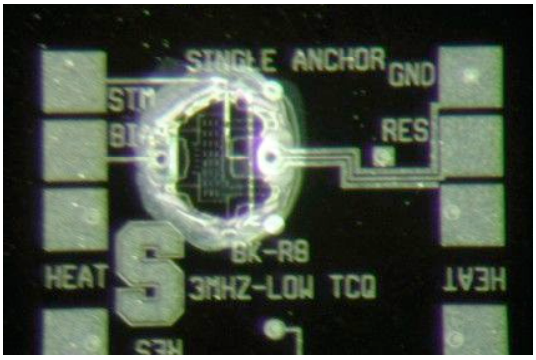

Optical microscope plan view of a completed resonator with a [unintentional] hole in the encapsulation. The coupling block of a resonator can be seen in the hole. The bondpads on the sides of the die are 100 μm square (standard size). The depression in the metal from a CA opening is visible in the bondpad at upper right (a “ground contact”).

Process Finish

Bondplan for Dual Oscillator Boards

Incl. MADUALOSC, HM_AGC, CM_GB

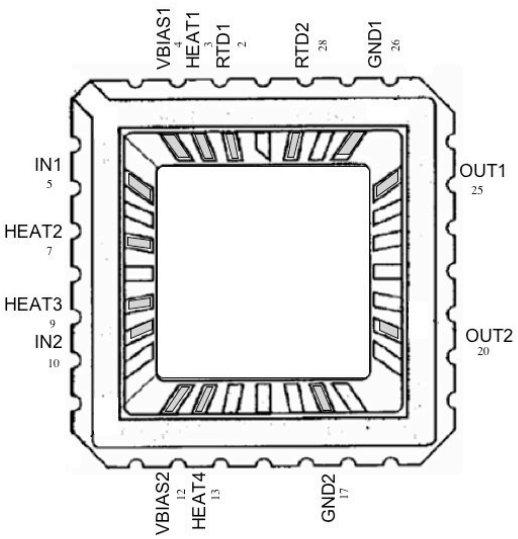

Eagle part: "RESONATOR_LCC28_DUAL"

Bondplan for Single Oscillator Boards

Incl. KK_OSC

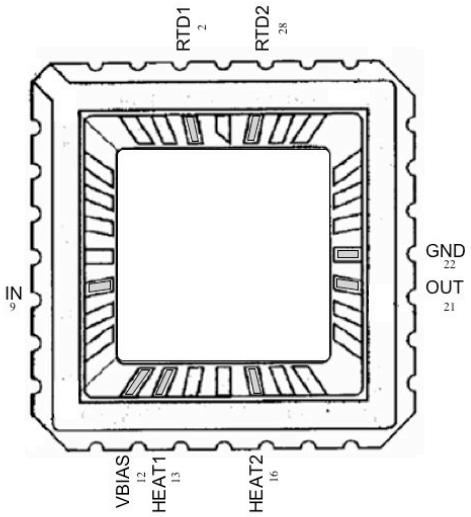

Eagle part: "RESONATOR_LCC28_SINGLE"

Note: use dual package layout if possible.

Bondplan for Single Resonator Boards

Incl. MH_Amp[4/5]X, PickX

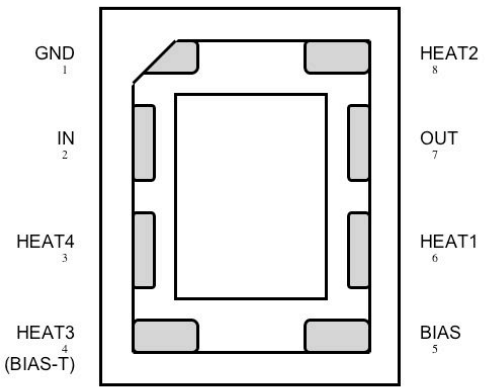

Eagle part: "RESONATOR_8PIN"

Pinout for 7-Pin Molex Connector

Oscillator	HEAT 1	HEAT 2	Vbias	GND	Vgain	Vset	GND/ Temp
Aux 2	GND	VH / V+	VL / V-	SRC+	SENS +	SENS -	SRC-
Aux 1	HEAT 4	GND	HEAT 3	GND	HEAT 2	GND	HEAT 1
Resonator	Temp	GND	Vbias	GND	V+	V-	GND

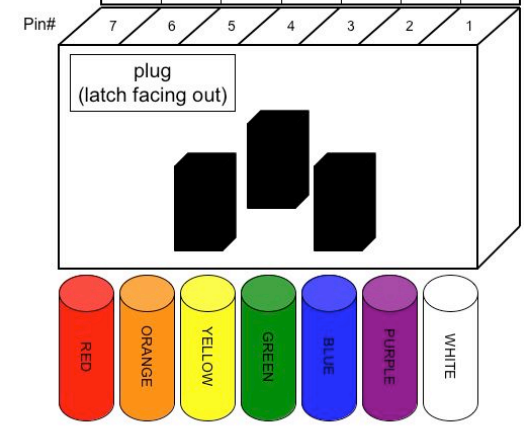

Eagle part: "MOLEX7"

Standard wirebond connections ("bondplans") for electrical packages. The metal bondpads should be designed with the bondplan in mind.

Process Finish
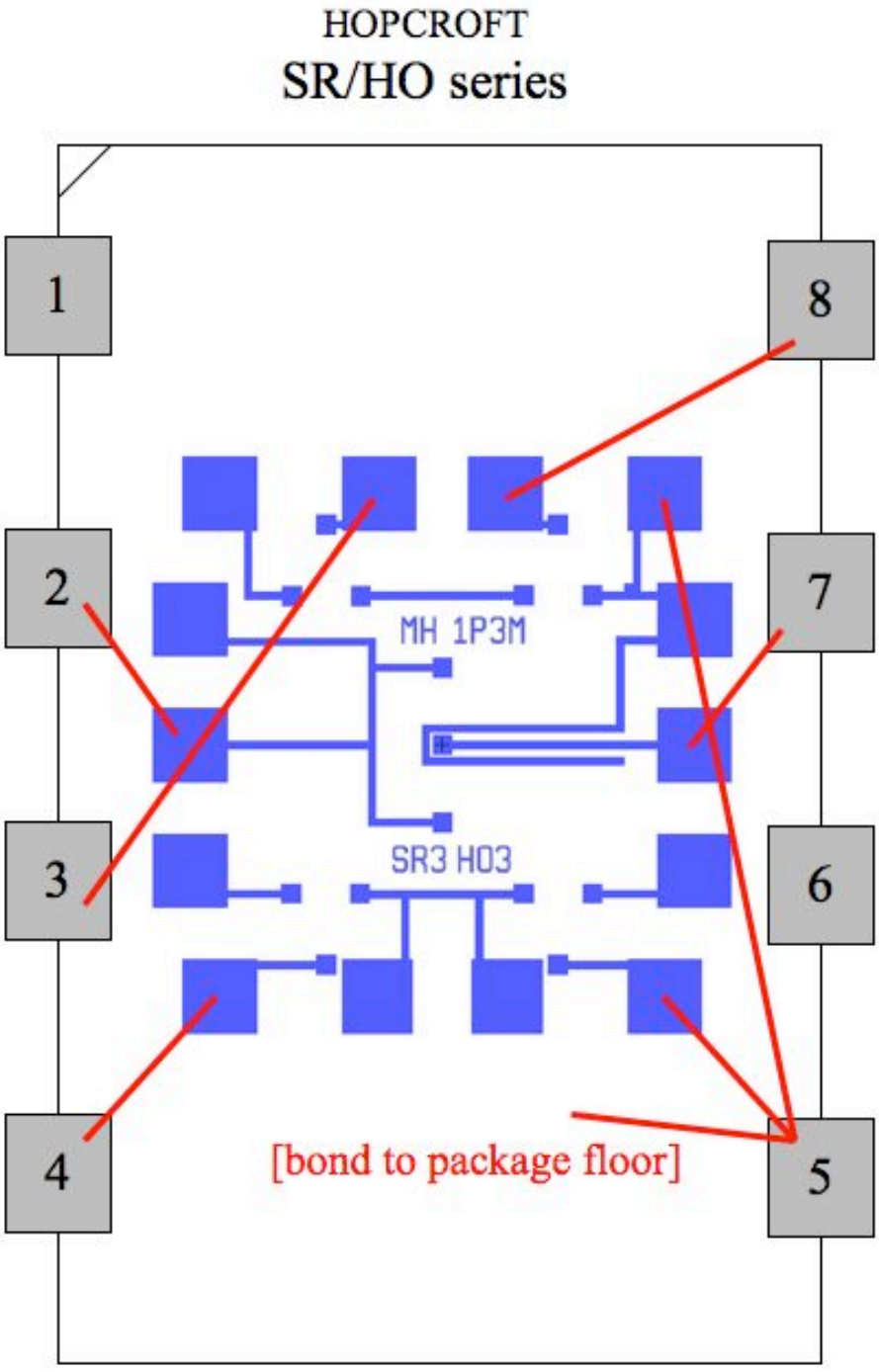

Typical wirebond diagram for an SR-DETF. This part is configured for "same-side" heating. Note the connection from bias (pin 5) to the "ground contact" or "shield" pad at the upper right corner of the die.

Everything should be made as simple as possible, but not simpler.
-Albert Einstein

C. Allan Deviation

The statistical quantity called Allan deviation is used to describe oscillator frequency stability [53, 54, 230-233]. Allan variance (σ_y^2) and Allan deviation (σ_y) are analogous to variance (σ^2) and standard deviation (σ); they are quantities that describe the variation in a set of data points. The standard deviation is a measurement of the difference between each data point and the mean value of the data set. It describes the width of the Gaussian fit to the data set, which is useful when the data approximates a Gaussian distribution. As more data points are added to the set, the standard deviation value trends asymptotically toward a "true" value. However, for oscillators, the set of data points is the output frequency measured at sequential points in time. This data does not have a Gaussian distribution; in general, each point is strongly correlated with the points near it in the sequence. Consequently, this type of data does not have a fixed standard deviation, and the standard deviation value is unbounded as more data points are added to the set.

The Allan variance, σ_y^2, is based on a "two-sample" variance measurement of the data. Instead of measuring the difference between each data point and the mean, it measures the difference between each data point (y_n) and the next one (y_{n+1}):

$$\sigma_y^2(\tau) = \frac{1}{2(m-1)} \sum \left(y_{n+1} - y_n \right)^2 \quad . \tag{C-1}$$

The Allan variance is the fundamental quantity, but Allan deviation, σ_y, is more commonly used because it has the units of the quantity of interest:

$$\sigma_y(\tau) = \sqrt{\frac{1}{2(m-1)} \sum \left(y_{n+1} - y_n \right)^2} \quad . \tag{C-2}$$

M is the number of *y* data points in the calculation. The quantity τ is the sample time of the frequency measurement. Longer sample times increase the averaging of the frequency measurement, which reduces the influence of random noise. Allan deviation results are presented as a plot of deviation vs. sample time, or given as a value at a certain τ, e.g., "Allan deviation of 2 Hz at 10 seconds".

For example, consider the data plotted in Figure C.1, which shows the frequency output from an oscillator based on a silicon MEMS DETF resonator, and the corresponding Allan deviation. The frequency result has some short-term noise around each data point, which makes the frequency trace appear as a thick band. There is also some long-term temperature fluctuation, which causes the frequency trace to have a sinusoidal appearance over a period of hours.

Frequency data is typically collected at a certain rate. In the example here, the data was collected every second. Therefore, the calculation of the Allan deviation at τ = 1 second is straightforward using (C-2). Longer sample times are calculated by grouping or binning the data into bins of length τ. The average value of the data points in each bin is then used for the Allan deviation calculation. This is illustrated in the following two figures. Note that as the size of the bin increases, the number of data points (*M*) decreases, and so the uncertainty in the result increases.

Allan deviation plots typically have a "U" shape, with a minimum noise floor at a certain τ. The deviation increases above this τ as the influence of non-random effects, such as temperature drift and aging, become dominant. The slope of the plot at small τ values can be correlated with certain types of noise processes.

The Allan deviation equation (C-2) assumes that there is no pause or dead time between the frequency measurements. In practice, this is often impossible. The effect of dead time can be accounted for using bias functions [234]. When the dead time is similar to the sample time, the effect of dead time can be ignored.

MATLAB code which calculates the Allan deviation for a frequency measurement was written during the course of this work. This code is too lengthy to reproduce here, but it can be downloaded from the MATLAB code repository at:

http://www.mathworks.com/matlabcentral/fileexchange/

File name: allan v1.5

File ID: 13246

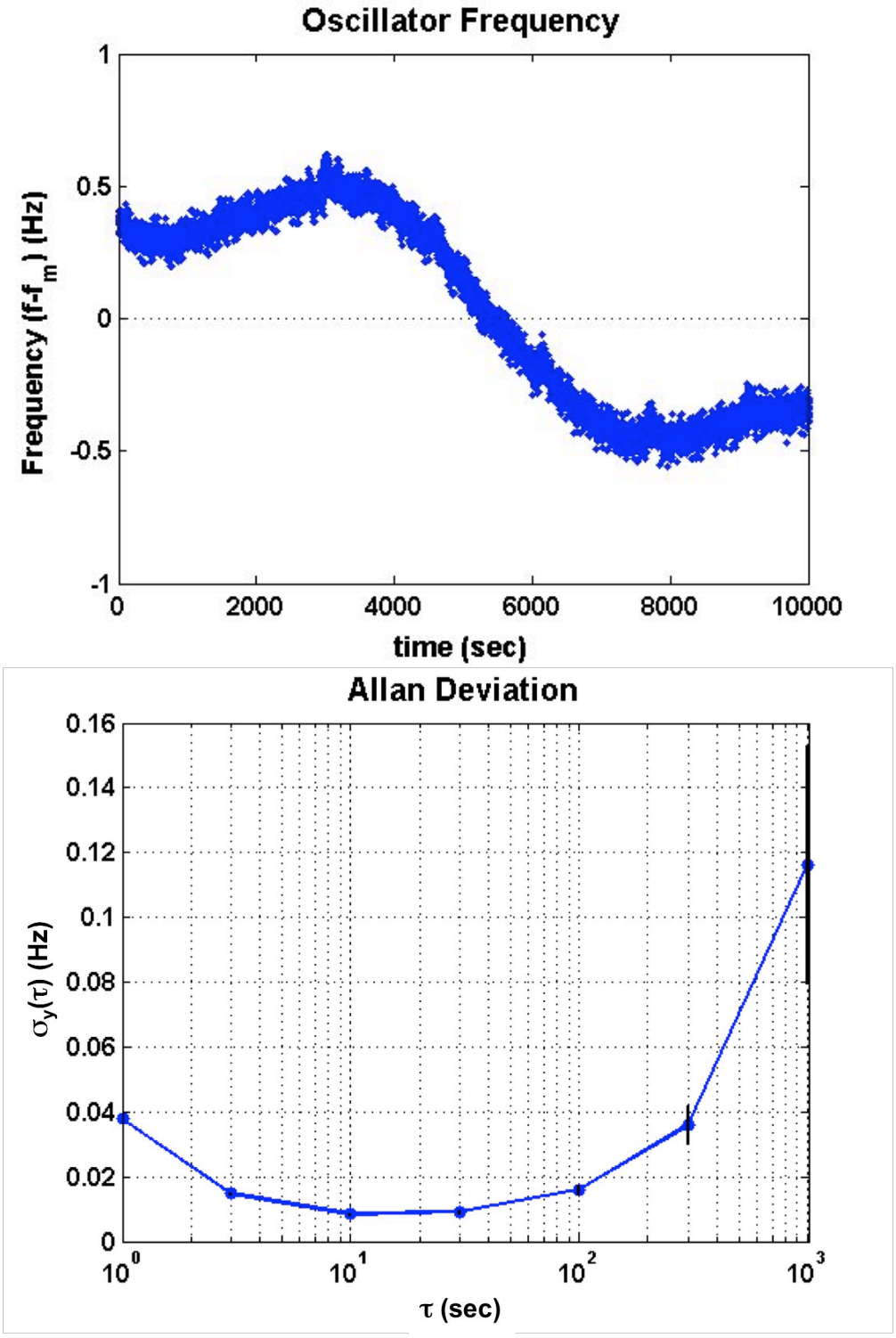

Figure C.1: Typical DETF oscillator data and corresponding Allan deviation Uncertainty in the σ_y values is shown by vertical black lines. The uncertainty increases as the number of data points decreases.

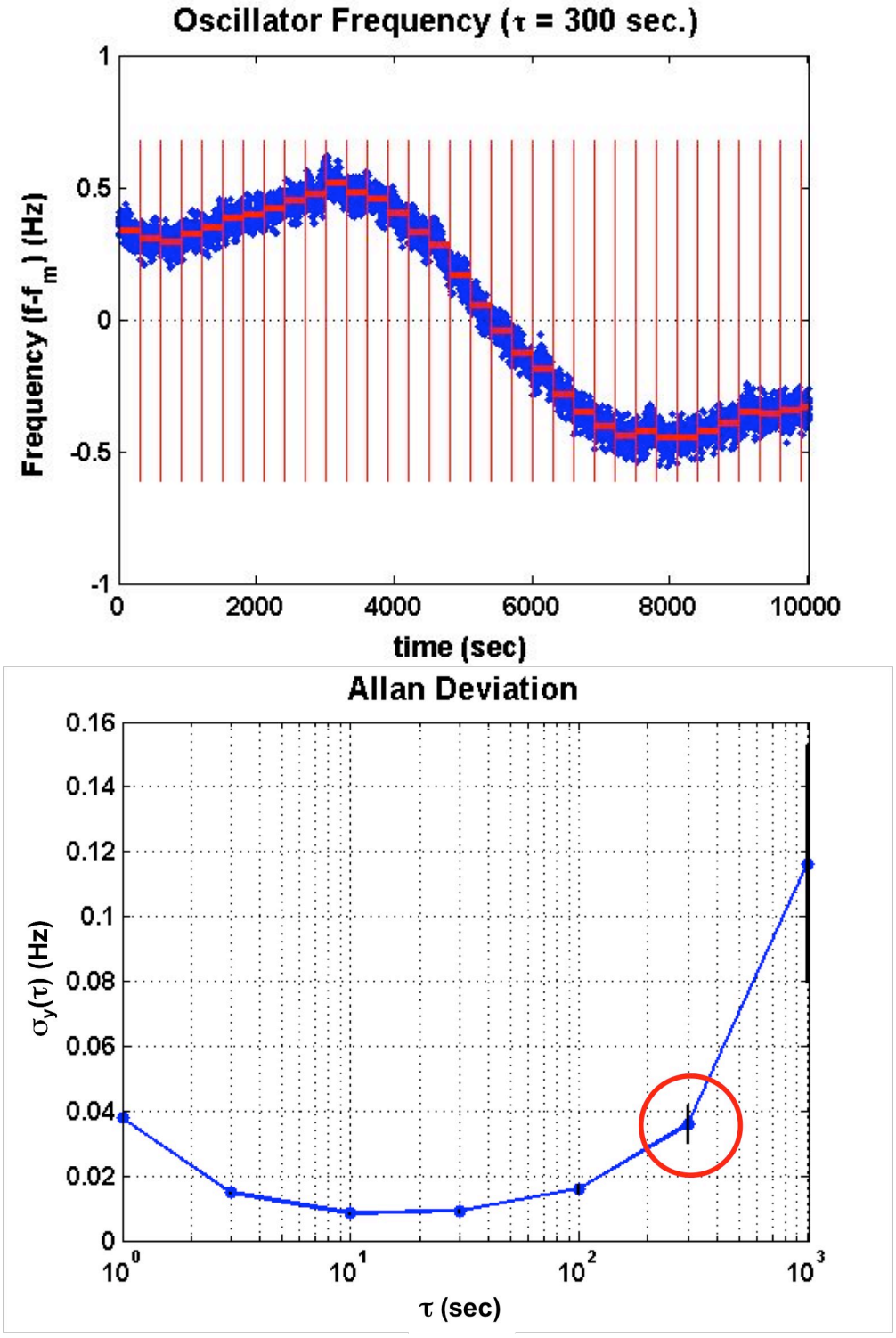

Figure C.2: Allan deviation for τ = 300 seconds
The values of y_n in (C-2) for τ = 300 are the average value in each bin, shown as horizontal red lines on the frequency plot.

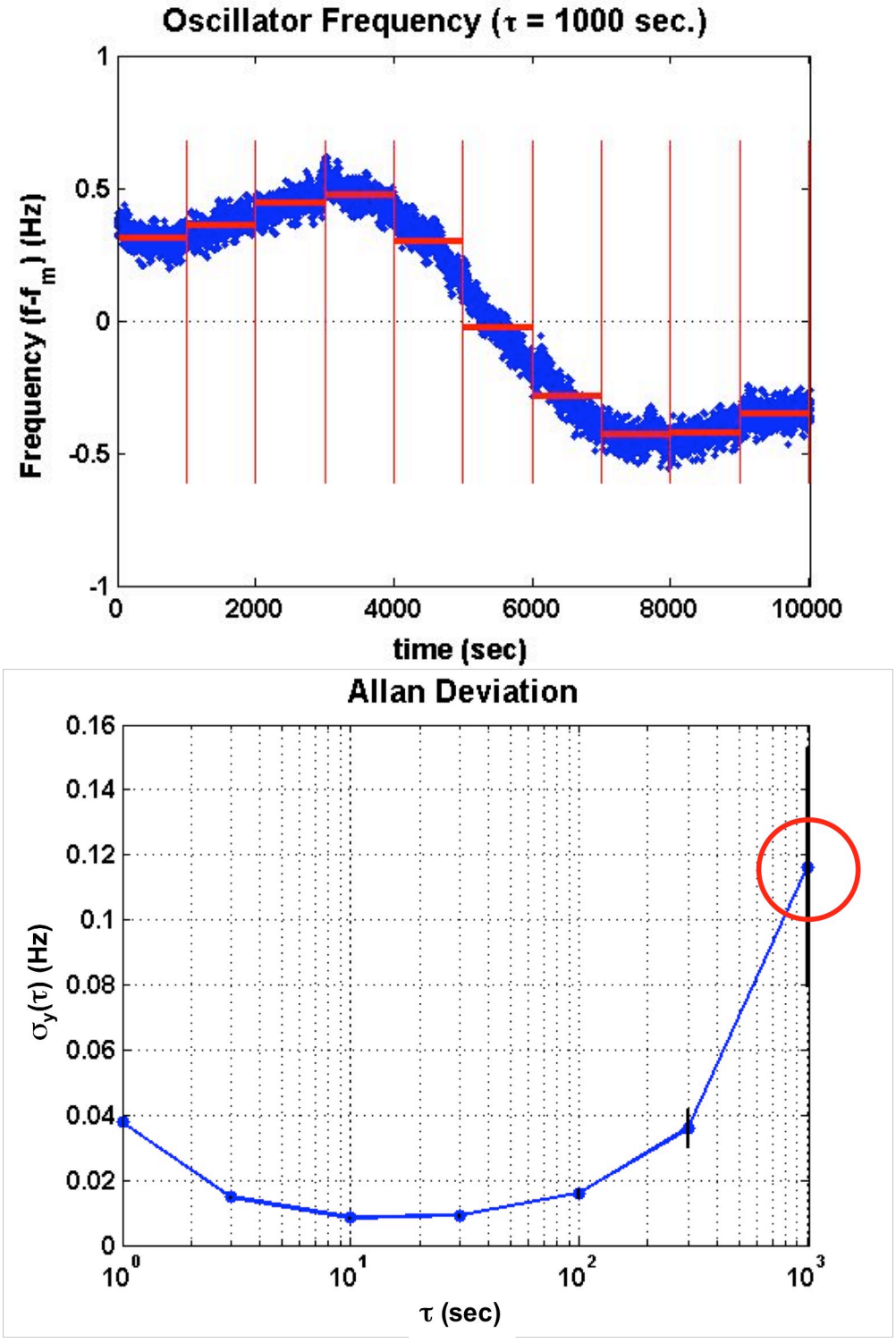

Figure C.3: Allan deviation for τ = 1000 seconds
The values of y_n in (C-2) for τ = 1000 are the average value in each bin, shown as horizontal red lines on the frequency plot.

*many many thanks for your wonderful work, to my great joy, it can extract data from a *.fig with more than 1 axes. Thanks again!*

- guanwenye@tju.edu.cn

D. MATLAB Code

A large amount of MATLAB [197] code (12k+ lines) was written to perform the experiments described in this thesis. The individual functions and programs are briefly described here. For more detail about how to use the programs, type "`help` program_name" in MATLAB. Much of the code is specific to the experiments and research described in this thesis, and has little use for other researchers. Some of it, however, has broader application. The code with some general-purpose use has been uploaded to the online MATLAB code repository, where it is freely available. As of this writing, code generated by this project has been downloaded by other users over 1000 times. The code repository address is:

http://www.mathworks.com/matlabcentral/fileexchange/loadCategory.do .

Program Name and latest version	Description
kpib.m, v4.48	kpib.m contains the instruments drivers for all of the instruments used in the experiments. For example, the command `T = kpib('blueoven',5,'read');` will return the current temperature inside the Thermotron S-1 thermal chamber (aka "Blue Oven"). The kpib commands form the core of the experimental code. The help file for kpib.m has a lot of information regarding the general use of kpib commands. For commands specific to each instrument, scroll down in the code to the block for that instrument.

Standard_Tools.m
 	
`tools`
	"`tools`" is the name of a variable which stores the descriptions of the instruments that will be used in a particular experiment. `tools` is a structure, for example:
	
	`tools.pwrsupply.instr = 'HP_E3634A';`
	`tools.pwrsupply.gpib = 12;`
	`tools.pwrsupply.channel = 2;`
	`tools.scope.instr = 'TDS_540';`
	`tools.scope.gpib = 8;`
	`tools.scope.channel = 3;`
	`...(etc.)`
	
	Standard_Tools.m is a script that assembles the `tools` variable for you. Edit it to reflect your experimental setup.
	
	Use of the tools structure is a recommendation. A large amount of code has been written following this convention, and following it can help you work with the existing code. Certain functions expect to find certain fields in tools, and you may add your own fields as necessary. It is recommended to use existing field names for the same function for compatibility.

measure_res.m, v3.81 bandqr.m, v1.24	measure_res.m performs a sweep measurement of a resonator using a network analyzer. It returns the raw sweep data, as well as certain key features of the measurement (peak frequency, Q, bandwidth, etc.). For example, `r = measure_res(tools,1.3e6,10e3);` performs a sweep measurement with the frequency range centered at 1.3 MHz, spanning 10 kHz. Sweep measurements are often performed using a series of sweeps, starting at a large span in order to locate the resonator peak frequency, and then "zooming in" on the peak using smaller spans to increase the accuracy of the peak measurement. Measure_res.m supports this behavior,

Program Name and latest version	Description
	for example: `r = measure_res(tools,1.3e6,[10e3 5e3 1e3]);` performs a three-part measurement, using sweeps of 10, 5, and 1 kHz. These values are typical for the 1P3M DETF resonators. bandqr.m calculates several useful parameters from the sweep data downloaded from the network analyzer. Measure_res.m uses bandqr.m to calculate resonator Q, 3dB bandwidth, motional resistance, and equivalent RLC circuit values.
measure_osc.m, v1.5	measure_osc.m measures the oscillator frequency using the counter. It also downloads the trace from a spectrum analyzer, if available, and measures a large number of other parameters, including bias voltage, temperature, etc. For example, `o = measure_osc(tools);` records the data from all of the instruments in the variable `tools` (see below). Note that measure_osc.m is relatively slow, because it is recording data from many instruments. For fast repeated counter measurements, see timex.m

TCF_res.m, v3.0
 	
TCF_bias.m, v2.0
TCF_drive.m, v1.1
TCF_power.m, v1.1
	TCF_res.m performs a TCf measurement (measuring frequency versus temperature) of a resonator using a network analyzer and a thermal chamber or temperature chuck. TCf_res uses measure_res.m, so it also records the resonator Q, peak amplitude, bias voltage, etc. during the temperature cycle. For example,
	`tcf = TCF_res([0:10:70],'BD30',1.3e6,[10e3 5e3 1e3],tools);`
	performs a TCf measurement on a resonator designated "BD30" with an estimated initial center frequency of 1.3 MHz using a temperature cycle from 0 to 70 °C in 10 °C steps.
	
	TCF_bias.m performs a TCF measurement combined with a bias voltage sweep. At each temperature step, the bias is varied. For example,
	`tcfb = TCF_res([0:10:70],[8:2:14],'BD30',1.3e6,[10e3 5e3 1e3],tools);`
	performs a TCf measurement using a temperature cycle from 0 to 70 °C, and cycles the bias voltage from 8 to 14 V at each temperature step. The result is 4 separate TCf measurements, one each at 8 V, 10 V, 12 V and 14 V bias.
	
	TCF_drive.m performs a TCF measurement combined with a drive level sweep, analogous to TCF_bias.m.

Program Name and latest version	Description
	TCF_power.m performs a TCF measurement combined with a heating power sweep, analogous to TCF_bias.m.
TCF_osc.m, v2.1	TCF_osc.m performs a TCf measurement (measuring frequency versus temperature) of an oscillator using a counter. TCf_osc uses measure_osc.m, so it also records the resonator Q, peak amplitude, bias voltage, etc. during the temperature cycle. For example, `tcf = TCF_osc([0:10:70],'BD49',1.3e6,tools);` performs a TCf measurement on a oscillator designated "BD49" with an estimated initial center frequency of 1.3 MHz using a temperature cycle from 0 to 70 °C in 10 °C steps.
plottcf2.m, v2.5	plottcf2.m extracts the TCf data from the data files generated by TCF_res.m and TCF_osc.m and plots the results. For example, `c = plottcf2('TCF_BD30_MAR2006');` plots the results from the measurement file named "TCF_BD30_MAR2006.mat". plottcf2 has several options for generating many other plots (e.g., Q vs T) in addition to TCF (f vs T).
pvar.m, v2.2	pvar.m performs a measurement of frequency versus heating power (DC voltage) for a resonator, measured using a network analyzer.
plotpvar.m	plotpvar.m plots the results from pvar.m.
VarBiasOsc.m, v2.2 VarBiasVclamp.m, v2.2 VarBiasVheat.m, v2.2	VarBiasOsc.m measures oscillator frequency versus bias voltage for a range of voltages. For example, `v = VarBiasOsc([8:12],'BD49',tools);` performs a measurement of oscillator frequency at 9, 10, 11, and 12 Volts bias. VarBiasVclamp.m and VarBiasVheat.m measure oscillator frequency versus oscillator clamp voltage and heating voltage, respectively.
timex.m, v1.42 toscfreqrec.m, tVhstablebeat.m tVHstablefreq.m tVHstableVrms.m tovenstable4.m tovenstable5.m tovenstable5f.m tovenstable5w.m tovenstable5wf.m	timex.m uses the MATLAB "timer" feature to perform a sub-function on a regular schedule, for example, recording data from an instrument. The issue is that when a MATLAB executes a statement inside a loop, the time of the loop execution is not guaranteed, and will vary significantly from one iteration to the next. This is important for analyzing oscillator data, as the algorithms assume a regular period for sampling the frequency signal. There are three main uses for timex.m: recording oscillator frequency from the counter at regular intervals, performing feedback control on the resonator, and monitoring the thermal chamber temperature to determine when it has stabilized.

Program Name and latest version	Description
	timex.m uses sub-functions, or "plug-ins", which are in separate files. For example, `v = timex('toscfreqrec',tools,1.3e6,1,100,1);` would attempt to execute the function in the file "toscfreqrec.m" every 1 seconds for 100 repetitions. Timestamps are recorded with every execution. All of the timex.m sub-functions written to date are designed for oscillator measurements. Sub-function names begin with a lower-case "t". timex.m sub-functions: toscfreqrec.m: record oscillator frequency from the counter, and one or two other pieces of data, e.g., RTD temperature or RMS voltage. tVhstableXXX.m: these functions are feedback controllers which attempt to stabilize the value of signal XXX using a DC heating voltage. 'beat' a beat frequency, read from counter2. 'freq' the counter frequency. Used for heater calibration. 'Vrms': the RMS detector output voltage. tovenstableXXX.m: these functions record the thermal chamber temperature and determine when it has reached the setpoint. Different versions use different input signals and algorithms to determine when the temperature has stabilized. '4': uses Toven and Tsensor '5': uses Toven and Tsensor_avg 'f': uses the oscillator frequency, f 'w': uses a self-adjusting "moving window" of data to determine if the temperature is varying periodically, as it does at low temperatures (< 0°C).
feedthru.m, v1.2	feedthru.m extracts the resonator response from a sweep measurement with a high level of feedthrough capacitance. For example: `ex = feedthru(res,cap);` returns the extracted measurement from the resonator measurement `res`, given the feedthrough measurement in `cap`. `res` and `cap` are measurement structures such as returned by measure_res.m or res_meas.m.

Program Name and latest version	Description
res_meas.m, v4.59 res_meas.fig res_feed.m, v1.2	res_meas.m is a graphical user interface (GUI) for the network analyzers and oscilloscopes. It has three main uses: 1) Download ("grab") data from an instrument and save to a file 2) Load and view saved data files. 3) Perform resonator sweep measurements (using measure_res.m). When doing a large number of measurements on a wafer using the probe station, res_meas.m can automate a good deal of tedious button-pushing. Also, it is often a good idea to test to resonator measurement using res_meas.m before starting a TCf experiment using TCf_res.m. res_feed.m performs an extraction of a resonator characteristics from noisy measurements performed with res_meas.m (res_feed.m uses feedthru.m). This typically used in probe station measurements (where the feedthrough capacitance is higher) and/or high frequency device measurements (where the output signal is lower).
StabFreqXX.m	StabFreqXX.m performs a feedback-based frequency stability experiment.
tempcompXX.m	tempcompXX.m performs a lookup table -based frequency stability experiment.
mnoise.m, v0.96	mnoise.m performs a noise density measurement using the HP89410A signal analyzer.
allan.m, v1.5	allan.m calculates the Allan deviation of a set of frequency data. It can work directly with counter data saved by timex.m, but can also be used for other data.

Ah, I see you have the machine that goes ping. This is my favorite.
-from The Meaning of Life, Monty Python

E. Quartz OCXO Datasheet

Comparisons are made to the Corning (now Vectron) ovenized quartz frequency reference, part C4550. The current datasheet for this part is included here for reference. Test results are presented in Chapter 5 for the specific part code C4550-D107. These results are shown in Figure E.1

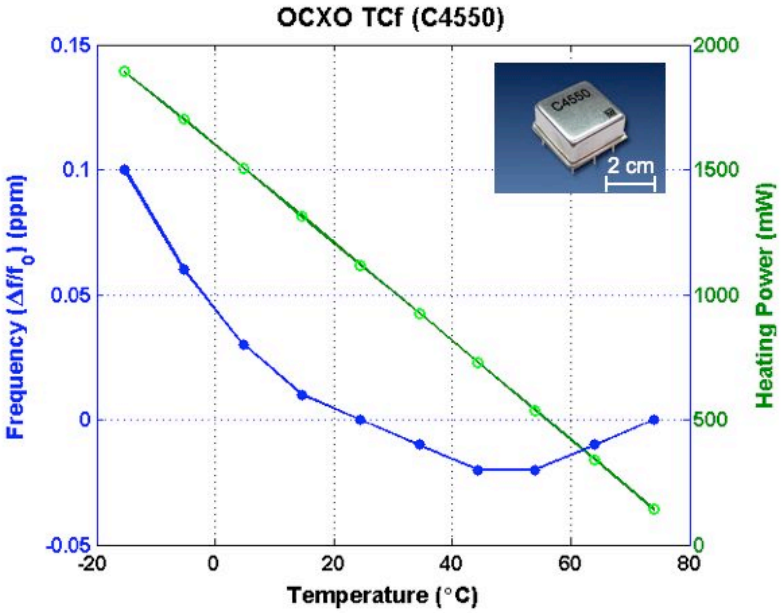

Figure E.1: TCf measurement of C4550 OCXO Frequency Reference
This figure is also shown in Chapter 5.

VECTRON INTERNATIONAL A DOVER COMPANY

C4550 OCXO

Typical Applications

Base Stations
Test Equipment
Synthesizers
Digital Switching

Features

Surface Mount Package Optional
Reflow Process Compatible Optional
AT-Cut and SC-Cut Crystal Options
Low Profile Compact Package

Previous Vectron Model Numbers 4853, 4853S, 4597, 4597S, 4859, 4859S, 4877, 4877S

Frequency range 10 MHz – 100 MHz

Standard frequencies 10; 12.8;13; 16.384;20; 32.768MHz; 100Mhz

Frequency stabilities[1] [AT Cut Crystal – Standard]

Parameter	Min	Typ	Max.	Units	Operating temp range	Ordering Code
vs. operating temperature range (Referenced to +25°C)	-50		+50	ppb	0 … +70°C	C508
	-100		+100	ppb	-20 … +70°C	D107
	-150		+150	ppb	-40 … +70°C	E157
	-200		+200	ppb	-40 … +85°C	F207
Parameter	**Min**	**Typ**	**Max.**	**Units**	**Condition**	
Initial tolerance	-300		+300	ppb	at time of shipment, nominal EFC	
vs. supply voltage change	-10		+10	ppb	V_S ± 5%	
vs. load change	-10		+10	ppb	Load ± 5%	
vs. aging /1 day	-2.0		+2.0	ppb	after 72 hours of operation	
vs aging /1 Year	-500		+500	ppb	after 72 hours of operation	
vs. aging / year (following Years)	-250		+250	ppb		
Warm-up Time			3	minutes	to ± 100ppb of final frequency (1 hour reading) @ +25°C	

Frequency stabilities[1] [SC Cut Crystal – Option]

Parameter	Min	Typ	Max.	Units	Operating temp range	Ordering Code
vs. operating temperature range (Referenced to +25°C)	-10		+10	ppb	0 … +70°C	C108
	-20		+20	ppb	-20 … +70°C	D208
	-25		+25	ppb	-40 … +70°C	E258
	-30		+30	ppb	-40 … +85°C	F308
Parameter	**Min**	**Typ**	**Max.**	**Units**	**Condition**	
Initial tolerance	-100		+100	ppb	at time of shipment, nominal EFC	
vs. supply voltage change	-5.0		+5.0	ppb	V_S ± 5%	
vs. load change	-5.0		+5.0	ppb	Load ± 5%	
vs. aging /1 day	-1.0		+1.0	ppb	after 72 hours of operation	
vs aging /1 Year	-100		+100	ppb	after 72 hours of operation	
vs. aging / year (following Years)	-50		+50	ppb		
Warm-up Time			3	minutes	to ± 10ppb of final frequency (1 hour reading) @ +25°C	

Supply voltage (Vs)

Parameter	Min	Typ	Max.	Units	Condition	Ordering Code
Supply voltage [Standard]	4.75	5	5.25	VDC		SV050
Supply voltage [Option]	11.4	12.0	12.6	VDC		SV120
Supply voltage [Option]	3.135	3.3	3.465	VDC		SV033
Power consumption			3.0	Watts	during warm-up	
			1.0	Watts	steady state @ +25°C	

Vectron International Headquarters
267 Lowell Road
Hudson, New Hampshire 03051
+1-888-328-7661 tel
+1-888-329-8328 fax

Vectron International LLC.
100 Watts Street
Mount Holly Springs, PA 17065
USA
+1 717-486-3411 tel
+1 717-486-5920 fax

Vectron International GmbH & Co. KG
Landstrasse
D-74924 Neckarbischofsheim
Germany
+49-07268-801-0 tel
+49-07268-801-281 fax

Vectron Asia Pacific Sales Office
Unit 3119 31st Floor, Jin Mao Tower, 88
Century Boulevard, Shanghai,
P.R. China 200120
+86 21 28909740 tel
+86 21 28909240 fax

RF output

Parameter	Min	Typ	Max.	Units	Condition	Ordering Code
Signal [Standard]		HCMOS				RFH
Load		15		pF		
Signal Level (Vol)			0.5	VDC	with Vs=12.0V or 5.0V and 15pF load	
			0.3	VDC	with Vs=3.3V and 15pF load	
Signal Level (Voh)	4.5			VDC	with Vs=12.0V or 5.0V and 15pF load	
	3.0			VDC	with Vs=3.3V and 15pF load	
Duty cycle	45		55	%	@ (Voh-Vol)/2	
Signal [Option]		Sinewave				RFS
Load		50				
Output Power	+3.0	+5.5	+8.0	dBm	50 Ohm load	
Harmonics			-30	dBc	50 Ohm load	

Frequency Tuning (EFC)

Parameter	Min	Typ	Max.	Units	Condition
Tuning Range	±0.75	±1.25	±2.0	ppm	with SC Cut Crystal
	±6.0	±8.0	±12	ppm	with AT Cut Crystal
Linearity			20	%	
Tuning Slope		Positive			
Control Voltage Range	0.0	2.0	4.0	VDC	with Vs=5.0VDC
	0.0	2.5	5.0	VDC	with Vs=12VDC
	0.0	1.4	2.8	VDC	with Vs=3.3VDC

Reference Voltage Output (Vref)

Parameter	Min	Typ	Max.	Units	Condition
Reference Voltage	3.92	4.0	4.08	VDC	with Vs=5.0VDC
	4.9	5.0	5.1	VDC	with Vs=12VDC
	2.75	2.8	2.85	VDC	with Vs=3.3VDC

Additional parameters

Parameter	Min	Typ	Max.	Units	Condition	
Phase Noise[3]			-80	dBc/Hz	1 Hz	with 10 MHz SC Cut
			-120	dBc/Hz	10 Hz	
			-140	dBc/Hz	100 Hz	
			-145	dBc/Hz	1 kHz	
			-150	dBc/Hz	10 kHz	
Phase Noise[3]			-75	dBc/Hz	1 Hz	with 10 MHz AT Cut
			-100	dBc/Hz	10 Hz	
			-130	dBc/Hz	100 Hz	
			-140	dBc/Hz	1 kHz	
			-150	dBc/Hz	10 kHz	
Weight			14	g		
Processing & Packing		Handling & processing note				

Absolute Maximum Ratings

Parameter	Min	Typ	Max.	Units	Condition
Supply voltage (Vs)			7.0	V	with Vs=5.0VDC
			15.0	V	with Vs=12VDC
			7.0	V	with Vs=3.3VDC
Output Load			50	pF	with HCMOS signal
			25	Ohms	with Sinewave signal
Operable temperature range	-55		+85	°C	
Storage temperature range	-55		+125	°C	

Vectron International Headquarters
267 Lowell Road
Hudson, New Hampshire 03051
+1-888-328-7661 tel
+1-888-329-8328 fax

Vectron International LLC.
100 Wallis Street
Mount Holly Springs, PA 17065
USA
+1 717-486-3411 tel
+1 717-486-5920 fax

Vectron International GmbH & Co. KG
Landstrasse
D-74924 Neckarbischofsheim
Germany
+49-07268-801-0 tel
+49-07268-801-281 fax

Vectron Asia Pacific Sales Office
Unit 3119 31st Floor, Jin Mao Tower, 88
Century Boulevard, Shanghai,
P.R. China 200120
+86 21 28909740 tel
+86 21 28909240 fax

Enclosures

Type A			Type B			Type C		
Package Codes:								
Code	Height "H"	Pin Length "L"	Code	Height "H"	Pin Length "L"	Code	Height "H"	Pin Length "L"
A1	11.25	6.35	B1	12.70	NA	C1	15.24	NA
A2	13.40	6.35	B2	15.24	NA	C2	13.00	NA
A3[5]	10.00	6.35	B3	11.30	NA	C3	11.70	NA

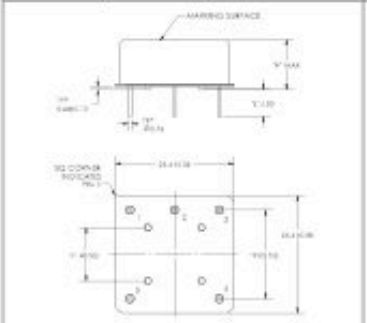

Dimensions: mm

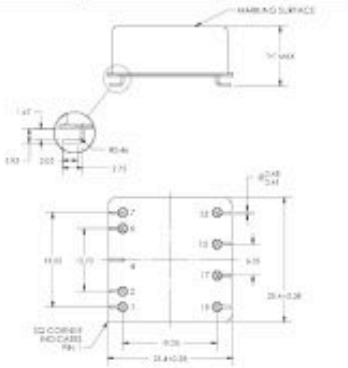

Dimensions: mm

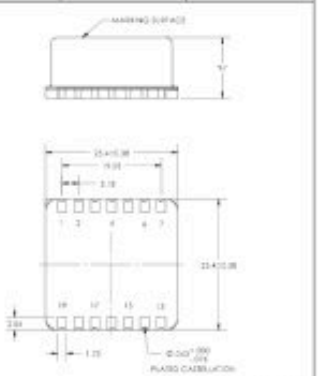

Dimensions: mm

Pin Connections	Pin Connections	Pin Connections
1 RF Output	1 RF Output	1 RF Output
2 Ground (Case)	2 N/C*	2 N/C*
3 Electronic Frequency Control Input (EFC)	4 Ground (Case)	4 Ground (Case)
4 Reference Voltage Output	6 N/C*	6 N/C*
5 Supply Voltage Input (Vs)	7 Electronic Frequency Control Input (EFC)	7 Electronic Frequency Control Input (EFC)
	13 Reference Voltage Output (Vref)	13 Reference Voltage Output (Vref)
	15 N/C*	15 N/C*
	17 N/C*	17 N/C*
	19 Supply Voltage Input (Vs)	19 Supply Voltage Input (Vs)

Standard Shipping Method (For SMD Type B and C Packages)

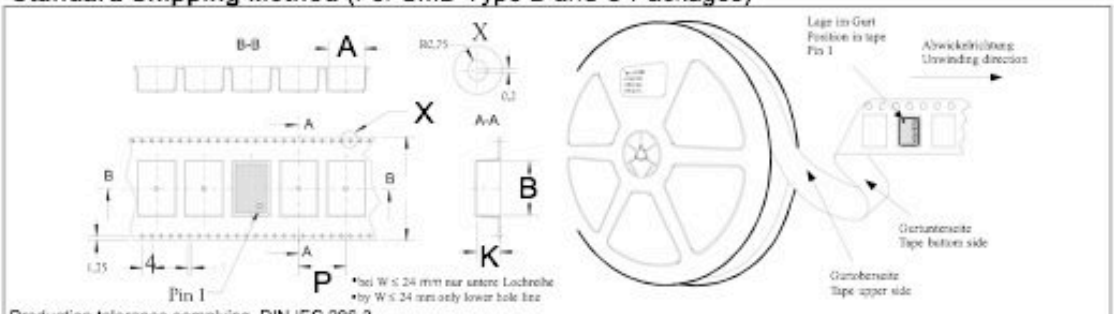

Production tolerance complying DIN IEC 286-3

Enclosure Type	Tape width W [mm]	Quantity per meter	Quantity per reel	Dimension P
Type B	44	33.3	250	34
Type C	44	33.3	250	34

Vectron International
Headquarters
267 Lowell Road
Hudson, New Hampshire 03051
+1-888-328-7661 tel
+1-888-329-8328 fax

Vectron International LLC.
100 Watts Street
Mount Holly Springs, PA 17065
USA
+1 717-486-3411 tel
+1 717-486-5920 fax

Vectron International GmbH & Co. KG
Landstrasse
D-74924 Neckarbischofsheim
Germany
+49-07268-801-0 tel
+49-07268-801-281 fax

Vectron Asia Pacific Sales Office
Unit 3119 31st Floor, Jin Mao Tower, 88
Century Boulevard, Shanghai,
P.R. China 200120
+86 21 28909740 tel
+86 21 28909240 fax

Recommended Reflow Profile

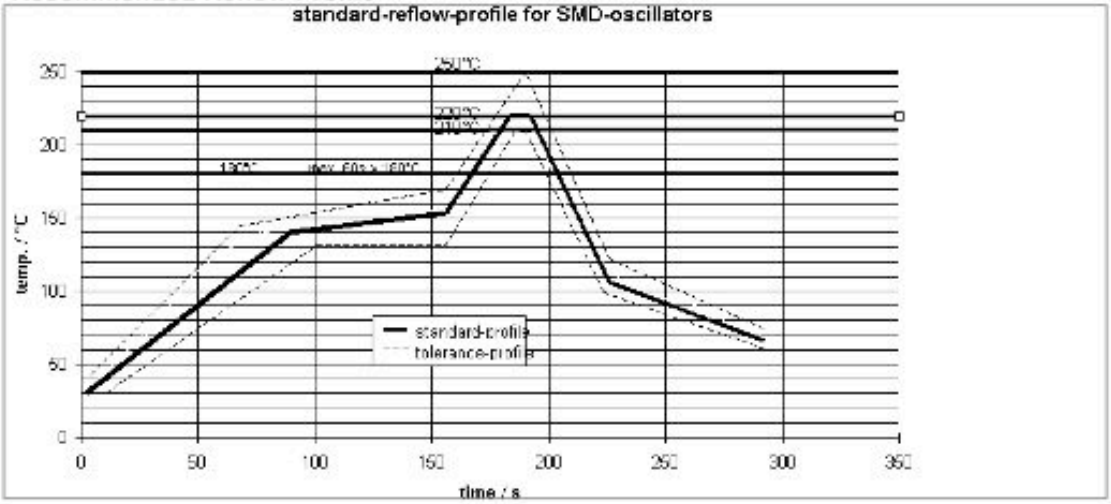

How to Order this Product:

Step 1	Use this worksheet to forward the following information to your factory representative:					
Model	Stability Code	Supply Voltage Code	RF Output Code	Package Code	Frequency
C4550					
Example: C4550	*D207*	*SV050*	*RFH*	*A1*	*10.000Mhz*

Step 2	The factory representative will then respond with a Vectron Model Number in the following configuration:		
Model	Package Code	Dash	Dash Number
C4550	[Customer Specified Package Code]	-	[Factory Generated 4 digit number]

Typical P/N = C4550A1-0001

Notes:

1. Contact factory for improved stabilities or additional product options. Not all options and codes are available at all frequencies.
2. Unless otherwise stated all values are valid after warm-up time and refer to typical conditions for supply voltage, frequency control voltage, load, temperature (25°C)
3. Phase noise degrades with increasing output frequency.
4. Subject to technical modification.
5. Contact factory for availability.

Vectron International Headquarters
267 Lowell Road
Hudson, New Hampshire 03051
+1-888-328-7661 tel
+1-888-329-8328 fax

Vectron International LLC.
100 Watts Street
Mount Holly Springs, PA 17065
USA
+1 717-486-3411 tel
+1 717-486-5920 fax

Vectron International GmbH & Co. KG
Landstrasse
D-74924 Neckarbischofsheim
Germany
+49-07268-801-0 tel
+49-07268-801-281 fax

Vectron Asia Pacific Sales Office
Unit 3119 31st Floor, Jin Mao Tower, 88
Century Boulevard, Shanghai,
P.R. China 200120
+86 21 28909740 tel
+86 21 28909240 fax

References

[1] I. Newton, "Longitude at sea. To consider what encouragement was fit to be given to such as should find longitude at sea.," UK House of Commons; Committee Who Were to Consider of What Encouragement...as Should Find Out the Longitude at Sea, London, 1714.

[2] D. Sobel, Longitude, The Story of a Lone Genius Who Solved the Greatest Scientific Problem of His Time. London, UK: Penguin Books Ltd, 1995.

[3] J. Bouchaud and B. Knoblich, "Has the time come for MEMS oscillators?," Wicht Technologie Consulting, Munich, Newsletter, 2006.

[4] W. G. Cady, "The Piezo-Electric Resonator," Proceedings of the IRE, vol. 10, pp. 83-114, 1922.

[5] W. A. Marrison, "Evolution of quartz crystal clock," Bell System Technical Journal, vol. 27, pp. 510-588, 1948.

[6] J. R. Vig and A. Ballato, "Frequency Control Devices," in Ultrasonic Instruments and Devices, E. P. Papadakis, Ed.: Academic Press, 1999, pp. 637-697.

[7] J. R. Vig, "Quartz Crystal Resonators and Oscillators for Frequency Control and Timing Applications - A Tutorial," US Army Communications-Electronics Research, Development & Engineering Center, Fort Monmouth, NJ USA, Powerpoint Presentation rev 8.5.3.0, 2005.

[8] C. T. C. Nguyen, "MEMS technology for timing and frequency control," IEEE Transactions on Ultrasonics, Ferroelectrics and Frequency Control, vol. 54, pp. 251-270, 2007.

[9] G. Moore, "Cramming More Components Onto Integrated Circuits," Electronics, vol. 38, 1965.

[10] H. Weinberg, "MEMS Sensors Are Driving the Automotive Industry," in Sensors, vol. 19, 2002.

[11] Texas Instruments, "How DLP technology works", online at: http://www.dlp.com/

[12] Y. Eo, S. Hyun, K. Lee, G. Oh, and J.-W. Lee, "Reference SAW oscillator on quartz-on-silicon (QoS) wafer for polylithic integration of true single chip radio," Electron Device Letters, vol. 21, pp. 393-395, 2000.

[13] R. L. Kubena, F. P. Stratton, D. T. Chang, R. J. Joyce, T. Y. Hsu, M. K. Lim, and R. T. M'Closkey, "Next Generation Quartz Oscillators and Filters for VHF-UHF Systems," presented at IEEE MTT-S International Microwave Symposium, San Francisco, CA, 2006.

[14] R. N. Candler, M. A. Hopcroft, B. Kim, W. T. Park, R. Melamud, M. Agarwal, G. Yama, A. Partridge, M. Lutz, and T. W. Kenny, "Long-Term and Accelerated Life Testing of a Novel Single-Wafer Vacuum Encapsulation for MEMS Resonators," Journal of Microelectromechanical Systems, vol. 15, pp. 1446-1456, 2006.

[15] A. Partridge, A. E. Rice, T. W. Kenny, and M. Lutz, "New thin film epitaxial polysilicon encapsulation for piezoresistive accelerometers," presented at MEMS 2001, the 14th IEEE International Conference on Micro Electro Mechanical Systems, Interlaken, Switzerland, 2001.

[16] W.-T. Park, R. N. Candler, H. Li, J. Cho, H. Li, T. W. Kenny, A. Partridge, G. Yama, and M. Lutz, "Wafer Scale Encapsulation of MEMS Devices," presented at InterPack 2003, International Packaging and Technical Conference and Exhibition, Maui, Hawaii USA, 2003.

[17] R. N. Candler, W.-T. Park, H. Li, G. Yama, A. Partridge, M. Lutz, and T. W. Kenny, "Single wafer encapsulation of MEMS devices," IEEE Transactions on Advanced Packaging, vol. 26, pp. 227-232, 2003.

[18] W. E. Newell, "Miniaturization of Tuning Forks," Science, pp. 1320-1326, 1968.

[19] H. C. Nathanson, W. E. Newell, R. A. Wickstrom, and J. R. Davis, Jr., "The Resonant Gate Transistor," Electron Devices, IEEE Transactions on, vol. 14, pp. 117-133, 1967.

[20] R. A. Buser and N. F. de Rooij, "Resonant silicon structures," Sensors and Actuators, vol. 17, pp. 145-154, 1989.

[21] G. Stemme, "Resonant silicon sensors," Journal of Micromechanics and Microengineering, vol. 1, pp. 113, 1991.

[22] R. N. Kleiman, G. K. Kaminsky, J. D. Reppy, R. Pindak, and D. J. Bishop, "Single-crystal silicon high-Q torsional oscillators," Review of Scientific Instruments, vol. 56, pp. 2088-2091, 1985.

[23] R. T. Howe and R. S. Muller, "Resonant-microbridge vapor sensor," IEEE Transactions on Electron Devices, vol. 33, pp. 499-506, 1986.
[24] T. P. Burg, A. R. Mirza, N. Milovic, C. H. Tsau, G. A. Popescu, J. S. Foster, and S. R. Manalis, "Vacuum-Packaged Suspended Microchannel Resonant Mass Sensor for Biomolecular Detection," Journal Microelectromechanical Systems, vol. 15, pp. 1466-1476, 2006.
[25] P. Parsons, A. Glendinning, and D. Angelidis, "Resonant sensors for high accuracy pressure measurement using silicon technology," presented at National Aerospace and Electronics Conference, 1992. NAECON 1992., Proceedings of the IEEE 1992, 1992.
[26] E. Stemme and G. Stemme, "A Balanced Resonant Pressure Sensor," Sensors and Actuators A: Physical, vol. 21, pp. 336-341, 1990.
[27] J. C. Greenwood, "Silicon in mechanical sensors," Journal of Physics E: Scientific Instruments, pp. 1114-1128, 1988.
[28] T. A. W. Roessig, Integrated MEMS Tuning Fork Oscillators for Sensor Applications, thesis in Mechanical Engineering at University of California, Berkeley, 1998.
[29] W. Yun, R. T. Howe, and P. R. Gray, "Surface micromachined, digitally force-balanced accelerometer with integrated CMOS detection circuitry," presented at Hilton Head 1992, the IEEE Solid-State Sensor and Actuator Workshop, Hilton Head, SC USA, 1992.
[30] H. C. Kim, S. Seok, I. Kim, S.-D. Choi, and K. Chun, "Inertial-Grade Out-of-Plane and In-Plane Differential Resonant Silicon Accelerometers (DRXLs) " presented at TRANSDUCERS '05, Solid-State Sensors, Actuators and Microsystems, Seoul, ROK, 2005.
[31] W.-T. Hsu, J. R. Clark, and C. T.-C. Nguyen, "A resonant temperature sensor based on electrical spring softening," presented at TRANSDUCERS '01 / Eurosensors XV, The 11th International Conference on Solid-State Sensors and Actuators, Munich, Germany, 2001.
[32] L. Lin, R. T. Howe, and A. P. Pisano, "Microelectromechanical filters for signal processing," Journal of Microelectromechanical Systems, vol. 7, pp. 286-294, 1998.
[33] C. T.-C. Nguyen, "Microelectromechanical devices for wireless communications," presented at MEMS '98, 11th Annual International Workshop on Micro Electro Mechanical Systems, Heidelberg, Germany, 1998.
[34] L. S. Fan, Y. C. Tai, and R. S. Muller, "Integrated movable micromechanical structures for sensors and actuators," Electron Devices, IEEE Transactions on, vol. 35, pp. 724-730, 1988.
[35] W. C. Tang, T.-C. H. Nguyen, and R. T. Howe, "Laterally Driven Polysilicon Resonant Microstructures," Sensors and Actuators, vol. 20, pp. 25-32, 1989.
[36] T. V. Roszhart, "Micromachined silicon resonators," presented at Electro International/91, New York, NY USA, 1991.
[37] L. Lin, C. T.-C. Nguyen, R. T. Howe, and A. P. Pisano, "Microelectromechanical filters for signal processing," presented at MEMS '92, An Investigation of Micro Structures, Sensors, Actuators, Machines and Robots, 1992.
[38] Y.-W. Lin, S. Lee, S.-S. Li, Y. Xie, Z. Ren, and C. T. C. Nguyen, "Series-resonant VHF micromechanical resonator reference oscillators," IEEE Journal of Solid-State Circuits, vol. 39, pp. 2477-91, 2004.
[39] K. S. Lebouitz, A. Mazaheri, R. T. Howe, and A. P. Pisano, "Vacuum encapsulation of resonant devices using permeable polysilicon," presented at MEMS '99, 12th Annual International Workshop on Micro Electro Mechanical Systems, Orlando, FL USA, 1999.
[40] G. K. Ho, K. Sundaresan, S. Pourkamali, and F. Ayazi, "Temperature compensated IBAR reference oscillators," presented at MEMS 2006, the 19th IEEE International Conference on Micro Electro Mechanical Systems, Istanbul, Turkey, 2006.
[41] O. Holmgren, K. Kokkonen, T. Mattila, V. Kaajakari, A. Oja, J. Kiihamaki, J. V. Knuuttila, and M. M. Salomaa, "Imaging of in- and out-of-plane vibrations in micromechanical resonator," Electronics Letters, vol. 41, pp. 121-122, 2005.
[42] C. T. C. Nguyen and R. T. Howe, "An integrated CMOS micromechanical resonator high-Q oscillator," IEEE Journal of Solid-State Circuits, vol. 34, pp. 440-55, 1999.
[43] Y.-W. Lin, S. Lee, S.-S. Li, Y. Xie, Z. Ren, and C. T. C. Nguyen, "60-MHz wine-glass micromechanical-disk reference oscillator," presented at International Solid-State Circuits Conference, 2004.

[44] S. Lee, M. U. Demirci, and C. T. C. Nguyen, "A 10-MHz micromechanical resonator Pierce reference oscillator for communications," presented at TRANSDUCERS '01. EUROSENSORS XV. 11th International Conference on Solid-State Sensors and Actuators, Munich, Germany, 2001.
[45] P. Rantakari, V. Kaajakari, T. Mattila, J. Kiihamaki, A. Oja, I. Tittonen, and H. Seppa, "Low noise, low power micromechanical oscillator," presented at TRANSDUCERS '05, Solid-State Sensors, Actuators and Microsystems, Seoul, ROK, 2005.
[46] T. A. Roessig, R. T. Howe, and A. P. Pisano, "Nonlinear mixing in surface-micromachined tuning fork oscillators," presented at FCS '97, The 1997 IEEE International Frequency Control Symposium, 1997.
[47] K. Sundaresan, G. K. Ho, S. Pourkamali, and F. Ayazi, "A two-chip, 4-MHz, microelectromechanical reference oscillator," presented at ISCAS 2005, IEEE International Symposium on Circuits and Systems, 2005.
[48] E. P. Quévy and R. T. Howe, "Redundant MEMS resonators for precise reference oscillators," presented at RFIC 2005, The 2005 IEEE Radio Frequency Integrated Circuits Symposium, Long Beach, CA USA, 2005.
[49] V. Kaajakari, J. Kiihamaki, A. Oja, S. Pietikainen, V. Kokkala, and H. Kuisma, "Stability of wafer level vacuum encapsulated single-crystal silicon resonators," Sensors and Actuators A: Physical, vol. 130-131, pp. 42-47, 2006.
[50] R. L. Filler and J. R. Vig, "Long-term aging of oscillators," IEEE Transactions on Ultrasonics, Ferroelectrics and Frequency Control, vol. 40, pp. 387-394, 1993.
[51] J. R. Vig, "Resonator Aging," presented at Ultrasonics Symposium, 1977.
[52] Vectron, Inc., "C4500 Ovenized Crystal Oscillator (OCXO)", 2006
[53] D. W. Allan, "Time and Frequency (Time-Domain) Characterization, Estimation, and Prediction of Precision Clocks and Oscillators," IEEE Transactions on Ultrasonics, Ferroelectrics and Frequency Control, vol. 34, pp. 647-654, 1987.
[54] Hewlett-Packard Company, "The Science of Timekeeping", 1997
[55] Hewlett-Packard Company, "GPS and Precision Timing Applications", 1996
[56] National Institute of Standards and Technology, "NIST-F1 Cesium Fountain Atomic Clock", online at: http://tf.nist.gov/cesium/fountain.htm
[57] E. Momosaki, "A brief review of progress in quartz tuning fork resonators," presented at FCS '97, The 1997 IEEE International Frequency Control Symposium, 1997.
[58] A. P. Partridge, Lateral Piezoresistive Accelerometer with Epipoly Encapsulation, thesis in Electrical Engineering at Stanford University, 2002.
[59] W.-T. Park, A. Partridge, R. N. Candler, V. Ayanoor-Vitikkate, G. Yama, M. Lutz, and T. W. Kenny, "Encapsulated submillimeter piezoresistive accelerometers," Journal of Microelectromechanical Systems, vol. 15, pp. 507-514, 2006.
[60] K. Petersen, "Silicon as a Mechanical Material," Proceedings of the IEEE, vol. 70, pp. 420-457, 1982.
[61] K. Sato, M. Shikida, T. Yoshioka, T. Ando, and T. Kawabata, "Micro tensile-test of silicon film having different crystallographic orientations," presented at TRANSDUCERS '97, the 9th International Conference on Solid State Sensors and Actuators, Chicago, IL USA, 1997.
[62] S. Nakao, T. Ando, M. Shikida, and K. Sato, "Temperature-dependent fracture toughness of single-crystal-silicon film," presented at TRANSDUCERS '05, Solid State Sensors, Actuators, and Microsystems, Seoul, ROK, 2005.
[63] H. Kahn, R. Ballarini, and A. H. Heuer, "Dynamic fatigue of silicon," Current Opinion in Solid State and Materials Science, vol. 8, pp. 71-76, 2004.
[64] C. L. Muhlstein, S. B. Brown, and R. O. Ritchie, "High-cycle fatigue of single-crystal silicon thin films," Journal of Microelectromechanical Systems, vol. 10, pp. 593-600, 2001.
[65] T. Namazu, Y. Isono, and T. Tanaka, "Evaluation of size effect on mechanical properties of single crystal silicon by nanoscale bending test using AFM," Journal of Microelectromechanical Systems, vol. 9, pp. 450-459, 2000.
[66] N. E. Aksenov, "http://onlineheavytheory.net/silicon.html", online

[67] K. Najafi, "Micropackaging Technologies for Integrated Microsystems: Applications to MEMS and MOEMS," presented at Micromachining and Microfabrication Process Technology VIII, San Jose, CA, USA, 2003.
[68] R. Knechtel, "Glass frit bonding: an universal technology for wafer level encapsulation and packaging," Microsystem Technologies, vol. 12, pp. 63-68, 2005.
[69] M. Lutz, W. Golderer, J. Gerstenmeier, J. Marek, B. Maihofer, S. Mahler, H. Munzel, and U. Bischof, "A precision yaw rate sensor in silicon micromachining," presented at TRANSDUCERS '97, the 9th International Conference on Solid State Sensors and Actuators, Chicago, IL USA, 1997.
[70] T. Corman, P. Enoksson, and G. Stemme, "Low-pressure-encapsulated resonant structures with integrated electrodes for electrostatic excitation and capacitive detection," Sensors and Actuators A: Physical, vol. 66, pp. 160-166, 1998.
[71] X. Du, D. Zhang, and T. Lee, "Chip level packaging for MEMS using silicon cap," presented at Electronics Manufacturing Technology Symposium, 2004.
[72] Y.-T. Cheng, W.-T. Hsu, K. Najafi, C. T.-C. Nguyen, and L. Lin, "Vacuum packaging technology using localized aluminum/silicon-to-glass bonding," Journal of Microelectromechanical Systems, vol. 11, pp. 556-565, 2002.
[73] L.-S. Huang, E. M. S.-S. Lee, M. C. Wu, and C.-J. Kim, "MEMS Packaging for Micro Mirror Switches," presented at ECTC '98, 48th Electronic Components & Technology Conference, Seattle, WA, USA, 1998.
[74] J. Oberhammer, F. Niklaus, and G. Stemme, "Sealing of adhesive bonded devices on wafer level," Sensors and Actuators A: Physical, vol. 110, pp. 407-412, 2004.
[75] D. Sparks, S. Massoud-Ansari, and N. Najafi, "Long-term evaluation of hermetically glass frit sealed silicon to Pyrex wafers with feedthroughs," Journal of Micromechanics and Microengineering, vol. 15, pp. 1560, 2005.
[76] R. Legtenberg and H. A. C. Tilmans, "Electrostatically driven vacuum-encapsulated polysilicon resonators Part I. Design and fabrication," Sensors and Actuators A: Physical, vol. 45, pp. 57-66, 1994.
[77] C. Liu and Y.-C. Tai, "Sealing of micromachined cavities using chemical vapor deposition methods: characterization and optimization," Journal Microelectromechanical Systems, vol. 8, pp. 135-145, 1999.
[78] H. Guckel, J. J. Sniegowski, T. R. Christenson, and F. Raissi, "The application of fine-grained, tensile polysilicon to mechanicaly resonant transducers," Sensors and Actuators A: Physical, vol. 21, pp. 346-351, 1990.
[79] K. Ikeda, H. Kuwayama, T. Kobayashi, T. Watanabe, T. Nishikawa, T. Yoshida, and K. Harada, "Three-dimensional micromachining of silicon pressure sensor integrating resonant strain gauge on diaphragm," Sensors and Actuators A: Physical, vol. 23, pp. 1007-1010, 1990.
[80] A. J. Gallant and D. Wood, "Surface micromachined membranes for wafer level packaging," Journal of Micromechanics and Microengineering, vol. 15, pp. S47-S52, 2005.
[81] B. H. Stark and K. Najafi, "A low-temperature thin-film electroplated metal vacuum package," Journal of Microelectromechanical Systems, vol. 13, pp. 147-157, 2004.
[82] P. Monajemi, F. Ayazi, P. J. Joseph, and P. A. Kohl, "A low cost wafer-level MEMS packaging technology," presented at MEMS 2005, the 18th IEEE International Conference on Micro Electro Mechanical Systems, 2005.
[83] K. S. Lebouitz, R. T. Howe, and A. P. Pisano, "Permeable Polysilicon Etch-access Windows For Microshell Fabrication," presented at TRANSDUCERS '95, Solid-State Sensors and Actuators and Eurosensors IX, Stockholm, 1995.
[84] R. L. Alley, G. J. Cuan, R. T. Howe, and K. Komvopoulos, "The effect of release-etch processing on surface microstructure stiction," presented at Hilton Head 1992, the IEEE Solid-State Sensor and Actuator Workshop, Hilton Head, SC USA, 1992.
[85] G. T. Mulhern, D. S. Soane, and R. T. Howe, "Supercritical Carbon Dioxide Drying of Microstructures," presented at TRANSDUCERS '93, the International Conderence on Solid-State Sensors and Actuators, Yokohama, Japan, 1993.

[86] C. W. Dyck, J. H. Smith, S. L. Miller, E. M. Russnick, and C. L. J. Adkins, "Supercritical carbon dioxide solvent extraction from surface-micromachined micromechanical structures," presented at Micromachining & Microfabrication Conference, Austin, TX USA, 1996.
[87] Y. I. Lee, K. H. Park, J. Lee, C. S. Lee, H. J. Yoo, C. J. Kim, and Y. S. Yoon, "Dry release for surface micromachining with HF vapor-phase etching," Journal of Microelectromechanical Systems, vol. 6, pp. 226-233, 1997.
[88] B. Diem, J. C. Barbe, F. de Crecy, S. Giroud, D. Renaud, H. Grange, J. Hammond, J. Vandemeer, R. Roop, and B. Gogoi, "Polysilicon packaging and a new anchoring technology for thick SOI MEMS - dynamic response model and application to over-damped inertial sensors," presented at TRANSDUCERS '05, Solid-State Sensors, Actuators and Microsystems, 2005.
[89] D. G. Jones, R. G. Azevedo, M. W. Chan, A. P. Pisano, and M. B. J. Wijesundara, "Low Temperature Ion Beam Sputter Deposition of Amorphous Silicon Carbide for Wafer-Level Vacuum Sealing," presented at MEMS 2007, The 20th IEEE International Conference on Micro Electro Mechanical Systems, Kobe, Japan, 2007.
[90] B. Kim, R. N. Candler, M. A. Hopcroft, M. Agarwal, W.-T. Park, and T. W. Kenny, "Frequency stability of wafer-scale film encapsulated silicon based MEMS resonators," Sensors and Actuators A: Physical, vol. 136, pp. 125-131, 2007.
[91] B. Kim, R. N. Candler, M. Hopcroft, M. Agarwal, W.-t. Park, J. T. Li, and T. Kenny, "Investigation of MEMS Resonator Characteristics During Long-term Operation and Wide Temperature Variation Operation," presented at IMECE '04, the ASME International Mechanical Engineering Congress and Exposition, Anahiem, CA USA, 2004.
[92] M. Koskenvuori, T. Mattila, A. Haara, J. Kiihamaki, I. Tittonen, A. Oja, and H. Seppa, "Long-term stability of single-crystal silicon microresonators," Sensors and Actuators A: Physical, vol. 115, pp. 23-27, 2004.
[93] A. A. Ayón, R. Braff, C. C. Lin, H. H. Sawin, and M. A. Schmidt, "Characterization of a Time Multiplexed Inductively Coupled Plasma Etcher," Journal of The Electrochemical Society, vol. 146, pp. 339-349, 1999.
[94] S. Pourkamali and F. Ayazi, "Fully single crystal silicon resonators with deep-submicron dry-etched transducer gaps," presented at MEMS '04, 17th IEEE International Conference on Micro Electro Mechanical Systems, Maastricht, 2004.
[95] S. A. Campbell, The science and engineering of microelectronic fabrication. New York: Oxford University Press, 1996.
[96] M. J. Madou, Fundamentals of Microfabrication, 2nd ed: CRC Press LLC, 2001.
[97] M.-C. M. Lee and M. C. Wu, "3D Silicon Transformation Using Hydrogen Annealing," presented at Hilton Head 2004, the IEEE Solid-State Sensor, Actuator and Microsystems Workshop, Hilton Head, SC USA, 2004.
[98] S. D. Senturia, Microsystem Design: Kluwer Academic Publishers, 2001.
[99] C. Liu, Foundations of MEMS: Pearson Education, Inc., 2006.
[100] D. J. Gorman, Free vibration analysis of beams and shafts. New York: John Wiley and Sons, 1975.
[101] S. Timoshenko, D. H. Young, and W. Weaver, Vibration Problems in Engineerig, 4th ed. New York: John Wiley and Sons, 1974.
[102] R. D. Blevins, Formulas for natural frequency and mode shape. New York: Van Nostrand Reinhold, 1979.
[103] R. N. Candler, Thermoelastic Dissipation in Silicon Micromechanical Resonators, thesis in Electrical Engineering at Stanford University, 2006.
[104] W. C. Young, Roark's Formulas for Stress and Strain, 6th ed: McGraw-Hill, Inc., 1989.
[105] V. Kaajakari, T. Mattila, A. Oja, and H. Seppa, "Nonlinear limits for single-crystal silicon microresonators," Journal of Microelectromechanical Systems, vol. 13, pp. 715-724, 2004.
[106] T. Mattila, J. Kiihamaki, T. Lamminmaki, O. Jaakkola, P. Rantakari, A. Oja, H. Seppa, H. Kattelus, and I. Tittonen, "A 12 MHz micromechanical bulk acoustic mode oscillator," Sensors and Actuators A: Physical, vol. 101, pp. 1-9, 2002.

[107] S. Pamidighantam, R. Puers, K. Baert, and H. A. C. Tilmans, "Pull-in voltage analysis of electrostatically actuated beam structures with fixed-fixed and fixed-free end conditions," Journal of Micromechanics and Microengineering, vol. 12, pp. 438-443, 2002.
[108] V. Kaajakari, "Nonlinearity in Micromechanical Resonators: A Tutorial", online at: http://www.kaajakari.net/~ville/research/tutorials/tutorials.html
[109] M. Agarwal, K. K. Park, R. N. Candler, M. A. Hopcroft, C. M. Jha, R. Melamud, B. Kim, B. Murmann, and T. W. Kenny, "Non-Linearity Cancellation in MEMS Resonator for Improved Power Handling," presented at IEEE International Electron Devices Meeting, Washington, DC USA, 2005.
[110] W. T. Hsu, Temperature Insensitive Micromechanical Resonators, thesis in Electrical Engineering at University of Michigan, 2001.
[111] M. Agarwal, S. A. Chandorkar, R. N. Candler, B. Kim, M. A. Hopcroft, R. Melamud, C. M. Jha, T. W. Kenny, and B. Murmann, "Optimal drive condition for nonlinearity reduction in electrostatic microresonators," Applied Physics Letters, vol. 89, pp. 214105-7, 2006.
[112] J. J. Gagnepain, "Nonlinear Properties of Quartz Crystal and Quartz Resonators: A Review," presented at FCS '81, The 35th Annual Symposium on Frequency Control, 1981.
[113] M. W. Putty, S. C. Chang, R. T. Howe, A. L. Robinson, and K. D. Wise, "One-port active polysilicon resonant microstructures," presented at MEMS '89, An Investigation of Micro Structures, Sensors, Actuators, Machines and Robots, Salt Lake City, USA, 1989.
[114] J. R. Clark and C. T.-C. Nguyen, "Measurement techniques for capacitively-transduced VHF-to-UHF micromechanical resonators," presented at TRANSDUCERS '01 / Eurosensors XV, The 11th International Conference on Solid-State Sensors and Actuators, Munich, Germany, 2001.
[115] B. Kim, C. M. Jha, T. White, R. N. Candler, M. A. Hopcroft, M. Agarwal, K. K. Park, R. Melamud, and T. W. Kenny, "Temperature Dependence of Quality Factor in MEMS Resonators," presented at MEMS 2006, The 19th IEEE International Conference on Micro Electro Mechanical Systems, Istanbul, Turkey, 2006.
[116] Y.-H. Park and K. C. Park, "High-fidelity modeling of MEMS resonators. Part I. Anchor loss mechanisms through substrate," Jounral of Microelectromechanical Systems, vol. 13, pp. 238-247, 2004.
[117] B. L. Foulgoc, T. Bourouina, O. L. Traon, A. Bosseboeuf, F. Marty, C. Breluzeau, J.-P. Grandchamp, and S. Masson, "Highly decoupled single-crystal silicon resonators: an approach for the intrinsic quality factor," Journal of Micromechanics and Microengineering, vol. 16, pp. S45-S53, 2006.
[118] K. Y. Yasumura, T. D. Stowe, E. M. Chow, T. Pfafman, T. W. Kenny, B. C. Stipe, and D. Rugar, "Quality factors in micron- and submicron-thick cantilevers," Journal of Microelectromechanical Systems, vol. 9, pp. 117-125, 2000.
[119] F. D. Bannon, J. R. Clark, and C. T.-C. Nguyen, "High-Q HF microelectromechanical filters," IEEE Journal of Solid-State Circuits, vol. 35, pp. 512-526, 2000.
[120] C. Zener, "Internal Friction in Solids. I. Theory of Internal Friction in Reeds," Physical Review, vol. 52, pp. 230, 1937.
[121] C. Zener, "Internal Friction in Solids II. General Theory of Thermoelastic Internal Friction," Physical Review, vol. 53, pp. 90, 1938.
[122] T. V. Roszhart, "The effect of thermoelastic internal friction on the Q of micromachined silicon resonators," presented at Hilton Head '90, the Solid-State Sensor and Actuator Workshop, Hilton Head, SC USA, 1990.
[123] R. N. Candler, A. Duwel, M. Varghese, S. A. Chandorkar, M. A. Hopcroft, W.-T. Park, K. Bongsang, G. Yama, A. Partridge, M. Lutz, and T. W. Kenny, "Impact of geometry on thermoelastic dissipation in micromechanical resonant beams," Journal of Microelectromechanical Systems, vol. 15, pp. 927-934, 2006.
[124] A. Duwel, R. N. Candler, T. W. Kenny, and M. Varghese, "Engineering MEMS Resonators With Low Thermoelastic Damping," Journal of Microelectromechanical Systems, vol. 15, pp. 1437-1445, 2006.

[125] K. G. Lyon, G. L. Salinger, C. A. Swenson, and G. K. White, "Linear thermal expansion measurements on silicon from 6 to 340 K," Journal of Applied Physics, vol. 48, pp. 865-868, 1977.
[126] M. Asheghi, K. Kurabayashi, R. Kasnavi, and K. E. Goodson, "Thermal conduction in doped single-crystal silicon films," Journal of Applied Physics, vol. 91, pp. 5079-5088, 2002.
[127] C. J. Glassbrenner and G. A. Slack, "Thermal Conductivity of Silicon and Germanium from 3°K to the Melting Point," Physical Review, vol. 134, pp. A1058, 1964.
[128] Y. Okada and Y. Tokumaru, "Precise determination of lattice parameter and thermal expansion coefficient of silicon between 300 and 1500 K," Journal of Applied Physics, vol. 56, pp. 314-320, 1984.
[129] V. M. Glazov and A. S. Pashinkin, "The Thermophysical Properties (Heat Capacity and Thermal Expansion) of Single-Crystal Silicon," High Temperature, vol. 39, pp. 413-419, 2001.
[130] C. Bourgeois, E. Steinsland, N. Blanc, and N. F. de Rooij, "Design of resonators for the determination of the temperature coefficients of elastic constants of monocrystalline silicon," presented at FCS '97, The 1997 IEEE International Frequency Control Symposium, 1997.
[131] J.-h. Jeong, S.-h. Chung, S.-H. Lee, and D. Kwon, "Evaluation of elastic properties and temperature effects in Si thin films using an electrostatic microresonator," Journal of Microelectromechanical Systems, vol. 12, pp. 524-530, 2003.
[132] S. Nikanorov, Y. A. Burenkov, and A. Stepanov, "Elastic Properties of Silicon," Fizika Tverdogo Tela (Soviet Physics Solid State), vol. 13, pp. 3001-4, 1971.
[133] Y. A. Burenkov and S. Nikanorov, "Temperature dependence of the elastic constants of silicon," Fizika Tverdogo Tela (Soviet Physics Solid State), vol. 16, pp. 1496-8, 1974.
[134] Wikipedia, "Lennard-Jones potential", Published by Wikipedia, The Free Encyclopedia, online at: http://en.wikipedia.org/w/index.php?title=Lennard-Jones_potential&oldid=139923879
[135] R. A. Aziz, "A highly accurate interatomic potential for argon," The Journal of Chemical Physics, vol. 99, pp. 4518-4525, 1993.
[136] H. J. McSkimin, "Measurement of Elastic Constants at Low Temperatures by Means of Ultrasonic Waves--Data for Silicon and Germanium Single Crystals, and for Fused Silica," Journal of Applied Physics, vol. 24, pp. 988-997, 1953.
[137] H. Metzger and F. R. Kessler, "Debye-Sears Effect for Determination of Elastic Constants of Silicon," Zeitschrift fur Naturforschung Part A-Astrophysik Physik und Physikalische Chemie, vol. A 25, pp. 904-908, 1970.
[138] M. Agarwal, K. K. Park, S. A. Chandorkar, R. N. Candler, B. Kim, M. A. Hopcroft, R. Melamud, T. W. Kenny, and B. Murmann, "Acceleration sensitivity in beam-type electrostatic microresonators," Applied Physics Letters, vol. 90, pp. 014103-3, 2007.
[139] M. J. Tudor, M. V. Andres, K. W. H. Foulds, and J. M. Naden, "Silicon resonator sensors: interrogation techniques and characteristics," Control Theory and Applications, IEE Proceedings, vol. 135, pp. 364-368, 1988.
[140] G. K. Ho, K. Sundaresan, S. Pourkamali, and F. Ayazi, "Low-motional-impedance highly-tunable I^2 resonators for temperature-compensated reference oscillators," presented at MEMS 2005, the 18th Annual International Conference on Micro Electro Mechanical Systems, Miami, FL USA, 2005.
[141] A. Giridhar, F. Verjus, F. Marty, A. Bosseboeuf, and T. Bourouina, "Electrostatically-driven Resonator on SOI with Improved Temperature Sensitivity," presented at Design, Test, Integration and Packaging of MEMS and MOEMS, Stresa, Lago Maggiore, Italy, 2006.
[142] S. G. Adams, F. M. Bertsch, K. A. Shaw, and N. C. MacDonald, "Independent tuning of linear and nonlinear stiffness coefficients [actuators]," Journal of Microelectromechanical Systems, vol. 7, pp. 172-180, 1998.
[143] W. Ye, S. Mukherjee, and N. C. MacDonald, "Optimal shape design of an electrostatic comb drive in microelectromechanical systems," Journal of Microelectromechanical Systems, vol. 7, pp. 16-26, 1998.
[144] K. B. Lee, L. Lin, and Y.-H. Cho, "A frequency-tunable microactuator with a varied comb-width profile," presented at MEMS '04, the 17th IEEE International Conference on Micro Electro Mechanical Systems, Interlaken, CH, 2004.

[145] J. H. Seo, K. S. Demirci, A. Byun, S. Truax, and O. Brand, "Novel Temperature Compensation Scheme for Microresonators based on Controlled Stiffness Modulation," presented at TRANSDUCERS '07 / Eurosensors XXI, the 14th International Conference on Solid-State Sensors, Actuators and Microsystems, Lyon, France, 2007.
[146] W.-T. Hsu and C. T.-C. Nguyen, "Stiffness-compensated temperature-insensitive micromechanical resonators," presented at MEMS 2002, The 15th IEEE International Conference on Micro Electro Mechanical Systems, Las Vegas, NV USA, 2002.
[147] W.-T. Hsu, J. R. Clark, and C. T.-C. Nguyen, "Mechanically temperature-compensated flexural-mode micromechanical resonators," presented at Electron Devices Meeting, 2000. IEDM Technical Digest. International, 2000.
[148] R. Melamud, M. Hopcroft, C. M. Jha, B. Kim, S. Chandorkar, R. Candler, and T. W. Kenny, "Effects of stress on the temperature coefficient of frequency in double clamped resonators," presented at TRANSDUCERS '05, Solid-State Sensors, Actuators and Microsystems, Seoul, ROK, 2005.
[149] E. Stemme and G. Stemme, "A capacitively excited and detected resonant pressure sensor with temperature compensation," Sensors and Actuators A: Physical, vol. 32, pp. 639-647, 1992.
[150] G. Piazza, R. Abdolvand, and F. Ayazi, "Voltage-tunable piezoelectrically-transduced single-crystal silicon resonators on SOI substrate," presented at MEMS 2003, the 16th Annual International Conference on Micro Electro Mechanical Systems, 2003.
[151] T. Remtema and L. Lin, "Active frequency tuning for micro resonators by localized thermal stressing effects," Sensors and Actuators A: Physical, vol. 91, pp. 326-332, 2001.
[152] R. R. A. Syms, "Electrothermal frequency tuning of folded and coupled vibrating micromechanical resonators," Journal of Microelectromechanical Systems, vol. 7, pp. 164-171, 1998.
[153] F. Verjus, T. Bourouina, E. Belhaire, N. Mauduit, and A. Bosseboeuf, "Modeling and Simulation of a Stiffness-Controlled Micro-Bridge Resonator," presented at MSM '98, the International Conference on Modeling and Simulation of Microsystems, 1998.
[154] Y. S. Touloukian, "Thermophysical properties of matter." New York: IFI/Plenum, 1970.
[155] J. Mallon, personal communication with author, 2005
[156] R. Bechmann, A. D. Ballato, and T. J. Lukaszek, "Higher-Order Temperature Coefficients of the Elastic Stiffness and Compliances of Alpha-Quartz," Proceedings of the IRE, vol. 50, pp. 1812-1822, 1962.
[157] C. Bourgeois, "A new low frequency thermally compensated contour mode resonator," presented at FCS '90, The 44th Annual Symposium on Frequency Control, 1990.
[158] C. S. Lam, C. Y. J. Wang, and S. M. Wang, "A Review of the Recent Development of Temperature Stable Cuts of Quartz for SAW Applications " presented at Symposium on Piezoelectricity, Acoustic Waves, and Device Applications, Ningbo, Zhejiang, China, 2004.
[159] M. Takagi, E. Momosaki, M. Yamakita, and N. Oura, "K-cut quartz SAW resonators for stable frequency sources," IEEE Transactions on Ultrasonics, Ferroelectrics and Frequency Control, vol. 45, pp. 328-337, 1998.
[160] C. Frondel, The System of Mineralogy, vol. III, Silica Minerals, Seventh ed. New York: John Wiley and Sons, Inc., 1962.
[161] Fox Electronics, "Quartz Crystal Theory of Operation", 2004
[162] TXC Corporation, "Technical Terminology", http://www.txc.com.tw/en/d_support/01.html
[163] S. Spinner and G. W. Cleek, "Temperature Dependence of Young's Modulus of Vitreous Germania and Silica," Journal of Applied Physics, vol. 31, pp. 1407-1410, 1960.
[164] N. Faouzi, J. M. Saurel, J. Lassale, and G. Cambon, "Temperature Coefficients of the Elastic Constants of SiO2 Layers," Sonics and Ultrasonics, IEEE Transactions on, vol. 32, pp. 596-599, 1985.
[165] G. Cambon, E. L. Adler, J. Attal, and W. Shahab, "Temperature Effects on Acoustic Surface Wave Devices on Silicon," presented at Ultrasonics Symposium, 1979.
[166] M. B. Othman and A. Brunnschweiler, "Electrothermally Excited Silicon Beam Mechanical Resonators," Electronics Letters, IEE, vol. 23, pp. 728-730, 1987.
[167] F. Shen, P. Lu, S. J. O'Shea, K. H. Lee, and T. Y. Ng, "Thermal effects on coated resonant microcantilevers," Sensors and Actuators A: Physical, vol. 95, pp. 17-23, 2001.

[168] Y. Yoshino, M. Takeuchi, K. Inoue, T. Makino, S. Arai, and T. Hata, "Control of temperature coefficient of frequency in zinc oxide thin film bulk acoustic wave resonators at various frequency ranges," Vacuum, vol. 66, pp. 467-472, 2002.
[169] R. Sandberg, W. Svendsen, K. Mølhave, and A. Boisen, "Temperature and pressure dependence of resonance in multi-layer microcantilevers," Journal of Micromechanics and Microengineering, pp. 1454-1458, 2005.
[170] Y. Hongyu, P. Wei, Z. Hao, and K. Eun Sok, "Film bulk acoustic resonator at 4.4 GHz with ultra low temperature coefficient of resonant frequency," presented at MEMS 2005, the 18th Annual International Conference on Micro Electro Mechanical Systems, Miami, FL USA, 2005.
[171] W. Pang, H. Yu, H. Zhang, and E. S. Kim, "Temperature-compensated film bulk acoustic resonator above 2 GHz," Electron Device Letters, vol. 26, pp. 369-371, 2005.
[172] R. Melamud, B. Kim, M. A. Hopcroft, S. Chandorkar, M. Agarwal, C. M. Jha, and T. W. Kenny, "Composite Flexural-mode Resonator with Controllable Turnover Temperature " presented at MEMS 2007, The 20th IEEE International Conference on Micro Electro Mechanical Systems, Kobe, Japan, 2007.
[173] R. Melamud, B. Kim, S. A. Chandorkar, M. A. Hopcroft, M. Agarwal, C. M. Jha, and T. W. Kenny, "Temperature-compensated high-stability silicon resonators," Applied Physics Letters, vol. 90, pp. 244107-3, 2007.
[174] M. A. Huff, S. D. Senturia, and R. T. Howe, "A thermally isolated microstructure suitable for gas sensing applications," presented at Hilton Head 1988, the IEEE Solid-State Sensor and Actuator Workshop, Hilton Head, SC USA, 1988.
[175] M. Parameswaran, A. M. Robinson, D. L. Blackburn, M. Gaitan, and J. Geist, "Micromachined thermal radiation emitter from a commercial CMOS process," Electron Device Letters, IEEE, vol. 12, pp. 57-59, 1991.
[176] J. S. Suehle, R. E. Cavicchi, M. Gaitan, and S. Semancik, "Tin oxide gas sensor fabricated using CMOS micro-hotplates and in-situ processing," Electron Device Letters, IEEE, vol. 14, pp. 118-120, 1993.
[177] R. Gooch and T. Schimert, "Low-Cost Wafer-Level Vacuum Packaging for MEMS," MRS Bulletin, vol. 28, pp. 55, 2003.
[178] D. Barrettino, M. Graf, M. Zimmermann, C. Hagleitner, A. Hierlemann, and H. Baltes, "A Smart Single-Chip Micro-Hotplate-Based Gas Sensor System in CMOS-Technology," Analog Integrated Circuits and Signal Processing, vol. 39, pp. 275-287, 2004.
[179] T. Iwaki, J. A. Covington, F. Udrea, S. Z. Ali, P. K. Guha, and J. W. Gardner, "Design and simulation of resistive SOI CMOS micro-heaters for high temperature gas sensors," Journal of Physics: Conference Series, vol. 15, pp. 27-32, 2005.
[180] M. Afridi, A. Hefner, J. Geist, C. Ellenwood, A. Varma, and B. Jacob, "Microhotplate-based sensor platform for standard submicron CMOS SoC designs," presented at International Semiconductor Device Research Symposium, Bethesda, MD, USA, 2005.
[181] C. T.-C. Nguyen and R. T. Howe, "Microresonator Frequency Control and Stabilization Using an Integrated Micro Oven," presented at TRANSDUCERS '93, the International Conderence on Solid-State Sensors and Actuators, Yokohama, Japan, 1993.
[182] C. T. Nguyen, Micromechanical Signal Processors, thesis in Department of Electrical Engineering and Computer Sciences at University of California at Berkeley, 1994.
[183] Y. Sumi, S. Obote, K. Tsuda, K. Syoubu, and Y. Fukui, "Novel fractional-N PLL frequency synthesizer with reduced phase error," presented at IEEE Asia Pacific Conference on Circuits and Systems, 1996.
[184] D. Hillman, "Inherent Benefits of a Delta-Sigma Fractional-N PLL in Power-Conscious SoC Designs," in Chip Design Magazine, vol. February/March, 2007.
[185] C. S. Lam, "An Assesment of the Recent Development of MEMS Oscillators as Compared with Crystal OScillators," presented at Symposium on Piezoelectricity, Acoustic Waves, and Device Applications, Hangzhou, Zhejiang, China, 2006.
[186] F. P. Incropera and D. P. DeWitt, Fundamentals of Heat and Mass Transfer: John Wiley & Sons, Inc., 2002.
[187] Olin Brass, "Copper Alloy Guide", 2005

[188] Epoxy Technology (Epotek), "H20E Data Sheet", 2005
[189] H. F. Wolf, Silicon Semiconductor Data. New York: Pergamon Press 1969.
[190] W. G. Vincenti and C. H. K. Jr., Introduction to physical gas dynamics, N.Y.: Krieger, 1975.
[191] T. Satō, "Spectral Emissivity of Silicon," Japanese Journal of Applied Physics, vol. 6, pp. 339-347, 1967.
[192] N. M. Ravindra, B. Sopori, O. H. Gokce, S. X. Cheng, A. Shenoy, L. Jin, S. Abedrabbo, W. Chen, and Y. Zhang, "Emissivity Measurements and Modeling of Silicon-Related Materials: An Overview," International Journal of Thermophysics, vol. 22, pp. 1593-1611, 2001.
[193] C. Zhang and K. Najafi, "Fabrication of thick silicon dioxide layers for thermal isolation," Journal of Micromechanics and Microengineering, vol. 14, pp. 769-774, 2004.
[194] University of California Berkeley EECS Dept., "SPICE3 Version 3f3", 1993
[195] S. Middelhoek and S. A. Audet, Silicon Sensors. London: Academic Press, 1989.
[196] R. A. Witte, Spectrum and Network Measurements Noble Publishing Corporation, 2001.
[197] MathWorks, "MATLAB WWW page", Published by The Mathworks, Inc., online
[198] M. A. Hopcroft, R. Melamud, R. N. Candler, W.-T. Park, B. Kim, G. Yama, A. Partridge, M. Lutz, and T. W. Kenny, "Active Temperature Compensation for Micromechanical Resonators," presented at Hilton Head 2004, the IEEE Solid-State Sensor, Actuator and Microsystems Workshop, Hilton Head, SC USA, 2004.
[199] M. A. Hopcroft, M. Agarwal, K. K. Park, B. Kim, C. M. Jha, R. N. Candler, R. Melamud, G. Yama, B. Murmann, and T. W. Kenny, "Temperature compensation of a MEMS resonator using Quality Factor as a thermometer," presented at MEMS 2006, The 19th IEEE International Conference on Micro Electro Mechanical Systems, Istanbul, Turkey, 2006.
[200] M. A. Hopcroft, B. Kim, S. Chandorkar, R. Melamud, M. Agarwal, C. M. Jha, G. Bahl, J. Salvia, H. Mehta, H. K. Lee, R. N. Candler, and T. W. Kenny, "Using the temperature dependence of resonator quality factor as a thermometer," Applied Physics Letters, vol. 91, pp. 013505-3, 2007.
[201] Analog Devices, Inc. Product Catalog, "Part AD8361, TruPwer 2.5 GHz rms detector", 2006
[202] S. Chandorkar, H. Mehta, M. Agarwal, M. A. Hopcroft, C. M. Jha, R. N. Candler, G. Yama, G. Bahl, B. Kim, R. Melamud, K. E. Goodson, and T. W. Kenny, "Non-Isothermal Micromechanical Resonators " presented at MEMS 2007, The 20th IEEE International Conference on Micro Electro Mechanical Systems, Kobe, Japan, 2007.
[203] J. R. Vig, "Temperature-Insensitive Dual-Mode Resonant Sensors - a Review," IEEE Sensors Journal, vol. 1, pp. 62-68, 2001.
[204] J. Věříš, "Temperature compensation of silicon resonant pressure sensor," Sensors and Actuators A: Physical, vol. 57, pp. 179-182, 1996.
[205] C. M. Jha, G. Bahl, R. Melamud, S. A. Chandorkar, M. A. Hopcroft, B. Kim, M. Agarwal, J. Salvia, H. Mehta, and T. W. Kenny, "High resolution microresonator-based digital temperature sensor," Applied Physics Letters, vol. 91, pp. 074101-3, 2007.
[206] W. P. Mason, Physical acoustics and the properties of solids. Princeton, NJ USA: Van Nostrand, 1958.
[207] H. Chandrahalim, D. Weinstein, L. F. Cheow, and S. A. Bhave, "Channel-select micromechanical filters using high-dielectrically transduced MEMS resonators," presented at MEMS 2006, the 19th IEEE International Conference on Micro Electro Mechanical Systems, Istanbul, Turkey, 2006.
[208] J. F. Nye, Physical properties of crystals : their representation by tensors and matrices. Oxford: Oxford University Press, 1985.
[209] J. J. Wortman and R. A. Evans, "Youngs' Modulus, Shear Modulus and Poisson's Ratio in Silicon and Germanium," Journal of Applied Physics, vol. 36, pp. 153-156, 1965.
[210] J. Turley and G. Sines, "The anisotropy of Young's modulus, shear modulus and Poisson's ratio in cubic materials," Journal of Physics D: Applied Physics, vol. 4, pp. 264-271, 1971.
[211] K. Y. Kim, R. Sribar, and W. Sachse, "Analytical and optimization procedures for determination of all elastic constants of anisotropic solids from group velocity data measured in symmetry planes," Journal of Applied Physics, vol. 77, pp. 5589-5600, 1995.
[212] W. A. Brantley, "Calculated elastic constants for stress problems associated with semiconductor devices," Journal of Applied Physics, vol. 44, pp. 534-535, 1973.

[213] H. J. McSkimin and J. P. Andreatch, "Elastic Moduli of Silicon vs Hydrostatic Pressure at 25.0 °C and - 195.8 °C," Journal of Applied Physics, vol. 35, pp. 2161-2165, 1964.
[214] J. C. Suhling, R. A. Cordes, Y. L. Kang, and R. C. Jaeger, "Wafer-level calibration of stress sensing test chips," presented at ECTC '94: The 44th Electronic Components and Technology Conference, 1994.
[215] S. Timoshenko and S. Woinowsky-Krieger, Theory of Plates and Shells, 2nd ed: McGraw-Hill, Inc., 1959.
[216] M. A. Hopcroft, MAT-Test: A New Method for Thin-film Materials Characterization, thesis in Engineering at University of Cambridge, 2002.
[217] Course MSE353 - Mechanics of Thin Films, W. D. Nix, Stanford University, Spring, 2005
[218] J. Diz and M. Humbert, "Practical aspects of calculating the elastic properties of polycrystals from the texture according to different models," Journal of Applied Crystallography, vol. 25, pp. 756-760, 1992.
[219] W. N. Sharpe, Jr., B. Yuan, and R. L. Edwards, "A new technique for measuring the mechanical properties of thin films," Journal of Microelectromechanical Systems, vol. 6, pp. 193-199, 1997.
[220] A. George, "Elastic constants and moduli of diamond cubic Si," in Properties of Crystalline Silicon, vol. 20, EMIS Datareviews, R. Hull, Ed. London: INSPEC, IEE, 1997, pp. 98.
[221] J. Turley and G. Sines, "Representation of Elastic Behavior in Cubic Materials for Arbitrary Axes," Journal of Applied Physics, vol. 41, pp. 3722-3725, 1970.
[222] L. J. Walpole, "The elastic shear moduli of a cubic crystal," Journal of Physics D: Applied Physics, vol. 19, pp. 457-462, 1986.
[223] R. W. Keyes, "The Electronic Contribution to the Elastic Properties of Germanium," IBM Journal of Research and Development, vol. 5, pp. 266, 1961.
[224] J. J. Hall, "Electronic effects in the constants of n-type silicon," Physical Review, vol. 161, pp. 756, 1967.
[225] K. Shanker and N. D. Tripathi, "Acoustical investigation in pure and doped n-type germanium and silicon," Journal of the Acoustical Society of India, vol. 6, pp. 62-4, 1978.
[226] H. J. McSkimin, W. L. Bond, E. Buehler, and G. K. Teal, "Measurement of the Elastic Constants of Silicon Single Crystals and Their Thermal Coefficients," Physical Review, vol. 83, pp. 1080, 1951.
[227] C. Bourgeois, J. Hermann, N. Blanc, N. F. de Rooij, and F. Rudolf, "Determination Of The Elastic Temperature Coefficients Of Monocrystalline Silicon," presented at TRANSDUCERS '95 / Eurosensors IX, Solid-State Sensors and Actuators, 1995. The 8th International Conference on, 1995.
[228] W. N. Sharpe, Jr., M. A. Eby, and G. Coles, "Effect of Temperature on Mechanical Properties of Polysilicon," presented at TRANSDUCERS ‘01 / Eurosensors XV, The 11th International Conference on Solid-State Sensors and Actuators, Munich, Germany, 2001.
[229] W.-T. Park, Encapsulated Sub-Millimeter Piezoresistive Accelerometers for Biomedical Applications, thesis in Mechanical Engineering at Stanford University, 2005.
[230] F. L. Walls and D. W. Allan, "Measurements of frequency stability," Proceedings of the IEEE, vol. 74, pp. 162-168, 1986.
[231] S. R. Stein, "Frequency and Time- Their Measurement and Characterization," in Precision Frequency Control, vol. 2, E. A. Gerber and A. Ballato, Eds. New York: Academic Press, 1985, pp. 191-416.
[232] W. J. Riley, Presentation: "Techniques for Frequency Stability Analysis", given at FCS Tutorial Sessions, 2003
[233] W. J. Riley, "A test suite for the calculation of time domain frequency stability," presented at FCS '95, The 1995 IEEE International Frequency Control Symposium, San Francisco, CA USA, 1995.
[234] J. A. Barnes and D. W. Allan, "Variances Based on Data with Dead Time Between the Measurements," T. a. F. Division, Ed.: National Institutes of Standards and Technology, 1990, pp. 40.